Modelling, design and testing of a multi-antagonistic and hysteretic mechanism driven by shape memory alloy wires

Rym Boufayed

Université Clermont Auvergne

École Doctorale Sciences Pour l'Ingénieur
Specialty "Materials"

Ph.D. Thesis

Modelling, design and testing of a multi-antagonistic and hysteretic mechanism driven by shape memory alloy wires

Presented by

Miss. Rym BOUFAYED

Thesis submitted in partial fulfilment of the
requirements for the Degree of
"Doctor of Philosophy in Mechanical Engineering"

Defended on April 6, 2021 in front of the jury composed of:

Mr. Abdelfattah Mlika	Professor, Université de Sousse (Tunisie)	Reporter
Mr. Jérôme Szewczyk	Professor, Université de Sorbonne	Reporter
Mr. Benoît Blaysat	Professor, Université Clermont Auvergne	Examiner
Mrs. Karine Lavernhe-Taillard	Associate Professor HDR, ENS Paris Saclay	Examiner
Mr. Frédéric Chapelle	Associate Professor HDR, SIGMA Clermont	Co-supervisor
Mr. Xavier Balandraud	Professor, SIGMA Clermont	Supervisor
Mr. Jean-François Destrebecq	Professor, Université Clermont Auvergne	Invited

Institut Pascal- M3G department
UMR 6602 Université Clermont Auvergne, CNRS, Clermont Auvergne INP, F-63000
Clermont-Ferrand, France

"If we knew what it was we were doing, it would not be called research, would it?" — *Albert Einstein*

To mom, to dad,
To my sister and brothers
To my family and friends
To everyone who believed in me

Acknowledgements

About three years and five months ago, I started a doctoral adventure with lots of motivation and determination to fulfill one of my dreams. It was an exciting bumpy adventure full of surprises, pressure, lessons, feelings and discoveries. These few pages would not be enough to describe what I felt, did and experienced as a PhD candidate. At the end of this journey, although I could hardly find fitting words, I would like to acknowledge the persons to whom I am grateful.

This thesis was funded by a ministerial scholarship MESRI.

Firstly, I would like to sincerely thank the members of my jury for accepting to examine my dissertation, as well as for their time and remarks. I would like to express my deepest appreciation to my committee chair and examiner *Prof. Dr. Benoît Blaysat* for all the fruitful discussions that we have had. I am genuinely thankful to *Prof. Dr. Abdelfattah Mlika* and *Prof. Dr. Jérôme Szewczyk* who patiently reviewed this thesis as reporters and gave their insightful and valuable comments and for their positive and meticulous feedbacks. I am delighted to thank *Dr. Karine Lavernhe-Taillard* not only for kindly examining my thesis but also for her gentle yet generous behavior which put me immediately at ease to exchange with her.

Particularly, I would like to warmly give my gratitude to my supervisors for their patience, guidance and sharing their know-how. I would like to thank *Prof. Dr. Xavier Balandraud*, my thesis supervisor, for proposing me this thesis, giving me the wonderful opportunity to visit Thailand as an invited researcher, for allowing me teach and mentor. To Xavier, the passionate scientist and the humble colleague, thank you for your uncompromising commitment in the follow-up of my thesis, for your encouragement, for the sleepless nights and weekends we were working together before deadlines, I have learned a lot from you. My sincere gratitude also goes to *Dr. Frédéric Chapelle*, my co-supervisor, for sharing with me the ABCs of research during the first year of my thesis, for all the relevant questions he has asked me and for allowing me to teach and mentor. To Frédéric, the knowledgeable mentor, thank you for pointing out my shortcomings and helping me tackle them. I am earnestly thankful to *Prof. Dr. Jean-François Destrebecq*, my co-supervisor, for taking me as his last PhD student before retiring, for his calm

and composed attitude but mostly for his well-structured and wise ideas that cleared, at many times, ambiguous situations.

I address my thanks to *Mrs. Évelyne Gil*, the director of Institut Pascal and *Mrs. Sophie Commereuc*, the director of Sigma-Clermont for having welcomed me during these years of thesis. I would like to thank all the members of Institut Pascal, Sigma-Clermont and Université Clermont Auvergne that I had met and with whom I shared very pleasant moments. A big thank you to the administrative staff always helpful, friendly, smiling and especially professional. I particularly think of *Mrs. Jacqueline Madebene* for always being there when needed professionally and emotionally. I also would like to thank the technical staff of Sigma Clermont for their help during the experimentations: *Mr. Clément Weigel*, *Mr. Alexis Gravier*, *Mrs. Mylène Rozelier* and *Mr. Benoit Creugny-Bellec.*

To my fellow lab-mates, I would like to say a very special thank you for the fun, support, motivation and stimulating discussions. You made this journey memorable! My sincere thanks go to the "Coffee Team": *Zine*, *Corentin*, *Dimitri*, *Quentin*, *Siddharth* and *Antoine* with whom I shared way more than just an office. I want to thank the other colleagues and friends of Sigma-Clermont, especially *Chahrazed*, *Dana*, *Dong*, *Nataliya*, *Montassar*, *Asia*, *Amir*, *Jean-Baptiste*, *Jean-Charles*, etc. I would like to thank my intern *Mapan*.

I am tremendously thankful to my amazing friends from high school, engineering school and Clermont-Ferrand for encouraging me and helping me relieve the stress and pressure of my academic life.

Last but not least, fulfilling this journey would not be possible without my extraordinary family. It was difficult to do a PhD far from home, all alone in a different country and continent. However, no matter how far apart we were, we were always so close! Thus, I would like to thank my dear parents, *Abderrazak* and *Rafika* for their unfailing support, encouragement, unconditional love and confidence. I am endlessly indebted to both of you and I hope through this thesis, you would be, once again, proud of me. To my lovely sister *Sarah* and to my two supporting brothers *Mohamed Ali* and *Ghassen* thank you for being there for me, I love you to the moon and back. I also would like to thank my grandparents for their invocations, my aunts and uncles for their support and all my family members.

Finally, I would like to thank all those who have contributed in any way to the fulfillment of this work.

Yours lovely,
Rym Boufayed

"Translating is always about making sacrifices; however, nothing essential should be sacrificed." — Enrique Diez-Canedo

Extended French summary: Résumé étendu

Modélisation, conception et expérimentation d'un mécanisme multi-antagoniste et hystérétique actionné par des fils en alliage à mémoire de forme

Sommaire

I. Contexte v
II. Positionnement par rapport à l'état d'art vi
II.1. Généralités sur le Nickel – Titane : un alliage à mémoire de forme (AMF) vi
II.1.a. Le Nickel-Titane : un matériau intelligent vi
II.1.b. Les avantages et les limites d'AMF vii
II.1.c. Une transformation de phase solide-solide vii
II.2. Propriétés thermomécaniques inédites pour un alliage viii
II.3. Applications des AMF x
II.3.a. Les AMF dans plusieurs secteurs x
II.3.b. Applications robotiques des actionneurs à base d'AMF xii
II.4. Positionnement par rapport à l'état d'art xiv
III. Étude numérique par EF d'un mécanisme d'actionnement multi-antagoniste xvi
III.1. Cahier de charges de l'étude numérique xvi
III.2. Modélisation sous Ansys APDL xvi
III.2.a. Étapes préliminaires xvi
III.2.b. Configurations d'activation possibles xvii
III.3. Espace de travail discret xix
III.4. Influence des paramètres d'activation xx
III.4.a. Influence de l'angle α (avec εpre fixée à 3 %) xx
III.4.b. Influence du pré-étirement εpre (avec α fixé) xxii
III.5. Effet d'attraction et rigidité variable xxii
III.5.a. Effet d'attraction xxiii

III.5.b. Rigidité variable xxiv
IV. Conception d'un démonstrateur et préparation des fils AMF xxv
IV.1. Conception du démonstrateur xxv
IV.2. Caractérisation et entraînement mécanique de fils AMF xxvi
IV.3. Mise en place et pré-étirement des fils AMF xxvi
IV.3.a. Mise en place des fils AMF xxvii
IV.3.b. Pré-étirement des fils AMF xxviii
V. Expérimentations et résultats xxix
V.1. Analyse thermique préliminaire xxix
V.2. Cas d'étude simple : Rotation et translation cycliques expérimentales xxx
V.2.a. Rotation cyclique pour εpre= 1,6% et α = 90° xxx
V.2.b. Translation cyclique pour εpre = 1,6% et α = 60° xxxi
V.3. Espace de travail discret et effet d'attraction xxxii
V.3.a. Espace de travail discret pour εpre = 3,25% et α = 60° xxxii
V.3.b. Effet d'attraction expérimental pour εpre = 1,6% et α = 60° xxxii
V.4. Application d'une séquence thermique complexe et rigidité variable expérimentale xxxiii
V.4.a. Application d'une séquence thermique complexe xxxiii
V.4.b. Rigidité variable expérimentale xxxiv
VI. Conclusions et perspectives xxxiv
VI.1. Conclusions xxxiv
VI.2. Perspectives xxxv

I. Contexte

Afin de répondre à l'évolution exponentielle des besoins du marché industriel et des contraintes économiques et écologiques, les scientifiques ne cessent de chercher des nouveaux idées et concepts afin d'inventer et concevoir des solutions. Parmi plusieurs méthodes pour ce faire, intégrer des matériaux intelligents, également appelés matériaux actifs ou réactifs, dans des produits mécaniques, mécanismes et structures semble attirer l'intérêt de la communauté scientifique. Ceci est justifié par leur capacité de changer de forme ou de propriétés physiques sous l'influence de stimuli externes tels que température, contrainte, lumière, champs électriques, etc.

Particulièrement, les alliages à mémoire de forme (AMF) font partie de matériaux actifs capables de récupérer une forme pré-déformée lors du chauffage. Grâce à leurs caractéristiques thermomécaniques intéressantes, les AMF sont de plus en plus utilisés dans différents domaines et applications tels que des actionneurs dans des systèmes robotiques.

La littérature présente de nombreux actionneurs linéaires pilotés par des AMF. C'est un résultat logique vu qu'un AMF se rétrécit en le chauffant et s'allonge en le refroidissant, donc c'est facile de créer une translation. En outre, des actionneurs rotatifs à base des AMF ont été développés en transformant le mouvement prismatique des éléments AMF en une rotation. D'autres actionneurs intégrant des AMF à plusieurs degrés de liberté (ddl) existent aussi, comme pinces, origami, et robots parallèles. Cependant, les composants AMF sont pour la plupart arrangés parallèlement ou en série sans une étude appropriée de l'effet hystérétique d'AMF. L'influence des paramètres géométriques de l'agencement des éléments AMF est aussi sous-étudiée. Compte tenu des informations et des connaissances acquises sur les AMF dans des systèmes antagonistes et parallèles, cette thèse a pour objectif de créer un mécanisme actif précontraint actionné par des fils AMF multi-antagonistes à plusieurs degrés de liberté.

L'idée initiale était de concevoir une structure active avec plusieurs ddl, puis a été affinée pour avoir une plateforme mobile (flexible ou rigide) qui sera attachée à plusieurs fils AMF agissant en tant qu'actionneurs. On peut noter que le manque d'intérêt d'utiliser des actionneurs AMF multi-antagonistes dans des mécanismes parallèles s'explique par la réponse non linéaire et hystérétique de ce type de matériau, qui dépend fortement des paramètres d'actionnement. Par conséquent, les AMF ont été principalement utilisés dans des systèmes simples à un seul degré de liberté. Certainement, on sait que des technologies matures traitant des

mécanismes planaires sont largement disponibles et que des mécanismes précontraints utilisant des fils AMF existent déjà. Cependant, le positionnement multi-antagoniste des fils AMF dans un mécanisme planaire précontraint et l'exploration de l'influence des paramètres géométriques et mécaniques constituent la nouvelle approche abordée dans cette thèse.

Dans ce qui suit, seule l'analyse statique est envisagée en utilisant plusieurs configurations de chauffage où les fils AMF sont activés thermiquement. Bien que le mécanisme étudié soit très similaire à un robot à câble, son comportement est assez différent.

Ce résumé étendu fournit, dans un premier temps, des informations utiles sur l'alliage à mémoire de forme à base de nickel-titane et son phénomène physique afin de comprendre au mieux le fonctionnement du mécanisme étudié dans ce travail de recherche. En outre, on présente une synthèse succincte des applications les plus connues des AMF en tant qu'actionneurs, en particulier en robotique.

Dans un deuxième temps, on résume l'étude numérique par éléments finis qui analyse les propriétés hystérétiques et multi-antagonistes du mécanisme étudié à l'aide d'un modèle de matériau fourni par le logiciel Ansys. Plusieurs cas d'étude sont menés pour prouver différents concepts et en explorer d'autres.

Par la suite, des étapes intermédiaires mais cruciales pour la mise en œuvre d'un démonstrateur physique et la préparation préliminaire des fils AMF sont présentées, faisant le lien entre les résultats numériques et les essais expérimentaux.

Cette synthèse s'achève par une présentation du dispositif expérimental, une discussion des résultats et une comparaison avec les résultats numériques. Une analyse thermique préalable est effectuée. Plusieurs cas d'étude expérimentaux sont abordés : rotation et translation cycliques, espace de travail à actionnement binaire discret, effet d'attraction et rigidité variable.

II. Positionnement par rapport à l'état d'art

II.1. Généralités sur le Nickel – Titane : un alliage à mémoire de forme (AMF)

II.1.a. Le Nickel-Titane : un matériau intelligent

Un alliage à mémoire de forme (AMF) est un matériau actif capable de récupérer une forme pré-déformée par simple chauffage. Mais, il a d'autres propriétés mécaniques exceptionnelles pour un métal tels que sa superélasticité et son amortissement.

On peut distinguer plusieurs types d'AMF selon leur composition chimique. Principalement, on trouve des AMF à base de cuivre, à base de fer et à base de nickel-titane. On s'intéresse dans cette thèse aux AMF à base de nickel-titane souvent nommés « nitinol » faisant référence à leur établissement de découverte de leur mémoire de forme (Naval Ordnance Laboratory) ou encore NiTi. Ce choix d'AMF se justifie par le fait que ce sont les AMF les plus connus et les plus utilisés grâce à leurs paramètres thermomécaniques. Néanmoins, ils restent délicats à manipuler à cause de leur comportement variable en fonction de leur composition chimique, leur procédé de fabrication, du fournisseur, etc. On peut trouver des AMF sous des formes classiques, généralement des fils ou des ressorts mais aussi des tubes, lamelles, mailles, etc. Grâce à l'émergence de l'impression 3D métallique, des formes complexes des éléments AMF sont de plus en plus étudiées.

II.1.b. Les avantages et les limites d'AMF

Comme tous les matériaux, le nitinol présente des avantages et des limites. Parmi les qualités de NiTi, on peut citer son coût relativement faible, son mode de fonctionnement silencieux, sa biocompatibilité, sa simple activation par effet Joule, sa grande déformation réversible pour un métal de l'ordre de 10%, sa compacité, sa puissance, etc. Tous ces avantages expliquent l'intérêt de l'intégrer dans des mécanismes divers pour des applications prometteuses. Néanmoins, il reste un matériau complexe à modéliser à cause de sa réponse non-linéaire et hystérétique ainsi que son couplage thermomécanique, et donc, complexe à contrôler. Parmi les difficultés d'AMF, on a la difficulté de coupler à la fois l'isolation thermique et électrique des éléments AMF dans des systèmes et la difficulté d'assurer un bon serrage mécanique. Par conséquence, c'est plus compliqué de choisir un arrangement complexe des AMF. Dans ce travail de recherche, on essaye d'explorer, identifier et résoudre ces difficultés.

II.1.c. Une transformation de phase solide-solide

Avant de donner un aperçu sur les propriétés thermomécaniques d'AMF, il est plutôt intéressant de commencer par le phénomène physique derrière son comportement qui est une transformation de phase solide-solide. Un AMF se caractérise par deux phases principales ayant chacune un système cristallin différent : une phase mère à « haute » température et une phase fille à « basse » température, nommées respectivement par convention *austénite* (A) et *martensite* (M). On note que la phase « R » d'AMF n'est pas prise en compte dans ces travaux de recherche. On compte 24 variantes de martensite résultant d'un mécanisme de

cisaillement au sein du matériau, faisant naissance à des micro-maclages. Selon les proportions des variantes, on distingue deux formes de martensite : *martensite auto-accommodante* formée par toutes les variantes en proportions égales caractérisée par une forme macroscopique inchangée et *martensite orientée* lorsqu'on a quelques variantes dominantes et donc une déformation macroscopique.

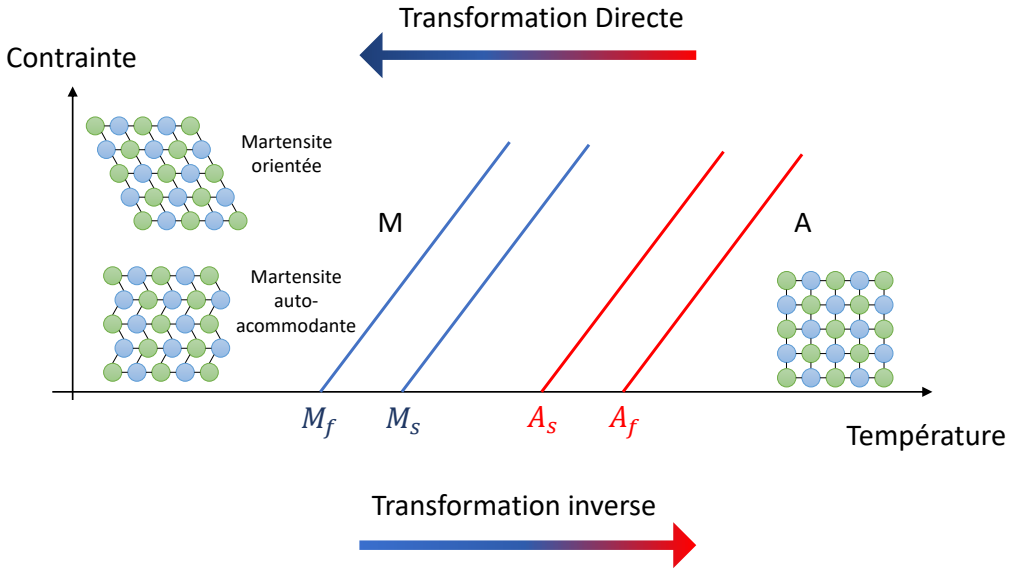

Figure II-1. Diagramme contrainte-température de la transformation de phase.

La transformation martensitique est caractérisée par quatre températures clés : *austenite start* (A_s), *austenite finish* (A_f), *martensite start* (M_s) et *martensite finish* (M_f). La Figure II-1 montre les deux transformations de phase nommées par convention *transformation directe* : de l'austénite vers la martensite et *transformation inverse* : de la martensite vers l'austénite.

Cette transformation de phase donne naissance à des propriétés thermomécaniques inédites pour un alliage et qui dépendent du chargement suivi.

II.2. Propriétés thermomécaniques inédites pour un alliage

La Figure II-2 illustre le principe derrière les trois principales propriétés d'AMF qui sont : l'effet d'amortissement, la superélasticité (SE) et la mémoire de forme (SME).

Le nitinol présente des bonnes propriétés d'amortissement lorsqu'il est en état martensitique mais encore des meilleures propriétés lorsqu'on a une coexistence de martensite et d'austénite. C'est dans ce cas-ci que le frottement interne au sein de l'AMF est maximal.

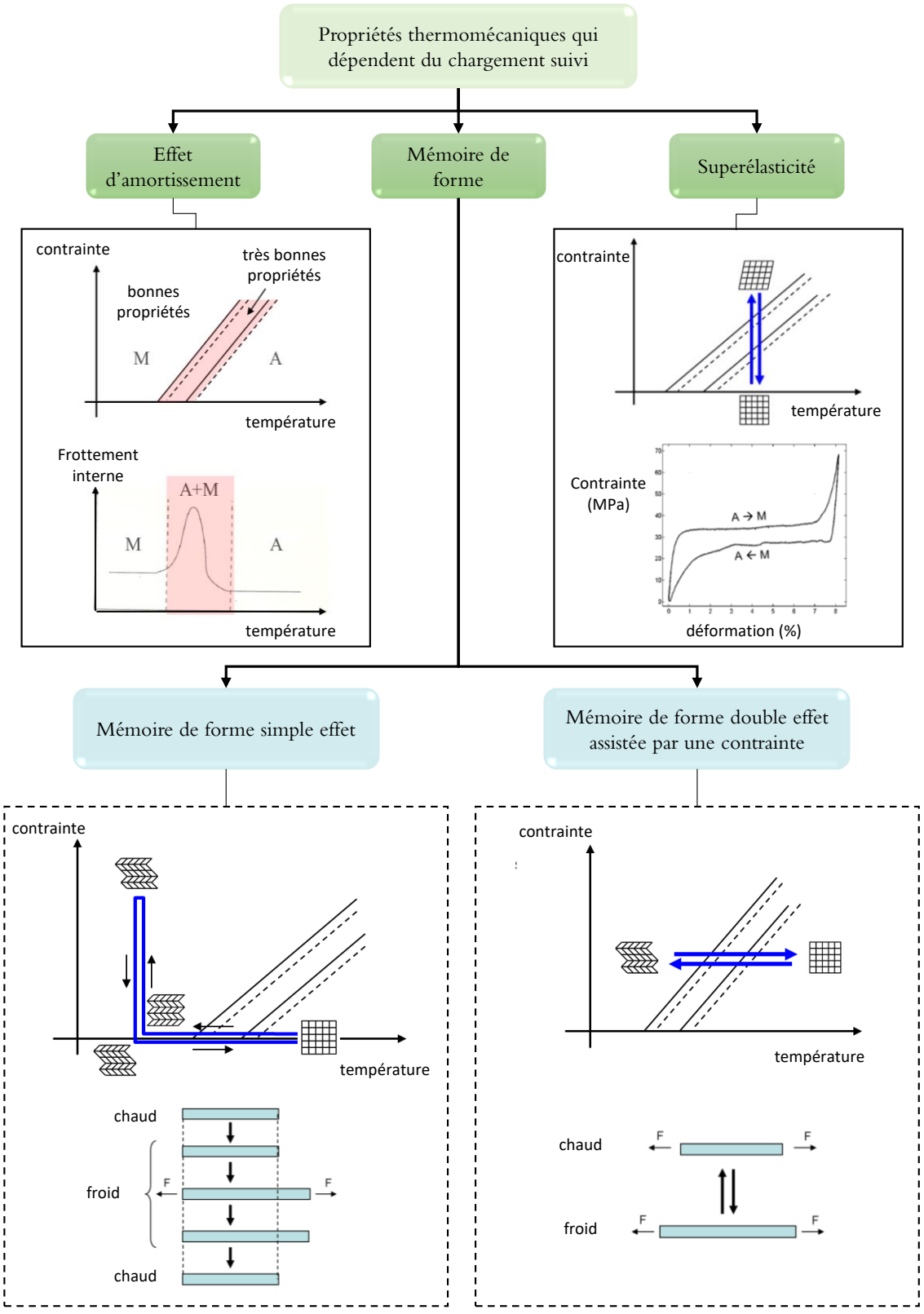

Figure II-2. Propriétés thermomécaniques d'un AMF.

La superélasticité est une propriété largement utilisée dans les applications d'AMF et elle est le résultat d'un chargement mécanique à température constante. Par conséquent, la martensite orientée est créée. Dans ce cas, la déformation

macroscopique peut aller jusqu'à 10 %. Cette déformation est totalement réversible après l'annulation de chargement. Quant à la troisième propriété, la mémoire de forme, elle peut exister sous deux formes : un effet mémoire de forme simple sens et un effet mémoire de forme double sens assistée par une contrainte. Pour la mémoire de forme simple sens, il s'agit de mémoriser l'état austénitique. En effet, à partir d'une température supérieure à A_f, on part d'un état austénitique d'AMF et on refroidit à contrainte nulle jusqu'à une température inférieure à M_f où le matériau se transforme en martensite auto-accommodante. Jusqu'à présent, aucune déformation macroscopique n'est observée. Puis, à température constante, on applique un chargement mécanique pour transformer la martensite auto-accommodante en martensite orientée. Ensuite, on décharge, toujours à température constante, et l'AMF reste dans son état de martensite orientée. Après, à contrainte nulle, on chauffe le matériau jusqu'à une température supérieure à A_f et donc on récupère l'état austénitique.

En outre, si on couple la mémoire de forme simple sens avec des forces de rappel, on peut créer un effet mémoire de forme double sens assisté par une contrainte. Cette mémoire double sens permet de mémoriser deux formes. En fait, à partir d'une température supérieure à A_f où l'AMF est à l'état austénitique, on refroidit tout en appliquant une contrainte non nulle jusqu'à une température inférieure à M_f pour avoir la martensite orientée. En réchauffant, on récupère l'état austénitique. Donc grâce à l'alternance de ce chargement thermomécanique, on peut retenir et récupérer deux formes : l'état austénitique et l'état martensite orientée. C'est cet effet de mémoire de forme qui nous intéresse dans cette thèse où les forces de rappel sont remplacées par les configurations multi-antagonistes de fils AMF.
Évidemment, ces propriétés ont contribué davantage à l'intégration des éléments AMF dans plusieurs secteurs et applications

II.3. Applications des AMF

II.3.a. Les AMF dans plusieurs secteurs

Grâce à ses avantages cités dans la section II.1.b. et II.2, l'AMF a fait partie de plusieurs applications. Parmi lesquelles, la Figure II-3 présente quelques exemples dans différents secteurs. On peut citer le pneu superélastique en AMF que NASA's Glenn Research Center développe depuis 2018 pour son robot martien. Ce choix de matériau se justifie par la durabilité d'AMF, sa forte résistance à l'usure et sa déformation réversible. L'AMF semble être un choix intéressant et adapté aux

terrains extrêmement rocheux et aux températures froides de Mars [S. Padula, NASA 2020].

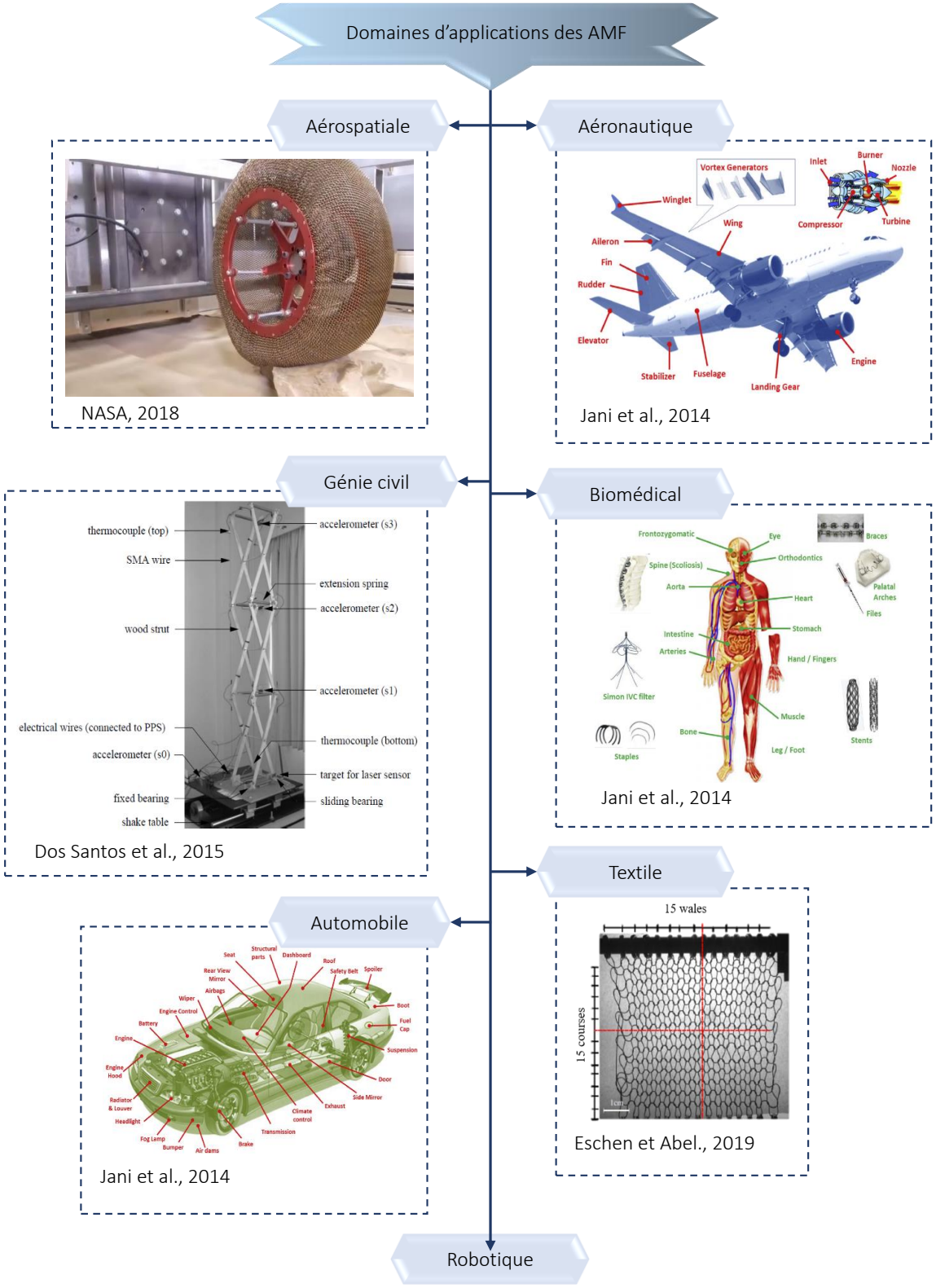

Figure II-3. Exemples d'applications d'AMF dans des domaines variés.

L'AMF a trouvé sa place aussi dans le secteur aéronautique et a été utilisé dans plusieurs composantes d'avions tel que le montre l'illustration proposée par [Jani et al., 2014]. Un autre domaine réglementaire qui a fortement intégré les AMF est le biomédical. Parmi les applications fréquentes d'AMF, on peut citer les appareils orthodontiques, les stents, les agrafes, etc. [Jani et al., 2014].

Pareil que le secteur aéronautique, le secteur automobile intègre aussi les AMF dans des différentes composantes de véhicule : moteur, partie électrique, airbags, rétroviseurs, etc. [Jani et al., 2014]. Dans le génie civil, on peut citer comme exemple la structure active proposée par [Dos Santos et al., 2015] où les AMF ont été utilisés pour un mécanisme de tenségrité reconfigurable. L'AMF a marqué sa présence aussi dans le domaine de textile avec des tissus reconfigurables en maille d'AMF tel que l'exemple proposé par [Eschen et Abel, 2019]. La propriété de la superélasticité est majoritairement utilisée dans ces applications, quant à la mémoire de forme, c'est plutôt dans les applications robotiques qu'elle est la plus utilisée où les AMF agissent en tant qu'actionneurs. Ces sont les applications dans le domaine robotique qui nous intéressent dans ce travail de recherche vu que l'application visée est robotique.

II.3.b. Applications robotiques des actionneurs à base d'AMF

Grâce à la mémoire de forme, les AMF actionnent différents mécanismes robotiques. La Figure II-4 en illustre quelques exemples de la littérature. L'application la plus répandue des AMF dans la robotique est en tant qu'un actionneur linéaire. Ceci s'explique par le fait qu'un AMF se contracte en le chauffant et s'allonge en le refroidissant ce qui rend simple la création d'une translation.

On trouve aussi des actionneurs rotatifs à base d'AMF qui sont désormais possibles grâce à des organes de transformations de mouvement tels que poulie ou encore levier afin de changer le mouvement naturel de translation en une rotation. Une autre solution est de suivre une architecture d'arrangement et d'activation des éléments AMF spécifique pour créer une rotation. Le moteur oscillant présenté par [Hwang et Higachi, 2016] et activé d'une façon alternative des quatre fils en AMF arrangés différentiellement en est un exemple.

En outre, un AMF peut intégrer un robot reconfigurable couplé avec une architecture en origami tel que l'exemple de [Salerni et al., 2016].

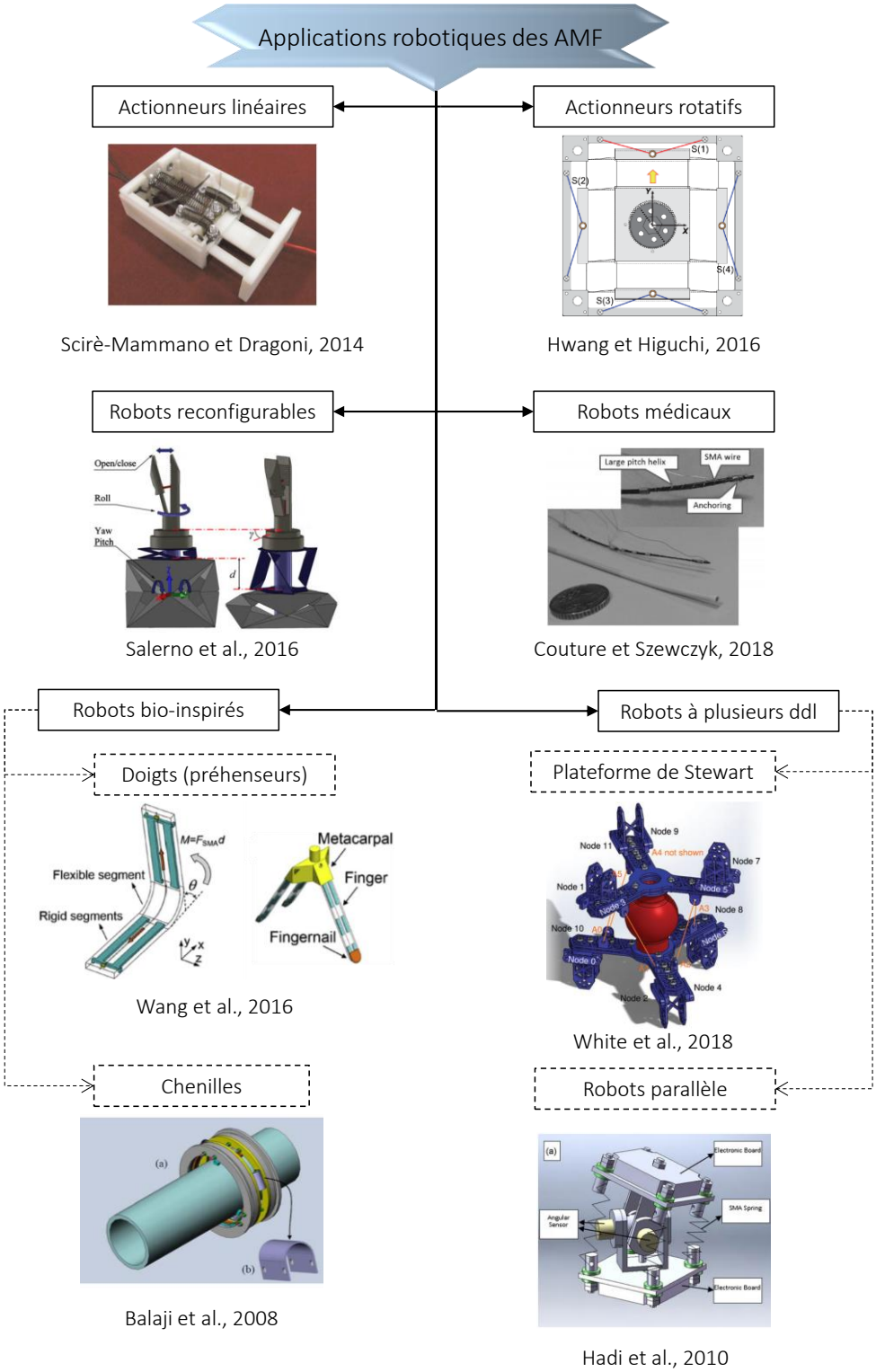

Figure II-4. Exemples d'applications robotiques d'AMF.

Parmi les applications les plus utilisées et récurrentes dans la littérature, on distingue les robots bio-inspirés qui sont principalement des doigts (ou des préhenseurs si on fait une conception modulaire) [Wang er al., 2016] ou encore des chenilles [Balagi et al., 2008].

Grâce à leur biocompatibilité et grande déformation (flexibilité), les AMF sont utilisés pour actionner des robots médicaux type endoscope ou cathéter actif comme l'exemple étudié par [Couture et Szewczyk, 2018]. De plus, on distingue les robots manipulateurs à plusieurs ddl comme les robots parallèles normaux [Hadi et al., 2010] ou les plateformes de Stewart [White et al., 2018] avec des agencements parallèles des fils ou des ressorts d'AMF.

II.4. Positionnement par rapport à l'état d'art

Lorsqu'on a évoqué les difficultés des AMF, on a précisé que la dépendance de son comportement aux paramètres géométriques le rend difficile à modéliser et à manipuler. La Figure II-5 récapitule les principales architectures d'arrangement avec des illustrations de la littérature, à savoir : agoniste-antagoniste, parallèle, circonférentielle, plateforme Stewart, différentielle ou en réseau.

On peut noter qu'on garde "fréquemment" un arrangement dont le fonctionnement est simple à prédire et dont les lois de commande sont plus au moins connues. Cette fois-ci, prenons le cas d'étude présenté par [White et al., 2018] qui est un robot parallèle sous forme de plateforme de Stewart. Les actionneurs sont des ressorts AMF positionnés en parallèle avec un angle non nul. Les auteurs ont constaté des difficultés à prédire les interactions entre les différents ressorts en AMF malgré l'application de commande à cause de la géométrie des superpositions des éléments actifs.

Les conclusions qu'on peut tirer sont la nécessité d'une meilleure compréhension des interactions entre les éléments des matériaux actifs et la nécessité de développer des modèles intégrés pouvant être utilisés à des fins de conception et d'analyse. C'est à partir de ces conclusions, qu'on fixe nos objectifs.

À travers cette thèse, on essaye, d'abord, de modéliser et concevoir un mécanisme actionné par des composants en AMF positionnés en multi-antagonisme, puis à comprendre et explorer l'influence des paramètres d'activation et de l'hystérésis sur les performances de ce mécanisme et enfin de valider les notions acquises à travers un démonstrateur physique.

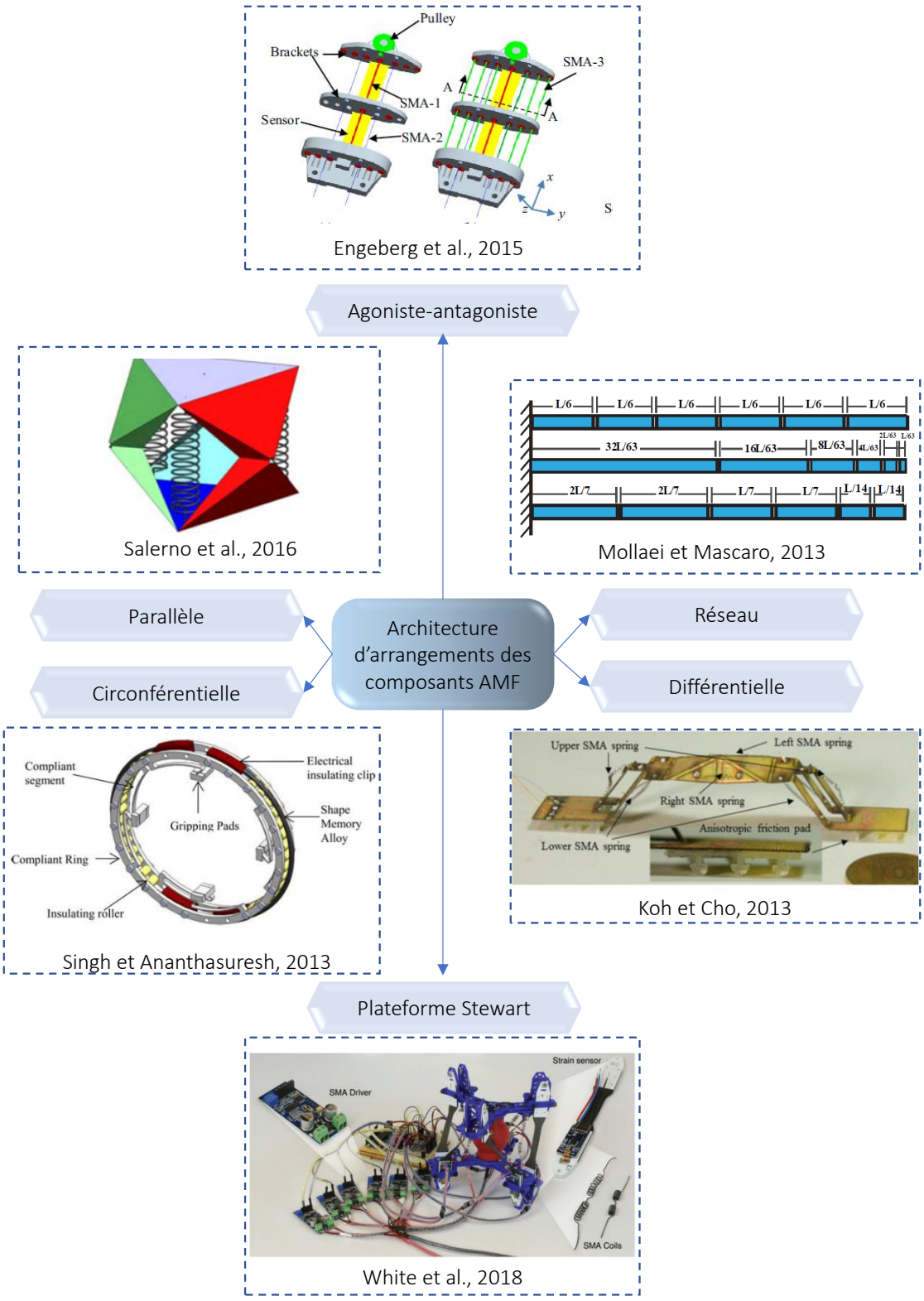

Figure II-5. Exemples des architectures d'arrangements des éléments AMF.

III. Étude numérique par EF d'un mécanisme d'actionnement multi-antagoniste

III.1. Cahier de charges de l'étude numérique

Avant d'entamer l'étude numérique, on fixe notre cahier de charges. On cherche à modéliser un mécanisme ayant trois ddl (deux translations dans le plan et une rotation autour de l'axe perpendiculaire au plan), actionné par six fils AMF de même longueur L et même diamètre fixé à 1 mm, attachés à une plateforme mobile et positionnés suivant une symétrie ternaire rotationnelle comme le montre la Figure III-1. On désigne par α l'angle entre deux fils adjacents. L'architecture de ce mécanisme est similaire à un robot à câble pleinement contraint. Donc, pour avoir n ddl on a besoins d'au moins n+1 actionneurs.

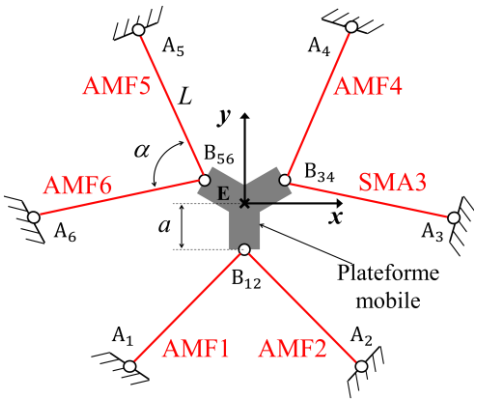

Figure III-1. Le mécanisme plan étudié.

Les fils AMF sont à base de nickel-titane fourni par la société Nimesis (Metz, France) avec Ni50,8-Ti49,2 (en %). La déformation de la transformation maximale de ces fils est de 6 %. Les températures de transformation M_f, M_s, A_s et A_f sont égales respectivement à -25 °C, -7 °C, 24 °C et 36 °C. On procède par une activation thermique binaire avec une température de refroidissement T_{amb} égale à 15 °C et une température d'activation T_1 égale à 100 °C.

III.2. Modélisation sous Ansys APDL

III.2.a. Étapes préliminaires

Pour la modélisation éléments finis de mon mécanisme, j'ai utilisé le modèle thermodynamique tridimensionnel d'Auricchio implémenté sous Ansys APDL (v19). Afin de reproduire la mémoire de forme, on a utilisé l'option MEFF qui

m'offre la possibilité d'avoir des modules d'Young d'austénite et de martensite différents et donc une rigidité variable. L'algorithme de résolution appliqué est non-linéaire avec des analyses statiques. Le même pré-étirement est gardé pour tous les fils tout au long de l'analyse. Trois étapes préliminaires sont respectées pour tous les cas d'étude et qui sont schématisées dans la Figure III-2. On commence toujours à partir d'une température T_1 suffisamment supérieure à A_f pour être sûr que le matériau est 100 % austénite (étape 0). Puis, on applique un retour à l'ambiante jusqu'à T_0 et le matériau reste austénitique vu qu'on est encore supérieur à M_s (étape 1). Troisièmement, on applique le pré-étirement simultanément dans tous les fils (étape 2). On peut choisir de continuer le chargement jusqu'à ce que le matériau se transforme en 100 % martensite ou de décharger pour avoir un retour élastique.

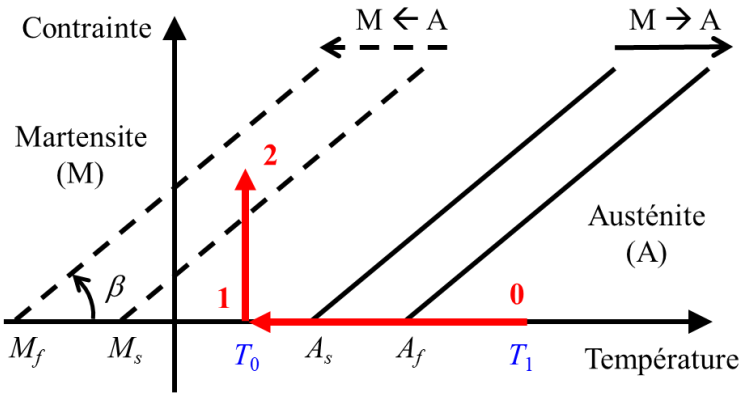

Figure III-2. Diagramme d'état d'un fil AMF en traction.

III.2.b. Configurations d'activation possibles

Comme le nombre des fils AMF a été prédéfini à six fils activés d'une manière binaire, la combinaison de ces deux paramètres (2^6) résulte en 64 configurations possibles illustrées dans la Figure III-3. Ces configurations d'activation peuvent être regroupées selon le nombre de fils qui sont actionnés. Un autre regroupement est possible selon l'amplitude de fonctionnement. D'ailleurs, on peut distinguer trois types de regroupement des configurations : qui offrent la même amplitude de translation et de rotation, qui offrent la même amplitude de translation et pas de rotation ou qui offrent la même amplitude de rotation et pas de translation. On désigne par « 0 » le fil à température ambiante et « 1 » le fil activé. À partir ces 64 configurations, différents cas d'étude sont conçus.

Avant de développer les cas étudiés, un exemple d'activation basique semble intéressant à ce stade pour mieux comprendre la suite. Pour ce faire, je prends

l'exemple de la configuration #24 qui correspond à l'activation simultanée des fils AMF 4, 5 et 6 (000111). Le point de départ est l'état précontraint (étape 2), où tous les fils sont pré-étirés de $\varepsilon_{pre} = 3\,\%$ avec un angle $\alpha = 90°$. Ensuite, les fils 4, 5 et 6 sont chauffés. La Figure III-4 suit le mouvement en vraie grandeur du centre de la plateforme mobile E dans le plan (u_x, u_y). Suite à cette activation, on obtient deux translations u_x et u_y dans le plan et une rotation θ_z autour de l'axe perpendiculaire au plan.

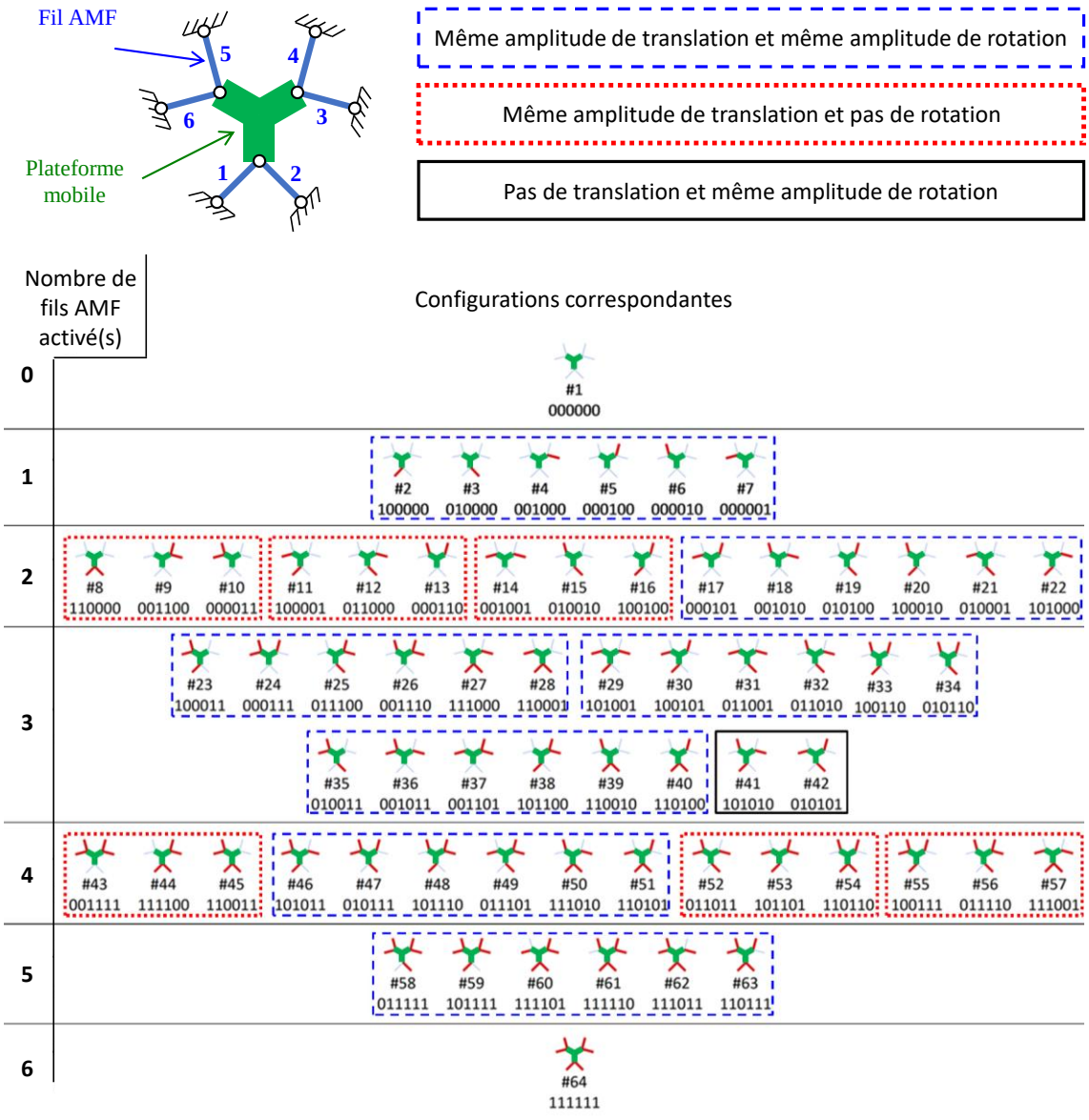

Figure III-3. Configurations d'activation possibles.

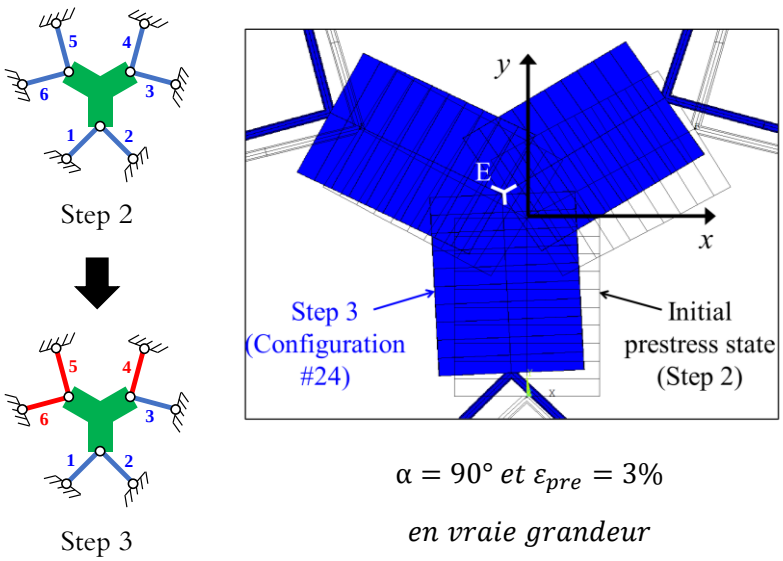

Figure III-4. Exemple d'activation : configuration #24.

III.3. Espace de travail discret

Cette section traite l'espace de travail généré par l'ensemble des 64 configurations d'activation présentées dans la section précédente. La déformation de pré-étirement ε_{pre} est fixée à 3% et l'angle α à 90°. Deux scénarios sont proposés dans la Figure III-5 : le premier consiste à balayer les 64 configurations d'activation et tracer l'espace de travail résultant de l'activation sans retour à l'ambiante et le deuxième consiste à tracer l'espace de travail après retour à l'ambiante. Le cas de l'activation sans retour à l'ambiante résulte en un espace de travail discret qui garde sa symétrie liée à celle du mécanisme. On distingue des poses où on a seulement un déplacement selon u_y telles que les poses correspondantes aux configurations #13, #14, #43, etc. On note aussi des poses avec un déplacement nul dans le plan et qui correspondent aux configurations #41 et #42 offrants une rotation pure ou #1 et #64 où le mécanisme maintient sa position. Les configurations #8-10 présentent des contraintes négatives liées à la géométrie du mécanisme. On suppose que ces poses sont interdites pour éviter le flambement du système. Si on ajoute le retour à l'ambiante à l'étape 4, on remarque une légère descente de pose. Néanmoins, on constate un maintien de la pose atteinte après retour à l'ambiante ce qui rend possible de verrouiller une configuration. Jusqu'à présent, on a fixé les paramètres d'activation, donc l'objectif de la prochaine section est d'étudier l'influence de ces paramètres.

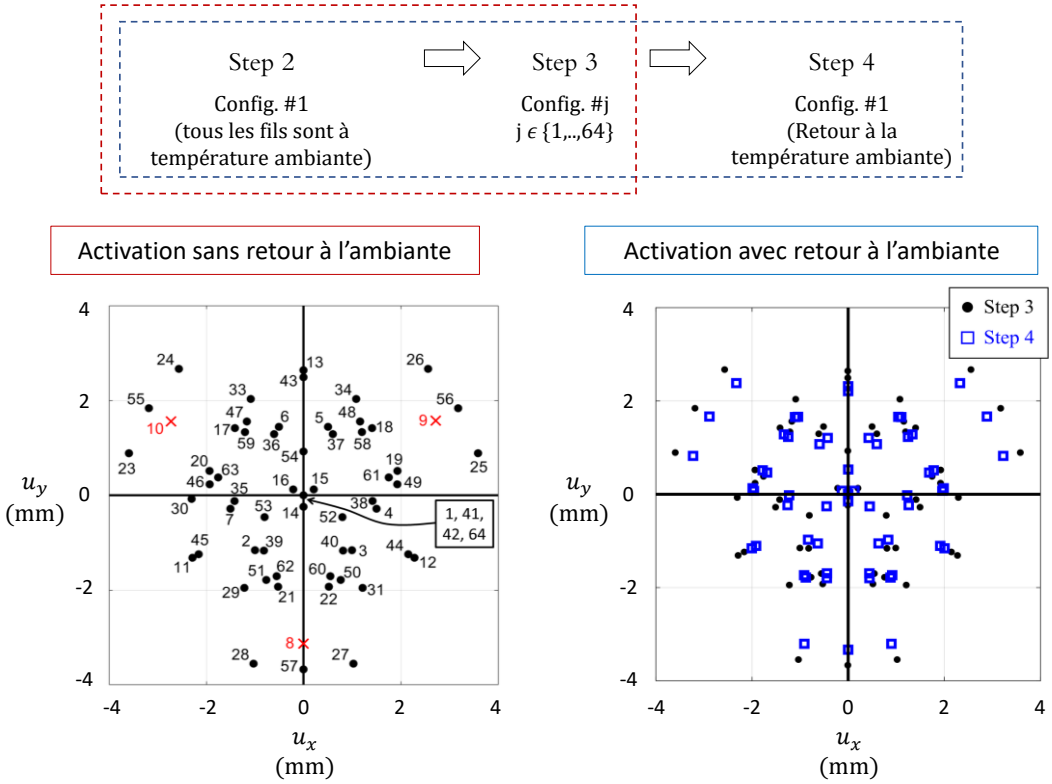

Figure III-5. Espace de travail dans le plan (u_x, u_y) généré par les 64 configurations d'activation sans et avec retour à l'ambiante.

III.4. Influence des paramètres d'activation

Afin d'analyser l'influence des paramètres d'activation, on se sert de cas d'étude simples qui sont la translation pure et la rotation pure. Afin d'obtenir une rotation cyclique, on procède par une activation thermique cyclique de la chaîne d'activation suivante {#1 → #41 (101010) → #1 → #42 (010101)}. La configuration #41 permet d'avoir une rotation dans le sens indirect alors que la configuration #42 permet d'avoir une rotation dans le sens direct. Pour le cas de translation, on considère la chaîne d'activation suivante {#1 → #13 (000110) → #1 → #8 (110000)}. Les configurations #13 et #8 permettent d'avoir respectivement une translation positive et une translation négative selon u_y.

III.4.a. Influence de l'angle α (avec ε_{pre} fixée à 3 %)

Dans le but d'étudier l'influence de l'angle α sur le mouvement de la plateforme, on fixe le reste des paramètres et on suit l'évolution de l'amplitude de rotation en fonction de l'angle en cas de rotation cyclique à travers la variation de l'amplitude rotationnelle maximale $(\Delta\theta_z)_{\max}$ calculée entre l'activation de la configuration #41 et #42 et à travers la variation de l'amplitude rotationnelle

minimale $(\Delta\theta_z)_{\min}$ calculée au retour à l'ambiante de chacune (voir Figure III-6-a). Pareil pour le cas de translation, on suit l'évolution de la variation de l'amplitude de translation maximale $(\Delta u_y)_{\max}$ calculée en l'activation de la configuration #13 et #8 et la variation de l'amplitude de translation minimale $(\Delta u_y)_{\min}$ calculée au retour à l'ambiante de chacune (voir Figure III-6-b). On constate que l'amplitude de rotation augmente en augmentant α, atteint son maximum de l'ordre de 20° pour α=90° et puis diminue. Pour le cas de translation, on note la présence de deux zones grises qui indiquent la présence d'une contrainte négative ou une contrainte supérieure à la limite élastique, donc les angles qui y correspondent sont à éviter. L'amplitude est maximale pour α=60° et diminue à partir de α=131°. On peut noter aussi à titre d'exemple la configuration #8 qui était interdite pour l'angle 90° (voir section III.3) et possible pour un autre angle.

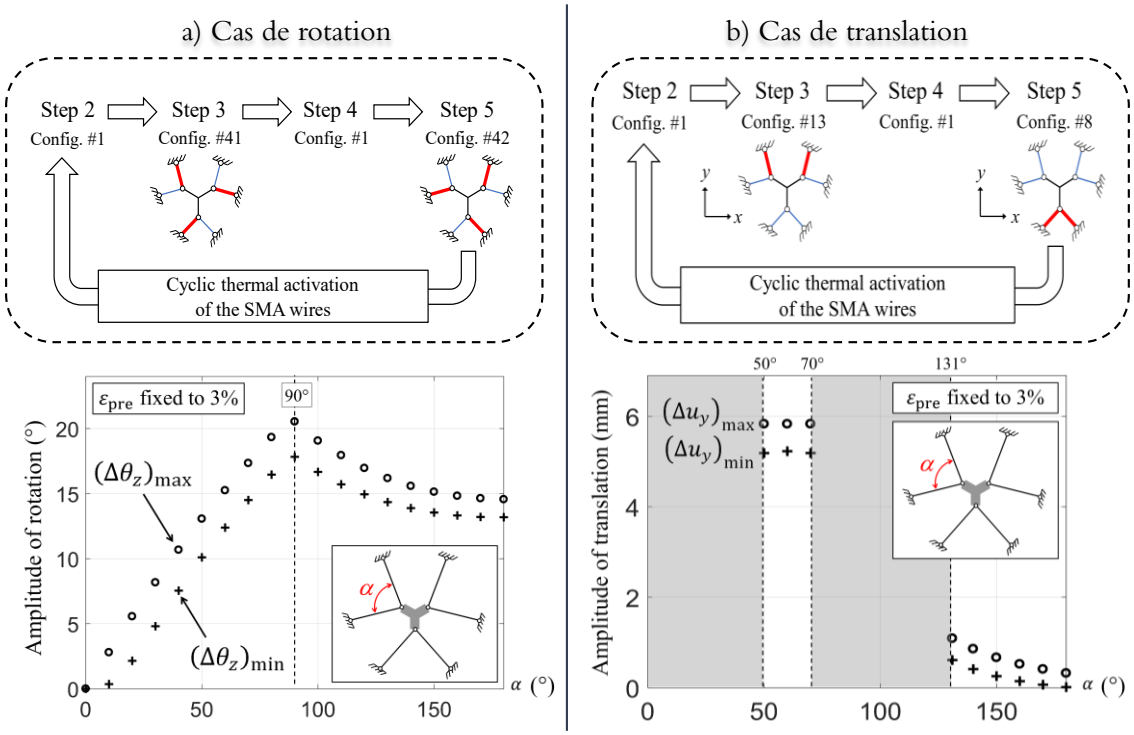

Figure III-6. Évolution des amplitudes de mouvement de la plateforme en fonction de l'angle α pour ε_{pre} = 3% : a) cas de rotation $(\Delta\theta_z)_{max}(\alpha)$ et $(\Delta\theta_z)_{min}(\alpha)$, b) cas de translation $(\Delta u_y)_{max}(\alpha)$ et $(\Delta u_y)_{min}(\alpha)$.

On peut conclure que l'angle optimal pour avoir un maximum de rotation n'est pas le même pour la translation, donc à un certain moment il faut faire des compromis.

III.4.b. Influence du pré-étirement ε_{pre} (avec α fixé)

En utilisant les valeurs optimales de l'angle α et en reprenant les cas de translation et de rotation, on étudie cette fois l'évolution des amplitudes du mouvement en fonction de la valeur de pré-étirement ε_{pre} illustrée dans la Figure III-7. On constate qu'en augmentant ε_{pre}, on gagne plus en termes d'amplitude de rotation atteignant un maximum de l'ordre de 20° à 3,3% de pré-étirement ; puis, l'amplitude diminue (voir Figure III-7-a). Pour le cas de translation, on note une zone interdite entre 4% et 6,8% de pré-étirement avec un maximum à 4% (voir Figure III-7-b).

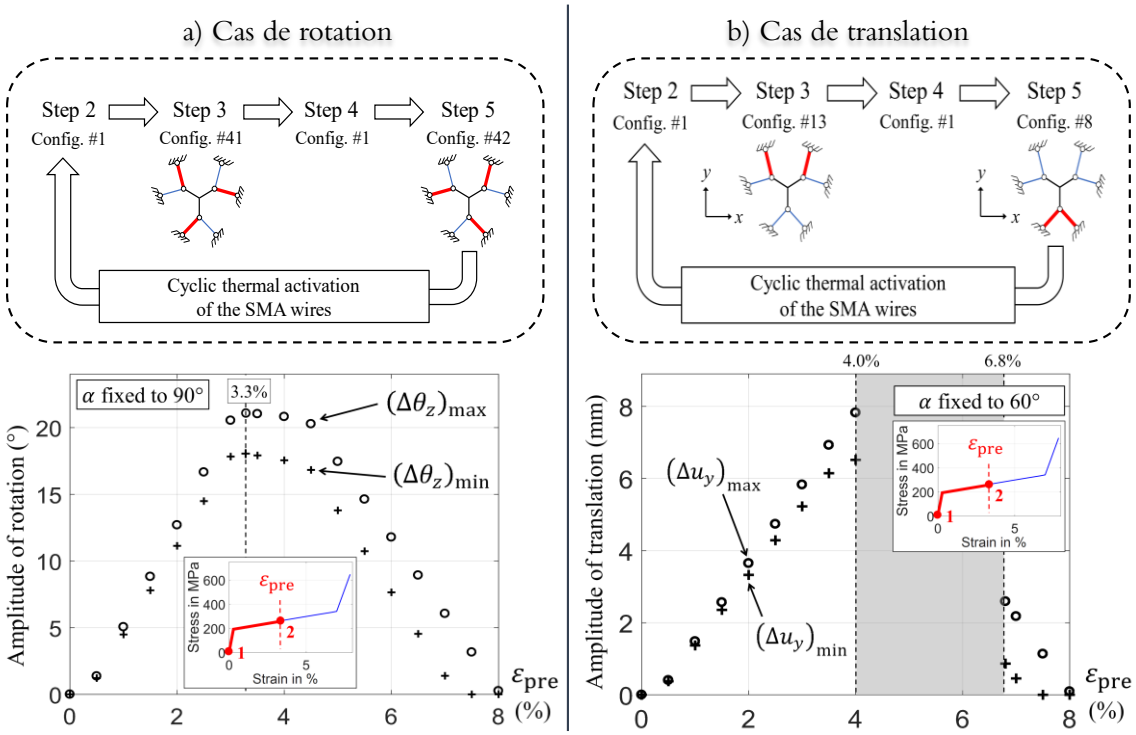

Figure III-7. Évolution des amplitudes de mouvement de la plateforme en fonction de pré-étirement ε_{pre}: a) cas de rotation $(\Delta\theta_z)_{max}(\varepsilon_{pre})$ et $(\Delta\theta_z)_{min}(\varepsilon_{pre})$ pour α=90°, b) cas de translation $(\Delta u_y)_{max}(\varepsilon_{pre})$ et $(\Delta u_y)_{min}(\varepsilon_{pre})$ pour α=60°.

Ces paramètres d'activation étudiés ont pour objectif d'optimiser au mieux le fonctionnement du mécanisme et éviter les singularités de robot.

III.5. Effet d'attraction et rigidité variable

Pour les cas d'études présentés précédemment, on a procédé par une activation thermique simple : une seule activation thermique après l'état initial ou à la limite des séquences d'activation cycliques. Dans ce qui suit, on considère des chaînes d'activation plus longues et plus complexes.

III.5.a. Effet d'attraction

On considère la séquence thermique suivante {#1 → #24 → #1 → #k} avec k ∈ {1 ... 64}. En traçant la pose atteinte pour chaque configuration, on obtient l'espace de travail discret tridimensionnel illustré dans la Figure III-8 et sa projection dans le plan (u_x, u_y). On note l'apparition d'un nuage de points condensé autour de la configuration intermédiaire de l'étape 3 où la configuration #24 attire comme un aimant les configurations qui la suivent. L'espace de travail perd sa symétrie et ce n'est plus facile de prédire intuitivement le mouvement de la plateforme mobile.

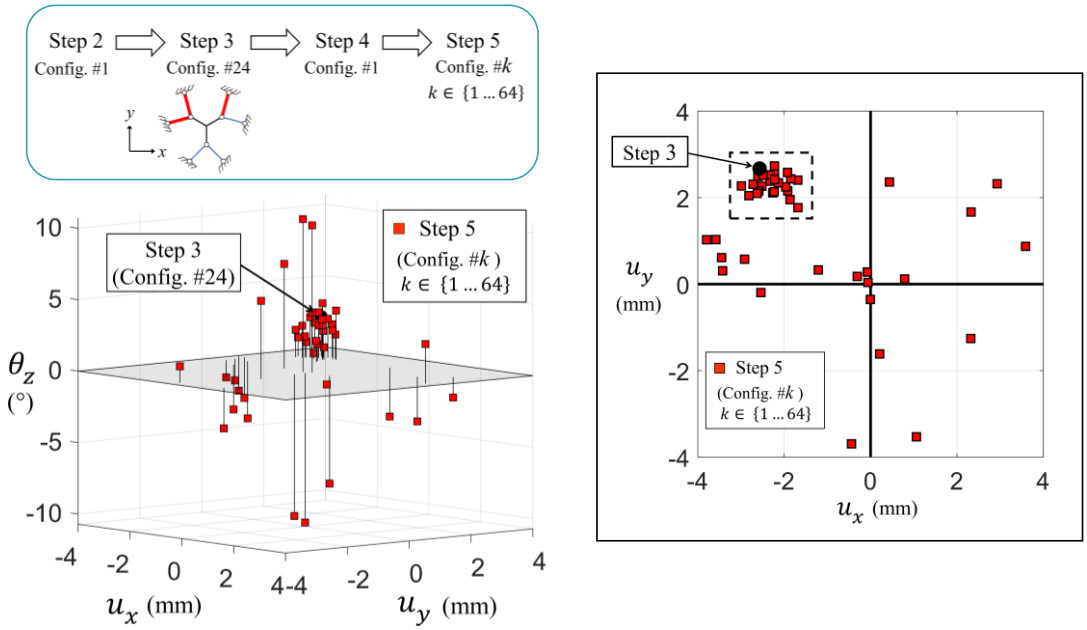

Figure III-8. Preuve d'effet d'attraction dans l'espace de travail lié à l'ajout de la configuration #24 dans la séquence thermique d'activation pour $\alpha = 90°$ and $\varepsilon_{pre} = 3\%$.

Le résultat intéressant est que grâce à l'ajout de cette configuration intermédiaire, on peut désormais atteindre des poses dans l'espace de travail qui n'étaient pas accessibles initialement sans elle (voir Fig. III-5). Subséquemment, le cas d'étude le plus intuitif est d'essayer de viser une pose cible empiriquement avec un retour à l'ambiante après chaque activation. À partir de l'espace de travail présenté ci-dessus, on choisit une cible au voisinage du nuage de points dont les coordonnées sont (U_x, U_y, θ_z)=(-2,80 mm ; 1,95 mm ; 1,2°) et on fixe une précision de 0,1 mm pour la translation et 0,1° pour la rotation. La Fig. III-9-a montre que les plus proches voisins de la cible sont les configurations #63, #30 et #16. On a évité de prendre la config. #63 vu qu'elle présente déjà 5 fils activés sinon on risque de le sur-contraindre. L'application de la config. #30 donne une contrainte négative

donc on l'évite aussi, d'où, la considération de la config. #16. Puis, on enchaîne en utilisant les conditions et les hypothèses établies ainsi que les données acquises. La Fig. III-9-b et Fig. III-9-c démontrent la convergence vers la cible. Il est important de noter que la configuration #10 qui était interdite pour $\alpha = 90°$ (contrainte négative) est désormais possible grâce à l'ajout d'une configuration intermédiaire.

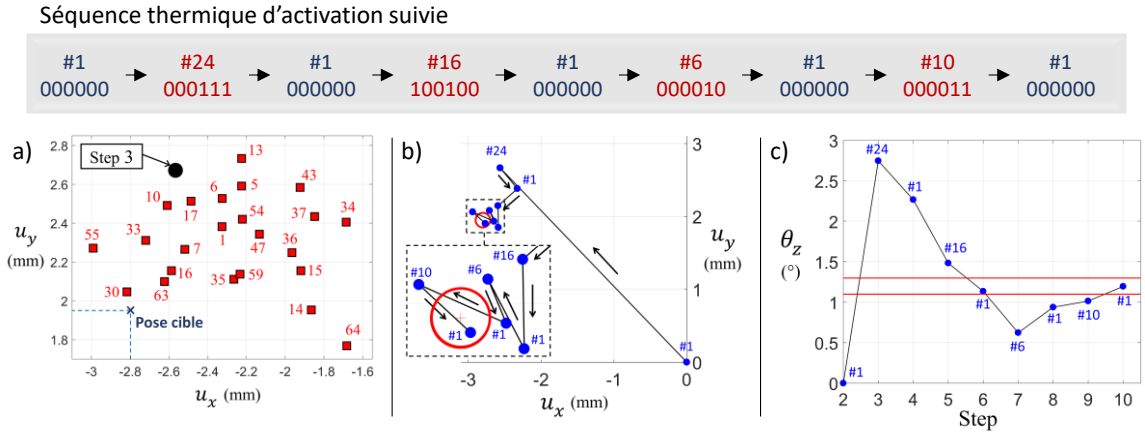

Figure III-9. Exemple d'une séquence d'activation thermique permettant d'atteindre une pose cible pour $\alpha = 90°$ and $\varepsilon_{pre} = 3\%$.

III.5.b. Rigidité variable

Étant donné que l'AMF présente un module d'Young de martensite différent de celui de l'austénite et que le mécanisme présente un fort multi-antagonisme, on s'intéresse dans cette section à vérifier sa rigidité variable.

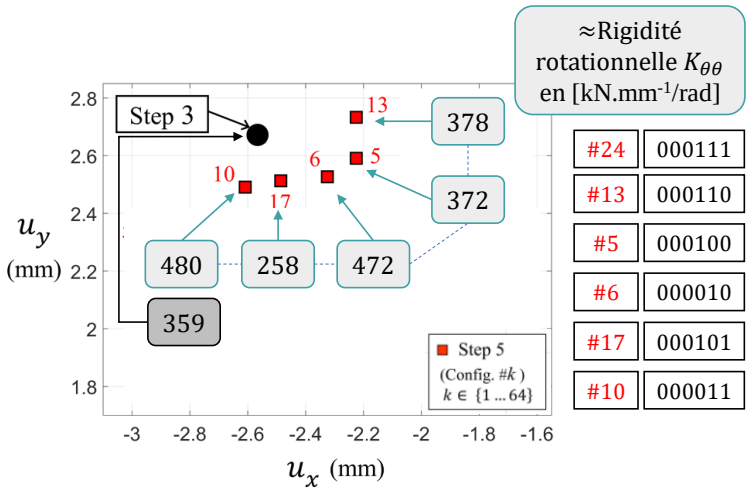

Figure III-10. Preuve de la rigidité variable du mécanisme.

Pour ce faire, on applique un couple égal à 100 N.mm à toutes les poses voisines de celle de la configuration #24 (cas présenté dans la Fig. III-8). La Figure III-10 démontre une rigidité rotationnelle qui varie entre 258 $kN.mm^{-1}.rad^{-1}$ et 480 $kN.mm^{-1}.rad^{-1}$. Cette variabilité est justifiée par la différence entre les proportions de martensite et d'austénite. Plus la proportion d'austénite est importante plus la rigidité globale du système l'est. En effet, la transformation en austénite d'un fil donné par chauffage tend à déformer les fils antagonistes qui se transforme donc en martensite. Avec ce cas d'étude, on clôture l'étude numérique.

IV. Conception d'un démonstrateur et préparation des fils AMF

IV.1. Conception du démonstrateur

La conception retenue pour les essais expérimentaux est le fruit d'évolution de plusieurs conceptions et prototypes. Pour répondre au cahier de charges, on cherche à minimiser le frottement, à assurer plus de précision d'emplacement des composants, à assurer l'isolation thermique et électrique entre les fils AMF et leur entourage et à minimiser le transfert thermique lors de l'activation. Par conséquent, une attention particulière était accordée au choix des matériaux.

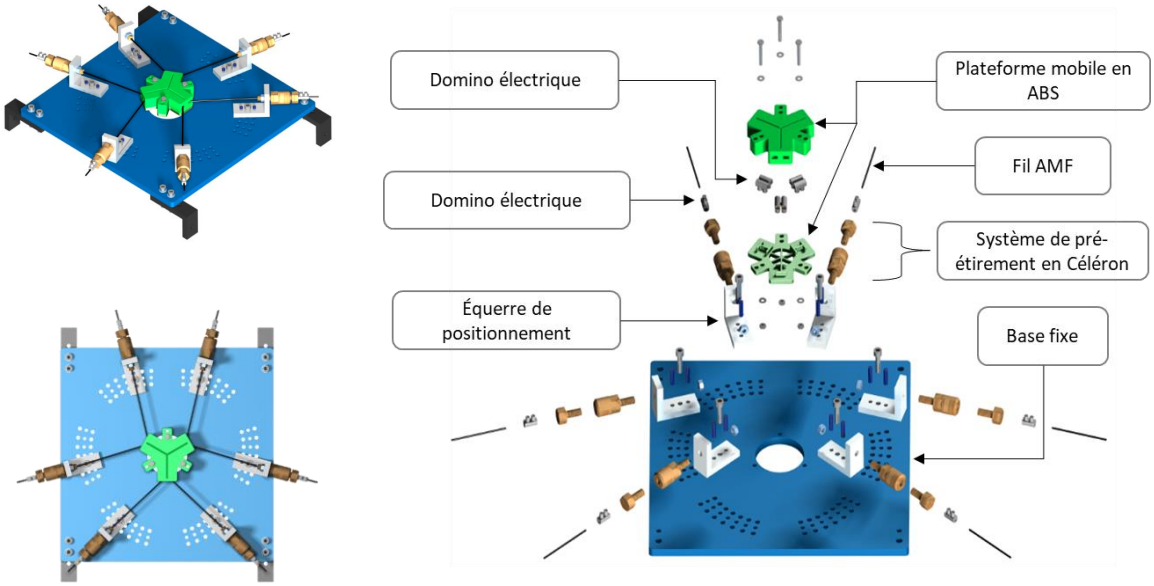

Figure IV-1. CAO du mécanisme.

La Fig. VI-1 illustre la CAO du mécanisme assemblé ainsi que sa vue éclatée. La plateforme mobile était imprimée en ABS. Le système de pré-étirement était

usiné en Celeron. La base et les équerres de positionnement sont usinées en aluminium. La base propose un choix multiple d'angle α.

IV.2. Caractérisation et entraînement mécanique de fils AMF

Les fils AMF sont les actionneurs dans notre mécanisme. Il est donc judicieux de les caractériser mécaniquement afin de maîtriser leur comportement. Pour ce faire, nous avons effectué un essai de traction à la rupture piloté en déplacement qui a montré un point d'inflexion à σ=650 MPa et qui correspond à la limite d'élasticité.

Sachant que les fils AMF vierges ont un comportement non répétable et non uniforme, il est crucial de les entraîner avant de les utiliser en tant qu'actionneurs. Cette nécessité d'entraînement est expliquée par la présence des déformations résiduelles lors des premiers cycles superélastiques. Ainsi, pour résoudre ce problème, on effectue plusieurs cycles charge-décharge jusqu'à ce que les déformations résiduelles n'évoluent plus. Dans notre cas, on a effectué cinquante cycles d'entraînements présentés dans la Figure IV-2 en commençant toujours par chauffage du fil pour être sûr qu'il soit en état austénitique.

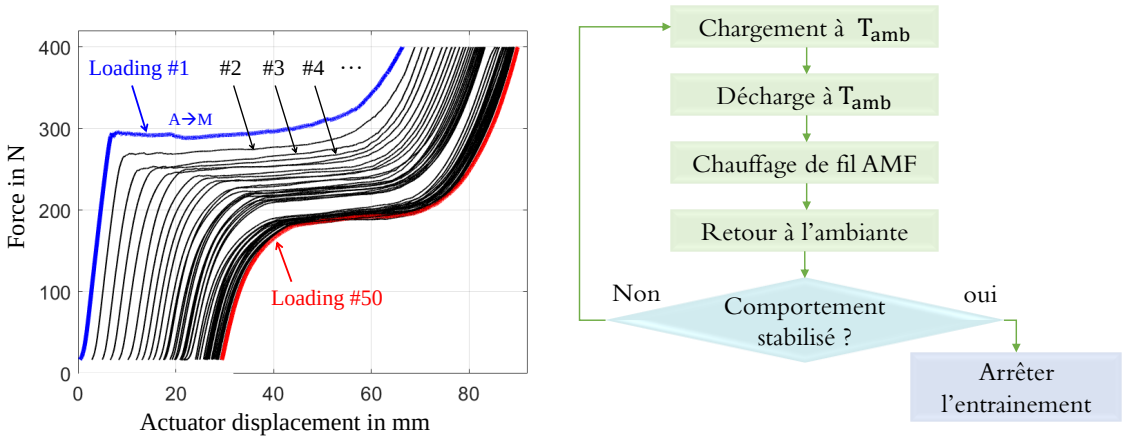

Figure IV-2. Entraînement d'un fil AMF jusqu'à stabilisation de mouvement.

Une fois les fils sont entraînés, il faut les mettre en place et les pré-étirer.

IV.3. Mise en place et pré-étirement des fils AMF

Avant de détailler les démarches de mise en place des fils et les pré-étirements, on montre dans la Figure IV-3 le dispositif expérimental utilisé dans la section V. Ce dispositif contient le démonstrateur physique fabriqué.

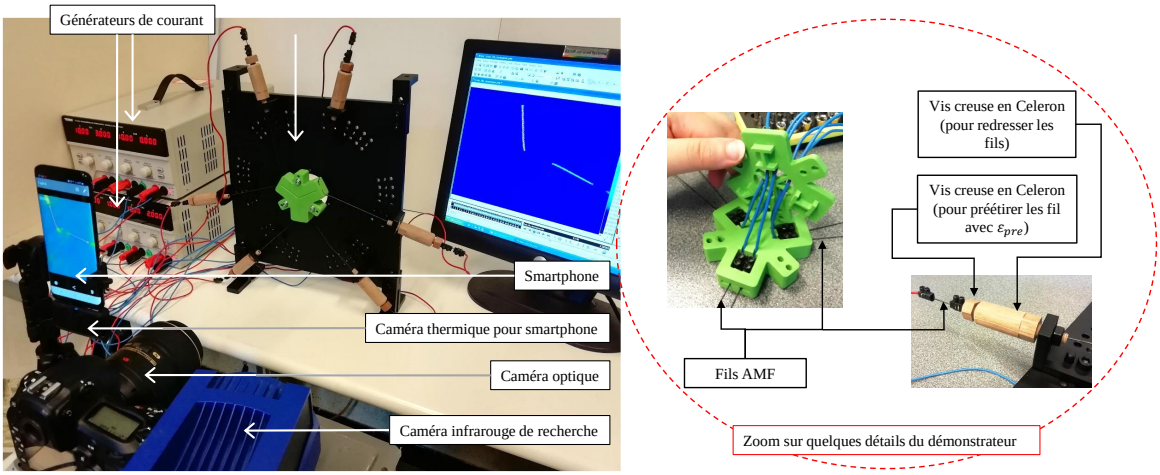

Figure IV-3. Dispositif expérimental et détails de démonstrateur.

IV.3.a. Mise en place des fils AMF

Le serrage de fils AMF est un problème à la fois récurrent et compliqué en raison de leur superélasticité. Dans la vue éclatée de la CAO du mécanisme illustrée dans la Figure IV-1, on note la présence de dominos électriques qui assurent le serrage des fils AMF. Ceci paraît peu fiable et simple. Par contre, grâce aux températures de transformation et d'activation spéciales de notre fils et en suivant un protocole de fixation qu'on le décrit dans la Figure IV-4, on assure un bon serrage.

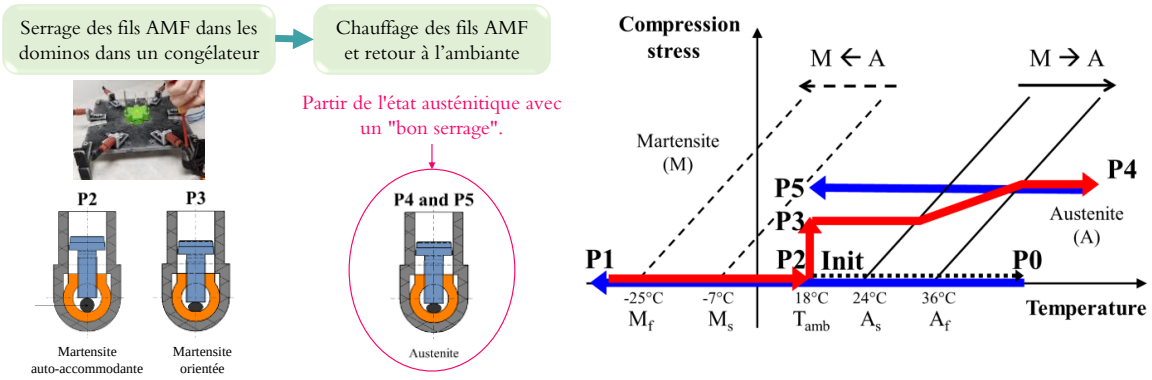

Figure IV-4. Protocole de serrage des fils AMF.

D'abord, on chauffe les fils AMF qui étaient à température ambiante (Init) jusqu'à une température supérieure à A_f (P0 ; 100% austénite). Ensuite, on place les éléments du mécanisme dans un congélateur ayant une température inférieure à M_f (P1 ; 100% martensite auto-accommodante). À température ambiante (P2), on serre les fils à l'aide des dominos et ils se transforment donc en martensite orientée (P3). Puis, on réchauffe les fils (P4) pour assurer la

transformation en austénite. Après le retour à l'ambiante (P5), on obtient un bon serrage à l'état austénitique.

IV.3.b. Pré-étirement des fils AMF

Le système de pré-étirement se compose de deux vis creuses : une pour redresser le fil AMF et l'autre pour le pré-étirer. La Figure IV-5 schématise la démarche à suivre pour pré-étirer les fils.

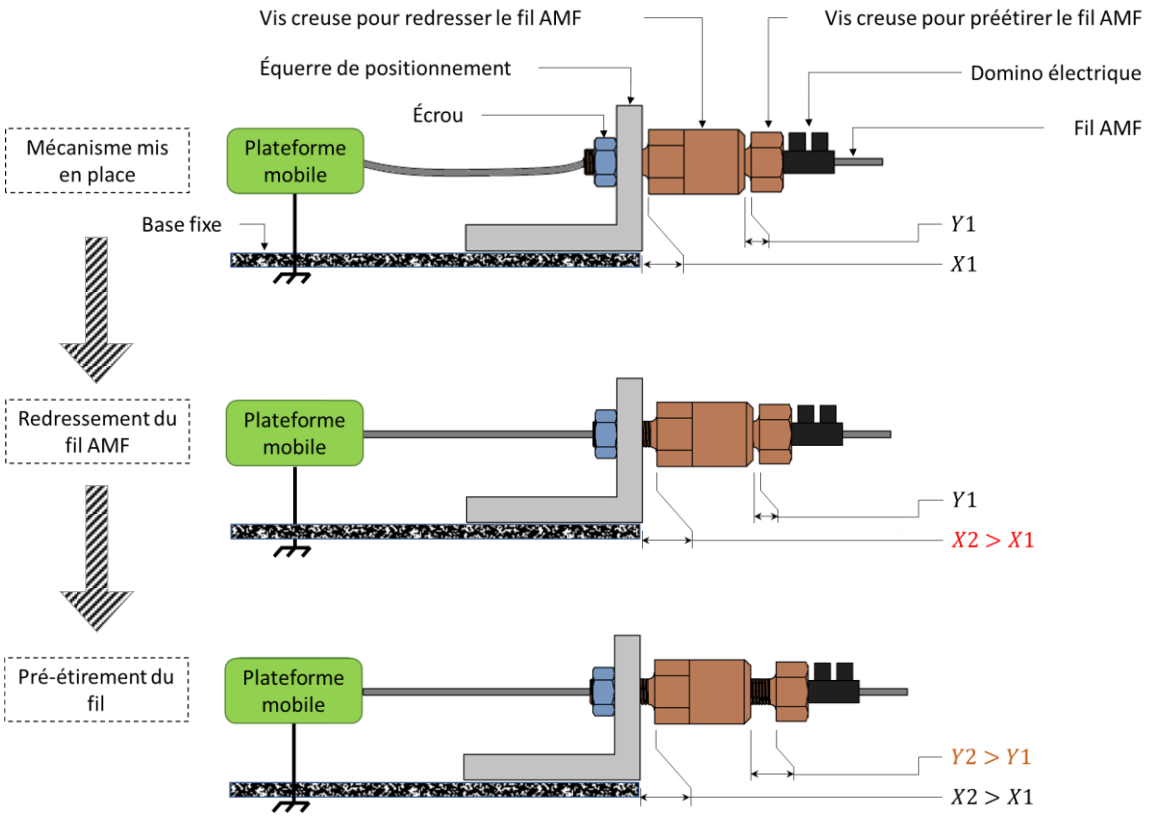

Figure résumé IV-5. Démarche de pré-étirement.

Après avoir mis les fils dans leurs positions et les avoir serrés avec des dominos, on dévisse la première vis creuse, en contact avec l'équerre de positionnement, pour redresser le fil. Ensuite, on bloque cette vis à l'aide d'un écrou. Enfin, on dévisse la deuxième vis creuse avec maintien de la position du domino, ce qui pré-étire les fils. On note qu'un tour complet d'une vis est équivalent à 1 mm de pré-étirement.

Après avoir terminé ces étapes préliminaires mais nécessaires, on passe à l'expérimentation et aux résultats.

V. Expérimentations et résultats

V.1. Analyse thermique préliminaire

Comme les fils AMF sont actionnés thermiquement, il faut donc vérifier l'isolation électrique et le transfert thermique. Pour ce faire, nous avons effectué une analyse thermique rapide en appliquant des champs de température stable présentés dans la Fig. V-1-a pour une intensité de 3A dans les fils AMF 1, 3 et 5 et avec des valeurs d'intensité différentes dans la Fig. V-1-b. Notez que les cartes des températures en Figures V-1-a et V-1-b sont données à 50°C et 30°C respectivement. L'isolation électrique est confirmée. On note que les parties connectées aux fils ont également été chauffées par conduction.

Il faut établir les paramètres nécessaires pour le fonctionnement du mécanisme tels que : le courant électrique nécessaire pour atteindre la température d'activation, le temps de chauffage et le temps de refroidissement. La Figure V-2 traite ces aspects. Par exemple, la Figure V-2-a montre que la température est maximale au centre du fil quel que soit l'ampérage appliqué avec une baisse aux extrémités indiquant la non-homogénéité de la distribution thermique.

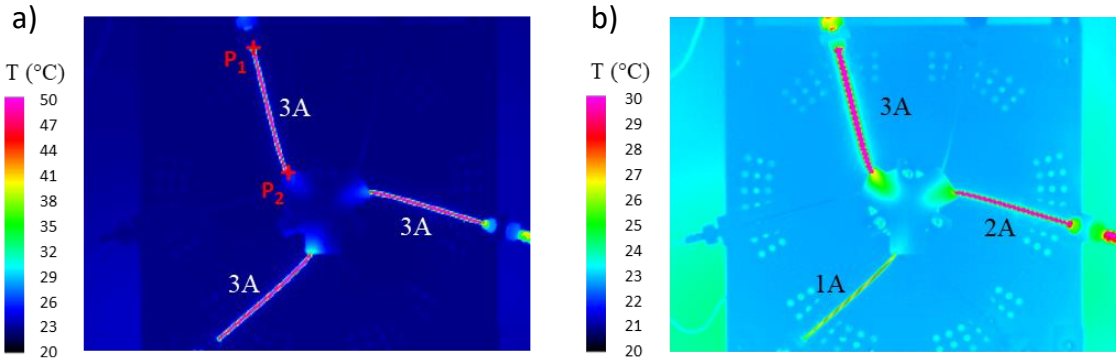

Figure V-1. Analyse thermique : a) exemple de champ de température stable pour une intensité de 3A dans AMF1, 3 et 5 ; b) idem pour d'autres valeurs d'intensité.

Afin de sélectionner la température d'activation, nous avons suivi la température générée en fonction de l'intensité du courant (voir Fig. V-2-c). Pour un courant de 3A, on obtient une température maximale de 88°C, suffisante pour transformer le fil en austénite. C'est donc cette valeur d'intensité qui est utilisée pour la suite. La Fig.V-2-b montre qu'au bout de trois minutes la température est stabilisée pour le chauffage ainsi que pour le retour à l'ambiante pour une intensité de courant égale à 3A.

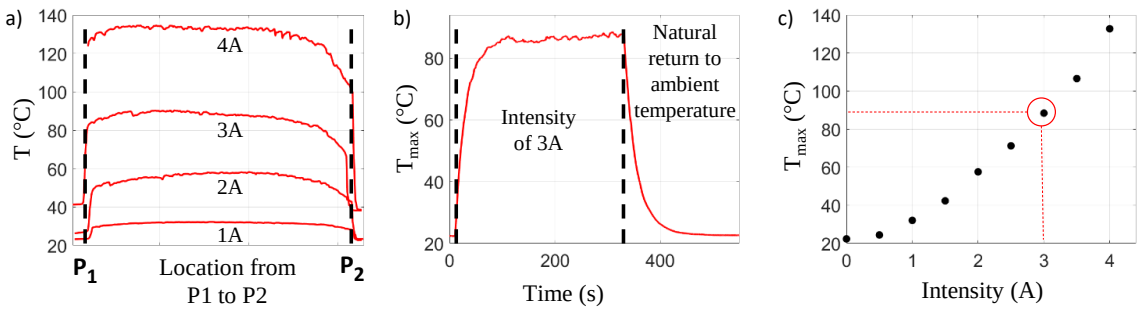

Figure V-2. Analyse thermique : a) profils de température constante le long du fil AMF5, b) évolution temporelle de la température maximale, c) température constante maximale en fonction de l'intensité.

V.2. Cas d'étude simple : Rotation et translation cycliques expérimentales

V.2.a. Rotation cyclique pour ε_{pre}= 1,6% et α = 90°

On reprend la même séquence d'activation que nous avons utilisé pour la rotation cyclique numérique (voir Fig. V-3-a). La Figure V-3-b montre que le comportement est stabilisé à partir du quatrième cycle où les amplitudes de rotation sont inférieures à celles de la simulation. On note aussi un décalage de l'axe de symétrie que l'on peut expliquer par un glissement au début de l'expérience.

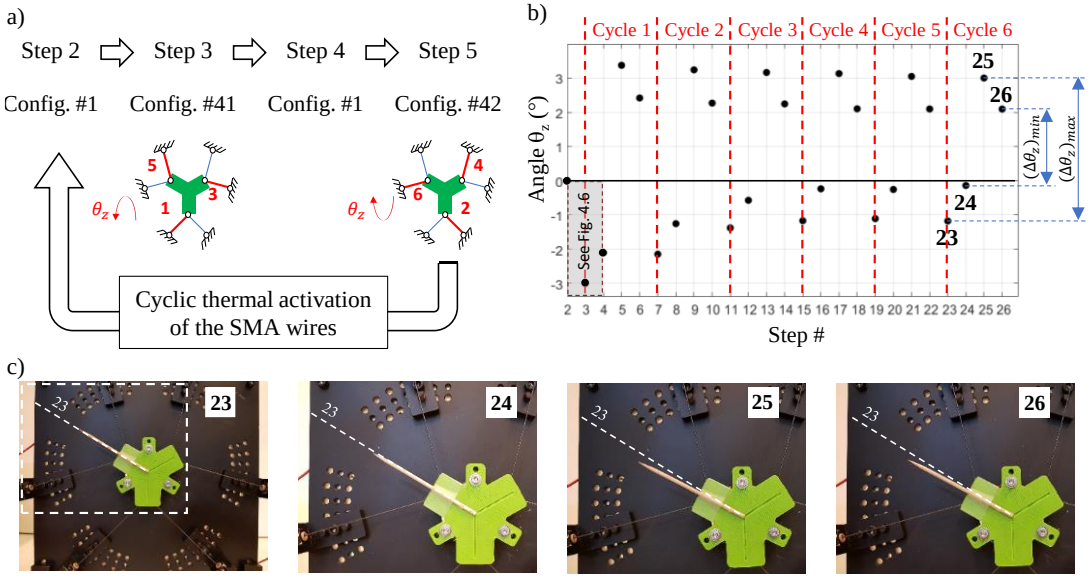

Figure V-3. Rotation cyclique expérimentale pour ε_{pre}= 1,6% et α = 90°.

Afin de vérifier expérimentalement l'influence de la valeur du pré-étirement sur l'amplitude de mouvement, nous avons suivi l'évolution de la rotation en fonction du temps pour deux ε_{pre} différentes 1,6% et 3% pour α = 90° (voir Figure

V-4). On note que plus la précontrainte est élevée, plus la rotation régulière est élevée, tant lors du chauffage que du refroidissement. Ceci confirme l'impact du pré-étirement sur les amplitudes de rotation. On note aussi que les valeurs expérimentales du cas de 3% de pré-étirement sont plus proche aux résultats numériques que pour 1,6% de pré-étirement.

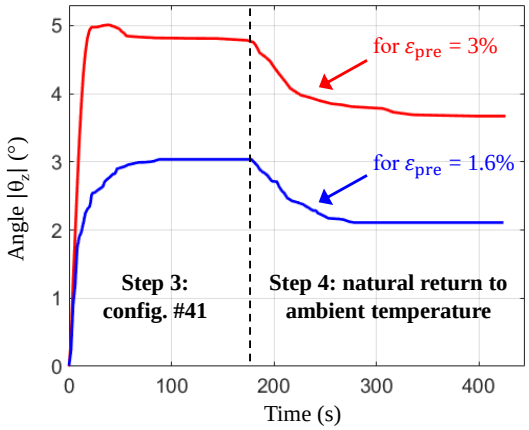

Figure V-4. Évolution de la rotation en fonction du temps pour deux ε_{pre} différentes 1,6% et 3% pour $\alpha = 90°$.

V.2.b. Translation cyclique pour ε_{pre} = 1,6% et α = 60°

On reprend la même séquence d'activation que nous avons utilisé pour la translation cyclique numérique (voir Fig. V-5-a). On note que le comportement est stabilisé à partir du cinquième cycle (voir Fig. V-5-b). Les amplitudes de translation sont proches des résultats numériques. On note aussi un décalage de l'axe de symétrie justifié par l'effet de la première configuration #13.

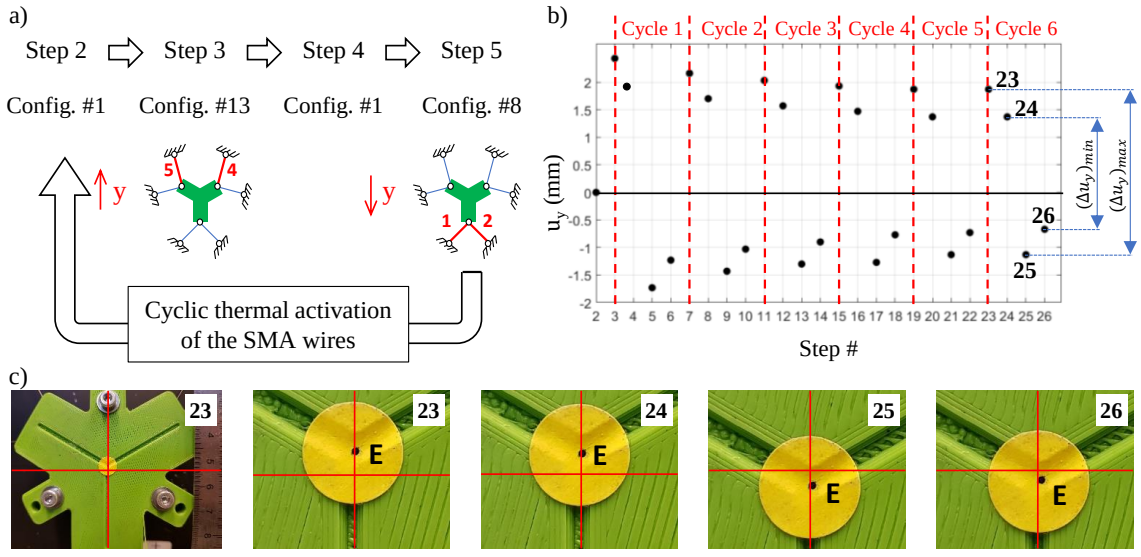

Figure V-5. Translation cyclique expérimentale pour ε_{pre}= 1,6% et $\alpha = 60°$.

V.3. Espace de travail discret et effet d'attraction

V.3.a. Espace de travail discret pour ε_{pre} = 3,25% et α = 60°

Pour ce cas d'étude, on a repris la même séquence d'activation pour l'espace de travail numérique avec ajout d'une étape intermédiaire présentée dans la Figure V-6-a où le choix d'une approche d'initialisation simple est adoptée : on chauffe les six fils en même temps sur le mécanisme. On suppose qu'aucune plasticité ne se produit lorsqu'ils se transforment tous en austénite. Les Figure V-6-a, -b et -c montrent une perte de la symétrie de l'espace de travail ainsi qu'une perte de l'amplitude. On peut conclure que le retour à la référence n'est pas « parfait ».

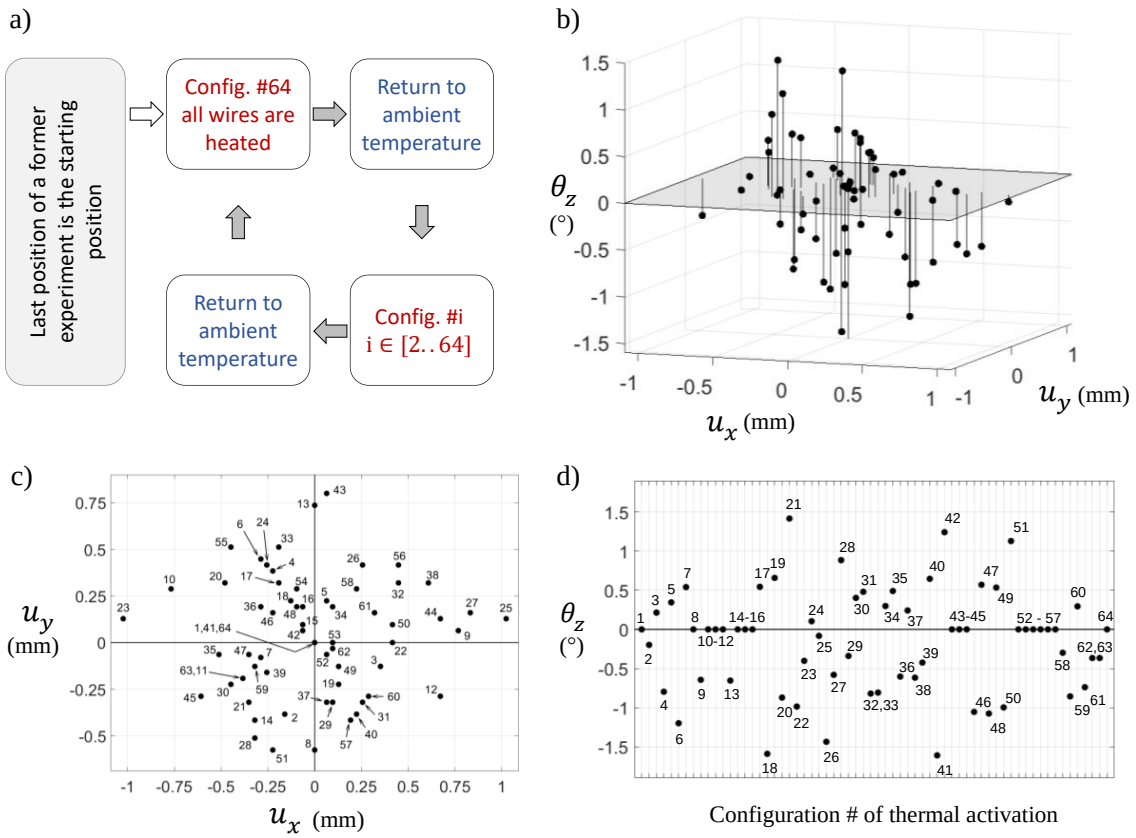

Figure V-6. Espace de travail discret expérimental ε_{pre} = 3,25% et α = 60°.

V.3.b. Effet d'attraction expérimental pour ε_{pre} = 1,6% et α = 60°

Autre aspect que nous avons pu vérifier expérimentalement est l'effet d'attraction. En faisant une activation rotationnelle des fils activés illustrée dans la Figure V-7, on peut créer une rotation complète qui se manifeste sous la forme d'un hexagone de six dents qui correspondent au chauffage et au refroidissement. Il est intéressant de noter que les poses correspondantes à la configuration #13 et la

configuration #8 et qui étaient censées être des translations pures selon u_y uniquement, gagnent une translation selon u_x. Les coordonnées $(u_x)_{(\#13)}$ et $(u_x)_{(\#8)}$ (..) qui devraient être nulles pour les configurations #13 et #8 ne le sont pas à cause des configurations #9 et #11, respectivement.

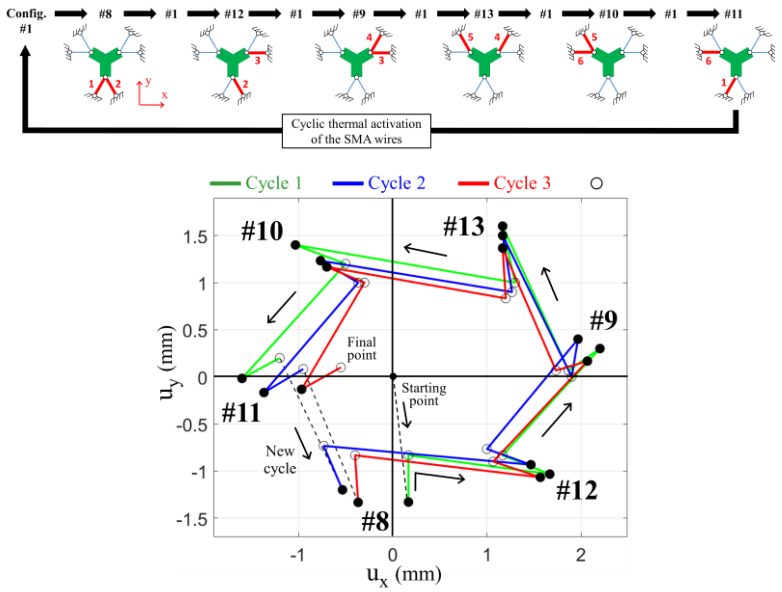

Figure V-7. Effet d'attraction expérimental $\varepsilon_{pre} = 1{,}6\%$ et $\alpha = 60°$.

V.4. Application d'une séquence thermique complexe et rigidité variable expérimentale

V.4.a. Application d'une séquence thermique complexe

Nous avons repris la même séquence thermique que l'étude numérique [#1→#24→#1→#16→#1→#6→#1→#10→#1]. Pour cette expérience, on a choisi $\alpha = 90°$, $L = 170$ mm, $\varepsilon_{\text{pre}} = 3.5\%$ and $T_1 = 105$ °C. La Figure V-8 montre qu'on a le même comportement qualitatif pour l'étude numérique comme pour l'étude expérimentale mais avec une différence d'amplitude.

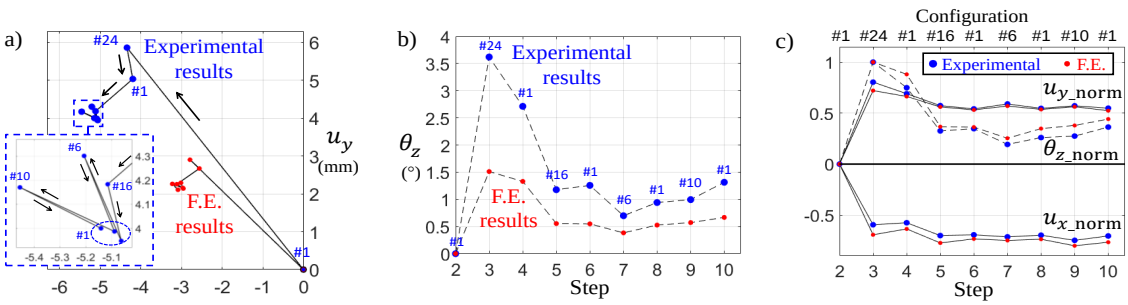

Figure V-8. Application d'une séquence thermique complexe entre numérique et expérimental.

V.4.b. Rigidité variable expérimentale

Pour finir la partie expérimentale, nous avons réalisé un essai de rigidité variable dont la séquence d'activation est présentée dans la Figure V-9. Le principe est le suivant : on attache une barre à la plateforme mobile ; ensuite, on accroche des masses différentes pour créer des couples et après, on calcule la rigidité. Par exemple, en prenant le cas de la masse de 2 N, on constate une rigidité rotationnelle variable entre la configuration #5 et sa précédente (143 kN.mm.rad^{-1} et 85 kN.mm.rad^{-1} respectivement).

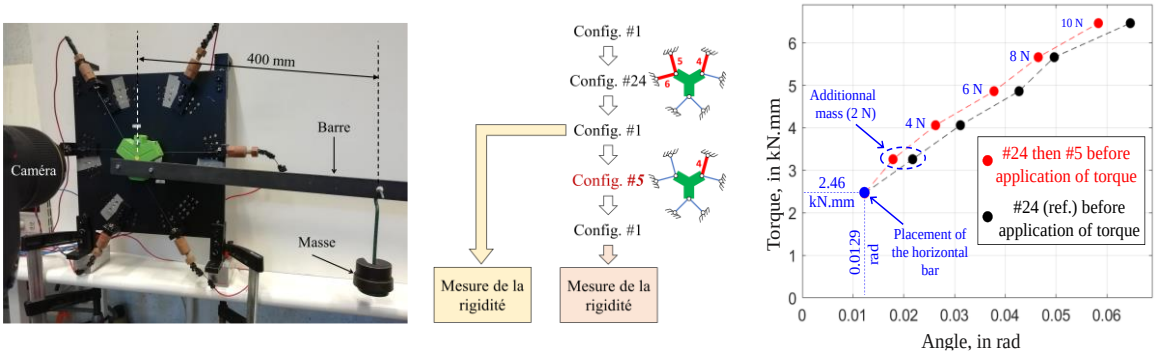

Figure V-9. Essai de la rigidité variable expérimentale.

VI. Conclusions et perspectives

VI.1. Conclusions

Lors de cette thèse, nous avons réalisé une modélisation éléments finis paramétrée d'un mécanisme précontraint activé par six fils AMF ayant 64 configurations d'activation possibles. À travers plusieurs cas d'études, nous avons pu identifier : la possibilité de verrouiller une position après cessation de l'activation, l'influence de l'angle entre les composants AMF, l'influence du pré-étirement des fils sur le mécanisme. En outre, nous avons étudié la rotation et la translation cycliques. De plus, nous avons constaté que le mécanisme présente de petits déplacements mais des rotations importantes.

Particulièrement, on note la possibilité d'atteindre une position cible dans l'espace de travail ainsi qu'un effet d'attraction d'une configuration sur celle qui la suit : résultant de la nature multi-antagoniste et hystérétique du mécanisme.

Nous avons démontré l'importance d'entraîner les fils AMF pour un actionnement optimum. Nous avons réussi à bien serrer des fils à l'état martensitique grâce aux températures de transformation spécifiques de notre fil. Grâce au démonstrateur physique que nous avons conçu, nous avons réalisé une

compagne d'essais qui nécessite beaucoup de préparation et du temps. Nous avons choisi de reproduire certaines séquences de chauffage réalisées dans l'étude numérique.

Nous avons mis en évidence expérimentale l'effet d'attraction ainsi que la rigidité variable du mécanisme. Nous avons noté la nécessité de réinitialiser le système pour avoir les mouvements souhaités

Nous pouvons conclure que les résultats sont qualitativement en bon accord avec les attentes, mais certains d'entre eux sont quantitativement éloignés des résultats simulés.

VI.2. Perspectives

Parmi les prochaines étapes à faire pour continuer ces travaux de recherche, on a la finalisation de la commande du mécanisme qui permettra éventuellement à réinitialiser le système, réaliser un mouvement continu, effectuer un contrôle en temps réel des fils activés et intégrer des capteurs.

Il est intéressant d'améliorer la conception du mécanisme afin d'optimiser le mécanisme du pré-étirement, réduire l'encombrement du système et ainsi sa taille.

Il faut automatiser le traitement d'images en utilisant la méthode de corrélation d'images par exemple. Ceci permettra d'étudier la précision et la répétabilité du mécanisme.

Comme le modèle EF est paramétré, on peut étudier l'influence d'autres paramètres sur la performance du mécanisme tels que :

- possibilité d'avoir des fils pré-étirés différemment,
- des angles différents entre les composants AMF,
- augmenter la redondance d'actionnement,
- etc.

Au lieu d'une analyse statique, on peut effectuer une analyse dynamique du système et une étude de compensation de la gravité.

Pour clôturer, c'est intéressant de remplacer les fils AMF en ressorts (solution pour les problèmes de pré-étirement, serrage ...) et d'intégrer des matériaux souples comme l'élastomère.

Table of contents

Acknowledgements ..... *i*

Extended French summary: Résumé étendu ..... *iii*

Table of contents ..... *xxxvi*

Table of figures ..... *xxxix*

Table of tables ..... *xliv*

Table of notations ..... *xlv*

General introduction *1*

Foreword **1**
Context and issues of the research work **2**
Organization of the manuscript **3**

Chapter 1: Literature review *5*

1.1. Introduction **6**
1.2. Shape-memory alloy as a smart material **6**
1.2.1. Definition and interest of NiTi-based SMAs 6
1.2.2. The underlying-physical phenomenon of SMAs 7
1.2.3. SMAs cooling methods 9
1.3. Interesting thermomechanical behaviors of SMAs **9**
1.3.1. Shape-Memory Effects 10
1.3.1.1. One-Way Memory Effect 10
1.3.1.2. Stress-Assisted Two-Way Memory Effect 11
1.3.1.3. Two-Way Memory Effect 11
1.3.2. Superelasticity 12
1.3.3. Damping behavior 14
1.4. Wide range of SMA-based applications **14**
1.4.1. Automotive applications 15
1.4.2. Aerospace applications 15
1.4.3. Biomedical applications 16
1.4.4. Textile applications 17
1.4.5. Civil engineering applications 18
1.5. Robotic applications of SMA-based actuators **19**
1.5.1. Biologically-inspired robots 20
1.5.1.1. Crawler robot 20
1.5.1.2. Fingers 21

1.5.1.3. Grippers 22
1.5.2. Origami and kirigami actuators 23
1.5.3. SMA mini-actuators 24
1.5.4. Prismatic and rotary actuators based on SMA 25
1.5.5. Multi-DOF SMA-based actuators 26
1.6. Conclusion and positioning of the present study with respect to the literature 28

Chapter 2: Finite element analysis of a multi-antagonistic actuation mechanism 31

2.1. Introduction 32
2.2. The parameters of the SMA modelling tool 32
2.2.1. Modeling with Ansys Mechanical APDL 32
2.2.2. Transition equations for Ansys inputs 33
2.2.2.1. Material parameters in Ansys 33
2.2.2.2. Ansys parameters inputs 36
2.3. Presentation of the multi-antagonistic actuation system 37
2.3.1. Topology of the mechanism 37
2.3.2. Behavior of the SMA wires 39
2.3.3. Justification of the mechanism topology 42
2.3.4. Definition of heating configurations and platform position 42
2.4. Analysis of the mechanism 44
2.4.1. Discrete workspace obtained in Step 3 45
2.4.2. Remark about maximum stress in the wires 47
2.4.3. Advantageous property of the system 48
2.4.4. Specific cases of cyclic rotation and translation 50
2.4.5. Evidence of an attraction effect 54
2.5. Possibility of reaching a target position in the workspace 57
2.6. Conclusion 58

Chapter 3: Design of the prestressed mechanism and preparation of the SMA wires . 59

3.1. Introduction 60
3.2. Specifications of the mechanism under study 60
3.3. Previous versions of the prototype 61
3.3.1. Initial design of the prototype. 62
3.3.2. Second design of the prototype 63
3.3.3. Third design of the prototype 64
3.4. Latest version of the prototype 64
3.4.1. Overview of the mechanism 65
3.4.2. Mobile platform CAD and its Finite Element validation 67
3.4.3. Tightening of the SMA wires 69
3.4.4. Prestraining of the SMA wires 71
3.5. Preliminary preparation of the SMA wires 74
3.5.1. Mechanical characterization of the SMA wire 74
3.5.2. Preliminary mechanical training of the SMA wires 75
3.6. Conclusion 77

Chapter 4: Experimentations and results 78

4.1. Introduction 79
4.2. Experimental setup and thermal analysis 80
4.2.1. Experimental setup 80

4.2.2. Preliminary thermal analysis 81
4.3. Experimental cases of cyclic rotation and translation 83
4.3.1. Cyclic rotation 84
4.3.2. Cyclic translation 86
4.4. Discrete workspace and attraction effect 87
4.4.1. Discrete workspace 87
4.4.2. Evidence of attraction effect 88
4.5. Example of a "complex" thermal sequence and stiffness variability 91
4.5.1. Example of a complex thermal sequence 91
4.5.2. Stiffness variability 92
4.6. Conclusion 94

Conclusions and perspectives 96
Conclusions 96
Perspectives 98

Bibliography 100

List of publications 108
Thesis related publications 108
International peer-reviewed journal 108
International peer-reviewed conference proceedings 108
National peer-reviewed conference proceedings 108
Communication 108
International collaborations 109

List of Appendices 110
Appendix A: Technical documentation of the CAD of the studied mechanism 111
Appendix B: Preliminary incremental model for the control of the mechanism 116
Input parameters for the model 116
General geometrical data 116
Geometrical data for the SMA wires: 116
Thermomechanical data for the SMA wires: 117
Wire operation mode at ambient temperature 117
Activation of a SMA wire (**j**) 120
Procedure 1 120
Procedure 2 121
Appendix C: Conference paper Actuator 21 122
Appendix D: Example of an Ansys APDL script used in the thesis 126

Abstract 133

Résumé 134

Table of figures

Figure 0.1. Key features of a multi-DOFs mechanism activated by SMA wires. 3

Figure 1.1. SMA phases and crystal structures, from [4]. 8

Figure 1.2. Stress-strain-temperature graph exhibiting the OWME [13]. 11

Figure 1.3. Schematic view of the SATWME at constant stress from [18]. 12

Figure 1.4. The superelastic effect, from [18]. (a) Two loading paths in the stress-temperature diagram, (b) same in the stress-strain diagram. 12

Figure 1.5. Existing and potential SMA applications in the automotive domain [4]. 15

Figure 1.6. Existing and potential SMA applications in the aerospace domain [4]. 16

Figure 1.7. Examples of SMA applications in aerospace field. (a) Structural configuration: Boeing variable geometry chevron using SMA beams [33]. (b) Propulsion system: wind tunnel model structural layout using SMA torque tube [34]. (c) Spacecraft application: a rotary latch using SMA torsion spring [35]. 16

Figure 1.8. Existing and potential SMA applications in the biomedical domain [4]. 17

Figure 1.9. Example of a contractile SMA-knitted: the contractile SMA knitted actuator prototypes consist of 15 wales and 15 courses. The displayed prototype is manufactured with Dynalloy Flexinol® wire (Af = 90°C, d=0.305mm) [53]. 18

Figure 1.10. Active variable stiffness (AVS) fibers. (a) Composition of an AVS fiber. (b) PLA-based AVS fiber (the PLA core and the SEBS coating are both transparent). (c) ABS-based AVS fiber. Scale bars are 1cm. [54] 18

Figure 1.11. Experimental test on a SMA damper device. The damper device, used to investigate the effect of SMA dampers during the cable vibration, was placed at several positions on the cable. The experimental setup was realized on a cable test bench [56]. 19

Figure 1.12. General view of the experimental prototype of an adaptive shape-morphing tensegrity structure, with frequency self-tuning capabilities, using SMAs [57]. 19

Figure 1.13. The Omegabot prototype with SMA spring actuators and anisotropic friction pads [60]. 20

Figure 1.14. (a) Solid model of a crawling device with clamping rings and three SMA U-shapes strips. The spring steel bias spring strips are not shown in this picture [61]. (b) Geometric model of the SMA-actuated radially deployable compliant mechanism [62]. 21

Figure 1.15. (a) Experimental setup of SMA muscle pairs in an artificial finger [63]. (b) Configuration of a soft finger with embedded SMA fibers [66]. (c) Anthropomorphic finger antagonistically actuated by SMA plates [67]. 22

Figure 1.16. (a) Self-sensing microgripper module with wide handling ranges [68]. (b) SMA gripper in a transition position [69]. (c) Schematic of the soft gripper and its hinge actuator [70]..... 23

Figure 1.17. (a) Two sets of SMA helical spring configurations for the origami parallel module (three and six actuators) [74]. (b) Actuation models of the kirigami structure (two and four actuators) [72]. 24

Figure 1.18. Examples of SMA mini-actuators. (a) Linear SMA mini-actuator. (b) Rotational SMA mini-actuator. (c) Ferromagnetic SMA mini-actuator [75]. 24

Figure 1.19. Basic SMA design approaches for linear and rotary motion [13]. 25

Figure 1.20. (a) Prototype of a compliant compensated SMA actuator (b) Modular assembly of elemental actuators to increase net stroke or output force [76]..... 26

Figure 1.21. Operating principle of the proposed wobble motor. (a)–(c) show schematically translational motions of the internal gear part caused by single activation of the S(1), dual activation of the S(1) and S(2), and single activation of S(3), respectively [78]. 26

Figure 1.22. Schematic view of the FlexiBot (a) assembly design and (b) exploded view [91]. 27

Figure 1.23. Soft parallel kinematic mechanism driven by six SMA coils and based on the Stewart platform [17]..... 27

Figure 1.24. Finite workspace of 6-segment SMA actuators in the case of linear (A), logarithmic (B) and paired logarithmic (C) segmentation of the SMA actuators [94]. 28

Figure 2.1. Different steps used for modelling the studied mechanism. 33

Figure 2.2. (a) Stress-strain diagram from the Ansys documentation with the MEFF option. (b) Definition of the MEFF option constants C1 to C7..... 34

Figure 2.3. Coordinates in the superelasticity diagram. (a) The state diagram. (b) The superelastic cycle. 35

Figure 2.4. a) Conceptual view of a mobile platform connected to several SMA wires, b) plane system studied. Output parameters are the rotation of the platform and the in-plane translation of point E as a function of the thermal activation of the SMA wires. 38

Figure 2.5. a) Simplified state diagram of a SMA wire in tension. The first three steps of the procedure are numbered 0, 1 and 2. Step 2 corresponds to the state of the six SMA wires before starting a thermal activation sequence. Due to the symmetry of the mechanical system, there is no movement of the platform from Step 0 to Step 2; b) model of the mechanical response of the SMA wires in tension; c) experimental stress-strain curve of a Ni50.8–Ti49.2 (at. %) SMA wire, 1 mm in diameter, until rupture. 41

Figure 2.6. Various heating configurations of the six SMA wires. Red bold lines correspond to wires at activation temperature ($T1$); blue lines correspond to wires at ambient temperature

($T0$). Each configuration is identified by a six-digit binary number corresponding to the thermal state of the wires, for which "0" and "1" correspond to $T0$ and $T1$ respectively..... 43

Figure 2.7. Movement of the mobile platform: a) definition of the in-plane translation ux, uy and the rotation θz of the platform, b) example of position in real scale obtained by finite element simulation, for α = 90°, εpre = 3% and Configuration #24 applied at Step 3. 44

Figure 2.8. a) Movement of the mobile platform for α = 90° and εpre = 3% for different heating configurations at Step 3. Each point is defined by the in-plane translation (ux,uy) of point E and the rotation θz of the platform. Red crosses correspond to configurations for which negative stresses are calculated in at least one SMA wire, meaning that these configurations are not valid; b) same in projection onto plane (ux,uy), c) rotation θz of the platform. Numbers refer to the heating configurations in Figure 2.6. 46

Figure 2.9. Overheating of the SMA wires leading to numerous non-valid configurations: same plot as in Figure 2.8-a, with the activation temperature increased until a *full* return to the austenitic state of the activated wires is achieved. Red crosses correspond to heating configurations for which stresses are negative or exceed the plastic yield stress of the SMA (non-valid configurations)..... 48

Figure 2.10. Platform movement is partially preserved when thermal activation is halted: a) thermal activation sequence considered, b) and c) same plot as in Figures 2.8.(a) and (b). Dots and squares correspond to Steps 3 and 4 respectively..... 50

Figure 2.11. Creation of cyclic rotation by alternating Configurations #41 and #42 with intermediate returns to ambient temperature: a) thermal activation sequence considered, b) variation in rotation θz from one step to the next for α = 90° and εpre = 3%, c) corresponding variation in stress and strain in the SMA wires. 52

Figure 2.12. Amplitude $\Delta\theta z$max of rotation obtained by alternating Configurations #41 and #42 as in Figure 8-a: a) as a function of angle α for εpre = 3%, b) as a function of εpre for α = 90°. Amplitudes $\Delta\theta z$min between intermediate returns to ambient temperature are also plotted. See Figure 2.11-b for the definition of $\Delta\theta z$max.and $\Delta\theta z$min..... 53

Figure 2.13. Cyclic translation obtained by alternating Configurations #8 and #13: a) thermal sequence considered, b) translation amplitude (Δuy)max as a function of angle α for εpre = 3%, c) same as a function of εpre for α = 60°. Amplitudes (Δuy)min between intermediate returns to ambient temperature are also plotted. Gray-shaded rectangles in the graphs correspond to non-valid situations. 54

Figure 2.14. Evidence of an attraction effect: a) thermal activation sequences considered to observe the effect of Configuration #24 in Step 3 on subsequent steps, b) and c) same plot as Figures 2.8.(a) and (b). Black dot and red squares correspond to Steps 3 and 5 respectively, for α = 90° and εpre = 3%..... 55

Figure 2.15. Close-up of Fig. 2.14-c. Numbers refer to the configurations in Fig. 2.6. 55

Figure 2.16. Example of a thermal activation sequence enabling a given platform position to be reached. The target was $(ux, uy, \theta z)$ = (-2.80 mm, 1.95 mm, 1.2°), with a precision of 0.1 mm and 0.1° required for the translation and the rotation respectively (red marks), for α = 90° and εpre = 3%. The sequence was defined empirically, with the constraint of returning to

ambient temperature (Configuration #1) after each heating configuration. Configuration numbers refer to Figure 2.6. 57

Figure 3.1. Architecture of the 6-RPR Prestressed Planar Parallel Mechanism (PPPM) under study. It can be noted that the actuated prismatic joints actually correspond to the SMA wire actuation. 61

Figure 3.2. First version of the system. 62

Figure 3.3. Main components of the second version of the system. (a) Assembly of the mechanism. (b) Exploded view of the moving platform. (c) Exploded view of the ring. 63

Figure 3.4. Main components of the third design. (a) Overview of the mechanism. (b) Exploded view of the mobile platform. 64

Figure 3.5. CAD of the final prototype: (a) Isometric view of the mechanism. (b) Top view of the mechanism. 65

Figure 3.6. Details of the exploded view of the mechanism. 66

Figure 3.7. Details about the components that ensure positioning of SMA wires. (a) Fixed base. (b) L-shaped fixing bracket. 66

Figure 3.8. Details of the mobile platform. (a) Functionality of the details of the mobile platform. (b) Isometric views of the CAD assembly of the mobile platform. 67

Figure 3.9. Finite element model of the moving platform. (a) Boundary conditions. (b) Mesh. 68

Figure 3.10. FE analysis of the moving platform using CATIA General Structural Analysis module: Von Mises stresses. 69

Figure 3.11. Tightening of the SMA wires. (a) Steps in the simplified state diagram. (b) Schematic view in the dominos. 70

Figure 3.12. Components of the prestraining system. 71

Figure 3.13. (a) Simplified state diagram of a SMA wire: b) with preliminary steps to pre-stretch the six SMA wires in the mechanism before starting a thermal activation sequence. 72

Figure 3.14. Principle of the prestraining system. (a) Initial state of SMA wire and hollow bolts. (b) Straightening the SMA wire by unscrewing the hollow bolt in contact with L-shape bracket. (c) Prestraining the SMA wire by unscrewing the hollow bolt in contact with the domino... 73

Figure 3.15. Mechanical characterization of the SMA wire: (a) experimental setup, (b) picture of the sample under test, 80 mm in gauge length, (c) stress-strain curves until rupture. 75

Figure 3.16. Mechanical training of the SMA wires before placement in the mechanism: displacement-controlled training of a long SMA wire (810 mm in useful length). Heating is performed after each load-unload cycle. 76

Figure 3.17. Stress-controlled stabilized mechanical cycle after training of a SMA wire (80 mm in useful length). 77

Figure 4.1. Manufactured prototype: a) assembly of the physical mechanism, b) details of the mobile platform, c) details of the prestraining system. 80

Figure 4.2. Experimental setup. 81

Figure 4.3. Thermal analysis: a) example of steady temperature field for an intensity of 3A in SMA1, 3 and 5; b) same for other intensity values. Note that temperature maps in a and b are yielded to 50°C and 30°C respectively. 82

Figure 4.4. Thermal analysis: a) steady temperature profiles along the SMA5 wire, b) time evolution of the maximum temperature, c) maximum steady temperature vs. intensity. 83

Figure 4.5. Creation of a cyclic rotation for α = 90°, L = 190 mm and εpre = 1.6%: a) thermal activation sequence considered, b) variation in rotation θz in each step, c) movement of the moving platform for the sixth cycle. 85

Figure 4.6. Comparison of two levels of SMA pre-strain εpre for α = 90° and L = 190 mm: time evolution of the absolute value of the rotation angle θz from Step 2 to Step 4. 85

Figure 4.7. Creation of a cyclic translation for α = 60°, L = 190 mm and εpre = 1.6%: a) thermal activation sequence considered, b) variation in displacement uy in each step, c) movement of the moving platform for the sixth cycle. 86

Figure 4.8. Workspace for α = 60°, L = 170 mm and εpre =3.25%: a) thermal actuation sequence, b) movement of the mobile platform for different heating configurations, c) same in projection onto plane (ux,uy), d) rotation θz of the platform. 88

Figure 4.9. Evidence of the attraction effect (for α = 60°, L = 190 mm and εpre = 1.6%): a) thermal activation sequence considered, b) in-plane translation of point E of the mobile platform, c) comparison with the results in Fig. 4.7-b (steps 23 to 26). 89

Figure 4.10. Evidence of an attraction effect: a) thermal activation sequences considered to observe the effect of Configuration #24 in Step 3 on subsequent steps, b) and c) same plot as Figures 4.8-a and -b. 90

Figure 4.11. Example of a thermal activation sequence for α = 90° and εpre = 3.5%: a) movement in the plane (ux, uy), b) variation in angle θz c) normalized experimental and F.E. results. 91

Figure 4.12. Stiffness variability trial: a) experimental setup, b) two thermal actuation sequences before measuring the stiffness 92

Figure 4.13. Measurement of stiffness for two heating actuations (for α = 60°, L = 170 mm and εpre = 3.25%), see Figure 4.12-b. 93

Figure 5.1. Proposed solutions for future work, using soft components. 99

Table of tables

Table 1.1. Details of the superelastic loading path 1 in Fig.1.4-a, from [18]..... 13

Table 1.2. Examples of SMA-based mechanisms in the literature 29

Table 2.1. Shape-memory effect option constants from the Ansys documentation. 34

Table 2.2. The coordinates of the points A, B, C and D of the superelastic cycle. 34

Table 2.3. Inputs of the Ansys parameters..... 37

Table 2.4. Parameters fixed for the FE study. 38

Table 2.5. Classification of the heating configurations applied at Step 3 leading to the same movement in terms of translation magnitude $\sqrt{(ux2 + uy2)}$ or rotation magnitude θz. Numbers refer to the configurations in Figure 2.6. Exponent "0" is used when the magnitude is equal to zero. Symbol "/" separates sets with the same rotation amplitude θz but opposite rotation sign. Exponents "+" and "-" refer to the sign of the rotation. 47

Table 2.6. Example of a (non-valid) thermal activation sequence leading to plasticity. Configurations #21 and #59 are successively applied at Steps 3 and 4 respectively (for α = 90° and $\varepsilon\mathrm{pre}$ = 3%). The stress value exceeding the plastic yield stress of the SMA is underlined. 48

Table 2.7. Evidence of strong variability of stiffness in a given zone of the workspace. Steps 3 and 5 refer to the thermal activation sequence in Figure 2.14-a. Components Kxx, Kyy and $K\theta\theta$ of the stiffness matrix were obtained by applying a force of 100 N and a torque of 100 kN.mm at point E..... 56

Table 4.1. Evidence of stiffness variability through both simulation and experiments. $K\theta\theta$ was obtained by applying a mass of 2 N on the bar in Fig. 4.12-a..... 94

Table of notations

Acronyms

APDL	Ansys Parametric Design Language
CAD	Computer Aided Design
DIC	Digital Image Correlation
DOF	Degree of Freedom
FE	Finite Element
MEFF	Memory Effect (option in Ansys)
NiTi	Nickel-Titanium
OWME	One Way Memory Effect
PE	Pseudo-elasticity
PPPM	Prestressed Planar Parallel Mechanism
SATWME	Stress-Assisted Two-Way Memory Effect
SE	Superelasticity
SMA	Shape Memory Alloy
SME	Shape Memory Effect
SUPE	Superelasticity (option in Ansys)
TWME	Two-Way Memory Effect

Symbols

A	Austenite
M	Martensite
E	Center of the moving platform
E_M	Young modulus of martensite
E_A	Young modulus of austenite
$\sigma_{\max}$	Maximum stress to prevent plasticity (elastic limit)
M_s	Martensite-start temperature
M_f	Martensite-finish temperature
A_s	Austenite-start temperature
A_f	Austenite-finish temperature
T_0	Ambient temperature
T_1	Activation temperature
ε_{pre}	Prestrain value
α	Angle between SMA wires
γ	Maximum transformation strain

β	Slope of the transformation lines in the state diagram
d	Diameter of the SMA wires
L	Length of the SMA wire
a	Length of the platform bar
$(\Delta u_y)_{\max}$	Maximum variation of displacement
$(\Delta u_y)_{\min}$	Minimum variation of displacement
$(\Delta\theta_z)_{\max}$	Maximum variation of rotation
$(\Delta\theta_z)_{\min}$	Minimum variation of rotation
K_{xx}	Stiffness component of the stiffness matrix according to x-axis
K_{yy}	Stiffness component of the stiffness matrix according to y-axis
$K_{\theta\theta}$	Rotational stiffness component of the stiffness matrix

"The journey of a thousand miles begins with one step."— Lao Tzu

General introduction

Foreword

This thesis, funded by a ministerial scholarship M.E.S.R.I. (Ministère de l'Enseignement Supérieur, de la Recherche et de l'Innovation), began in November 2017. It was prepared at the Institut Pascal laboratory within the M3G department (Mechanics, Mechanical Engineering, Civil Engineering, Industrial Engineering). It is a multidisciplinary thesis, which is part of three themes of the department: MRSI (Machines, Robots, and Industrial Systems), ME (Experimental Mechanics) and Mat Inn (Innovative Materials), allowing me to highlight my profile as a mechatronics engineer. The objective is to create a planar-parallel prestressed mechanism actuated by multi-antagonist shape memory alloy (SMA) wires.

The thesis work was carried out at SIGMA Clermont, which allowed exploiting the machines available at the CTT (Centre de Transfert Technologique: mechanical platform of SIGMA Clermont) in order to manufacture the prototype.

This thesis has been fruitful, with various contributions, which have already been highlighted by a journal article in Meccanica (an international journal of theoretical and applied mechanics), by an international conference paper in Actuator 21 (an international conference and exhibition on new actuator systems and applications), by a national conference paper in CFM 2019 that was awarded by the 3rd prize for poster design (24e Congrès Français de Mécanique), as well as a contribution in The French Robotics Workshop 2020 organized by the GdR Robotique (GT6 Innovative design and mechatronics). A second journal article is in preparation.

At the beginning of the second year, a period of one month was spent in Thailand as a visiting researcher in the framework of PHC SIAM 2018, project 40710SE. This was an international collaboration with Chiang Mai University, Department of Mechanical Engineering. My task was to model SMA wires in compression in a granular medium using my expertise in SMA modelling by finite element method. The aim of the project was to develop a new potential application

of SMAs in the field of granular media. This collaboration led to two scientific contributions: a journal article and a proceeding paper.

Context and issues of the research work

The constant search for better mechanical products, mechanisms, and structures to keep pace with ever-changing economic and societal constraints has led scientists to seek new technologies that satisfy their needs. As a consequence, smart materials have been drawing attention thanks to their unique features marking the 21st century as the "Smart Material Age" as mentioned by Gandhi and Thompson, 1992 [1]. Smart materials, also known as active or responsive materials, can change their shapes or physical properties under the influence of external stimuli such as temperature, stress, moisture, light, pH, electric or magnetic fields [2]. Further information about active materials and their applications are presented in the Encyclopedia of Smart Materials published in 2002 [3]. Shape memory alloys (SMAs) are active materials which are able to recover a pre-deformed shape upon heating [3]. They were used in various applications in different fields for their interesting thermomechanical features [4]. Thanks to their thermomechanical shape memory propriety, SMAs have been used as actuators in robotic systems [5].

The laboratory members carried out different studies on SMAs starting from applications in civil engineering [6] in order to create prestress states in concrete beams [7], [8], to the design of active structures [9]. Applications in mechanical engineering were also studied, for instance designing a rotary actuator prototype driven by a SMA [10], [11] and studying the variable stiffness of a planar mechanism [12]. In literature, there are many linear actuators driven by SMAs [13]. This is a logical and expected outcome since SMAs when heated they shrink and when cooled they lengthen; which make it is easy to create a translation. Besides linear actuators, many rotary actuators based on SMAs were developed transforming prismatic motion into rotation[14]. Some SMA-based actuators with several degrees-of-freedom exist, like origami [15], grippers [16] and parallel robots [17]. However, the SMA components are mostly arranged in a parallel or a serial architecture without a proper study of the hysteretic effect of SMA. Considering the acquired information and knowledge about SMAs, the natural evolution toward the creation of a pre-stressed active mechanism driven by multi-antagonistic SMAs with several degrees of freedom took place, and it was the starting point of this thesis. The idea was to design an active structure with several DOFs, then was refined to have a mobile platform (flexible or rigid) that will be attached to several

SMA wires as actuators and then we decided on the key properties of a multi-DOFs mechanism activated by SMA wires as illustrated in Figure 0.1. This type of mechanism should be useful for rotary actuation with the possibility of small translations for readjustment. By changing the setting of some of its key parameters, it is possible to adjust the relative displacements in translation and rotation. The potential applications of such mechanism include position locking and integration to an end-effector.

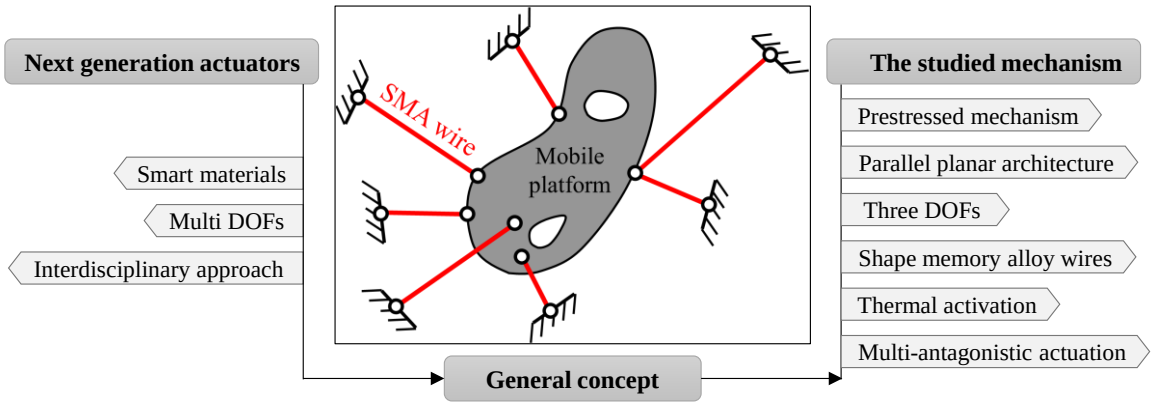

Figure 0.1. Key features of a multi-DOFs mechanism activated by SMA wires.

It is known that mature technologies about planar mechanisms are widely available and prestressed mechanisms using SMA wires already exist. However, the multi-antagonistic positioning of the SMA wires in a planar prestressed mechanism is a new approach, addressed in this thesis. In the following lines, only static analysis is considered using several heating configurations where the SMA wires are thermally activated. Although the studied mechanism is very similar to a cable-driven robot, its behavior is quite different. The main reasons why multi-antagonistic SMA actuators are not yet employed in parallel mechanisms are the non-linear and hysteretic responses of these materials, which are highly dependent to actuation parameters. Therefore, SMAs have been predominantly used in simple single DOF systems. Hence, in this thesis and through the following chapters, we will try to demonstrate that more sophisticated systems can be built (such as the here proposed planar mechanism), and controlled.

Organization of the manuscript

This thesis is divided into four main chapters followed by a general conclusion and description of future work.

Chapter 1 provides useful information about Nickel-Titanium based SMA and its underlying-physical phenomenon in order to understand the functioning of the studied mechanism in the following chapters. Besides, it reviews some of the most known applications of SMAs as actuators, particularly in robotics.

Chapter 2 presents a numerical study that analyses the hysteretic and multi-antagonistic properties of the studied mechanism using a material model provided by a finite element calculation software. Several cases of study are carried out to prove different concepts and to explore others.

Thereafter, intermediate but crucial steps are presented in Chapter 3, which are the process of building a physical demonstrator and the preliminary preparation of SMA wires. This chapter is the bridge between the numerical results and the experimental tests.

In chapter 4, the setup of experiments and the results are discussed and compared to numerical results. A preliminary thermal analysis is carried out. Several experimental cases of study are addressed: cyclic rotation and translation, discrete-binary-actuated workspace, attraction effect, and variable stiffness.

"If you want something you've never had, you must be willing to do something you've never done." — Thomas Jefferson

Chapter 1: Literature review

Contents

1.1. Introduction 6
1.2. Shape-memory alloy as a smart material 6
1.2.1. Definition and interest of NiTi-based SMAs 6
1.2.2. The underlying-physical phenomenon of SMAs 7
1.2.3. SMAs cooling methods 9
1.3. Interesting thermomechanical behaviors of SMAs 9
1.3.1. Shape-Memory Effects 10
1.3.1.1. One-Way Memory Effect 10
1.3.1.2. Stress-Assisted Two-Way Memory Effect 11
1.3.1.3. Two-Way Memory Effect 11
1.3.2. Superelasticity 12
1.3.3. Damping behavior 14
1.4. Wide range of SMA-based applications 14
1.4.1. Automotive applications 15
1.4.2. Aerospace applications 15
1.4.3. Biomedical applications 16
1.4.4. Textile applications 17
1.4.5. Civil engineering applications 18
1.5. Robotic applications of SMA-based actuators 19
1.5.1. Biologically-inspired robots 20
1.5.1.1. Crawler robot 20
1.5.1.2. Fingers 21
1.5.1.3. Grippers 22
1.5.2. Origami and kirigami actuators 23
1.5.3. SMA mini-actuators 24
1.5.4. Prismatic and rotary actuators based on SMA 25
1.5.5. Multi-DOF SMA-based actuators 26
1.6. Conclusion and positioning of the present study with respect to the literature 28

1.1. Introduction

The present chapter is dedicated to reviewing the literature related to the research work presented in the next chapters. Important notions, principles and limitations are addressed in the following sections giving an overview of the context of the study. This chapter is organized as follows:

- Section 1.2 presents basic notions and generalities about shape memory alloys (SMAs).
- Section 1.3 describes the thermomechanical behavior of SMAs.
- Section 1.4 illustrates significant SMA-based applications in different fields.
- Section 1.5 highlights some of the robotic applications of SMA-based actuators.
- Finally, section 1.6 explains the positioning of the present study with respect to the literature and concludes this chapter.

1.2. Shape-memory alloy as a smart material

The present section provides the useful information about SMAs for the following of this thesis. First, a brief presentation of Nickel-Titanium (Ni-Ti) and NiTi-based SMAs is given in section 1.2.1 as these alloys are the most used in engineering applications. Then, section 1.2.2 explains the underlying-physical phenomenon of SMAs. Lastly, section 1.2.3 presents some existing cooling methods of SMAs as this is the main difficulty in the use of SMAs in engineering applications.

1.2.1. Definition and interest of NiTi-based SMAs

A SMA is a smart metal known for its capacity to "remember" or recover a pre-deformed shape when stimulated by temperature (T) or stress (σ) resulting in a large deformation [3]. Consequently, SMAs exhibit two types of memories: a thermal memory called shape-memory effect (SME) and a mechanical memory called superelasticity (SE) or pseudoelasticity (PE) [2]. The coupling between thermal and mechanical fields within SMAs is illustrated by another feature known as SMA damping behavior. These features are the result of a solid-solid transformation between a high symmetry phase and a low symmetry phase [18]. This transformation is discussed in section 1.2.2. Further details about SME, SE and the damping behavior of SMAs are presented in section 1.3. The SME was first recognized by Buehler and Wang in a NiTi alloy in 1962 [19]. Since then, the

interest in NiTi-based SMAs has been increasing. The NiTi alloy is also known as nitinol in a reference to its material composition and its discovery place (i.e. a combination of NiTi and Naval Ordnance Laboratory) [20]. There are other types of SMAs, mainly iron-based and copper-based [4]. Each alloy has its own advantages for particular requirements and applications and its disadvantages. However, nitinol and more generally NiTi-based alloys are more preferable for most applications. They are cheaper to produce, easier and safer to handle, biocompatible and have better mechanical properties than other SMAs [4]. Essentially, the aim behind using SMAs is to create new intelligent systems with adaptative features that simplify products while upgrading their performances. In fact, NiTi-based SMAs offer an interesting package of qualities such as compactness and flexibility, noiseless operation mode, large deformation with small temperature change, easy operation mode by Joule Effect, compatibility with harsh environments, large thermal and mechanical energy density, biocompatibility, high force during shape change, etc. [4], [18]. These previous advantages offer opportunities of development in different fields and applications [4]. Further details about SMA-based applications are presented in section 1.4 and section 1.5.

1.2.2. The underlying-physical phenomenon of SMAs

SMAs are active materials whose mechanical response is driven by temperature and stress. The underlying physical phenomenon is a solid-solid transition between two phases, namely *austenite* (A) for the parent phase and *martensite* (M) for the product phase [18]. This crystallographic transition is known as “martensitic” transformation. Roughly, austenite and martensite are present at “high” and “low” temperatures respectively. In the austenitic state, a SMA sample has a unique shape that was memorized during material manufacturing. In the martensitic state, the sample can be “permanently” deformed by several percent (pseudoplasticity effect). The martensitic transformation occurs by shear lattice distortion, generating different crystallographic structures: the austenite, always cubic, whereas martensite can have monoclinic, orthorhombic or tetragonal structure depending on the chemical composition. It is important to note that each martensitic crystal formed can have different orientations with respect to the parent phase direction known as *variants of martensite*. The assembly of variants may have two forms: *detwinned martensite*, also known as *oriented martensite*, in which a specific variant is dominant, and *twinned martensite* or *self-accommodating martensite*, which is formed by all the variants in equal proportions. Figure 1.1 illustrates the different SMA phases and crystal structures and the needed process

(loading-unloading or heating-cooling) to create these two types of martensite. Note that another structure of martensite in NiTi-based SMAs is gathering attention within researchers: it is known as the *R-phase*, a rhombohedral-distorted martensite [21]. Researchers are actively looking for the impact and the influence of the R-phase on the behavior of SMAs.

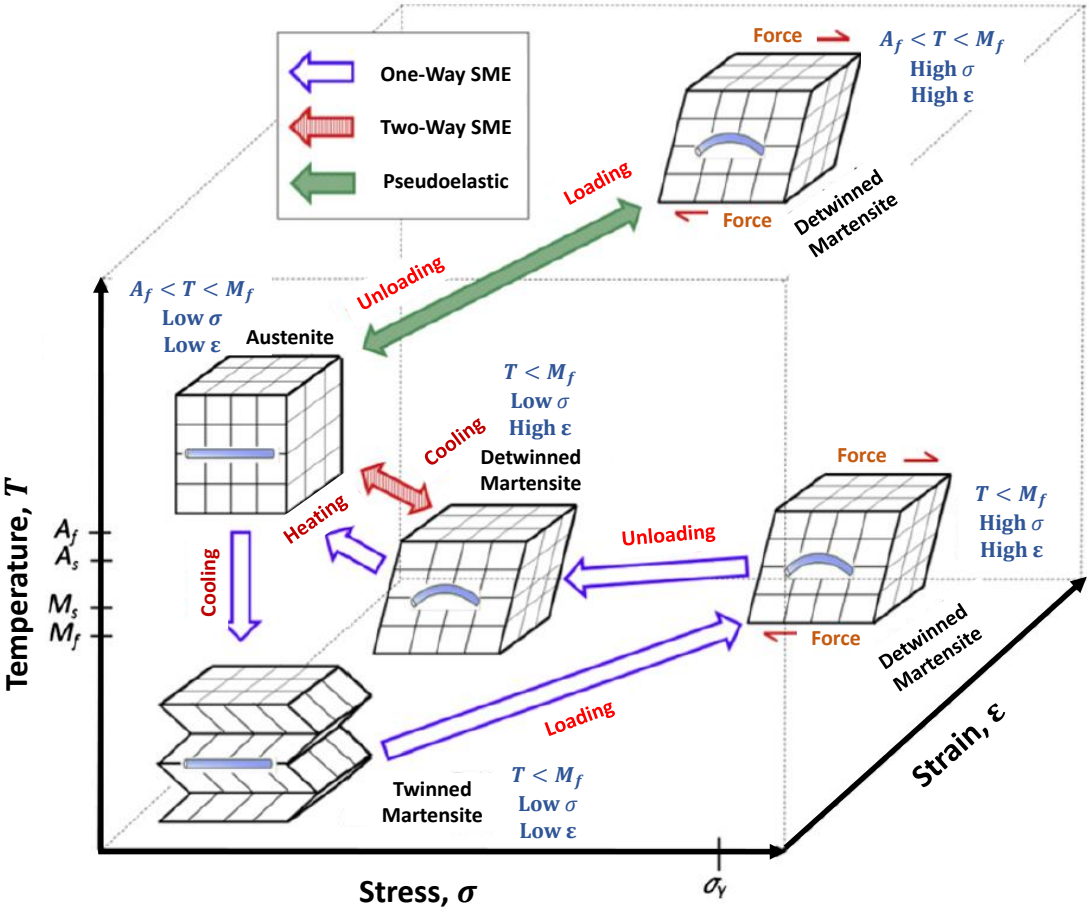

Figure 1.1. SMA phases and crystal structures, from [4].

The martensitic transformation is characterized by four key temperatures which are known as *austenite-start* (A_s), *austenite-finish* (A_f), *martensite-start* (M_s) and *martensite-finish* (M_f). Two transformations must be distinguished accordingly to the direction of transformation: the forward transformation that is a transition from austenite to martensite and the reverse transformation that is a transition from martensite to austenite. Under zero load, during the forward transformation, austenite begins to transform to twinned martensite at the M_s temperature and completes transformation to martensite at the M_f temperature. As a consequence, the material is entirely in the twinned martensitic phase. Likewise, during heating, the reverse transformation starts at the A_s temperature and is completed at the A_f

temperature. Detwinning the martensite is possible by applying a mechanical load from the twinned-martensitic phase. This process leads to a macroscopic shape change, where the new (deformed) configuration is maintained after releasing the load. A subsequent heating of the material to a temperature above A_f will result in the complete reverse phase transformation (from detwinned martensite to austenite) leading to a complete shape recovery. Cooling back to a temperature below M_f (forward transformation) leads to the formation of twinned martensite again with no associated shape change observed. The process described above is referred to as the Shape-Memory Effect (SME). If the temperature of the material is above A_f, a complete shape recovery is observed upon unloading to zero stress. This material behavior is called the pseudoelastic effect (PE) or also superelastic effect (SE) [18].

1.2.3. SMAs cooling methods

One of the reasons why researchers are interested in SMAs is their simple operating mode by Joule heating [7], [22]. Nevertheless, a proper monitoring and control of the heating process is needed to fulfill the requirements of SMA-based devices such as a rapid response time [23], [24] . Jani et al., gathered in their review about SMAs different cooling methods of SMAs, since cooling is one of the most challenges in SMA design that researchers need to overcome [4]. Among those methods, the reader may find active cooling procedures such as: heat conduction and convection, forced air, flowing liquids, thermoelectric modules like Peltier or semiconductor heat pumps, heat sinks and conductive materials [4]. However, active cooling has its drawbacks since it increases the cost, the weight, the volume and the mechanical and control complexity. As an alternative, a passive cooling is possible by improving the mechanical “design” and the control systems like: high surface-to-volume ratio design and control optimization of the surrounding environment [4].

1.3. Interesting thermomechanical behaviors of SMAs

SMAs are distinguished by their particular and unique features: they are non-linear materials and exhibit properties of metals combined with a wide elastic deformation range. The latter can reach up to 8% of elastic strain, which can be considered as large for metals [25]. This section introduces the different thermomechanical behaviors of SMAs. Section 1.3.1 explains the shape-memory

effect as it is the most renowned property of SMAs. Section 1.3.2 presents the superelasticity which is associated with the stress-induced phase transformation. Finally, section 1.3.3 describes succinctly the damping behavior of SMAs.

1.3.1. Shape-Memory Effects

The large elastic deformation of SMAs can be induced and recovered through temperature changes in a phenomenon called shape-memory effect (SME). Three types of SME can be distinguished: the *One-Way Memory Effect* (OWME), the *Two-Way Memory Effect* (TWME) and the *Stress-Assisted Two-Way Memory Effect* (SATWME) [4], [26].

1.3.1.1. *One-Way Memory Effect*

The OWME behavior occurs when the SMA material can only remember its "parent" shape (austenitic state) because the shape recovery is achieved only during heating after the material has been detwinned by an applied mechanical load. This phenomenon takes place when a SMA is preliminary deformed by load (leading to detwinned martensitic phase) and then unloaded at a temperature below A_s. Afterward, when it is heated above A_f, the SMA transforms back to austenite. To better understand the OWME, Figure 1.2 illustrates the thermomechanical uniaxial loading path in a combined stress-strain-temperature space [18]. The loading path starts from the parent phase (point A in Figure 1.2). Then, austenite cools below the forward transformation temperatures (M_s and M_f) in a stress-free transformation leading to the formation of twinned martensite (point B). Subsequently, applying stress with a magnitude that exceeds the start stress level σ_s (but remains under the plastic yield stress of martensite) initiates the reorientation process. A transformation plateau can be highlighted in the σ-ε diagram which starts at a stress level σ_s and ends at a stress level σ_f. Then, the detwinning process is completed (point C). The SMA is then elastically unloaded from C to D and the detwinned martensitic state is retained. Heating the SMA under stress-free state initiates the reverse transformation as the temperature reaches A_s (point E). The reverse transformation is completed at temperature A_f (point F), above which only the parent austenitic phase exists. In the absence of permanent plastic strain generated during detwinning, the original shape of the SMA is regained (indicated by A). The strain recovered due to the phase transformation from detwinned martensite to austenite is termed as the *transformation strain*. Subsequent cooling to martensite will again result in the

formation of self-accommodating twinned martensite with no associated shape change, and the whole cycle of the SME can be repeated [18].

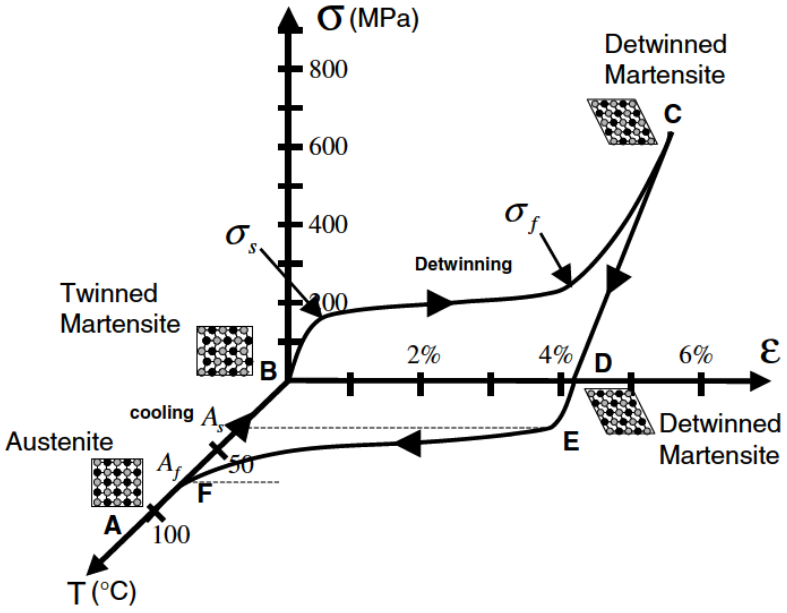

Figure 1.2. Stress-strain-temperature graph exhibiting the OWME [13].

1.3.1.2. *Stress-Assisted Two-Way Memory Effect*

When an austenitic SMA sample is cooled *under stress*, phase transformation occurs with creation of detwinned martensite, i.e. with a change in shape of the sample. Over thermal cycles, two shapes are thus observed. This phenomenon is known as the *stress-assisted two-way memory effect* (SATWME) [27]. Figure 1.3 illustrates the SATWME in the stress-temperature diagram for a constant stress

1.3.1.3. *Two-Way Memory Effect*

A two-way memory effect at zero stress is possible after a thermomechanical "training" consisting of numerous thermal cycles at fixed strain or stress, or from a constrained aging [26], [28]. However, these special SMAs require microstructural/ metallurgical optimization to achieve sufficient stability of the effect with respect to the applications [29]. They are rarely used in actuators [30], and are not considered in the present study. Compared to TWME, the SATWME is more reliable and is widely implemented in many engineering applications [30].

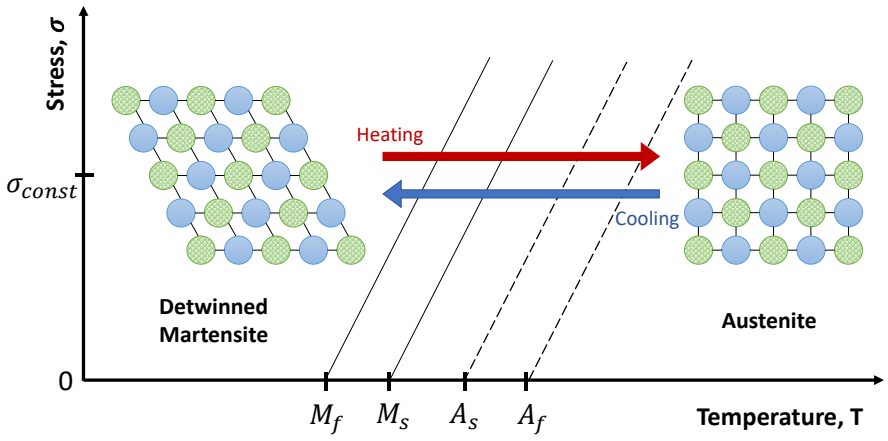

Figure 1.3. Schematic view of the SATWME at constant stress from [18].

1.3.2. Superelasticity

The superelasticity is associated with stress-induced transformation at temperatures beyond A_f. This transformation generates strain during mechanical loading, which is subsequently recovered upon unloading. Generally, a superelastic thermomechanical loading path starts at a constant high temperature from an austenite state. While applying load, SMA transforms into detwinned martensite. Finally, when unloading towards zero stress, it returns back to austenite. Two loading paths are possible: non-isothermal path and isothermal path which is the most commonly performed path [18]. Isothermal trials are usually used since they are slow, which allows the heat to be exchanged with the surrounding environment.

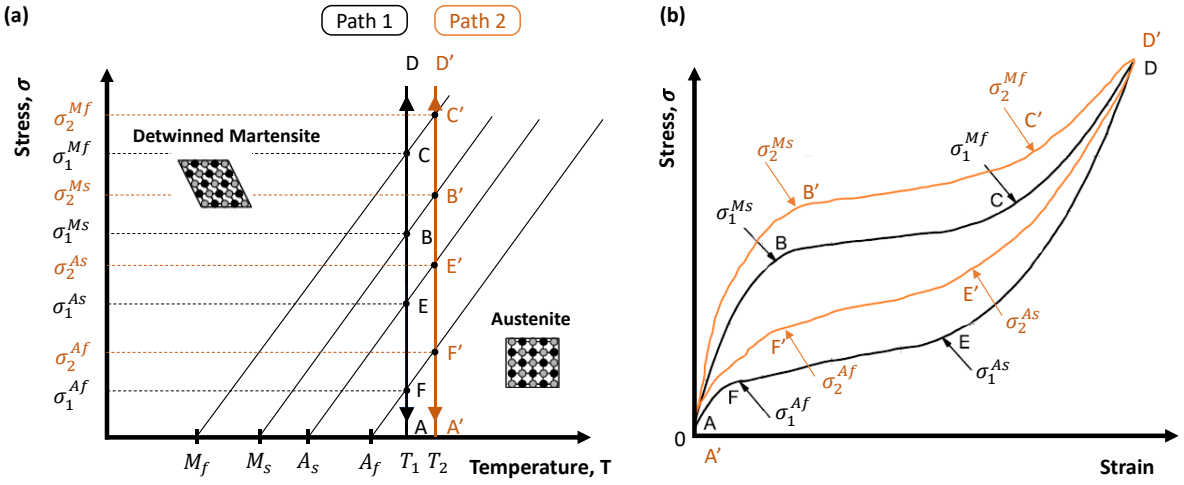

Figure 1.4. The superelastic effect, from [18]. (a) Two loading paths in the stress-temperature diagram, (b) same in the stress-strain diagram.

Figure 1.4 illustrates the impact of the thermomechanical coupling on the resulting loading cycle at a constant temperature. Two isothermal loading paths are considered: path 1 (A→B→C→D→E→F→A) at temperature T_1 and path 2 (A'→B'→C'→D'→E'→F'→A') at temperature T_2 higher than T_1 in the state diagram in Figure 1.4.(a), while the corresponding loading cycles seen in Figure 1.4.(b) are explained in Table 1.1. In fact, the consequences of the two paths 1 and 2 are the same, except for the differences in their magnitudes. Therefore, only path 1 is presented in Table 1.1. Note that, the higher the temperature of the loading is, the higher the equivalent stresses of transformation will be. As a result, it is advised to perform trials at a nominal temperature to facilitate the manipulation of SMA components.

Path	Comment	Stress level	Consequence
A → B	Austenite undergoes elastic loading.	$0 \rightarrow \sigma^{M_s}$	Initiation of martensitic transformation
B → C	Detwinned martensite undergoes elastic loading indicated by the change in slope on σ-ε curve.	$\sigma^{M_s} \rightarrow \sigma^{M_f}$	End of martensitic transformation
C → D	The stress causes no further transformation.	$\sigma^{M_f} \rightarrow \sigma > \sigma^{M_f}$	Elastic deformation of detwinned martensite
D → E	When the stress is released gradually by unloading, the martensite elastically unloads along the path.	$\sigma > \sigma^{M_f} \rightarrow \sigma^{A_s}$	Initiation of austenitic transformation
E → F	Recovery of the strain due to phase transformation at the end of unloading	$\sigma^{A_s} \rightarrow \sigma^{A_f}$	End of austenitic transformation
F → A	The material then elastically unloads to A.	$\sigma^{A_f} \rightarrow 0$	Return to the initial shape

Table 1.1. Details of the superelastic loading path 1 in Fig.1.4-a, from [18].

The forward and reverse phase transformations generate a mechanical hysteresis during a superelastic loading cycle. In the stress-strain space, this hysteresis illustrates the energy dissipated during the transformation cycle. The levels of the transformation stresses (σ^{M_s}, σ^{M_f}, σ^{A_s} and σ^{A_f}) that define the limits and the size of the hysteresis depend on the SMA material and testing conditions like the ambient temperature, the loading speed and the heat exchange properties [18]. Thermomechanical couplings have a strong and complex influence. On the one

hand, the faster the loading is, the "more adiabatic" the thermodynamical evolution is. On the other hand, the slower the loading is, the "more isotherm" the thermodynamical evolution is. And in both cases, the tendency is to minimize the mechanical hysteresis.

1.3.3. Damping behavior

During the SME and the SE, the SMA exhibits a crystalline structure change which does not occur in a reversible thermodynamic process. Indeed, an internal friction and the thermomechanical couplings produce an energy dissipation leading to a hysteretic behavior of the SMA and a high damping capacity. Researchers have shown that the damping behavior is related to the hysteretic mobility of interfaces between the variants of martensite (movement of twin boundaries) and internal defects in variants [31], [32]. Thermomechanical couplings are also involved because the temperature changes during phase transformation affecting the latter. Thus, the damping property is a manifestation of the hysteresis in the stress-strain curve. The hysteresis loop depends on many variables such as the type of material, heat treatment, temperature, frequency, etc. [31].

1.4. Wide range of SMA-based applications

Since the pursuit of new technologies is an endless process, developing new SMA technologies and improving the existing ones is an attractive solution for researchers and engineers. Thanks to their interesting features described in section 1.3, SMAs have opened wide applications and opportunities in different fields. A SMA component can effectively reduce the complexity of systems as it may replace multiple moving parts by a single active element. Thus, SMAs are most commonly used as actuators thanks to their motion and/or force generation. Therefore, in this section 1.4, a brief overview of SMA-based applications in the literature. Note that, robotic applications are addressed in further details in section 1.5 since the defined aim of the present study is to design a robotic mechanism driven by SMAs. This section is organized as following: section 1.4.1 presents examples of automotive applications; section 1.4.2 shows examples of aerospace applications. Section 1.4.3 describes some biomedical applications. Section 1.4.4 gives some SMA-based textile applications. Finally, section 1.4.5 presents some SMA-based civil engineering applications.

1.4.1. Automotive applications

The automotive industry is continuously growing and looking for new ways to develop its products in order to build safer, more comfortable and better performing vehicles. Subsequently, SMAs found its place within this growth. They usually function as linear actuators and active thermal actuators. Figure 1.5 illustrates some of the existing and potential SMA applications in the automotive domain [4].

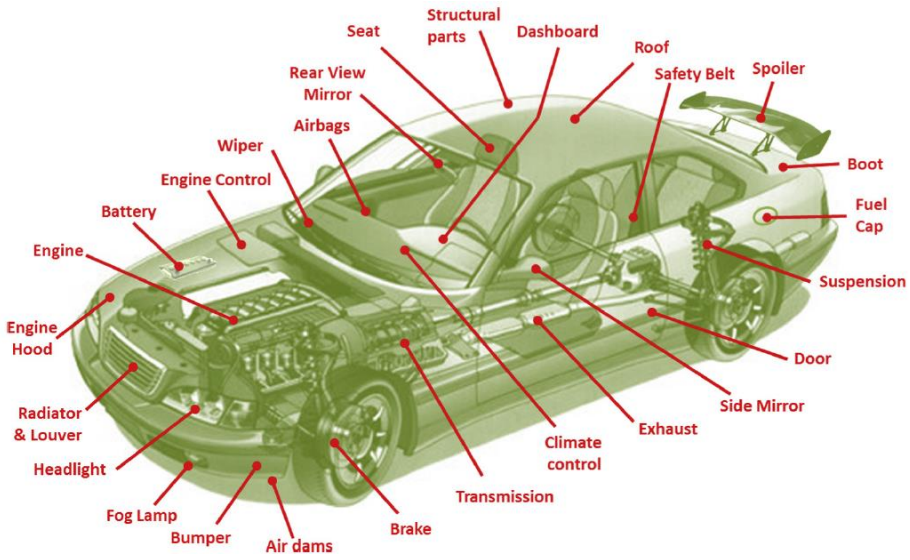

Figure 1.5. Existing and potential SMA applications in the automotive domain [4].

1.4.2. Aerospace applications

Similar to the automotive field, the unique features of SMAs, being both active and structural, have gathered interest in aerospace applications despite the high dynamic loads and the geometric space constraints of the field. Figure 1.6 presents some of the existing and potential SMA applications in aerospace applications within the fuselage parts and engine parts of a plane [4]. Some examples of these applications are structural connectors, release or deployment mechanisms, vibration dampers, etc. [4]. Hartl and Lagoudas described in their paper [25] the recently explored aerospace applications of SMAs dividing the technology into three areas: fixed wing aircraft, rotorcraft and spacecraft. Figure 1.7 shows three examples from the literature of the areas cited above that used the SME of SMAs [33]–[35]. Propulsion systems and structural configurations (morphing) are the two main SMA applications in aerospace [25]. In particular, SMA-based morphing-wing mechanisms witness a huge interest among researchers

[36]. Indeed, many experimental studies investigate the design and/or control of such mechanisms which reflects the efficiency of SMAs in this field [37]–[43].

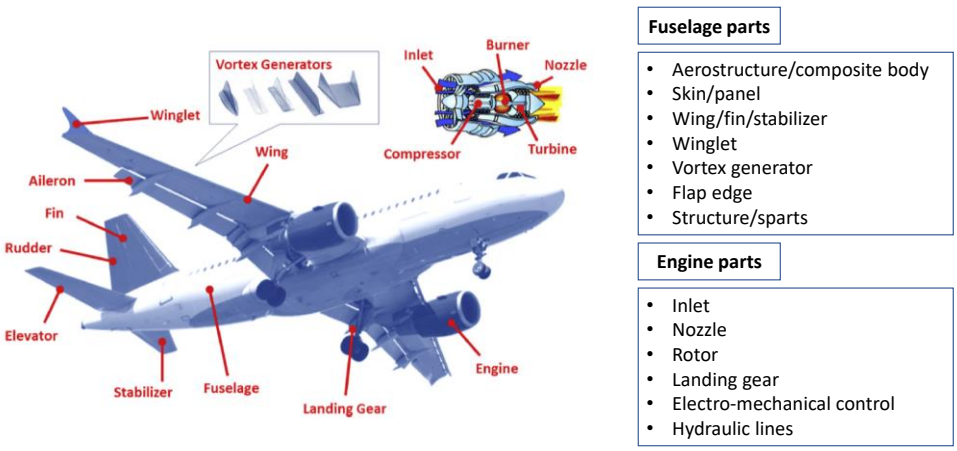

Figure 1.6. Existing and potential SMA applications in the aerospace domain [4].

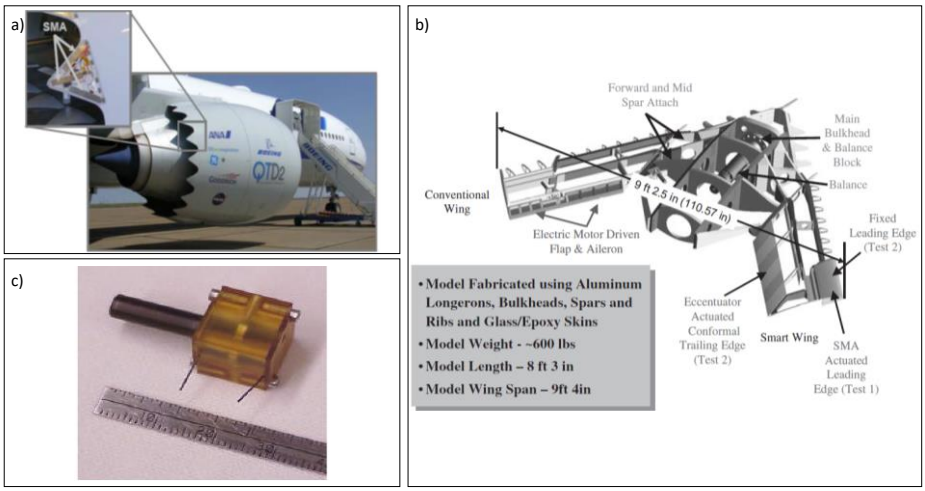

Figure 1.7. Examples of SMA applications in aerospace field. (a) Structural configuration: Boeing variable geometry chevron using SMA beams [33]. (b) Propulsion system: wind tunnel model structural layout using SMA torque tube [34]. (c) Spacecraft application: a rotary latch using SMA torsion spring [35].

1.4.3. Biomedical applications

Thanks to its biocompatibility and unique features, SMA has been widely used in biomedical applications like orthodontic, orthopedic, vascular, surgical instruments, etc. as shown in Figure 1.8 [4]. As an actuator, SMA is significantly integrated in minimally invasive surgery (MIS), which explains the interest of researchers in developing and improving SMA-based catheters [44]–[46] and endoscopes [47]–[51].

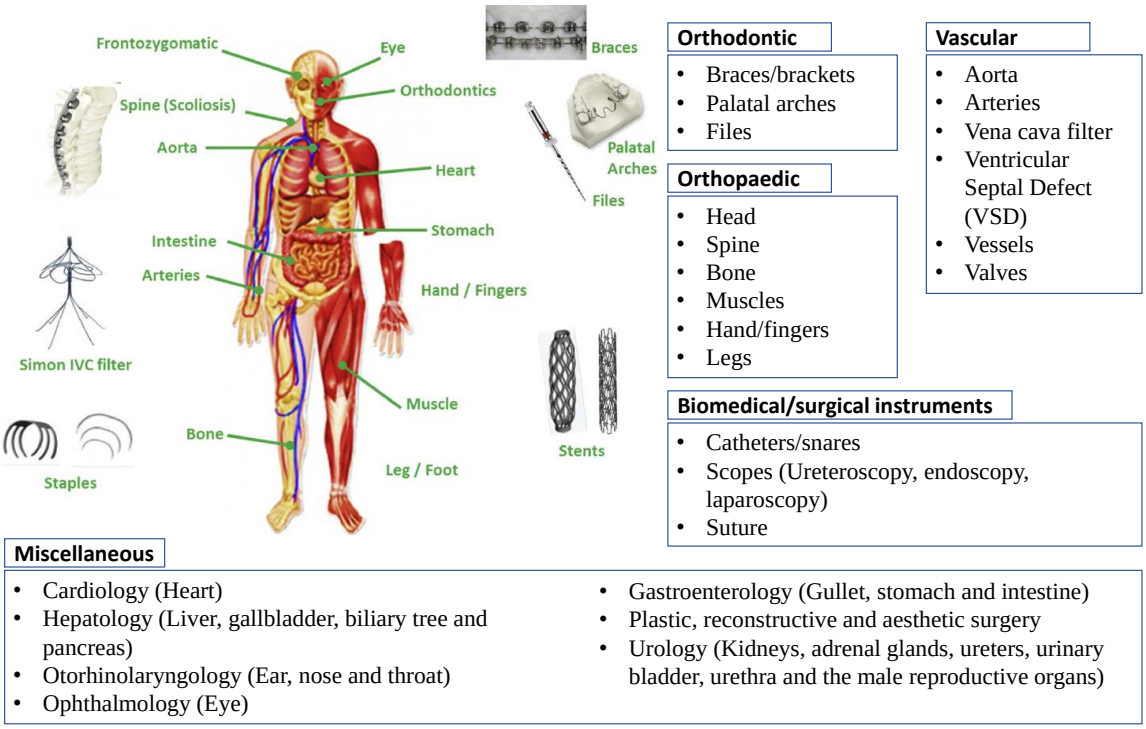

Figure 1.8. Existing and potential SMA applications in the biomedical domain [4].

1.4.4. Textile applications

Smart interactive textiles can be classified in two generations: first generation devoted to sensorics and second generation devoted to mechanical actuating outputs. Considering the scope of the thesis, it is the second generation that is discussed here. Smart textiles are considered essential to next-generation wearables, aerospace structures, medical devices and soft robotics [52]. In fact, as they are compliant, pliable, and have large deformation actuating functional fabrics. They are an interesting solution that amplifies force as well as strain in fabrics [52], [53]. Among different types of active materials that are relevant for textiles, SMAs have been widely used. An SMA-based actuating textile is a result of weaving and knitting textile embedded SMA components like NiTi wires. Contractile SMA-knitted actuators are specially used to create actuating functional fabrics. Eschen et Abel, 2019 established an empirical model using Dynalloy Flexinol® (see figure 1.9) that predicts the performance of large deformation contractile SMA-knitted actuators with dimensionless geometric parameters [53]. SMA can be combined with other active materials in order to create active variable stiffness (AVS) fibers as it is demonstrated by Yuen et al. [54]. The latter used SMA wires and thermally responsive polymers to make multifunctional fibers, as shown in Figure 1.10, that can move to a new position then hold that position without requiring additional power [54].

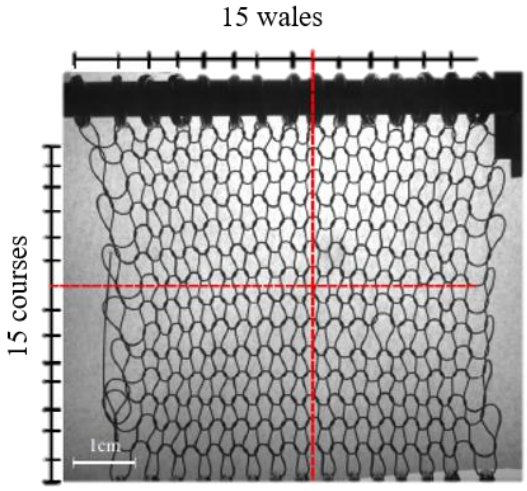

Figure 1.9. Example of a contractile SMA-knitted: the contractile SMA knitted actuator prototypes consist of 15 wales and 15 courses. The displayed prototype is manufactured with Dynalloy Flexinol® wire (A_f = 90°C, d=0.305mm) [53].

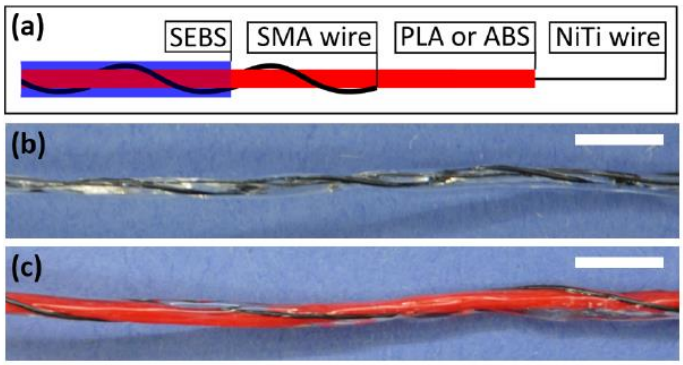

Figure 1.10. Active variable stiffness (AVS) fibers. (a) Composition of an AVS fiber. (b) PLA-based AVS fiber (the PLA core and the SEBS coating are both transparent). (c) ABS-based AVS fiber. Scale bars are 1cm. [54]

1.4.5. Civil engineering applications

In order to meet the large size and practical application in civil engineering, SMA cables have been developed and increasingly used thanks to their superelasticity, moderate energy dissipating and damping capabilities [55]. Vibration control and prestressed strengthening are two common SMA applications in civil engineering. For instance, Dieng et al. used SMA damper device to mitigate vibration amplitudes of bridge cables (see Figure 1.11) [56]. Santos et al. designed an adaptive shape-morphing tensegrity structure, with frequency self-tuning capabilities, using SMAs to do an active vibration control as shown in Figure 1.12 [57].

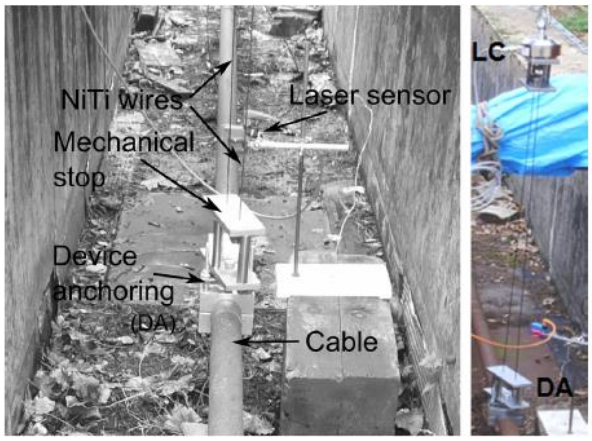

Figure 1.11. Experimental test on a SMA damper device. The damper device, used to investigate the effect of SMA dampers during the cable vibration, was placed at several positions on the cable. The experimental setup was realized on a cable test bench [56].

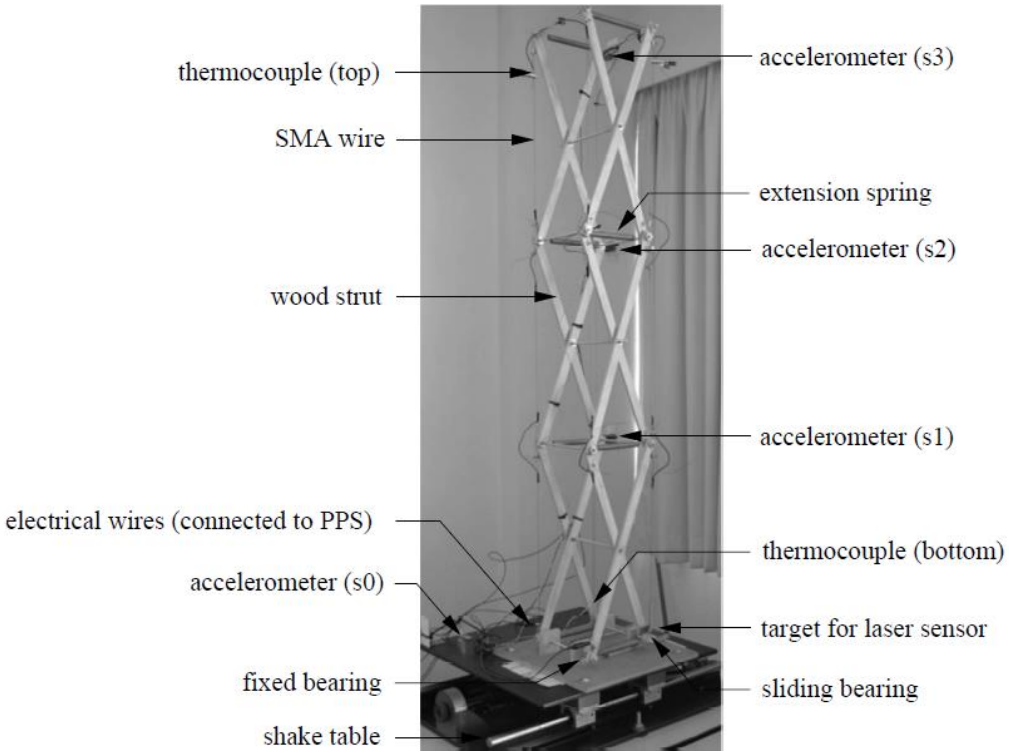

Figure 1.12. General view of the experimental prototype of an adaptive shape-morphing tensegrity structure, with frequency self-tuning capabilities, using SMAs [57].

1.5. Robotic applications of SMA-based actuators

SMAs offer an appealing alternative to the classical drives such as the electric or hydraulic motors [58]. SMA actuators in robotics may overlap with other applications such as textile for making soft robots or biomedical like endoscopes

and examples are wide. Thus, in this section, further applications in robotics are presented as following:

- Section 1.5.1 presents biologically-inspired SMA-based robots.
- Section 1.5.2 highlights some SMA-based origami and kirigami robots.
- Section 1.5.3 gives some examples of SMA mini-actuators.
- Section 1.5.4 presents some prismatic and rotary SMA-based actuators.
- Lastly, section 1.5.5 illustrates some multi-DOF SMA-based actuators.

1.5.1. Biologically-inspired robots

Having an excellent strength-to-weight feature and a large deformation capability allows SMA to take part of bioinspired robotic systems, which can be found in different sizes including microstructures and microrobots [59]. In the following sections, some biologically inspired robots, where SMAs are used as muscle-like actuators, are succinctly presented.

1.5.1.1. *Crawler robot*

Creating a locomotion mechanism provides a solution to penetrate through narrow areas, access-limited zones and various environments. Inspired by inchworms, SMA-crawler robots have been developed in order to create a locomotion such as the Omegabot designed by Koh and Cho [60]. The final design of the crawling robot Omegabot using SMA springs, illustrated in Figure 1.13, can move in a 2D plane using anisotropic friction pads. In this robot, 8 SMA coil springs were used: two upper SMA springs each one is parallel to two lower SMA springs working in antagonism and one left SMA spring parallel to a right SMA spring.

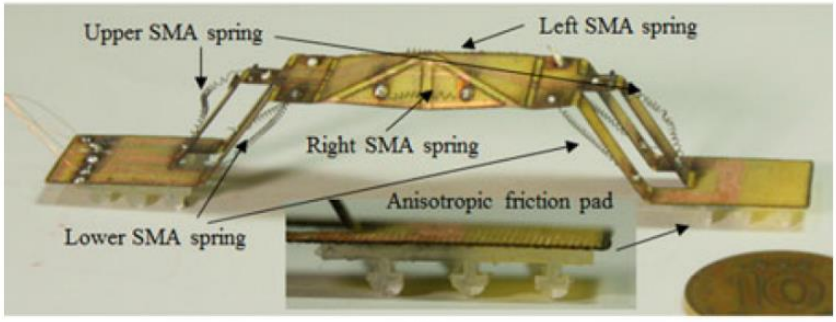

Figure 1.13. The Omegabot prototype with SMA spring actuators and anisotropic friction pads [60].

Moreover, external pipe-crawling robots based on SMA actuation for inspection were also developed and usually have the shape of compliant rings as seen in Figure 1.14 [61], [62]. Example (a) shows a crawling device where two SMA

wires and three pairs of circumferentially arranged U-shaped SMA strips are used. The device with a clamp-and-push motion is composed of two rings attached to each other by the SMA strips while the SMA wire is attached to the compliant mechanism and embedded within the housing with proper electrical isolation creates the circumferential motion for the compliant mechanism [61]. Example (b) illustrates a newer version of a compliant ring able to generate circumferential motion by using two SMA wires rather than one SMA wire in one ring in example (a) [62].

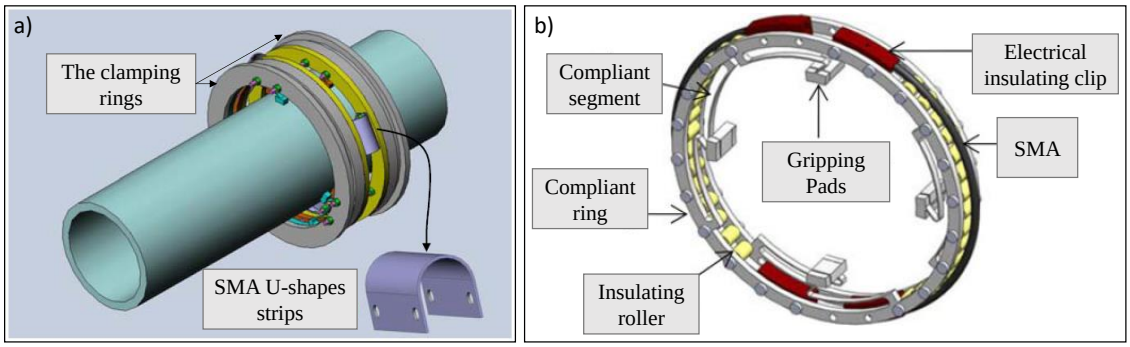

Figure 1.14. (a) Solid model of a crawling device with clamping rings and three SMA U-shapes strips. The spring steel bias spring strips are not shown in this picture [61]. (b) Geometric model of the SMA-actuated radially deployable compliant mechanism [62].

1.5.1.2. *Fingers*

Rehabilitation robotics is a field of research dedicated to help people who require assistance where biomimetic-robotic devices are used to improve a certain functionality. For instance, artificial fingers are in a continuous progress. Researchers are trying to find new ways of actuation to have both soft and efficient finger such as using SMA components, often in antagonism, to develop variable stiffness mechanism [63]. Thus, controlling the bending and the stiffness is the crucial part. Some prototypes use SMA wires to bend the finger [64]–[66] others use plates [67] or different shapes. Figure 1.15 illustrates some examples. Example (a) presents a contracting antagonistic SMA muscle pairs in an artificial finger controlled by a Fuzzy PWM-PID where six one-way SMA wires were used to rotate the joints of the finger [63]. Example (b) shows a soft finger with three types embedded SMA wires where one SMA-1 wire is used as the bone structure to support the finger, two SMA-2 wires actuate the deformation of the mechanism while six parallel SMA-3 wires provide the variable stiffness of the actuator [66]. Example (c) illustrates the actuation through Joule heating of the flexor and

extensor causing the finger to flex and extend using a thermomechanical trained NiTi plate [67].

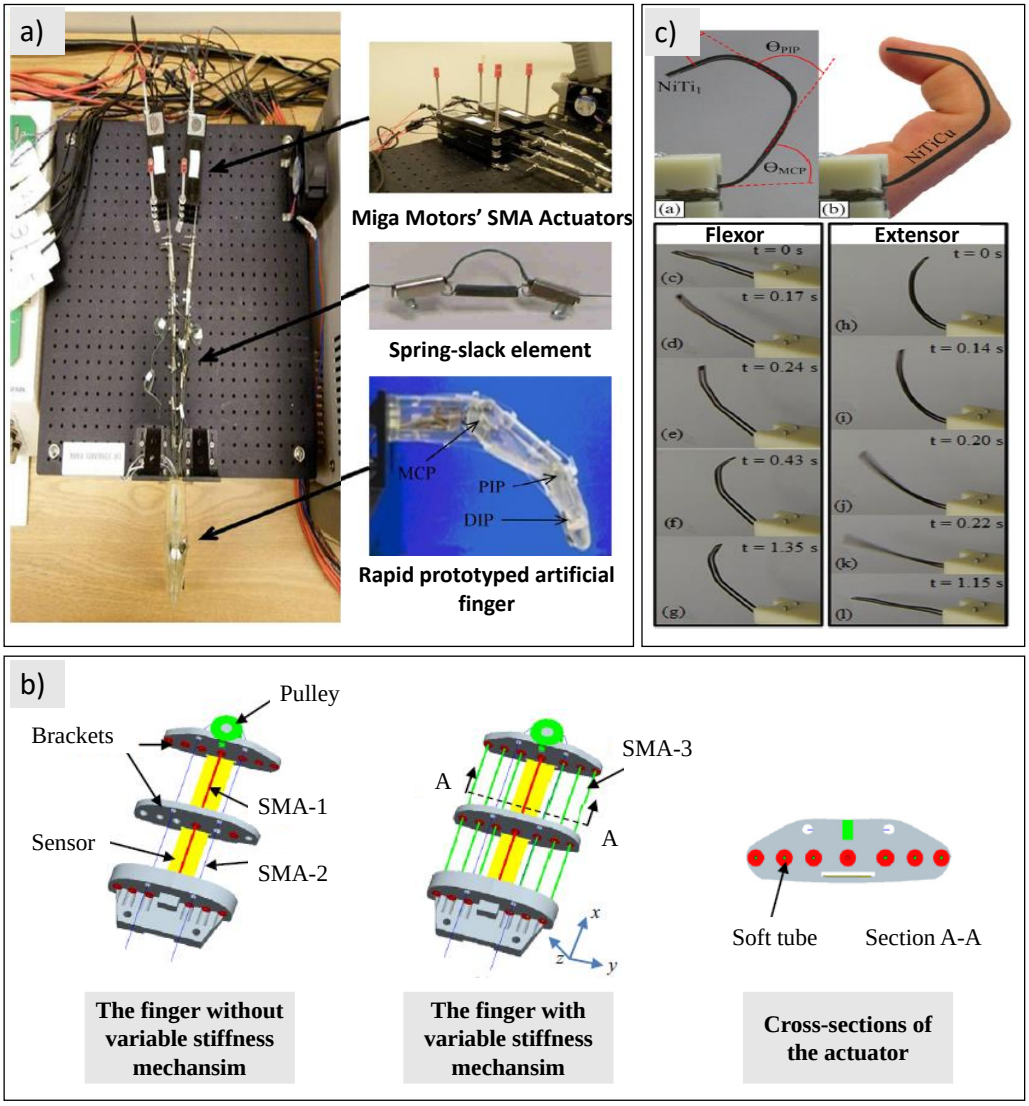

Figure 1.15. (a) Experimental setup of SMA muscle pairs in an artificial finger [63]. (b) Configuration of a soft finger with embedded SMA fibers [66]. (c) Anthropomorphic finger antagonistically actuated by SMA plates [67].

1.5.1.3. *Grippers*

Similar to fingers, SMAs are also used as actuators for soft and smart grippers. For instance, a self-sensing 2-DOF microgripper module with wide handling ranges was designed by Lan et al., using two distributed SMA wires, as it can be seen in Figure 1.16.(a) [68]. Figure 1.16.(b) shows the design of a 2-DOF gripper actuated by a NiTi spring connected to the jaws: the gripper opens by applying voltage and closes by cooling [69]. SMA wires can be combined with other

soft materials in order to create soft grippers as demonstrated by Wang et al. [70]: Figure 1.16.(c) illustrates the structure of the finger where a SMA wire is embedded along the length of polydimethylsiloxane (PDMS) matrix (composite) to actuate the hinges by bending [70].

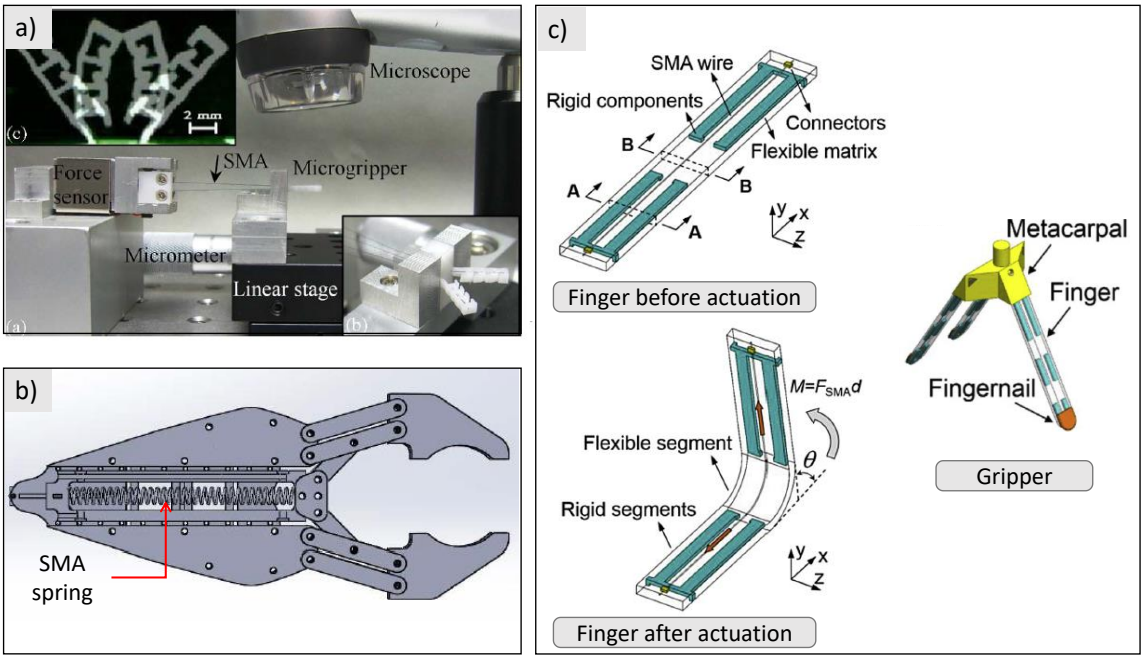

Figure 1.16. (a) Self-sensing microgripper module with wide handling ranges [68]. (b) SMA gripper in a transition position [69]. (c) Schematic of the soft gripper and its hinge actuator [70].

1.5.2. Origami and kirigami actuators

Reconfigurable structures and robots have been sought in engineering applications where the art of origami and kirigami presents an interesting approach [71]. The origami is produced by folding a single sheet of paper and combining basic folds in a variety of flexible ways while the kirigami is a variation of origami with cut papers [72]. Incorporating SMA components, mainly SMA springs, in an origami structure helps its actuation and transforms it into an active mechanism with an outstanding deformable feature [73]. Moreover, an origami may have the architecture of a 3D parallel robot as shown in Figure 1.17. For instance, Salerno et al. build an origami parallel module that generates two rotations and one translation [74]: see Figure 1.17.(a). Another example is a kirigami parallel structure with helical motion providing three degrees-of-freedom (DOF) per the screw theory [72]: see Figure 1.17.(b). The compliance of origami enhanced by the actuation of SMA components forms multi-DOF actuators.

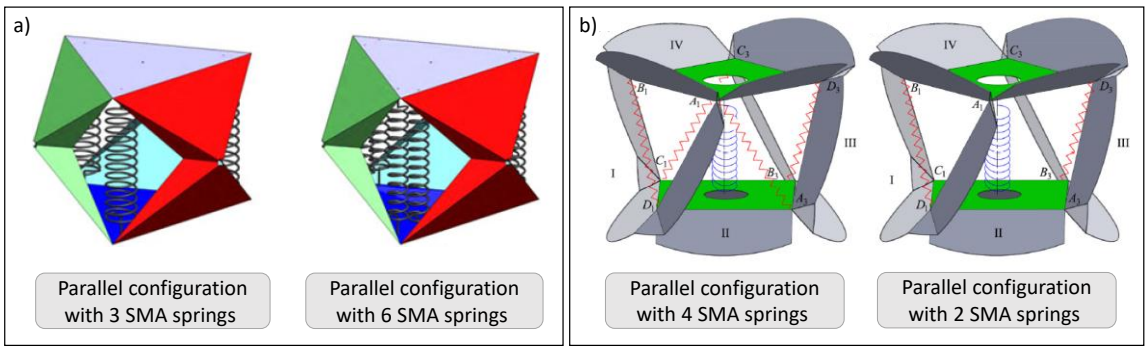

Figure 1.17. (a) Two sets of SMA helical spring configurations for the origami parallel module (three and six actuators) [74]. (b) Actuation models of the kirigami structure (two and four actuators) [72].

1.5.3. SMA mini-actuators

Miniaturization is increasingly sought while developing actuators as a solution of the limited space. As a result, mini-actuators need to be light and compact to fit the aim. Considering that SMA actuators have a high power-to-weight ratio among light-weight technologies, they are qualified as high potential actuators for miniaturization [4]. Nespoli et al. presented in their review an overview of publications and patents concerning SMA mini-actuators, grouped according to whether they provide linear or rotational motion, Figure 1.18 presents three examples of SMA mini-actuators [75]. It can be seen in (a) an SMA actuator with a maximum stroke of 0.8 mm against a force of 98 N. Figure 1.18.(b) shows a smart-servo actuator which is able to turn 30° right and left achieving a torque of 1.5 N.mm. Figure 1.18.(c) shows another actuator that can reach a stroke of 0.7–0.8 mm with an output of 5–7 N. The examples cited above are one-DOF mini-actuators; nevertheless, multi-DOF SMA mini-actuators exist such as example (a) in Figure 1.17, section 1.5.2.

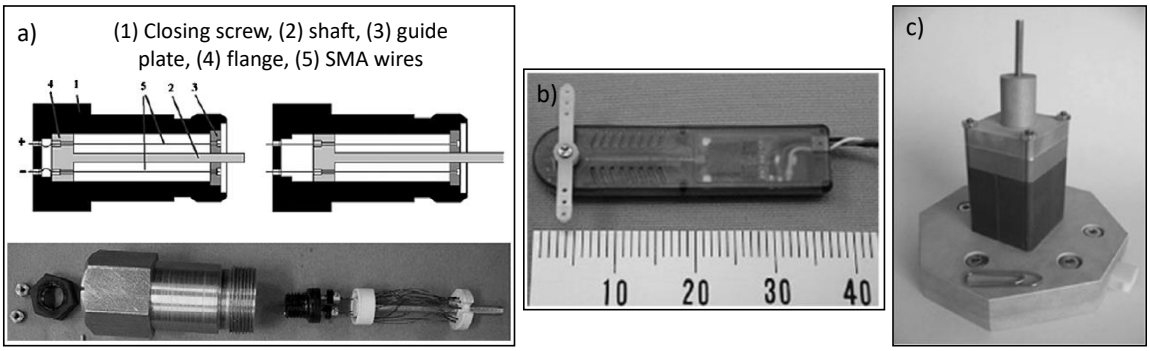

Figure 1.18. Examples of SMA mini-actuators. (a) Linear SMA mini-actuator. (b) Rotational SMA mini-actuator. (c) Ferromagnetic SMA mini-actuator [75].

1.5.4. Prismatic and rotary actuators based on SMA

Basically, a linear SMA wire (or spring) contracts when heating and elongates upon cooling under a bias load; hence, generating a motion. However, it is possible to change either the direction or the type of motion by using specific mechanisms like a lever or a pulley (e.g. from linear to revolute and vice versa) as shown in Figure 1.19 [13]. Different designs were considered with three main objectives: power (force or load), displacement (stroke or angle) and bandwidth (speed or frequency). Modular architecture is among the solutions to increase the stroke covered or the force generated by linear SMA actuators [62] or rotational SMA actuators [77]. Figure 1.20 shows an arrangement of four helical SMA springs inside a compliant compensated linear actuator and its modular assembly as illustrated by Mammano and Dragoni [76]. The modular assembly increases the stroke generated by the 1-DOF actuator.

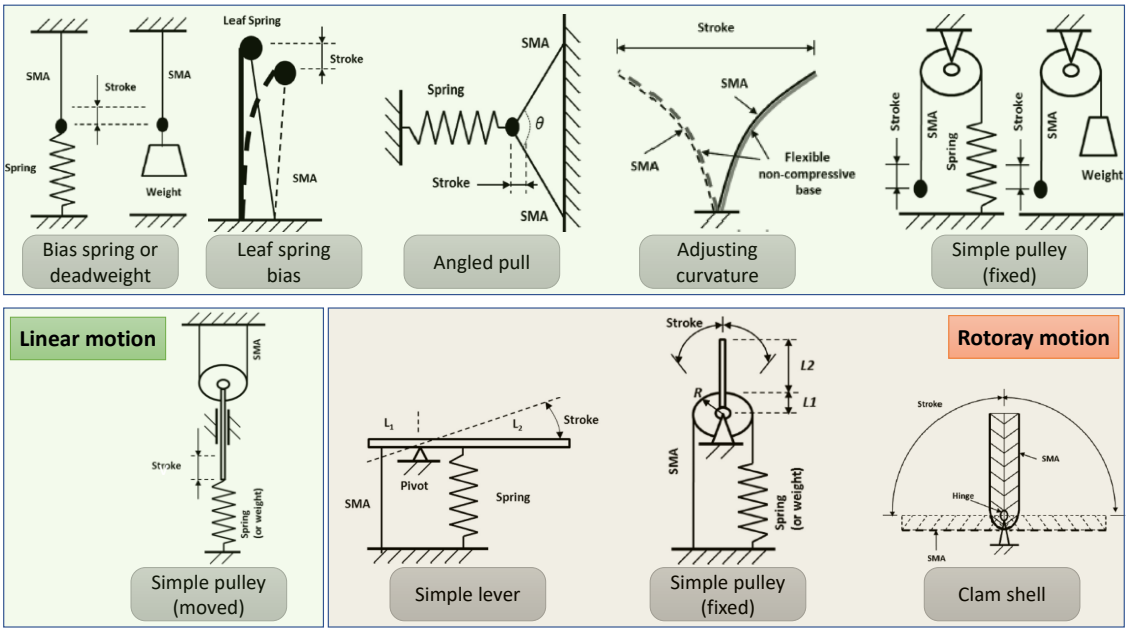

Figure 1.19. Basic SMA design approaches for linear and rotary motion [13].

An extensive review about SMA-based rotary actuators (Yuan et al., 2017) listed references based on research articles and patents, and presented around eighty actuators driven by SMA classified according to their rotation type: continuous or non-continuous, single or reversible direction [14]. As an example of a rotary actuator with continuous rotation ability, the planar wobble motor designed by Hwang and Higuchi could generate bidirectional high-torque motion using four SMA wires [78]. Due to the curvilinear translation achieved by

alternation of single activation and dual activation of the SMA wires, the internal gear part is wobbly driven and the central external gear is rotated as illustrated in Figure 1.21 [78]. The sequencing of activation of SMA wires generates a rotation, creating a 1-DOF actuator.

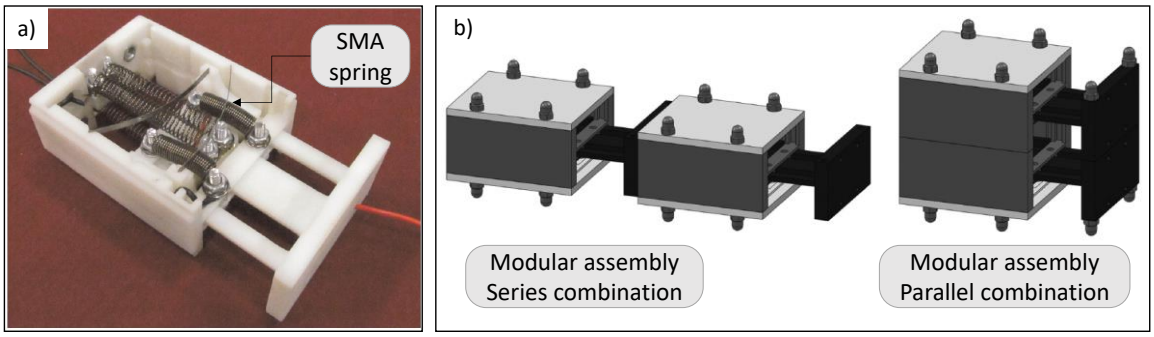

Figure 1.20. (a) Prototype of a compliant compensated SMA actuator (b) Modular assembly of elemental actuators to increase net stroke or output force [76].

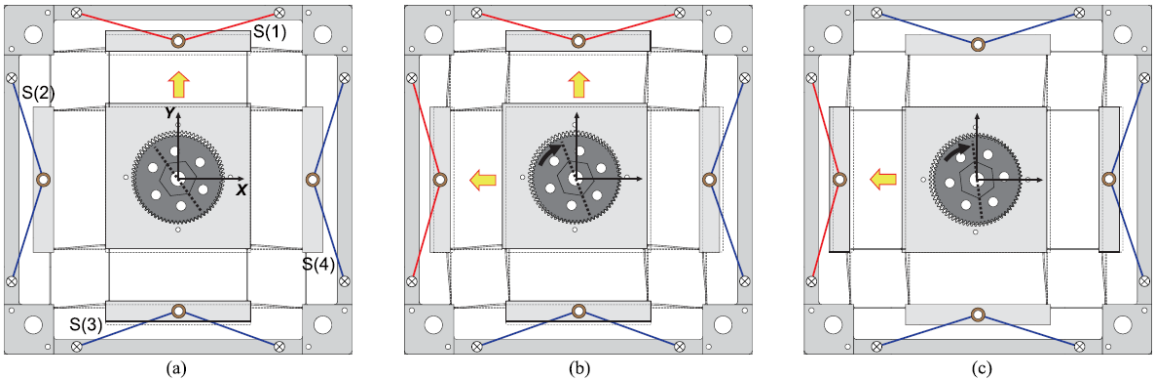

Figure 1.21. Operating principle of the proposed wobble motor. (a)–(c) show schematically translational motions of the internal gear part caused by single activation of the S(1), dual activation of the S(1) and S(2), and single activation of S(3), respectively [78].

1.5.5. Multi-DOF SMA-based actuators

In robotics, many studies deal with the behavior of SMA actuators and the influence on the behavior of mechanisms in which they are integrated [79]–[83]. The use of SMA requires usually the arrangement of at least one SMA element in an antagonism with a springback component [84]–[86] or another SMA component [87]–[90]. Actuators based on antagonistic systems with more than two components allowing several degrees-of-freedom (DOFs) are still rare in the literature. For instance, Figure 1.22 presents FlexiBot, a 2-DOF modular robot using four SMA

springs in parallel capable of creating a relative motion (two rotations) between the bottom and the upper plates [91].

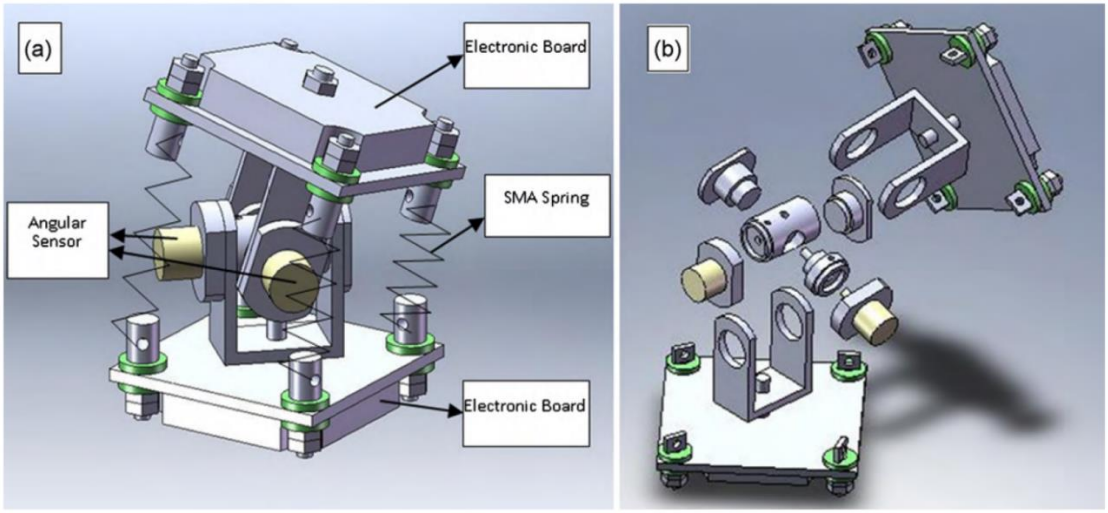

Figure 1.22. Schematic view of the FlexiBot (a) assembly design and (b) exploded view [91].

Creating 6-DOF parallel robots using SMA components is typically present in the "intelligent" Stewart platforms where conventional actuators are replaced with active alloys [17], [92], [93]. Figure 1.23 shows a soft parallel kinematic mechanism driven by six SMA coils and based on the Stewart platform providing six DOF [17]. This soft robot exhibits a central compliant elastomer joint that provides an antagonistic force for the SMA actuators. The robot was designed, tested and controlled to demonstrate its repeatability; however, the activation sequences and the workspace limitations related to hysteretic behavior of SMAs were not addressed in the paper [17].

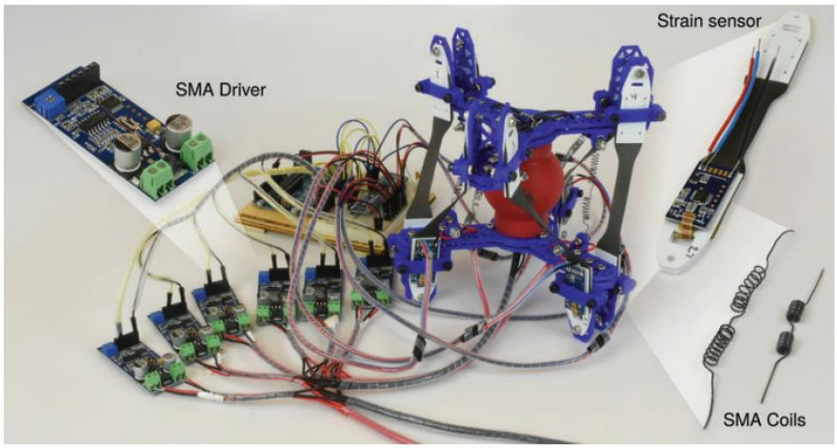

Figure 1.23. Soft parallel kinematic mechanism driven by six SMA coils and based on the Stewart platform [17].

Some researchers focused on the control and optimization of the SMA actuators to create multi-DOF robots like Mollaei et Mascaro who established a control algorithm for three-DOF robot manipulator driven by multi-input binary-segmented SMA actuators [94]. Figure 1.24 gives the discrete workspace of the robot with 6-segment SMA actuators in the case of linear, logarithmic and paired logarithmic segmentation of wet SMA actuators, configured in a Network Array Architecture. In this paper [94], the authors studied the influence of segmenting the SMA actuators on the final discrete workspace.

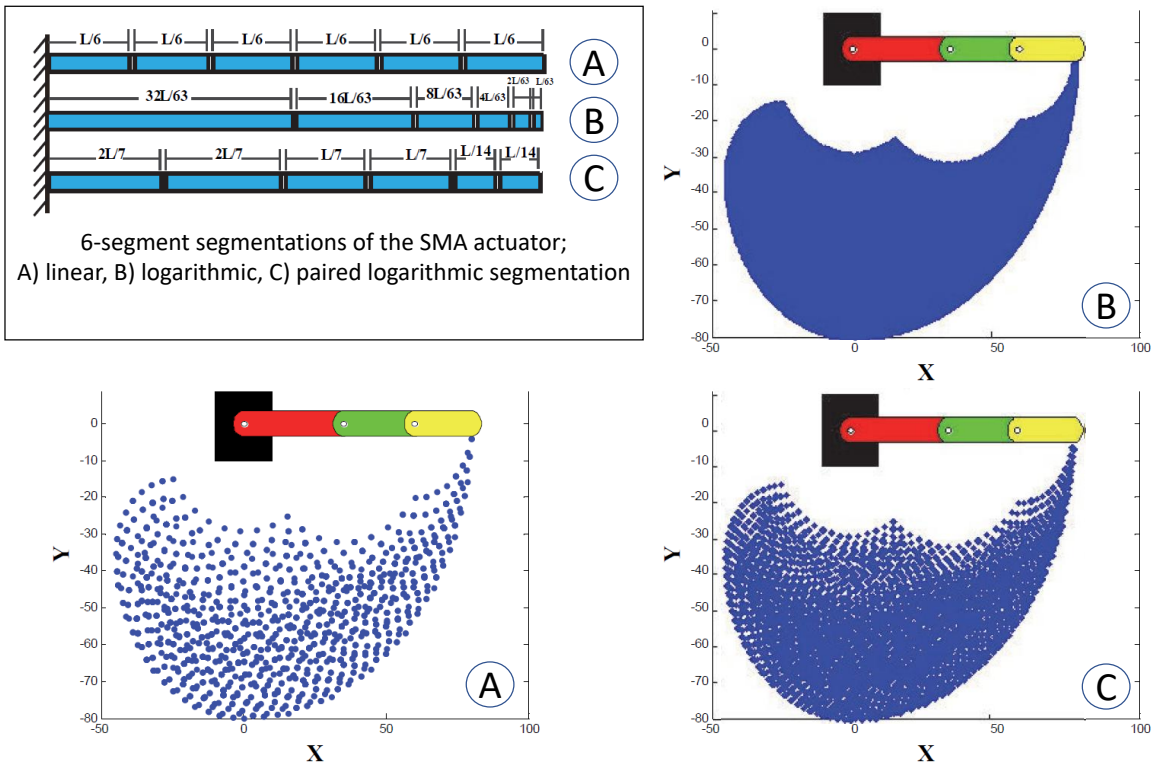

Figure 1.24. Finite workspace of 6-segment SMA actuators in the case of linear (A), logarithmic (B) and paired logarithmic (C) segmentation of the SMA actuators [94].

1.6. Conclusion and positioning of the present study with respect to the literature

This chapter highlighted the fundamental notions about SMAs and introduced the vocabulary and the applications related to the present work. In this chapter, various design approaches of SMA-based mechanisms and actuators used in different fields of engineering were presented. As illustrated previously, generally SMA actuators can be classified into three groups: linear, revolute and multi-DOF actuators according to which motion they provide. The arrangements of SMAs

included in such mechanisms can be designed differently: antagonistic, parallel, serial, differential, circumferential (pulley), telescopic etc. [13]. Table 1.2 summarizes significant mechanisms actuated by various SMA components (springs, wires ...) and the corresponding architecture of their arrangements in order to generate DOFs. It is worth noting that none of these mechanisms have been analyzed using a specific material model for the SMA components. Although the possibility of locking a configuration of SMA-based mechanism without energy input is well known within SMA actuators, the *multi-antagonistic* and *hysteretic* response after a thermal activation sequence is rarely addressed in the literature. The lack of full understanding of how such a mechanism functions, hinders the design development and the potential applications of multi-antagonistic SMA-based structures.

Mechanism	SMA components	Architecture	DOF	Reference
Crawler robot	8 SMA coils	Differential	2	[60]
	2 SMA wires and 3 U-shaped SMA strips	Circumferential	2	[61]
	2 SMA wires per ring 4 SMA wires in total	Circumferential	2	[62]
Fingers	6 SMA wires	Differential	3	[63]
	9 SMA wires	Parallel	1	[66]
	1 SMA plate	Agonist-antagonist	1	[67]
Grippers	2 SMA wires	Parallel	2	[68]
	1 SMA spring	-	2	[69]
	3 SMA wires	Differential	1	[70]
Origami	6 SMA springs	Parallel	3	[74]
Kirigami	6 SMA springs	Parallel	3	[72]
Mini-actuator	2 SMA wires	Parallel	1	[75]
Prismatic actuator	4 helical SMA springs	Parallel	1	[76]
Rotary actuator	4 SMA wires	Differential	1	[78]
Flexibot	4 SMA springs	Parallel	2	[80]
Soft parallel robot	6 SMA coils	Stewart platform	6	[83]
Binary robot	12 SMA wires	Network array	3	[84]

Table 1.2. Examples of SMA-based mechanisms in the literature

In the following chapter, a planar mechanism with 3 DOFs actuated by six SMA wires (allowed to be thermally activated individually) is presented. A finite element analysis using the Auricchio's model for the SMA behavior will be

addressed detailing the characteristics of this multi-antagonistic mechanism. In order to have an efficient *multi-antagonistic* design, a further exploration of workspace, features and controllability of the mechanism to tackle the *hysteretic* behavior of SMAs will be discussed. Such a design would offer certain applications like an end effector, manipulator, micro positioning or micro robotics.

"The only way of discovering the limits of the possible is to venture a little way past them into the impossible." — Arthur C. Clarke

Chapter 2: Finite element analysis of a multi-antagonistic actuation mechanism

Contents

2.1. Introduction 32
2.2. The parameters of the SMA modelling tool 32
2.2.1. Modeling with Ansys Mechanical APDL 32
2.2.2. Transition equations for Ansys inputs 33
2.2.2.1. Material parameters in Ansys 33
2.2.2.2. Ansys parameters inputs 36
2.3. Presentation of the multi-antagonistic actuation system 37
2.3.1. Topology of the mechanism 37
2.3.2. Behavior of the SMA wires 39
2.3.3. Justification of the mechanism topology 42
2.3.4. Definition of heating configurations and platform position 42
2.4. Analysis of the mechanism 44
2.4.1. Discrete workspace obtained in Step 3 45
2.4.2. Remark about maximum stress in the wires 47
2.4.3. Advantageous property of the system 48
2.4.4. Specific cases of cyclic rotation and translation 50
2.4.5. Evidence of an attraction effect 54
2.5. Possibility of reaching a target position in the workspace 57
2.6. Conclusion 58

2.1. Introduction

Based on the literature review in the first chapter, it can be seen that no SMA material model has been employed in the literature to analyze complex hysteretic effects in the case of more than two SMA components. This second chapter aims to analyze the hysteretic and multi-antagonistic properties of a prestressed mechanism with several DOFs driven by several SMA wires, using a material model (namely the Auricchio's model [95]). The architecture will be chosen to have a redundant actuation, where each SMA wire is allowed to be thermally activated individually (heating and return to ambient temperature), one or more at a time. The study was carried out via finite element (FE) calculation software with the purpose of identifying and illustrating the specific actuation characteristics of the chosen mechanism, which may be generalized in the future to the design of any complex multi-antagonistic SMA systems and their control modes. This chapter is organized as follows:

- Section 2.2 presents the parameters of the Auricchio's model within the FE package of Ansys.
- Section 2.3 presents the multi-antagonistic actuation system to be studied.
- Section 2.4 details the FE analysis of the mechanism focusing on: the important design parameters, the possibility of locking a configuration without energy input, as well as on the multi-antagonistic hysteretic behavior, highlighting its restrictive and attractive effects on the workspace.
- Section 2.5 illustrates and discusses the capability of the mobile platform to reach a given position in the workspace.

2.2. The parameters of the SMA modelling tool

A FE model was developed under Ansys Mechanical APDL V19 software [96]. Auricchio's SMA model is implemented in Ansys. We used the MEFF option for the shape-memory effect and BEAM188 for the wires. Details are given in the present section.

2.2.1. Modeling with Ansys Mechanical APDL

In order to have a reliable FE model, the numerical parameters need to be coherent to the physical parameters of the considered SMA material, namely a NiTi

alloy in the present study. Figure 2.1 illustrates the different steps needed to obtain the FE model of a mechanism (see Section 2.3 for the presentation of the multi-antagonistic actuation system under study). To model the SMA behavior using APDL, two options are possible: the MEFF option and the SUPE option. In the present work, the MEFF option is used thanks to its ability to model both the superelasticity and the memory effect through a thermal actuation. In addition to that, the MEFF option allows having different values of Young moduli for the austenite and the martensite phases.

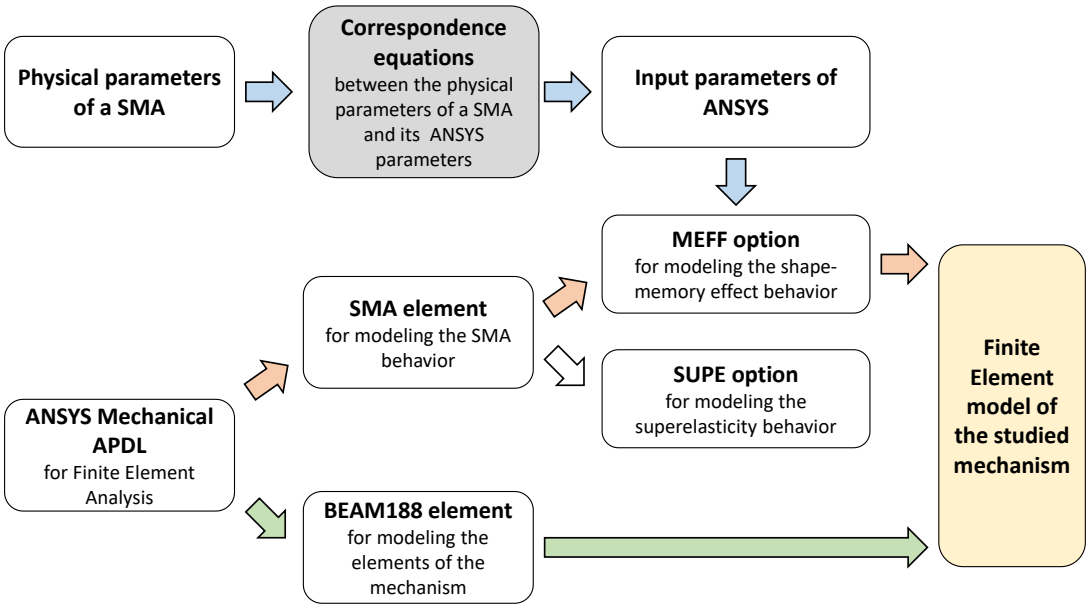

Figure 2.1. Different steps used for modelling the studied mechanism.

2.2.2. Transition equations for Ansys inputs

The transition equations between the SMA physical parameters and the Ansys parameters were established from the state diagram and the superelasticity cycle in uniaxial tension (illustrated in section 1.3.1, Figure 1.2). We felt it was important to keep track of these transition equations for future development of the model. However, the reader can go directly to the next section 2.3 if he or she wishes to do so.

2.2.2.1. *Material parameters in Ansys*

The MEFF option needs seven constants $C1 \rightarrow C7$. Table 2.1 provides the information about these constants according to the Ansys documentation. Figure 2.2-a shows the stress-strain graph in uniaxial tension in which the important data are displayed. Figure 2.2-b provides the links between the seven parameters and the physical parameters. Parameters σ_s^{AS}, σ_f^{AS}, σ_s^{SA}, σ_f^{SA} are defined on the stress-

strain diagram. Note that the Young's modulus of austenite is defined in APDL through the command *MP, EX*.

Constant	Meaning	Property
C1	h	Hardening parameter
C2	T_0	Reference temperature
C3	R	Elastic limit
C4	β'	Temperature scaling parameter
C5	$\bar{\varepsilon}_L$	Max. transformation strain as defined in Aurrichio's model
C6	E_M	Martensite modulus
C7	m	Lode dependency parameter

Table 2.1. Shape-memory effect option constants from the Ansys documentation.

Point	Ansys notation	Ordinate	Abscissa
A	σ_s^{AS}	$\sigma_A = \beta(T - M_s)$	$\varepsilon_A = \beta(T - M_s)/E_A$
B	σ_f^{AS}	$\sigma_B = \beta(T - M_f)$	$\varepsilon_B = \beta(T - M_f)/E_M + \gamma$
C	σ_s^{SA}	$\sigma_C = \beta(T - A_s)$	$\varepsilon_C = \beta(T - A_s)/E_M + \gamma$
D	$--$	$\sigma_D = \beta(T - A_f)$	$\varepsilon_D = \beta(T - A_f)/E_A$

Table 2.2. The coordinates of the points A, B, C and D of the superelastic cycle.

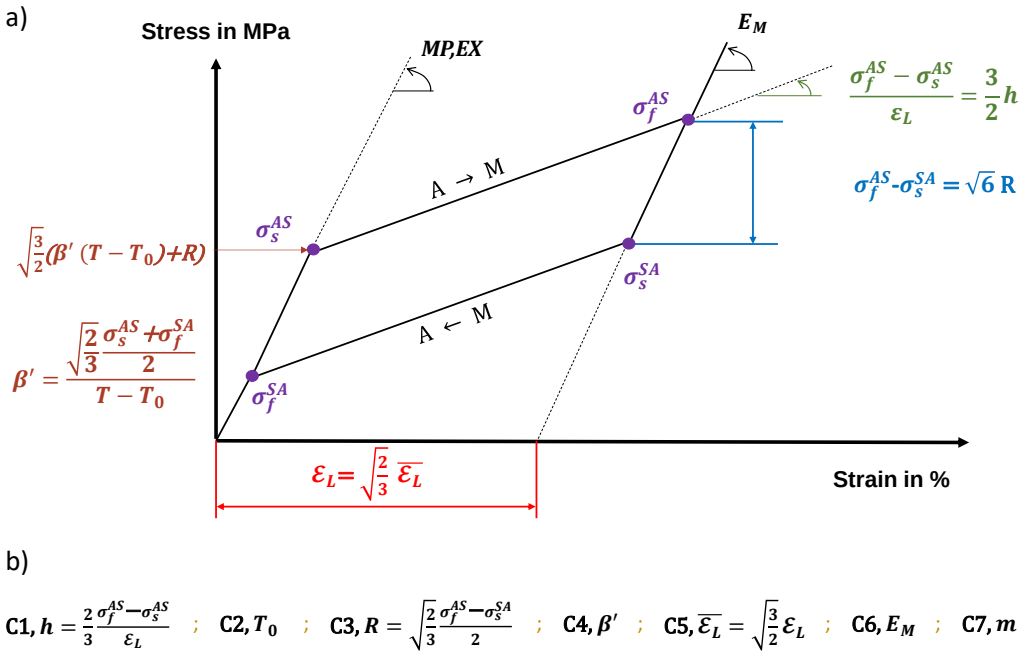

Figure 2.2. (a) Stress-strain diagram from the Ansys documentation with the MEFF option. (b) Definition of the MEFF option constants C1 to C7.

The seventh constant, m, characterizes the difference in response between tension and compression. Indeed, numerous experimental tests reveal an asymmetric behavior of SMA in a tensile and compressive loading. The Auricchio's thermomechanical model is tri-dimensional (3D). It describes the SMA as an isotropic material with a Prager-Lode-type limit surface. The yield criterion is assumed to be:

$$F(\mathbb{X}_{tr}) = \sqrt{2J_2} + m\frac{J_3}{J_2} - R$$

$$J_2 = \frac{1}{2}(\mathbb{X}_{tr}^2 : \mathbb{1})$$

$$J_3 = \frac{1}{3}(\mathbb{X}_{tr}^3 : \mathbb{1})$$

$$m = \sqrt{\frac{27}{2}}\frac{\sigma_c - \sigma_t}{\sigma_c + \sigma_t}$$

$$R = 2\sqrt{\frac{2}{3}}\frac{\sigma_c\sigma_t}{\sigma_c + \sigma_t}$$

where J_2 and J_3 are the second and third invariants of transformation stress $\mathbb{X}_{tr}$, σ_t is the uniaxial tension stress and σ_c is the uniaxial compression stress. In the present study, SMA wires are subjected to tension only. So, parameter m was set as null without penalizing our study.

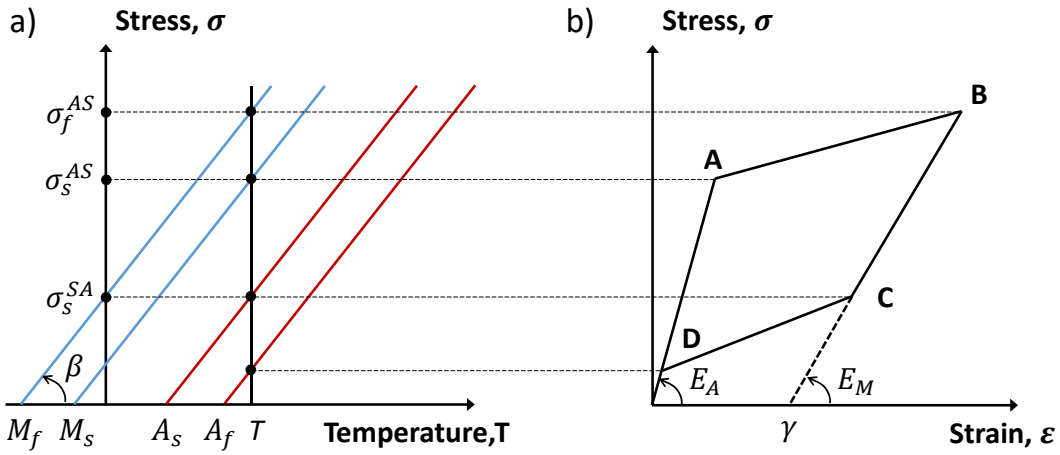

Figure 2.3. Coordinates in the superelasticity diagram. (a) The state diagram. (b) The superelastic cycle.

The known physical parameters, shown in Figure 2.3, are:

- transformation temperatures: M_f, M_s, A_s and A_f,
- slope of the transformation lines in the state diagram: β,

- young moduli: E_A and E_M for the austenite and martensite respectively,
- maximum transformation strain: γ (i.e. ε_L),
- temperature: T.

The coordinates of the four points A, B, C and D in Figure 2.3.(b) are given in as a function of these known physical parameters.

2.2.2.2. *Ansys parameters inputs*

By injecting the formulas presented in Fig. 2.2 into the formulas of Table 2.2, the following relations can be extracted:

$$* \quad \beta = \beta' \sqrt{\frac{3}{2}}$$

$$\Longrightarrow \quad C4 = \beta' = \beta \sqrt{\frac{2}{3}}$$

$$* \quad \sigma_A = \beta(T - M_s) = [\beta'(T - T_0) + R] \sqrt{\frac{3}{2}}$$

$$\text{or} \quad R \sqrt{\frac{3}{2}} = \frac{\sigma_B - \sigma_C}{2}$$

$$\Longrightarrow \quad \beta(T - M_s) - \beta(T - T_0) = \frac{\beta(T - M_f) - \beta(T - A_s)}{2}$$

$$\Longrightarrow \quad \beta(T_0 - M_s) = \frac{\beta(A_s - M_f)}{2}$$

$$\Longrightarrow \quad C2 = T_0 = M_s + \frac{(A_s - M_f)}{2}$$

$$* \quad C1 = \frac{2}{3} \frac{\sigma_B - \sigma_A}{\varepsilon_L} = \frac{2}{3} \frac{\beta(T - M_f) - \beta(T - M_s)}{\gamma}$$

$$\Longrightarrow \quad C1 = \frac{2\beta(M_s - M_f)}{3\gamma}$$

$$* \quad R = \sqrt{\frac{2}{3}} \frac{\sigma_B - \sigma_C}{2} = \frac{\beta(T - M_f) - \beta(T - A_s)}{\sqrt{6}}$$

$$\Longrightarrow \quad C3 = R = \frac{\beta(A_s - M_f)}{\sqrt{6}}$$

$$* \quad C5 = \bar{\varepsilon}_L = \varepsilon_L \sqrt{\frac{3}{2}}$$

or $$\varepsilon_L = \gamma$$

$$\Longrightarrow \quad C5 = \gamma\sqrt{\frac{3}{2}}$$

Finally, Table 2.3 summarizes the expressions of the seven Ansys inputs as a function of the known parameters for a FE simulation.

Parameter in MAPDL	Corresponding expression
TEMP	T
EX	E_A
C1	$2\,\beta(M_s - M_f)/3\gamma$
C2	$M_s + (A_s - M_f)/2$
C3	$\beta(A_s - M_f)/\sqrt{6}$
C4	$\beta\,\sqrt{(2/3)}$
C5	$\gamma\,\sqrt{(3/2)}$
C6	E_M
C7	0 (symmetrical behavior)

Table 2.3. Inputs of the Ansys parameters.

2.3. Presentation of the multi-antagonistic actuation system

2.3.1. Topology of the mechanism

Figure 2.4-a illustrates the general concept of the mechanism: a mobile platform is connected to several SMA wires whose thermal activation enables movement. Assuming a low bending stiffness of the wires (small diameter-to-length ratio), it can be considered that their connections with the base and the platform are of ball-joint type whatever the construction solution employed. In a general case, the platform could be compliant. In this case, its geometry plays a role in the kinematics of the mechanism, and anchoring the platform to the base could be allowed. In the present study, we focused on a simpler case, illustrated in Figure 2.4-b: the system is composed of a rigid platform with six SMA wires in the (x,y) plane and features a ternary rotational symmetry. Taking into account platform compliance is a prospect that will be considered in another study; see the conclusion section. The justification of the topology chosen here is discussed in Section 2.3.3, after the presentation of the mechanism's main features.

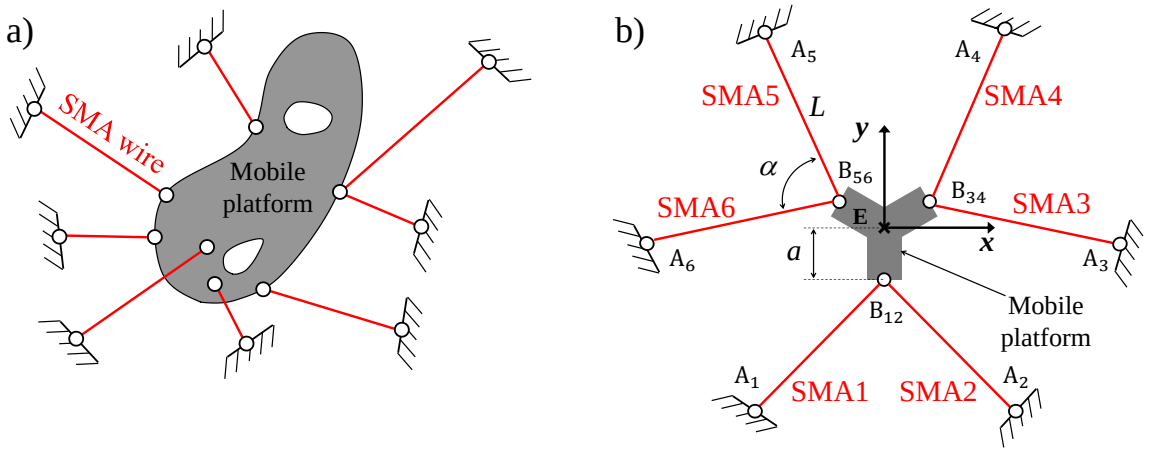

Figure 2.4. a) Conceptual view of a mobile platform connected to several SMA wires, b) plane system studied. Output parameters are the rotation of the platform and the in-plane translation of point E as a function of the thermal activation of the SMA wires.

Symbol	Signification	Value
E_M	Young modulus of martensite	35,000 MPa
E_A	Young modulus of austenite	63,000 MPa
$\sigma_{\max}$	Maximum stress to prevent plasticity (elastic limit)	650 MPa
M_s	Martensite-start temperature	-7 °C
M_f	Martensite-finish temperature	-25 °C
A_s	Austenite-start temperature	24 °C
A_f	Austenite-finish temperature	36 °C
T_0	Ambient temperature	15 °C
T_1	Activation temperature	100 °C
γ	Maximum transformation strain	6 %
β	Slope of the transformation lines in the state diagram	8 MPa/°C
d	Diameter of the SMA wires	1 mm
L	Length of the SMA wire	100 mm
a	Length of the platform bar	20 mm

Table 2.4. Parameters fixed for the FE study.

All the wires have the same length L and diameter d. They are placed symmetrically along the three-fold rotation axis z. The three pairs of wires (1-2), (3-4) and (5-6) form the same angle, denoted α in the following. Each pair shares the same connection point with the platform. As the latter is considered as non-deformable, its geometry is simply defined by parameter a, corresponding to the distance between the effector point E (center of the platform) and the connection points with the wires (Figure 2.4-b). Analysis in the following focuses on the

rotation of the platform and on the in-plane translation of point E, consecutive to the heating of the SMA wires. Out-of-plane deformations (due to gravity for instance) are not considered. Three geometric parameters were fixed throughout the study: $d = 1$ mm, $L = 100$ mm and $a = 20$ mm (see Table 2.4), whereas different values were tested for angle α.

2.3.2. Behavior of the SMA wires

This section provides some background information about the SMA wires used for this study in addition to the information given in Chapter 1, Section 1.2 and 1.3. Figure 2.5-a shows the simplified state diagram of a SMA wire in tension [97], [98]. Material properties in this study are taken from previous experimental work (Ref. [99]) on a Ni50.8–Ti49.2 (at.%) SMA wire 1 mm in diameter. The four transformation temperatures at zero stress, namely Martensite-start (M_s), Martensite-finish (M_f), Austenite-start (A_s) and Austenite-finish (A_f), were defined as -7°C, -25°C, 24°C and 36°C respectively; see Table 2.4. Classically, A→M and M→A transformations do not occur at the same temperatures ($M_s \neq A_f$ and $M_f \neq A_s$), which leads to a so-called thermal hysteresis. It can be noted that, non-generically, $M_s < A_s$. The ambient temperature T_0 was set to 15°C, so that $M_s < T_0 < A_s$. This inequality is a key point of the system's operation, as will be explained in Section 3.3. The activation temperature T_1 was set to 100°C. Experimentally, this value can easily be reached by the Joule effect [19]. To "initialize" the SMA wires in the austenitic state, they must first be heated above A_f at zero stress (Step 0 in Figure 2.5-a). The austenitic state is preserved when cooling to ambient temperature (Step 1) as $M_s < T_0$. The six wires are then prestressed simultaneously in an equivalent way on the system (Step 2), leading to their partial transformation into martensite without movement of the platform, thanks to the symmetry of the mechanism. Figure 2.5-b shows the corresponding stress-strain curve of the SMA wire. Five points can be highlighted from this graph.

- During monotonic loading, the A→M transformation occurs progressively along a so-called *stress plateau*. The non-linear stress-strain curve is thus defined by the elasticity line of pure austenite (100% A), then the stress plateau, and finally the elasticity line of pure martensite (100% M).
- Let us designate ε_{pre} the pre-strain level at Step 2. It is worth noting that, starting from Step 2, an increase or decrease in stress will result in different behaviors: see blue arrows A and B. An increase in stress will lead to a continuation of the transformation into martensite, while a decrease in stress

will result in an "elastic" response. History effects and mechanical hysteresis are features of SMAs.

- The Young's modulus of austenite E_A and martensite E_M are different (see values in Table 2.4). During the A→M transformation, a mixture law is classically employed to calculate the Young's modulus of the austenite-martensite "composite".
- The higher the temperature is, the greater the load level is required to activate the A→M transformation. This property is characterized by parameter β in Figure 2.5-a and Table 2.4.
- A maximum stress $\sigma_{\max}$ was considered in the study to prevent the plasticity of the wires. Figure 2.5-c shows the experimental stress-strain curve until rupture, which we obtained using a uniaxial testing machine at 25°C. After the A→M transformation, the plastic yield stress of the stress-induced martensite was identified as 650 MPa. The strain recoverability of NiTi SMAs was recently discussed in Ref. [49], showing that the plastic yielding of martensite appears at nearly the same stress at any test temperature. The same property was identified for austenite, but at a stress level a little higher than that of martensite [100]. In the present study, austenite measurement would have required mechanical loading at high temperature, which was not possible due to practical constraints. As the plastic yield stress of austenite is *a priori* a little higher than that of martensite [100], the value $\sigma_{\max} = 650$ MPa was employed in the present study whatever the material's phase, which is conservative.

From Step 3, a heating sequence is applied to the SMA wires, which may involve any wire. Note that the actuation times in a real physical system are expected to be long, see Section "Heating and cooling methods" of Ref. [101] for orders of magnitude of actuation times with respect to wire diameter and current intensity. The heating of a wire is accompanied by a partial or total disappearance of its martensitic phase (reverse transformation M→A). In the absence of the other wires, a heated wire would return to its initial length (one-way memory effect). However, here, the six wires interact mechanically with each other. This "multi-antagonistic" operation is a key point of the system, which is analyzed in Section 2.3.3.

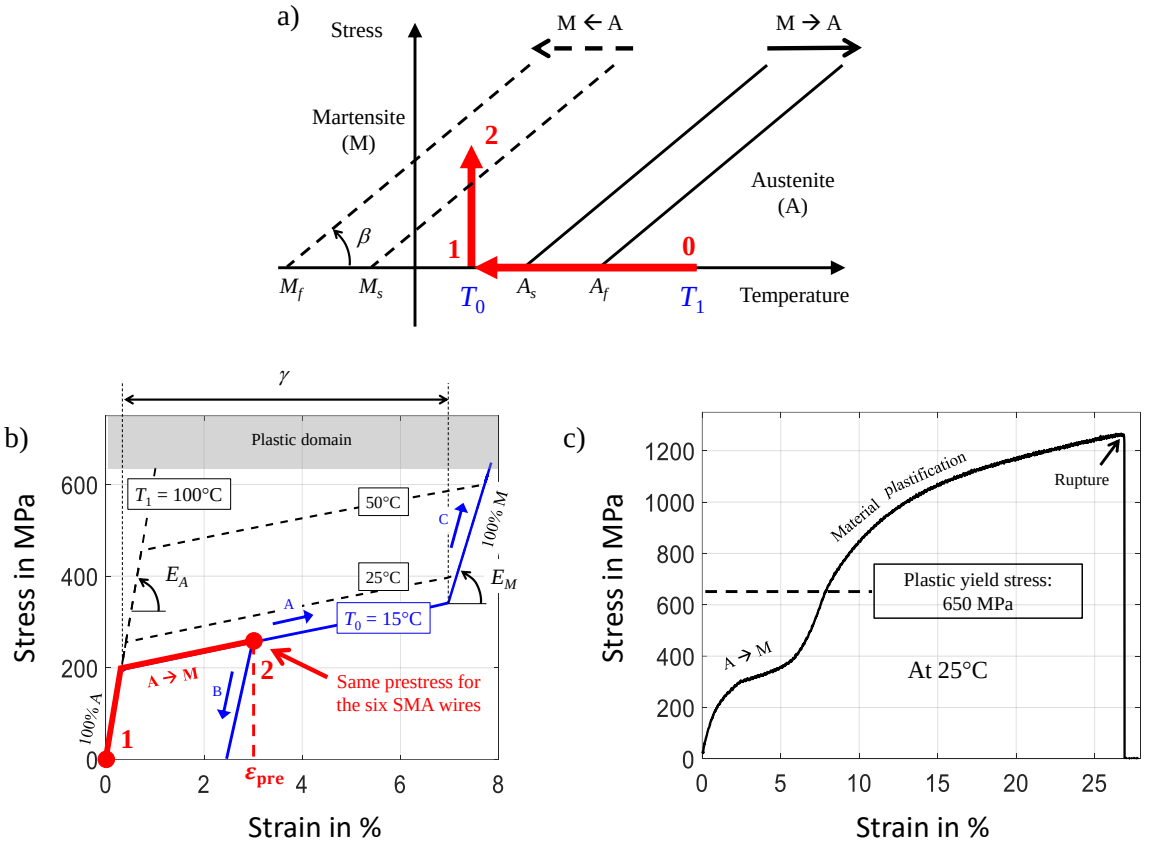

Figure 2.5. a) Simplified state diagram of a SMA wire in tension. The first three steps of the procedure are numbered 0, 1 and 2. Step 2 corresponds to the state of the six SMA wires before starting a thermal activation sequence. Due to the symmetry of the mechanical system, there is no movement of the platform from Step 0 to Step 2; b) model of the mechanical response of the SMA wires in tension; c) experimental stress-strain curve of a Ni50.8–Ti49.2 (at. %) SMA wire, 1 mm in diameter, until rupture.

Since rotations were allowed at both ends of all the SMA wires (no bending and only tension in the wires), the model results do not depend on the number of finite elements used to mesh each wire. The mobile platform was considered to be made of steel (Young's modulus of 200 GPa) with a cross-section of 150 mm^2 for each of its three branches (see Figure 2.4.(b), which makes it effectively rigid compared to the SMA wires. It was meshed using thirty finite elements. Prestrain, at Step 2, was applied by moving simultaneously the connection points of the six wires with the base, along their respective directions. Displacements were imposed at points A_i, $i = 1, 2, ..., 6$ (see Figure 2.4.(b)): A_1 and A_2 were moved by $\varepsilon_{pre} \times L$ along directions $B_{12}A_1$ and $B_{12}A_2$ respectively; the same was done for points A_3 and A_4 (along directions $B_{34}A_3$ and $B_{34}A_4$ respectively) and points A_5 and A_6 (along directions $B_{56}A_5$ and $B_{56}A_6$ respectively). Note that calculations were made under the assumption of "large displacements", as required for SMAs. This assumption

means that mechanical equilibrium is verified in the *deformed* state of the system at any step of the calculus.

2.3.3. Justification of the mechanism topology

The topology of the mechanism was chosen by considering several points. First, geometrical symmetry was sought. It enables in particular the same pre-strain level ε_{pre} at Step 2 without platform movement. Breaking the symmetry would lead to a complex definition of the initial states of the SMA wires (distinct stresses and strains at Step 2). In addition, the history of the stretching sequence of the wires from Step 1 to Step 2 would have an influence. Second, a minimum of four wires is required in theory to achieve a plane mechanism with three independent DOFs [102]. Using six SMA wires increases the global stiffness as well as the antagonistic character of the actuation. Let us recall that antagonism is required for a *two-way* actuation of each SMA wire (reversible movement of each wire whose basic property is one-way memory effect). Finally, the topology was in part inspired by the system developed by Jin and Zhang in Ref. [103]. In their work, the authors advantageously developed a three-arm planar compliant parallel mechanism with three linear piezoelectric actuators along constant directions. In our study, a pair of SMA wires replaces each actuator. One of the advantages of SMAs is their ability to deform elastically (and non-linearly) by several percent, making them relevant to creating larger movements. Note that although a small translation workspace (order of magnitude of $\gamma \times L = \pm 3$ mm) is expected compared to the dimensions of the mechanism (order of magnitude of $2L + 2a = 240$ mm), significant angular strokes (order of magnitude of $\gamma \times L \,/\, a \times 180/\pi = \pm 8.5°$) are a priori achievable.

2.3.4. Definition of heating configurations and platform position

For the sake of simplicity, analysis was performed by considering two thermal states per wire: either ambient temperature T_0 =15°C or activation temperature T_1 = 100°C. Intermediate temperatures were not considered. This point will be developed in a later study. Figure 2.6 shows the 64 possible *heating configurations* of the six SMA wires. A number is associated with each configuration, as well as a six-digit binary number for which "0" and "1" correspond to T_0 and T_1 respectively. For instance, the case for which all the wires are at ambient temperature corresponds to Configuration #1 or [000000]. The case for which all the wires are at the activation temperature corresponds to Configuration

#64 or [111111]. As indicated above, the *thermal activation sequence* is defined from Step 3 by a series of heating configurations. The output data is a sequence of platform positions. Figure 2.7-a illustrates the rigid body movement of the platform. Three quantities are recorded at each step of the thermal activation sequence: the displacements u_x and u_y of point E and the rotation angle θ_z of the platform. Throughout the study, these quantities are defined from the initial position at Step 2.

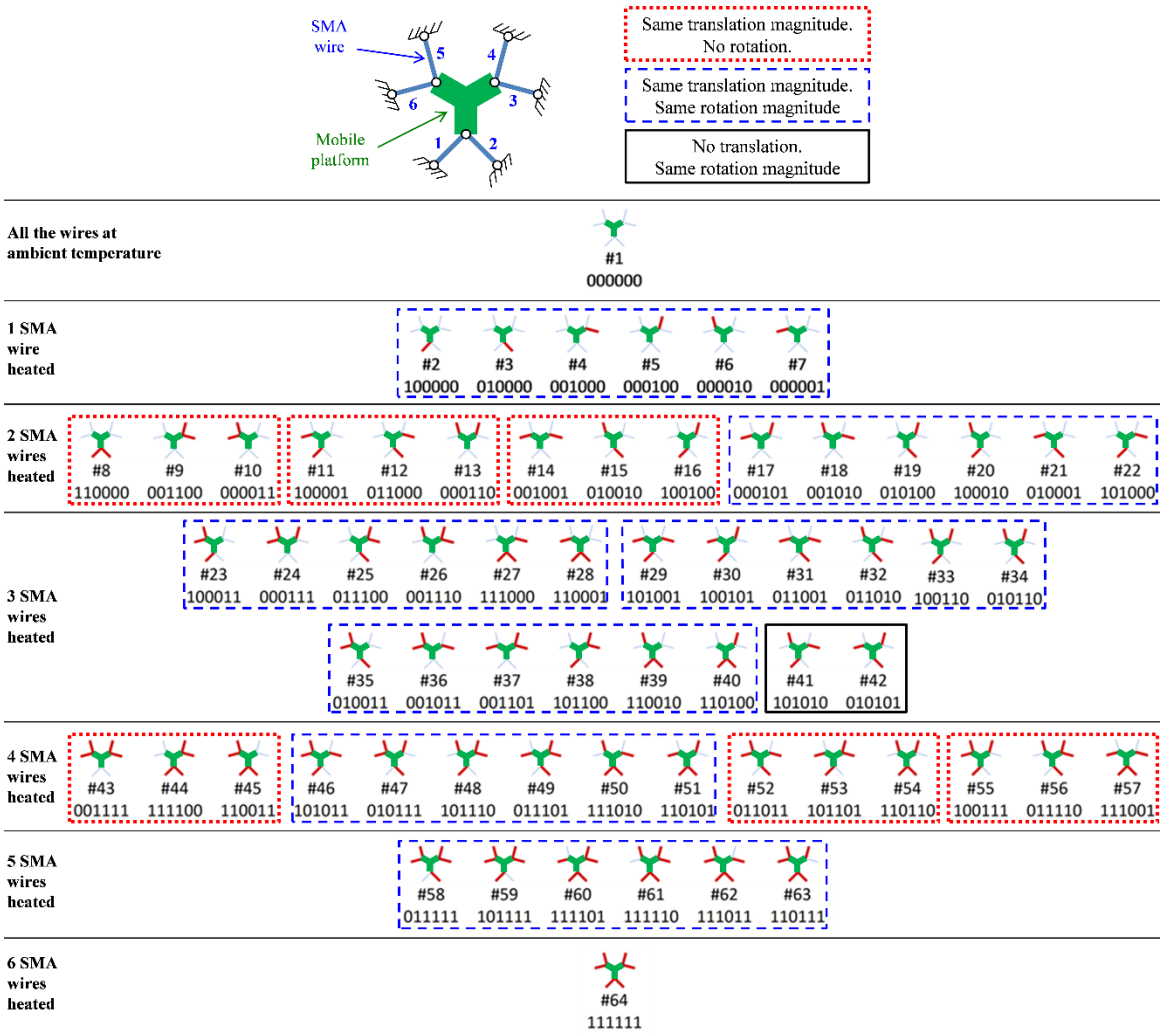

Figure 2.6. Various heating configurations of the six SMA wires. Red bold lines correspond to wires at activation temperature (T_1); blue lines correspond to wires at ambient temperature (T_0). Each configuration is identified by a six-digit binary number corresponding to the thermal state of the wires, for which "0" and "1" correspond to T_0 and T_1 respectively.

Figure 2.7-b shows an example in real scale of the platform position obtained for a Step 3 corresponding to Configuration #24 or [000111]. From Fig. 2.6, a classification of "identical" heating configurations at Step 3 can be done from

rotation symmetry considerations: {#1}, {#2–7}, {#8–10}, {#11–13}, {#14–16}, {#17–22}, {#23–28}, {#29–34}, {#35–40}, {#41, #42}, {#43–45}, {#46–51}, {#52–54}, {#55–57}, {#58–63}, {#64}. Each of these sets contains heating configurations leading by construction to the same magnitudes of rotation and translation at Step 3.

Before starting the analysis of the mechanism, the following point should be noted. The heating of a SMA wire from T_0 to T_1 tends to increase its stress level due to the other SMA wires (multi-antagonism). Thus, although $T_1 > A_f$, heating a SMA wire to T_1 does not necessarily guarantee its complete return to the austenitic state. Indeed, any increase in stress is accompanied by a shift in the thermal range of the phase transformation: see angle β in Fig. 2.5-a.

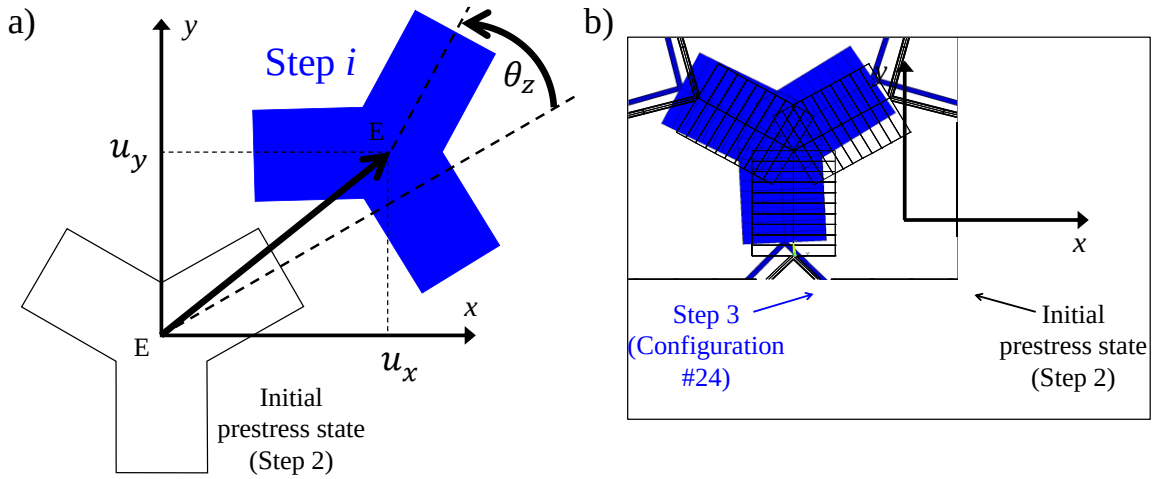

Figure 2.7. Movement of the mobile platform: a) definition of the in-plane translation (u_x, u_y) and the rotation θ_z of the platform, b) example of position in real scale obtained by finite element simulation, for $\alpha = 90°$, $\varepsilon_{pre} = 3\%$ and Configuration #24 applied at Step 3.

2.4. Analysis of the mechanism

The multi-antagonistic and hysteretic behavior of the mechanism is now presented by progressively analyzing specific points.

- Section 2.4.1 presents the discrete workspace obtained at Step 3;
- Section 2.4.2 deals with limiting stress to avoid plasticity;
- Section 2.4.3 describes an advantageous property of the mechanism when stopping thermal activation;
- Section 2.4.4 deals with the specific cases of cyclic rotation and translation;

- Section 2.4.5 evidences an "attraction" effect, which is useful to reach new platform positions after Step 3.

Angle α and prestrain ε_{pre} were set at 90° and 3% respectively, except in Section 2.4.4 for which the influence of these two parameters is discussed.

2.4.1. Discrete workspace obtained in Step 3

Figure 2.8-a shows the different movements of the mobile platform obtained when applying the 64 heating confirmations at Step 3, for $\alpha = 90°$ and $\varepsilon_{pre} = 3\%$. Each movement is defined in the graph by three coordinates (u_x, u_y, θ_z) whose definition was given in the previous section. For an easier visualization, Figure 2.8-b provides the projection of the points in the (u_x, u_y) plane, highlighting the translation only, while Figure 2.8-c provides the values θ_z for platform rotation only. Numbers in these figures refer to the heating configurations defined in Fig. 2.6.

Several points can be noted from Fig. 2.8:

- Red crosses correspond to situations for which negative stresses are calculated in at least one SMA wire. Such cases are considered as not permissible, in order to avoid buckling situations. Even if buckling does not systematically prevent the mechanism from operating, it is difficult to correctly predict the bending behavior of SMA wires which will then have to work in tension again.
- As expected, Configurations #1 (no wire heated) and #64 (all the wires heated) led to no movement. The latter case is due to the symmetry of both the geometry and the actuation. Heating configurations #41 and #42 led to pure rotation, i.e. $u_x = 0$ and $u_y = 0$. This observation is logical because of the three-fold symmetry of the heated wires (see Fig. 2.6). The maximum rotation magnitude $|\theta_z|$ was obtained for these two heating configurations: almost 10.3° (see Fig. 2.8-c). Heating configurations #8–16, #43–45 and #52–57 led to pure translation, i.e. $\theta_z = 0$. This property is inherited from a two-fold symmetry of the heated wires in these cases. The maximum translation magnitude $\sqrt{{u_x}^2 + {u_y}^2}$ reached is almost 3.7 mm, for Configurations #23–28 and #55–57. Table 2.5. sums up the sets of identical heating configurations in terms of translation magnitude, as well as in terms of rotation by taking into account the sign of the rotation angle θ_z (null, strictly positive or strictly negative). For example, positive and negative rotations with same magnitude are obtained for $\{\#3, \#5, \#7\}^+$ and $\{\#2, \#4, \#6\}^-$ respectively.

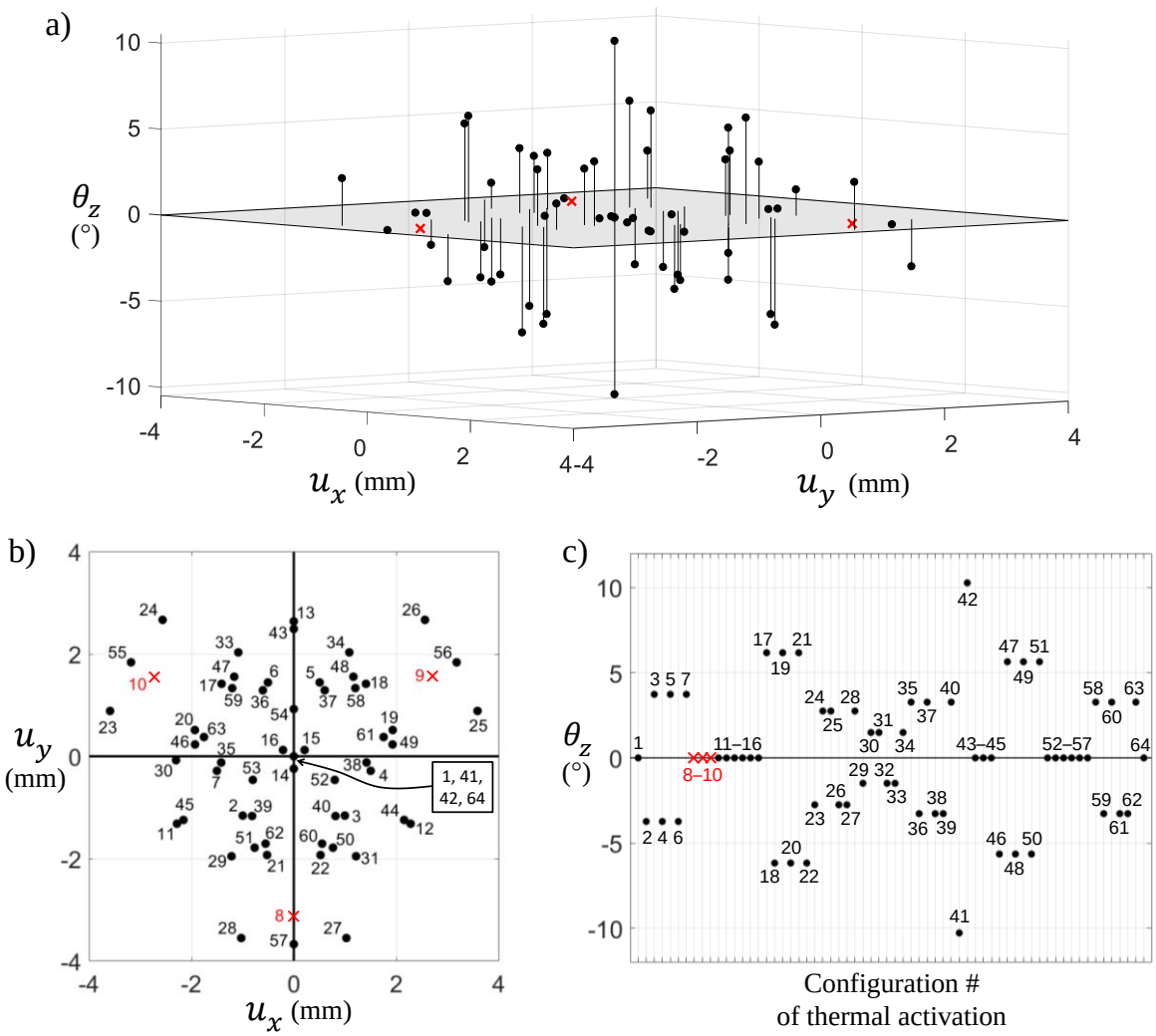

Figure 2.8. a) Movement of the mobile platform for $\alpha = 90°$ and $\varepsilon_{pre} = 3\%$ for different heating configurations at Step 3. Each point is defined by the in-plane translation (u_x,u_y) of point E and the rotation θ_z of the platform. Red crosses correspond to configurations for which negative stresses are calculated in at least one SMA wire, meaning that these configurations are not valid; b) same in projection onto plane (u_x,u_y), c) rotation θ_z of the platform. Numbers refer to the heating configurations in Figure 2.6.

The dot cloud of the discrete workspace in Fig. 2.8-b exhibits a three-fold symmetry, as a consequence of the symmetry of the mechanism. Other locations can be achieved in (u_x, u_y, θ_z) space with adequate thermal activation sequences, as shown later in this chapter. Before that, the next section is dedicated to a remark about limitations in terms of the stress level in the SMA wires.

Property	Set of similar heating configurations at Step 3
Same translation magnitude	{#1, #41, #42, #64}^{0}, {#14–16}, {#52–54}, {#35–40}, {#2–7}, {#58–63}, {#46–51}, {#17–22}, {#29–34}, {#43–45}, {#11–13}, {#8–10}, {#55–57}, {#23–28}
Same rotation magnitude	{#1, #8–16, #43–45, #52–57, #64}^{0}, {#30, #31, #34}$^+$ / {#29, #32, #33}$^-$, {#24, #25, #28}$^+$ / {#23, #26, #27}$^-$, {#35, #37, #40, #58, #60, #63}$^+$ / {#36, #38, #39, #59, #61, #62}$^-$, {#3, #5, #7}$^+$ / {#2, #4, #6}$^-$, {#47, #49, #51}$^+$ / {#46, #48, #50}$^-$, {#17, #18, #21}$^+$ / {#18, #20, #22}$^-$, {#42}$^+$ / {#41}$^-$

Table 2.5. Classification of the heating configurations applied at Step 3 leading to the same movement in terms of translation magnitude $\sqrt{({u_x}^2 + {u_y}^2)}$ or rotation magnitude $|\theta_z|$. Numbers refer to the configurations in Figure 2.6. Exponent "0" is used when the magnitude is equal to zero. Symbol "/" separates sets with the same rotation amplitude $|\theta_z|$ but opposite rotation sign. Exponents "+" and "-" refer to the sign of the rotation.

2.4.2. Remark about maximum stress in the wires

Calculations were performed using a FE model that does not take plasticity into account. This potentially leads to stress values higher than the maximum allowed (σ_{max} = 650 MPa; see Section 2.3.2). Table 2.6 gives an example of results obtained by applying successively Configurations #21 and #59 at Steps 3 and 4 respectively (again for α = 90° and ε_{pre} = 3%). It can be observed that stress in wire 3 at Step 4 exceeds σ_{max}, meaning that the thermal activation sequence is not valid. Attention was paid in the data analysis to cancelling any thermal activation sequence for which the stress in at least one wire at any step exceeds the plastic yield stress of the SMA.

From a general point of view, excessive stresses can be avoided by limiting either the number of activated wires or the activation temperature. Figure 2.9 illustrates for instance the effect of overheating the SMA wires (above T_1 = 100°C): the plot is similar to that in Fig. 2.8-a but the activation temperature was increased until a *full* return to the austenitic state of the heated wires was achieved. Red crosses correspond to non-valid configurations, for which stresses are either negative or exceed the plastic yield stress of the SMA. It can be seen that many heating configurations are not valid. In the following, the activation temperature was maintained at T_1 = 100°C, which is actually a good compromise to limit the number

of non-valid configurations. In the rest of the chapter, non-valid configurations are no longer indicated in the graphs and are removed from the analysis.

Step	Config	Positions of the platform			Stresses in the six wires (in MPa)					
		u_x (mm)	u_y (mm)	θ_z (°)	1	2	3	4	5	6
Step 2	#1	0 for the three quantities			255 in the six wires					
Step 3	#21	-0.52	-1.93	6.2	203	357	289	267	324	386
Step 4	#59	-3.00	1.02	2.4	472	326	<u>709</u>	521	430	622

Table 2.6. Example of a (non-valid) thermal activation sequence leading to plasticity. Configurations #21 and #59 are successively applied at Steps 3 and 4 respectively (for α = 90° and ε_{pre} = 3%). The stress value exceeding the plastic yield stress of the SMA is underlined.

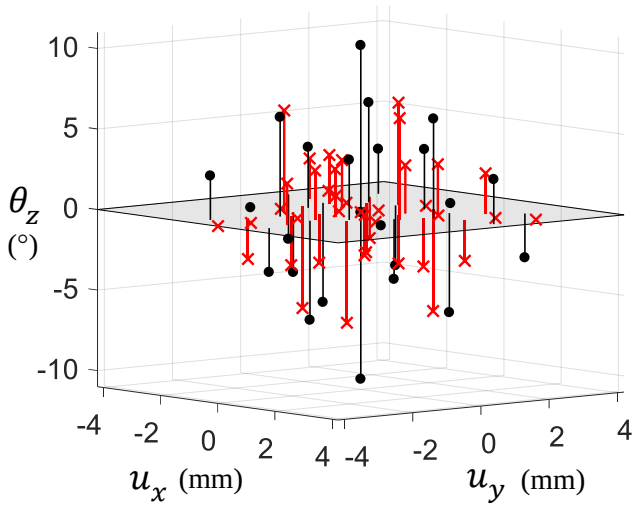

Figure 2.9. Overheating of the SMA wires leading to numerous non-valid configurations: same plot as in Figure 2.8-a, with the activation temperature increased until a *full* return to the austenitic state of the activated wires is achieved. Red crosses correspond to heating configurations for which stresses are negative or exceed the plastic yield stress of the SMA (non-valid configurations).

2.4.3. Advantageous property of the system

An interesting feature of the system can be highlighted. Indeed, Figure 2.10 shows that platform position is partially preserved when thermal activation is halted. This was illustrated by applying a return to ambient temperature (Configuration #1 or [000000]) at Step 4 *after* any Configuration #j applied at Step 3: see Figure 2.10-a. Figure 2.10-b shows the coordinates (u_x, u_y, θ_z) obtained

at Steps 3 and 4, while Figure 2.10-c provides the projection in the plane (u_x, u_y). It can be observed that the platform positions at Steps 3 and 4 do not coincide. Moreover, the platform at Step 4 (square blue symbols) is not returned to the initial position $(u_x = 0, u_y = 0, \theta_z = 0)$, obviously except for $j = 1$ and $j = 64$, for which the platform was already in its initial position at Step 3. It can be noted that only a small part of the movement was "lost"; the square blue symbols (Step 4) are close to the black dots (Step 3). This property is interesting from an applicative point of view: it is possible to stop the activation of the system while maintaining an activation state. This feature is a consequence of the choice of the Martensite-start and Austenite-start temperatures such that $M_s < T_0 < A_s$ (see Section 2.3.2). This inequality means that cooling to T_0 does not imply systematically an A→M transformation because $M_s < T_0$ (transformation may however occur due to the stress which shifts the transformation domain, as explained in Section 2.3.4). The wire remains thus completely or nearly completely austenitic once it is returned to ambient temperature. In the following, any heating step is followed by a return to ambient temperature of the activated wires. This choice was made to obtain a series of "bi-stable" states ("multi-stable" mechanism).

As indicated above, a complex interaction exists between the six wires. This interaction involves several constraints:

(i) elasticity governed by Young's modulus;

(ii) phase transformation governed by the state diagram in Figure 2.5-a and the thermomechanical history of the wires;

(iii) static equilibrium of the platform, in deformed configuration as indicated in Section 2.3.2;

(iv) geometrical compatibility of the lengths of the wires (which defines the position of the platform).

The advantageous property of the system presented in this section is an illustration of this complex interaction. In particular, constraint (*ii*) is at the origin of the system's hysteretic response, whose consequences will be explored in the following sections.

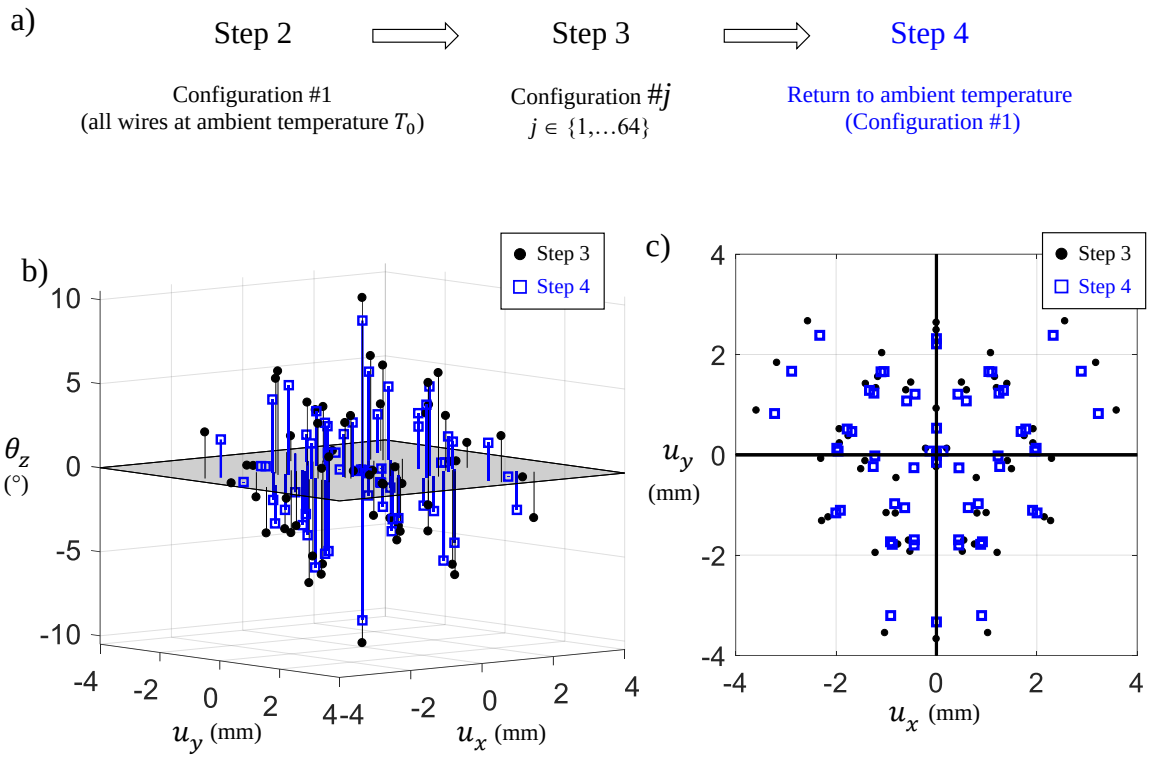

Figure 2.10. Platform movement is partially preserved when thermal activation is halted: a) thermal activation sequence considered, b) and c) same plot as in Figures 2.8.(a) and (b). Dots and squares correspond to Steps 3 and 4 respectively.

2.4.4. Specific cases of cyclic rotation and translation

Before applying thermal activation sequences involving various heating configurations, this section is dedicated to the cyclic use of *two* configurations aiming at creating a cyclic movement of the platform. In particular, the specific cases of pure rotation and pure translation are here discussed.

First, Figure 2.11-a describes the thermal activation sequence considered to obtain a cyclic rotation, by alternating Configurations #41 and #42 with intermediate returns to ambient temperature. Variations in rotation angle θ_z for $\alpha = 90°$ and $\varepsilon_{pre} = 3\%$ can be visualized in Figure 2.11-b. Negative (-10.3°) and positive (10.3°) rotations are obtained for Configurations #41 and #42 respectively, leading to a signal amplitude $(\Delta\theta_z)_{max} = 20.6°$. A partial preservation of the rotation angle when stopping the thermal activation is observed at Steps 4, 6, 8, 10, etc., as expected from the discussion in the previous section. The rotation amplitude, taking into account these intermediate returns to ambient temperature, is equal to $(\Delta\theta_z)_{min} = 17.8°$. Further analysis can be carried out by extracting the stress and strain values after each step: see Figure 2.11-c. Several comments can be made from these graphs.

- Due to the three-fold symmetry of the heating configurations #41 and #42, variations were the same in wires 1, 3 and 5 (left graph) and in wires 2, 4 and 6 (right graph).
- From Step 2 to Step 3, strain decreased in wires 1, 3, 5 (memory effect) and increased in wires 2, 4, 6 by compensation. Moreover, as noted in Section 2.3 (blue arrow A in Fig. 2.5-b), the continuation of the transformation into martensite of wires 2, 4, 6 is accompanied by a stress increase. Note also that, at Step 3, the stress in wires 2, 4, 6 (about 312 MPa) is different from the stress in wires 1, 3, 5 (about 454 MPa). Indeed, constraint (*iii*) in Section 3.3 regarding the static equilibrium of the platform can be rewritten as follows:

  (*iii*-1) the three force vectors created by each pair of wires (F_1+F_2, F_3+F_4 and F_5+F_6) must intersect at the same point;

  (*iii*-2) the sum of the six force vectors F_1+F_2+F_3+F_4+F_5+F_6 must be equal to zero.

  No equality between magnitudes F_1 and F_2 (or F_3 and F_4, or F_5 and F_6) is required for the equilibrium of the system.
- From Step 3 to Step 4, the strain slightly decreases in wires 2, 4, 6, and slightly increases in wires 1, 3, 5 by compensation. The decrease in wires 2, 4, 6 is due to "elastic" unloading, which was indicated by the blue arrow B in Fig. 2.5-b.
- The other subsequent steps can be explained from the same principles.

For the same thermal activation sequence as in Fig. 2.11-a (cyclic rotation by alternating heating configuration #41 and #42 with intermediate returns to ambient temperature), Figure 2.12-a shows the influence of angle α on the rotation amplitudes $(\Delta\theta_z)_{max}$ and $(\Delta\theta_z)_{min}$, see Fig. 2.11-b for the definition of these two quantities. Prestrain ε_{pre} was again fixed to 3% in these calculations. As expected, when the angle is closed ($\alpha = 0°$), no rotation is obtained. As also expected, when the wires are aligned ($\alpha = 180°$), large rotations are obtained. The maximum values for $(\Delta\theta_z)_{max}$ and $(\Delta\theta_z)_{min}$ are obtained here for $\alpha = 90°$. However, larger rotation amplitudes can be obtained by changing the pre-strain level ε_{pre}. Figure 2.12-b shows the influence of ε_{pre} maintaining α at 90°.

Following comments can be made from this graph.

- As expected, no rotation is obtained if the SMA wires were not pre-strained at Step 2 ($\varepsilon_{pre} = 0\%$). Increasing the pre-strain level tends first to increase the rotation amplitudes. This observation is logical, as the memory effect in

the heated wires depends on this parameter (in the absence of stress, the heated wires would return to their initial length, i.e., the strain change from Step 3 to Step 4 would be equal to $-\varepsilon_{pre}$).

- Increasing the pre-strain level excessively tends to decrease the rotation amplitudes. Indeed, let us consider for instance the case for which all wires are completely martensitic (100% M) at Step 2: when wires 1, 3, 5 are heated at Step 3, their memory effect is countered by the high stiffness E_M of the martensitic wires 2, 4, 6 (see blue arrow C in Fig. 2.5-b). The more the pre-strain level approaches the end of the stress plateau, the faster a high stiffness value is reached for wires 2, 4, 6 when wires 1, 3, 5 are heated.
- The optimal value of ε_{pre} to maximize the rotation amplitude corresponds to the middle of the stress plateau of the stress-strain curve. Its value can be expressed as follows

$$(\varepsilon_{pre})_{opt} = \frac{\gamma}{2} + \frac{\beta \times (T_0 - M_S)}{E_A} \quad (1)$$

where γ is the total phase deformation strain (see Table 2.4 and Fig. 2.5-b). In this equation, the last term is the strain at the onset of the A→M transformation. Using data from Table 2.4, Equation (1) gives $(\varepsilon_{pre})_{opt} = 3.3\%$, leading then to $[(\Delta\theta_z)_{max}]_{opt} = 21.1°$ and $[(\Delta\theta_z)_{min}]_{opt} = 18.1°$.

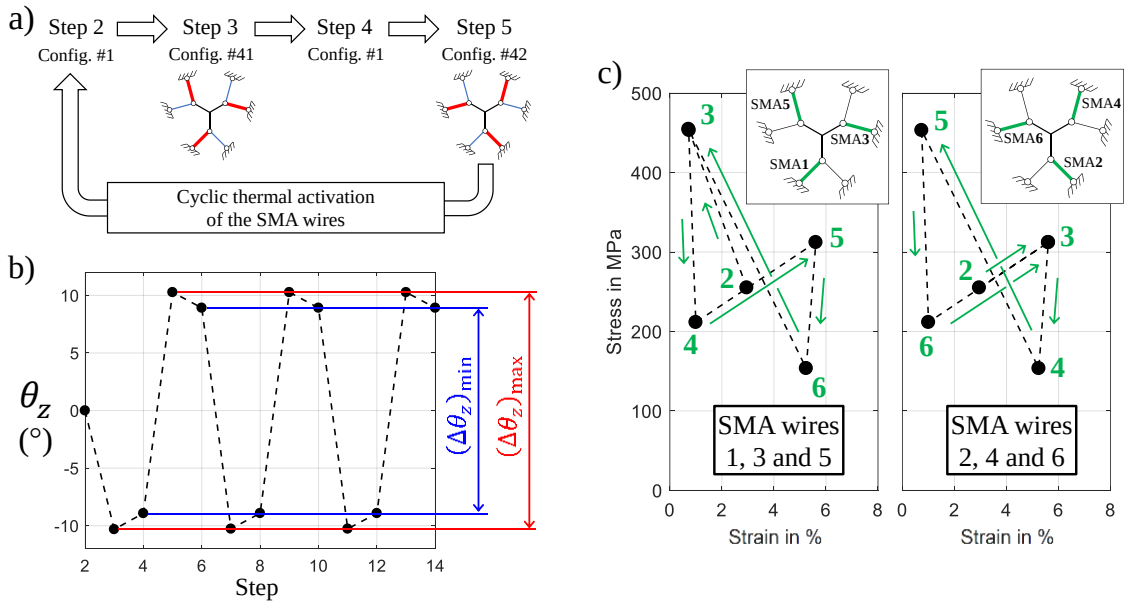

Figure 2.11. Creation of cyclic rotation by alternating Configurations #41 and #42 with intermediate returns to ambient temperature: a) thermal activation sequence considered, b) variation in rotation θ_z from one step to the next for $\alpha = 90°$ and $\varepsilon_{pre} = 3\%$, c) corresponding variation in stress and strain in the SMA wires.

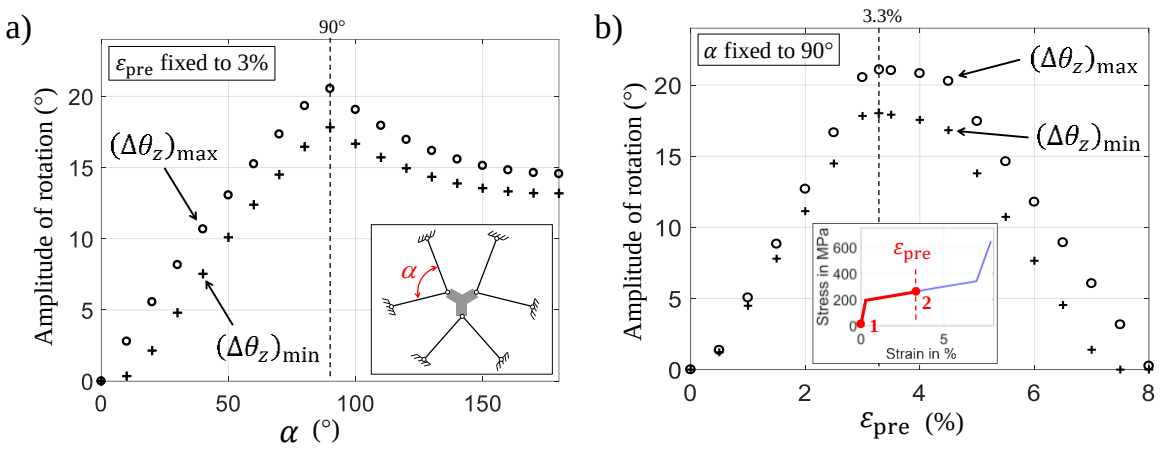

Figure 2.12. Amplitude $(\Delta\theta_z)_{max}$ of rotation obtained by alternating Configurations #41 and #42 as in Figure 8-a: a) as a function of angle α for $\varepsilon_{pre} = 3\%$, b) as a function of ε_{pre} for $\alpha = 90°$. Amplitudes $(\Delta\theta_z)_{min}$ between intermediate returns to ambient temperature are also plotted. See Figure 2.11-b for the definition of $(\Delta\theta_z)_{max}$.and $(\Delta\theta_z)_{min}$.

The same approach was developed for the case of a cyclic translation, by alternating Configurations #8 and #13 with intermediate returns to ambient temperature: see Figure 2.13-a. These two heating configurations lead to translations along the y-axis only, due to the vertical symmetry of these heated wires. Figure 2.13-b shows the influence of angle α on the translation amplitudes $(\Delta u_y)_{max}$ and $(\Delta u_y)_{min}$, keeping ε_{pre} at 3%. The gray-shaded rectangles in the graph correspond to non-valid configurations, i.e. situations for which stresses are negative or exceed the plastic yield stress of the SMA. It can be noted that there are large ranges of values for angle α which are not valid, and from 131° to 180°, only translations lower than 1 mm are possible. As expected, when the heated wires are aligned and parallel to the x-axis ($\alpha = 180°$), no translation is obtained. From 50° to 70°, greater translations are possible. Values are nearly constant: $(\Delta u_y)_{max} = 5.8$ mm and $(\Delta u_y)_{min} = 5.2$ mm. Figure 2.13-c shows the influence of ε_{pre} for $\alpha = 60°$. Similar to the rotation case above, increasing the pre-strain level excessively (here $\varepsilon_{pre} > 6.8\%$) tends to decrease movement amplitudes. Furthermore, translation amplitudes increase with ε_{pre} in the range [0%; 4.0%]. Optimal values are $[(\Delta u_y)_{max}]_{opt} = 7.8$ mm and $[(\Delta u_y)_{min}]_{opt} = 6.8$ mm at $\varepsilon_{pre} = 4.0\%$. It can be noted that this latter value actually corresponds to the boundary of a non-valid domain. This means that, in an experimental context, attention should be paid to avoid falling into an undesired situation, by applying for instance a pre-strain slightly lower than 4.0%. It can be noted that, as expected, the optimal parameters

for translation and for rotation are distinct. Seeking both a large rotation and a large translation requires a compromise.

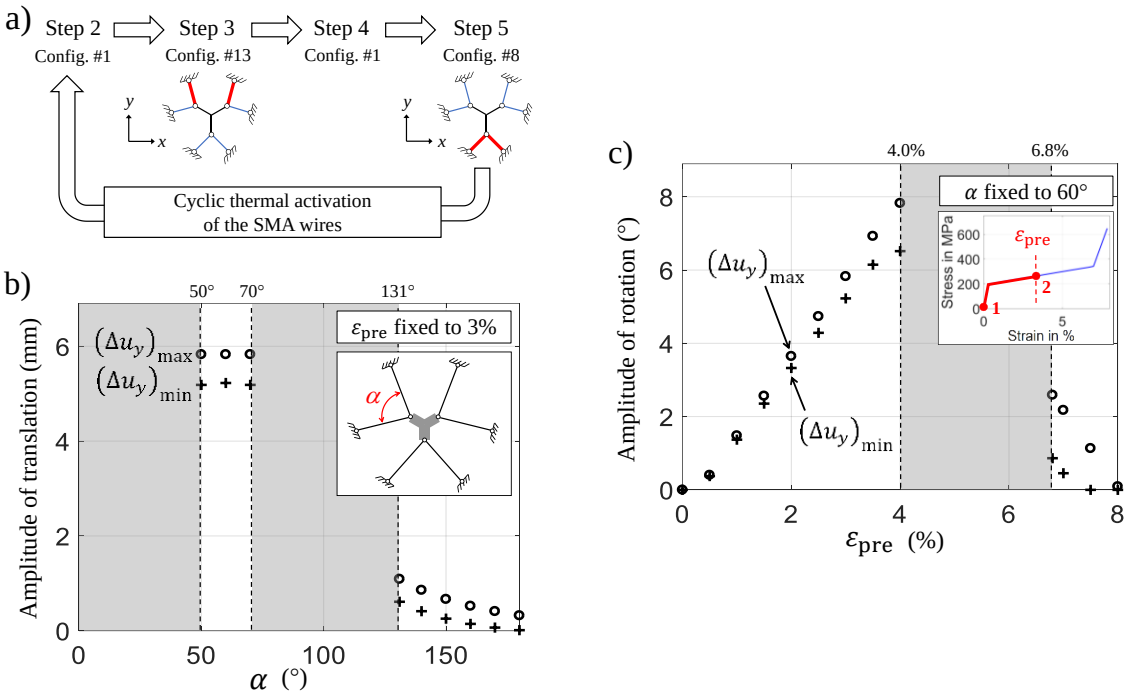

Figure 2.13. Cyclic translation obtained by alternating Configurations #8 and #13: a) thermal sequence considered, b) translation amplitude $(\Delta u_y)_{max}$ as a function of angle α for $\varepsilon_{pre} = 3\%$, c) same as a function of ε_{pre} for $\alpha = 60°$. Amplitudes $(\Delta u_y)_{min}$ between intermediate returns to ambient temperature are also plotted. Gray-shaded rectangles in the graphs correspond to non-valid situations.

2.4.5. Evidence of an attraction effect

An "attraction effect" can be evidenced by analyzing the impact of a given heating configuration at Step 3 on the subsequent steps. Let us consider for instance Configuration #24 at Step 3, followed by a return to ambient temperature at Step 4, and finishing by Configuration #k at Step 5 with $k \in \{1...64\}$: see Figure 2.14-a. For $\alpha = 90°$ and $\varepsilon_{pre} = 3\%$, Figure 2.14-b shows the coordinates (u_x, u_y, θ_z) obtained at Steps 3 and 5, while Figure 2.14-c provides the projection in the plane (u_x, u_y). It can be seen in these graphs that many points at Step 5 are close to the point at Step 3. More precisely, a point cloud is located in a neighborhood of Step 3 (see close-up in Figure 2.15), whereas other points remain far away. This property opens the possibility of reaching various new platform positions around any given position, while retaining the ability to "jump" far away in the workspace at any time.

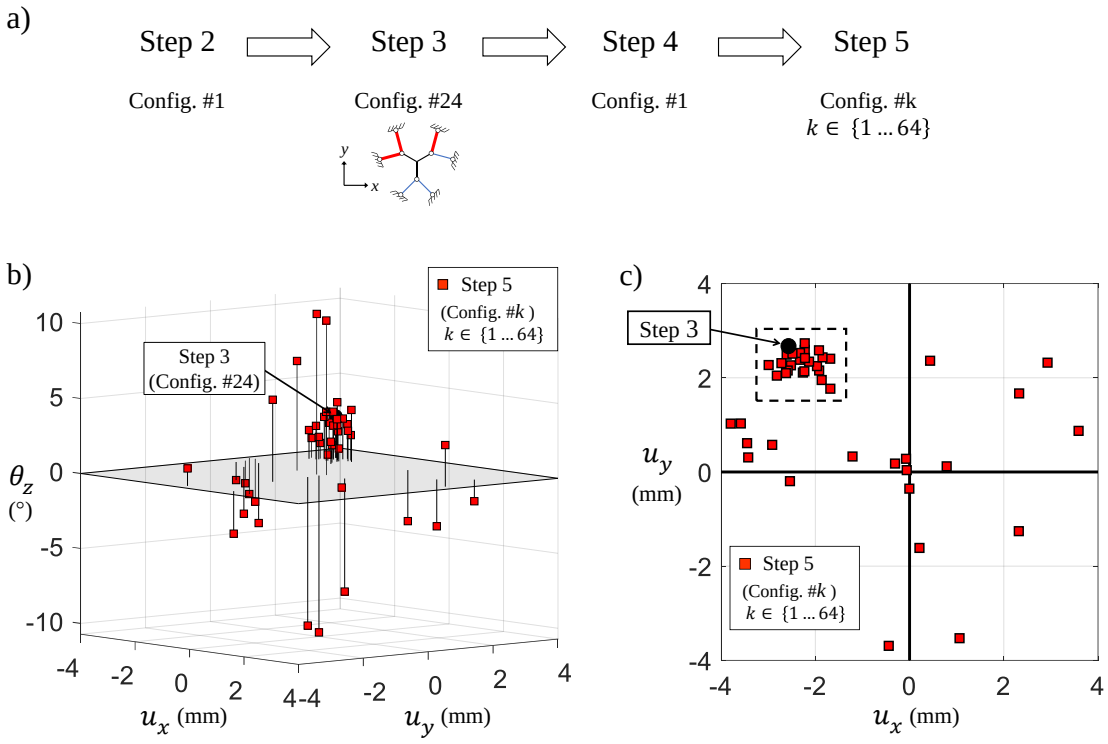

Figure 2.14. Evidence of an attraction effect: a) thermal activation sequences considered to observe the effect of Configuration #24 in Step 3 on subsequent steps, b) and c) same plot as Figures 2.8.(a) and (b). Black dot and red squares correspond to Steps 3 and 5 respectively, for $\alpha = 90°$ and $\varepsilon_{\text{pre}} = 3\%$.

In the example developed in Fig. 2.14, from the heating configuration #24 at Step 3, it is possible to reach a *close* position for the platform at Step 5 (red square symbols *inside* the dashed rectangle in Fig. 2.14-c), but it is also possible to reach a *distant* position (red square symbols *outside* the dashed rectangle).

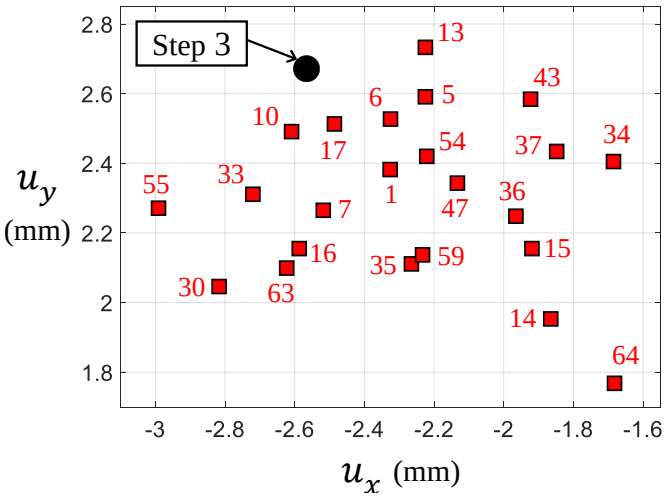

Figure 2.15. Close-up of Fig. 2.14-c. Numbers refer to the configurations in Fig. 2.6.

It is also interesting to note that the platform positions at Step 5 that are close to the position at Step 3 exhibit strongly distinct global stiffnesses: see Table 2.7. Calculations were made at Step 5 for Configurations #5, #6, #10, #13 and #17, corresponding to the closest five platform positions to Step 3 (#24); see Fig. 2.15. Stiffness at Step 3 was also calculated for comparison purposes. Components K_{xx} and K_{yy} of the stiffness matrix were obtained by applying a force of 100 N along the x-axis and y-axis, respectively, at point E of the platform. Component $K_{\theta\theta}$ was obtained by applying a torque of 100 N.mm along the z-axis. Note that each component was calculated from a specific simulation because of the non-additivity of the effects of each force component; see Refs. [97], [104] for details about the non-linearity and anisotropy of stiffness variability when SMA components are employed in a mechanism. Variability in the stiffness values is evidenced from Table 2.7. It can be explained by differences in the proportion of austenite and martensite of the SMA wires. Globally, the higher the proportion of austenite in the system, the higher the global stiffness, because $E_A > E_M$ (see Table 2.4). However, let us recall that the transformation to austenite of a given wire by heating tends to deform antagonistic wires, which therefore transform to martensite... We note that the value K_{yy} at Step 3 (0.91 kN.mm^{-1}) is lower than all the values calculated at Steps 5 (max 1.22 kN.mm^{-1} for Configuration #6). This can be explained by the fact that all the heated wires in Configurations #5, #6, #10, #13 and #17 (Steps 5) had already been activated at Step 3. Wider variabilities are observed for the K_{xx} (min 0.42 kN.mm^{-1}, max 1.04 kN.mm^{-1}) and $K_{\theta\theta}$ (min 258 kN.mm.rad^{-1}, max 480 kN.mm.rad^{-1}) components. This variability opens prospects for the optimization of variable global stiffness.

Heating configuration at Step 5	K_{xx} **[kN.mm^{-1}]**	K_{yy} **[kN.mm^{-1}]**	$K_{\theta\theta}$ **[kN.mm.rad^{-1}]**
#5	0.42	1.00	372
#6	0.53	1.22	472
#10	1.04	1.06	480
#13	0.42	1.01	378
#17	0.75	1.02	258
Step 3 (#24) for comparison	0.85	0.91	359

Table 2.7. Evidence of strong variability of stiffness in a given zone of the workspace. Steps 3 and 5 refer to the thermal activation sequence in Figure 2.14-a. Components K_{xx}, K_{yy} and $K_{\theta\theta}$ of the stiffness matrix were obtained by applying a force of 100 N and a torque of 100 kN.mm at point E.

2.5. Possibility of reaching a target position in the workspace

Finally, before concluding this chapter, this section shows that it is possible to reach a target position for the platform using a sequence of heating configurations. It is important to note that the objective here is *not* to develop a direct or inverse model of the studied mechanism. The objective is simply to show that it is possible reach a given platform position using an empirical approach. Starting from Step 2, the following target was arbitrary defined: (u_x, u_y, θ_z) = (-2.80 mm, 1.95 mm, 1.2°) with a precision of 0.1 mm and 0.1° for the translation and the rotation respectively. As a constraint, each heating configuration must be followed by a return to ambient temperature T_0 (Configuration #1), creating thus a series of "bi-stable" states. In particular, the thermal activation sequence must finish with Configuration #1.

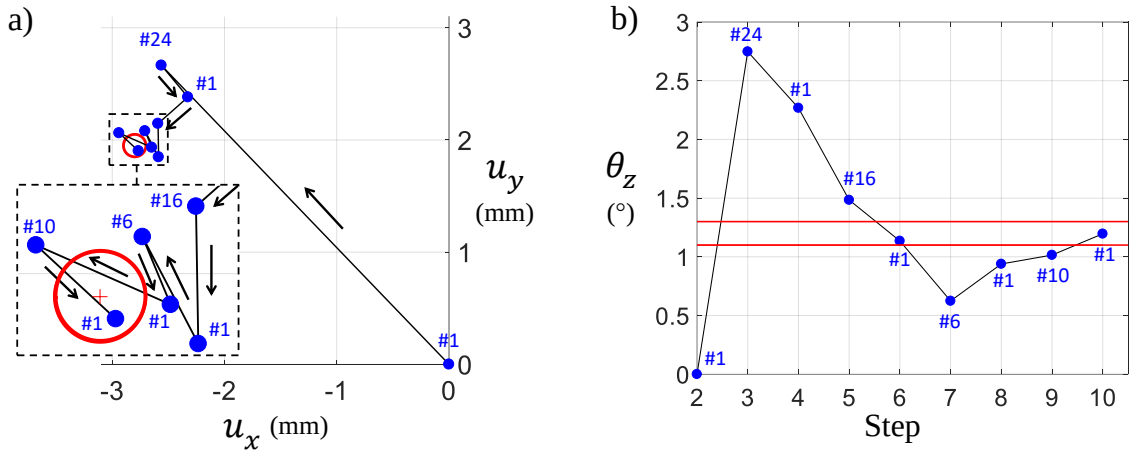

Figure 2.16. Example of a thermal activation sequence enabling a given platform position to be reached. The target was (u_x, u_y, θ_z) = (-2.80 mm, 1.95 mm, 1.2°), with a precision of 0.1 mm and 0.1° required for the translation and the rotation respectively (red marks), for $\alpha = 90°$ and $\varepsilon_{pre} = 3\%$. The sequence was defined empirically, with the constraint of returning to ambient temperature (Configuration #1) after each heating configuration. Configuration numbers refer to Figure 2.6.

Figure 2.16-a shows the different steps obtained in the (u_x, u_y) plane; Figure 2.16-b shows the variation in angle θ_z. The target is reached here in four heating configurations (and four returns to ambient temperature). Numerous other thermal activation sequences can lead to the same target. However, the following simple principle can be expressed a priori: it is possible to reach a target by applying a sequence of heating configurations in the "neighborhood" of each other. For instance, Configuration #16 is in the vicinity of Configuration #24 (see Figure

2.15); then Configuration #6 is in the vicinity of Configuration #16; etc., until the target is attained. This opens perspectives for the control of the mechanism.

2.6. Conclusion

A mechanism with six SMA wires (allowed to be thermally activated individually) was analyzed using a FE simulation based on Auricchio's model for the memory effect of the SMA material. This analysis highlighted the multi-antagonistic and hysteretic effects using various thermal activation sequences. Important points were discussed, such as:

(1) the possibility of locking a configuration without energy input;
(2) the avoidance of plasticity of the SMA wires;
(3) the attraction effect of any heating step on the following steps;
(4) stiffness variability as a function of the applied thermal sequence.

Although point (1) is well known in the literature, the other three points are rarely addressed, although they are important for the control of multi-antagonistic SMA systems. Prior to any design, thermo-mechanical models available in the literature for SMA components should be employed for the proper simulation of new multi-antagonistic actuation systems based on these active materials, in order to correctly address all four points.

The studied mechanism featured a small translation workspace (about 7 mm) but a quite significant angular stroke (about 20°). This makes it potentially interesting as a hollow shaft rotary actuator with additional (small) translation DOFs. Let us note that the concept can easily accommodate size reduction. Homothetic reduction of the dimensions can be implemented while retaining the same amplitude of rotation; in addition, size reduction is advantageous for improving (reducing) activation times, both for Joule heating and convection cooling. The proposed design could therefore find potential applications in micro-robotics for applications requiring long-term and stable positioning at ambient temperature (i.e. without energy input).

In the following chapter, the design and manufacturing of the prototype of this multi-antagonistic SMA-driven mechanism is detailed.

"Design is an opportunity to continue telling the story, not just to sum everything up." — Tate Linden

Chapter 3: Design of the prestressed mechanism and preparation of the SMA wires

Contents

3.1. Introduction 60
3.2. Specifications of the mechanism under study 60
3.3. Previous versions of the prototype 61
3.3.1. Initial design of the prototype. 62
3.3.2. Second design of the prototype 63
3.3.3. Third design of the prototype 64
3.4. Latest version of the prototype 64
3.4.1. Overview of the mechanism 65
3.4.2. Mobile platform CAD and its Finite Element validation 67
3.4.3. Tightening of the SMA wires 69
3.4.4. Prestraining of the SMA wires 71
3.5. Preliminary preparation of the SMA wires 74
3.5.1. Mechanical characterization of the SMA wire 74
3.5.2. Preliminary mechanical training of the SMA wires 75
3.6. Conclusion 77

3.1. Introduction

In the previous chapter, we tried to explore numerically the capacities and limits of the prestressed mechanism under study. Some primary conditions for a prototype were established such as the angles between SMA wires, the number of SMA wires and the possible configurations for actuation. In order to move from numerical to experimental studies, a physical demonstrator is required. In the present chapter, the process of building a prototype will be discussed in the following sections:

- Section 3.2 gives the specifications of the mechanism.
- Section 3.3 presents the evolution of the design through different previous versions.
- Section 3.4 shows the latest version of the design and the details of its components.
- Section 3.5 discusses the importance of the mechanical training of the SMA wires to ensure a good functioning of the mechanism, and presents the experimental tasks for this purpose.

3.2. Specifications of the mechanism under study

Generally, in order to have a functional mechanism, it is essential to carefully draw up its specifications and adjust them as and when required. Previously, in section 2.3.1, the desired topology of the mechanism was defined as a ternary symmetrical moving platform (also known as mobile platform) actuated by six SMA wires. Section 2.3.3 justified the chosen topology. However, between the initial sketch and the final design some compromises were needed. In fact, compared to Fig. 2.5-a, Figure 3.1 presents the planar parallel mechanism within a kinematic modelling. Figure 3.1 illustrates a *6-RPR* prestressed planar parallel mechanism, where *R* stands for passive revolute joints and *P* for actuated prismatic joints. The latter actually corresponds to the "actuation mechanism" of the SMA wires. This redundantly actuated manipulator is composed of two structural components, namely a base and a moving platform.

To ensure a good performance of the mechanism, some key features must be respected, which are accuracy, precision (repeatability) and resolution of the mechanism components, as well as the manner in which they are combined. Consequently, factors that might affect those features need to be avoided or at least minimized, such as friction, wear and sliding (in particular at both ends of the

wires). Besides, as the SMA wires are the actuators in this study and they are positioned in a multi-antagonistic way with respect to specific chosen angles, their placements must be as accurate as possible. Furthermore, since the SMA wires are actuated by heat, thermal insulation between the wires and their surrounding components is of utmost importance. Ideally, heat transfer should be minimized during the actuation phase of the SMA wires and maximized during the cooling phase. The heating is classically carried out by the Joule effect. In practice, for the present work, the return to room temperature will be done by natural cooling (natural convection in the air and by contact at the ends of the wires), which does not really allow an optimization of the cooling time.

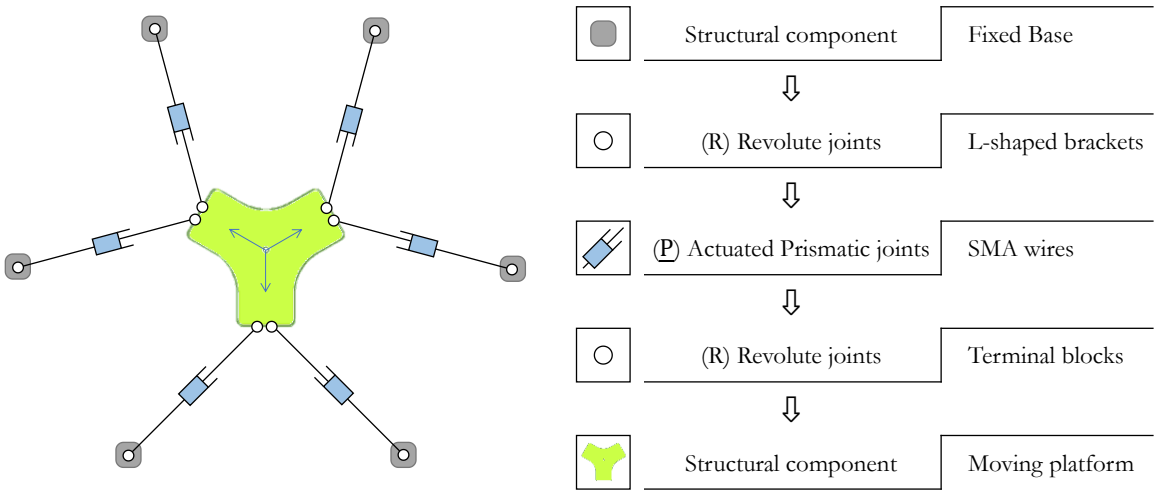

Figure 3.1. Architecture of the 6-RPR Prestressed Planar Parallel Mechanism (PPPM) under study. It can be noted that the actuated prismatic joints actually correspond to the SMA wire actuation.

The next step is to properly select the adequate components that best meet the predefined requirements. In the following sections, the evolution of the design from a scratch version to a final prototype will be demonstrated.

3.3. Previous versions of the prototype

Mechanical design of the plane system is about transforming a 2D sketch into a functional 3D system where several components are assembled in a way to fulfil a certain objective. This transformation is usually not immediate, some flaws are bound to happen which leads to several versions before a first functional one. Following, three versions of design are presented through their main components.

It shall be noted that in this section, the design swill be described without further details.

3.3.1. Initial design of the prototype.

In section 3.2, the specifications of the mechanism were drawn up and from now on we will try to turn the thinking into visual. The initial design was drafted and manufactured during a school project of SIGMA students. Figure 3.2 shows the main components of the first version of the system displaying the manufactured system with a 3D-printed moving platform and CNC-machined brackets and base. In the middle of the figure, a one-part moving platform exhibits six passages where clamps can be positioned. The set of the clamp and its screw works as a gripper for the SMA wires. Each SMA wire has a pair of a clamp set attached from both ends, one set is located in the moving platform, while the other grippes the second end of the wire passing through the L-shaped fixing bracket. Each bracket has three aligned holes for the positioning on the fixed base. The shorter side of the bracket contains a horizontal threaded hole where a hollow screw will be positioned. In this version, three possible angular positions were intended for each SMA wire.

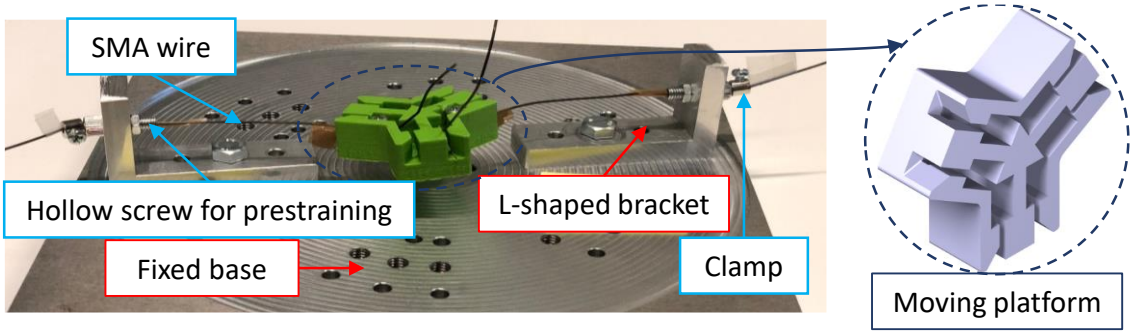

Figure 3.2. First version of the system.

Some tests were conducted to evaluate how much the design fits the defined specifications; namely, sliding tests for the SMA wires, thermal insulation and stability tests. The tests pointed out several flaws:

- the clamp failed to grip firmly the heated SMA wire leading to its sliding;
- due to the metallic material of the clamp in direct contact with the SMA wire and the metallic bracket, the system had experienced a heat dissipation;
- the designed positions of the brackets were not symmetrical;

- the prestraining is done by unscrewing the hollow screw; however, since its head is cylindrical, it was not easy to prestrain the SMA wire;
- and finally, there were out-of-plane translations of the SMA wires along the z-axis (axis perpendicular to the plane).

For all the reasons above, the design needed to be improved. Hence, the next section proposes a second version.

3.3.2. Second design of the prototype

In collaboration with a Thai engineering student, a second version of the system using a "ring" was proposed. Figure 3.3 shows the CAD of the mechanism where (a) is the assembly of the main parts, (b) an exploded view of the moving platform and (c) an exploded view of the ring. In this version, double-block electric dominos, not presented in the figure, replaced the clamps inside the moving platform. The reason behind the choice of the electric dominos will be detailed in section 3.4.

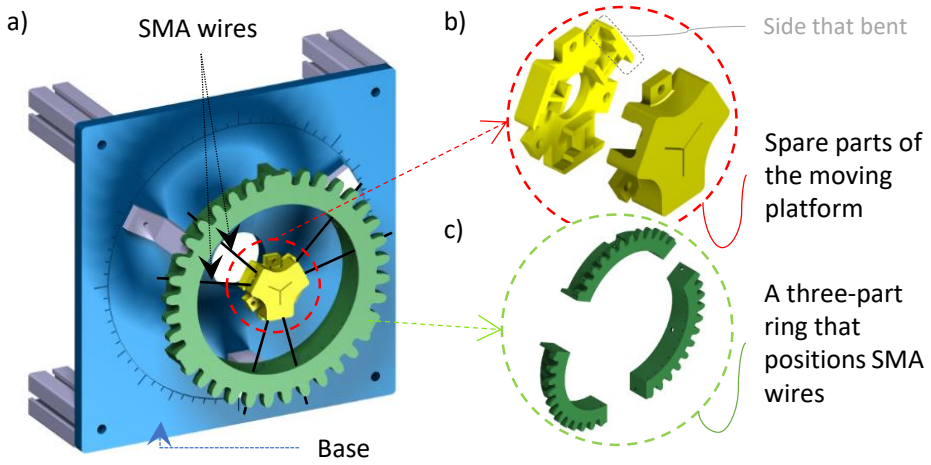

Figure 3.3. Main components of the second version of the system. (a) Assembly of the mechanism. (b) Exploded view of the moving platform. (c) Exploded view of the ring.

The moving platform is composed of two parts that incorporate the SMA wires and the dominos in order to avoid out-of-plane movement of the set. Rather than using L-shaped brackets to position SMA wires, we thought about replacing them with an ABS three-part ring. This ring allows six possible angular positions for each SMA wire. Three L-shaped brackets attached to a fixed base support the ring. Only the moving platform was 3D-printed and tested using components of the previous prototype. During the tests, the sides, in which the SMA wires were inserted, bent slightly, which affected the accuracy of the system. Therefore, the

design must be thicker around the functional sides. The other components of the CAD were disregarded, because after thorough consideration, ensuring the planarity of the mechanism and the repeatability of the results did not seem feasible. In fact, using an ABS ring could have been affected by heated wire. As a result, a third design was proposed.

3.3.3. Third design of the prototype

As a continuity of her project, the engineering student proposed another design considering different recommendations. Figure 3.4 shows an overview of the mechanism alongside with an exploded view of the moving platform. The latter presents placements for single-block electric domino instead of a double-block. In this version, we chose to return to L-shaped brackets to position the SMA wires. Each wire was allowed to have seven angular positions marked by the threaded holes on the fixed base. None of the components of the third design was manufactured; however, it has inspired, as well as the previous versions of design, the latest prototype that will be presented in detail in section 3.4.

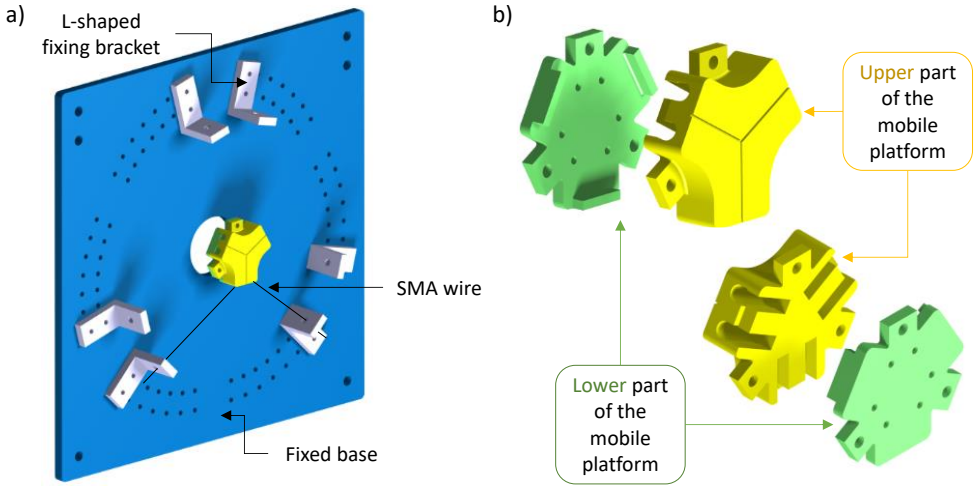

Figure 3.4. Main components of the third design. (a) Overview of the mechanism. (b) Exploded view of the mobile platform.

3.4. Latest version of the prototype

In section 3.3, the evolution of the design was presented through different choices while explaining the logic behind each decision. In this current section, more

details will be given to describe the latest design that was used for the experimental tests.

3.4.1. Overview of the mechanism

In the previous designs, we tried to meet the specifications described in section 3.2. Consequently, we have gathered several ideas on how to improve the mechanism. This resulted in the design presented in Figure 3.5, where (a) shows an isometric view of the assembled mechanism and (b) shows its top view. As for Figure 3.6, it displays how the whole mechanism should be assembled through an exploded view. Following, we are going to detail each component separately and explain its role.

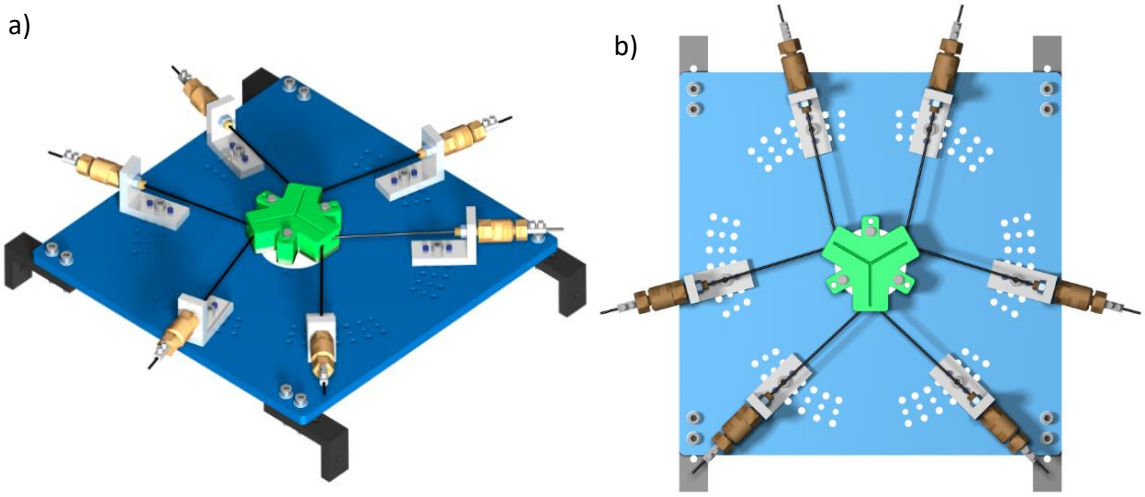

Figure 3.5. CAD of the final prototype: (a) Isometric view of the mechanism. (b) Top view of the mechanism.

First of all, let us recall the main purpose of this study, which is the building of a prestressed planar mechanism actuated by multi-antagonistic SMA wires. As a result, ensuring the positioning of the SMA wires is one of the key features of the design. Therefore, Figure 3.7 gives more information about the fixed base (a) and the L-shaped fixing brackets (b). A ternary rotational symmetry is guaranteed where two SMA wires occupy each third of the base. Each wire can have up to seven angular positions, separated from each other by fifteen degrees. If we consider a symmetry inside each third, we have an angle between two SMA wires that varies between 30° and 120° with a step of 15°. This multitude of angles allows more possibilities of test cases. For instance, in Fig. 3.5-b, the chosen angle is ninety degrees. To guarantee better angular accuracy, two positioning axes are used to

align the bracket and a hexagon socket screw that fixes it on the base: see Figure 3.6.

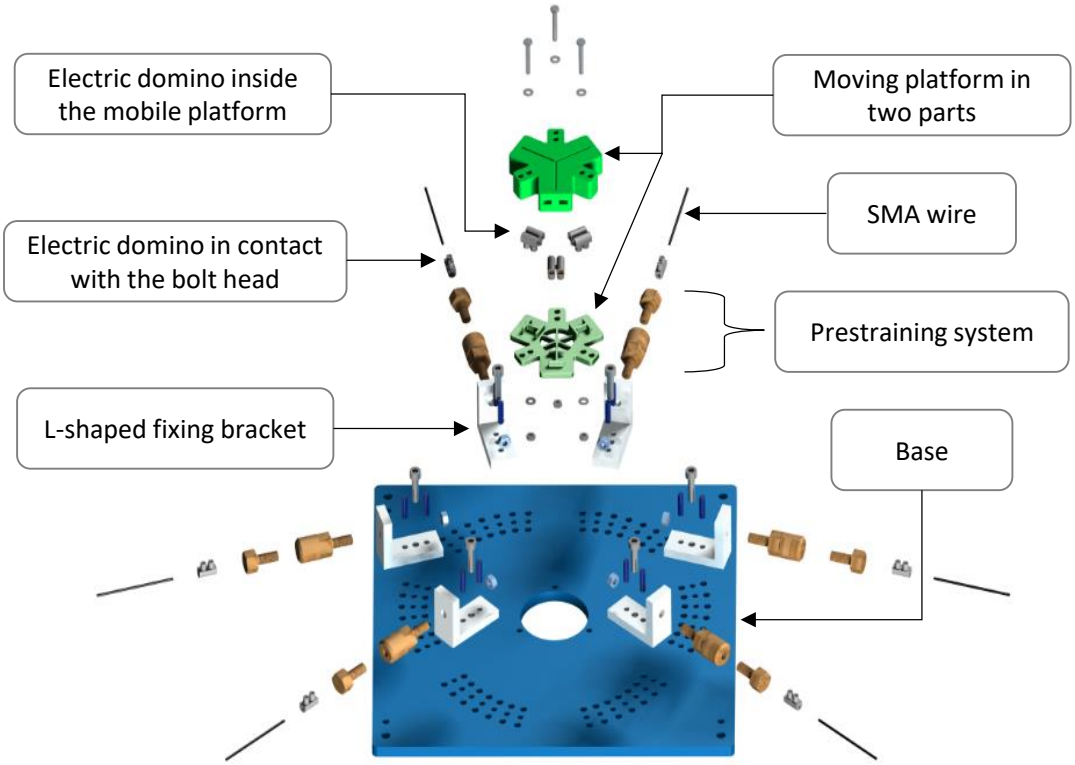

Figure 3.6. Details of the exploded view of the mechanism.

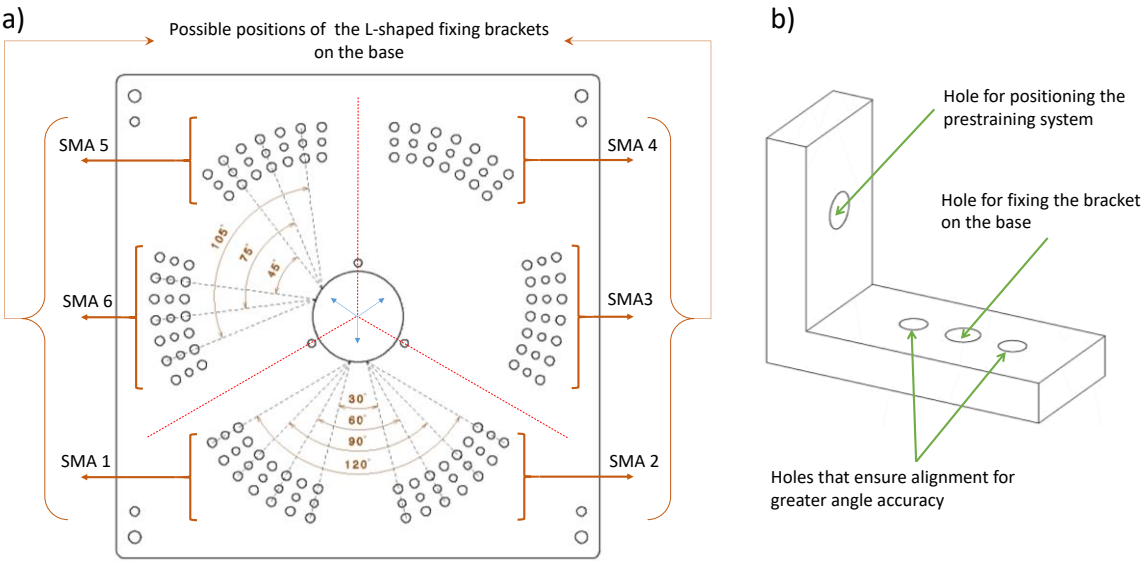

Figure 3.7. Details about the components that ensure positioning of SMA wires. (a) Fixed base. (b) L-shaped fixing bracket.

In the middle of the base, we find a large hole to pass through the electrical wires that transmit power in a closed circuit. Besides, we may find three holes that

are used to block the moving platform during the prestraining step of the SMA wires, which is essential in order to guarantee as best as possible an accurate result (see details in Section 3.4.3). Both the base and the L-shaped fixing brackets are machined using aluminum alloy. Another important component in the mechanism is the moving platform, which is presented in the next section.

3.4.2. Mobile platform CAD and its Finite Element validation

In parallel planar mechanisms, the moving platform is the part of the mechanism that supports the end-effector. Thus, its design must be both robust and functional. Since electric insulation is one of the biggest concerns of the design, the material of the moving platform must be carefully selected. Therefore, using a thermoplastic polymer seems an interesting choice, for instance ABS (i.e. Acrylonitrile Butadiene Styrene). Actually, all the previous versions of the mobile platform were 3D printed using ABS filaments, which led to rapid verifications and building design ideas.

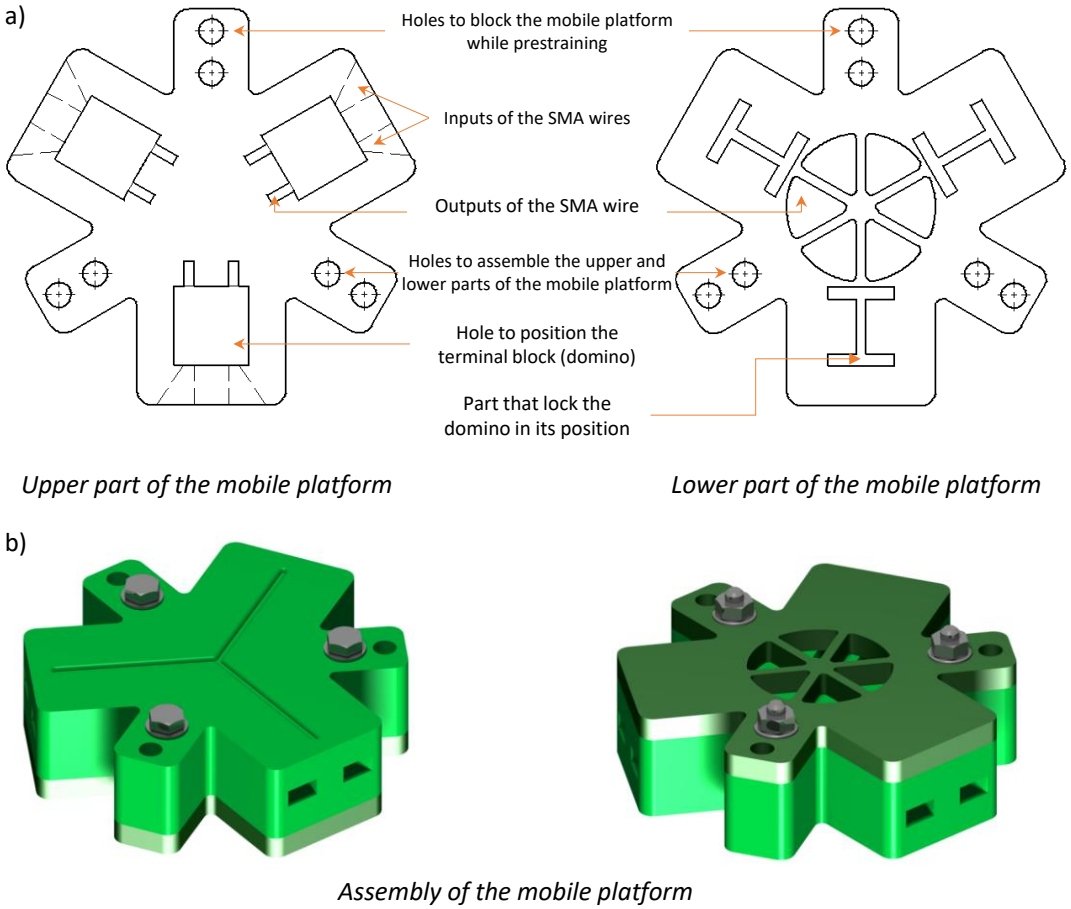

Figure 3.8. Details of the mobile platform. (a) Functionality of the details of the mobile platform. (b) Isometric views of the CAD assembly of the mobile platform.

Figure 3.8 gives details about the latest CAD of the moving platform. The concept of composing the moving platform of two parts was conserved. Fig. 3.8-a shows the inner sides of the upper and lower parts of the mobile platform which are designed to be in contact with each other while Fig. 3.8-b displays its external sides through a 3D assembly. Basically, we can identify the positions of the dominos that will fix the SMA wires and both the inputs and outputs of the wires. Three holes are positioned in a way to face the holes in the base which are designed to block the moving platform while prestraining. Further details about the design (technical files) are given in Appendix A.

Before printing the moving platform, a quick finite element (FE) analysis was done using CATIA General Structural Analysis module in order to approve the design. To do so, ABS polymer material was applied to the CAD model. For the static analysis, the mesh, seen in Figure 3.9-b, contained 491463 nodes and 317679 parabolic tetrahedron elements. Then, prior running the simulation, the boundary conditions need to be defined. Figure 3.9-a displays the applied constraints to block the displacement in the three directions. Besides, it shows the directions and orientations of the applied loads. As the plastic yield stress of the SMA wires used in this study is equal to 650 MPa (see Fig 3.15-c), the latter value is chosen as the applied pressure for this analysis of the simulation results.

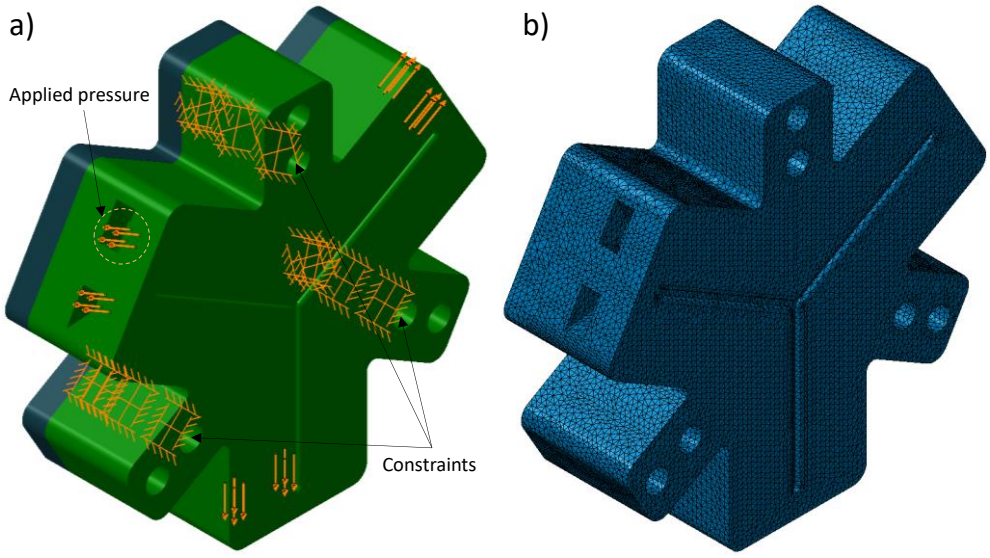

Figure 3.9. Finite element model of the moving platform. (a) Boundary conditions. (b) Mesh.

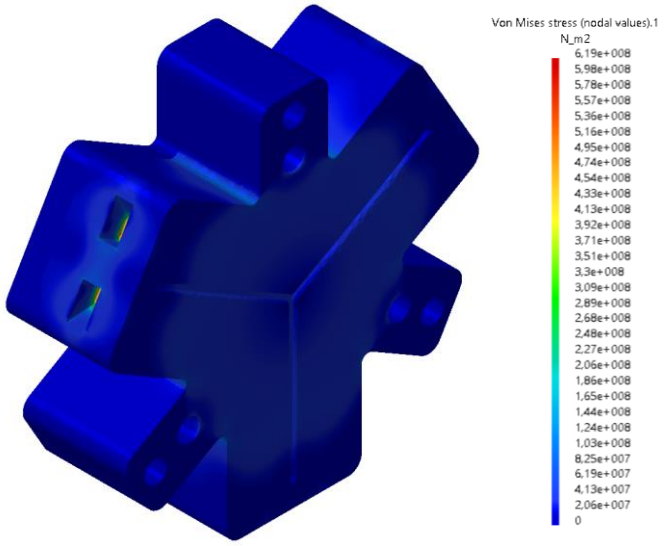

Figure 3.10. FE analysis of the moving platform using CATIA General Structural Analysis module: Von Mises stresses.

After computing the simulation, Figure 3.10 views the Von Mises stress field. The load induced in most of the structure is practically insignificant (lower than 1 MPa). More precisely, the Von Mises stress values are low except on the contact surface of the SMA wires. However, these values can be justified by the sharp angles in the mentioned areas. Consequently, we can safely conclude that the design of the moving platform is reliable and can fulfil its stiffness and strength efficiently.

This section presented details about the moving platform while the following describes the tightening of the SMA wires, which is a very important point.

3.4.3. Tightening of the SMA wires

In the present study, we use Ni50.8–Ti49.2 (at. %) SMA wire 1 mm in diameter, provided by Nimesis, Metz, France. The transformation temperatures of the wire are -25 °C, -7 °C, 24 °C and 36 °C (respectively M_f, M_s, A_s and A_f). Starting now, the ambient temperature is changed to 18 °C (rather than 15 °C used in the FE analysis in the second chapter). In fact, in order to ensure a stable ambient temperature throughout the experimental tests that will be presented in chapter 4, we worked in an air-conditioned test room where the temperature was set at 18 °C.

The sliding of the SMA wires at their two ends in the clamping system is one of the major concerns for designers of SMA wire-based mechanisms. In our device, despite a strong tightening of the SMA wire using the two screws of each domino at the two ends, it may slide and thus causing inaccurate actuation. To solve this problem, it was decided to tighten the wire when it is in its martensitic

state before heating and returning to ambient temperature. It is important to note that this was made possible thanks to the specific transformation temperatures of the used SMA: the fact that $M_s < T_{amb} < A_s$ enabled us to successfully solve the problem of tightening the SMA wire at their two ends simply using dominos.

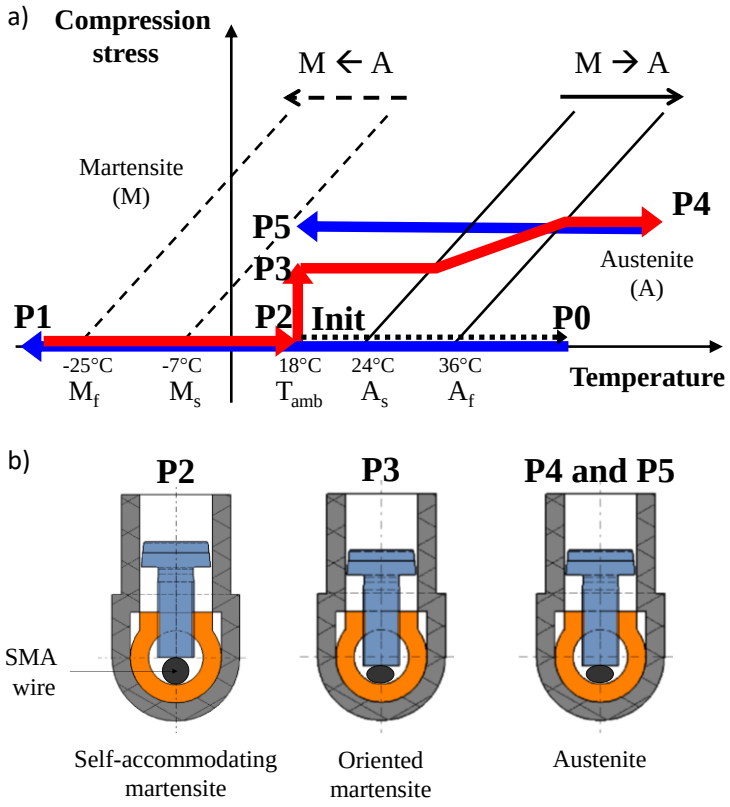

Figure 3.11. Tightening of the SMA wires. (a) Steps in the simplified state diagram. (b) Schematic view in the dominos.

Figure 3.11 illustrates the procedure. The preliminary step is to heat the SMA wire using a hot dryer (Init→P0). Consequently, the SMA wire turns into austenite (P0). Then, we let it cool at zero stress until it transforms to self-accommodating martensite (P1). For this step, we used a freezer of -35 °C (i.e. lower than M_f). Afterwards, the mechanism is taken out of the freezer at room temperature (18 °C, which is lower than A_s), the SMA wire is still in a self-accommodating martensite state (P2). At the same temperature, we apply a radial compression stress at the two ends of the SMA wire by fastening the screws of the dominos. Consequently, the compressed zones change from self-accommodating martensite to oriented martensite (P3). The next step is to transform the SMA wire into its austenitic state by heating it far above A_f (P4). Regardless, it must be noted that the compressed zone of the SMA wire keeps the same shape, leading

to an increase in the compression level. Furthermore, it can be assumed that it mainly remains at the same compression state when it cools down to ambient temperature (P5).

This tightening procedure was found after several tests. Thanks to this procedure, ensuring a good tightening of SMA wires through electric dominos seems to be a good and simple solution to a frequent and recurring problem in the SMA community. As a result, we were able to perform experimental tests that will be presented in chapter 4.

3.4.4. Prestraining of the SMA wires

Previously in this chapter, we introduced the structural components of the mechanism; moreover, we established the connections between each part of the mechanism. Because prestraining the SMA wires is a key step before their actuations in the frame of the SAOWME (stress-assisted one-way memory effect), this section explains how the process is done. As a matter of fact, allowing a certain prestrain ε_{pre} of the SMA wires in the system must be as accurate as possible. In chapter 2 section 2.4.4, the dependency of the movement amplitude on the prestrain of the SMA wire was proven through a case of study using a finite element simulation. Therefore, it is interesting to anticipate a design allowing such variety of prestrain values. For an SMA wire that is clamped at its both ends, we decided to use a hollow bolt to extend its length. However, before prestraining, the SMA wires must be straightened. As a result, the choice was set to have two hollow bolts where one is fastened inside the other.

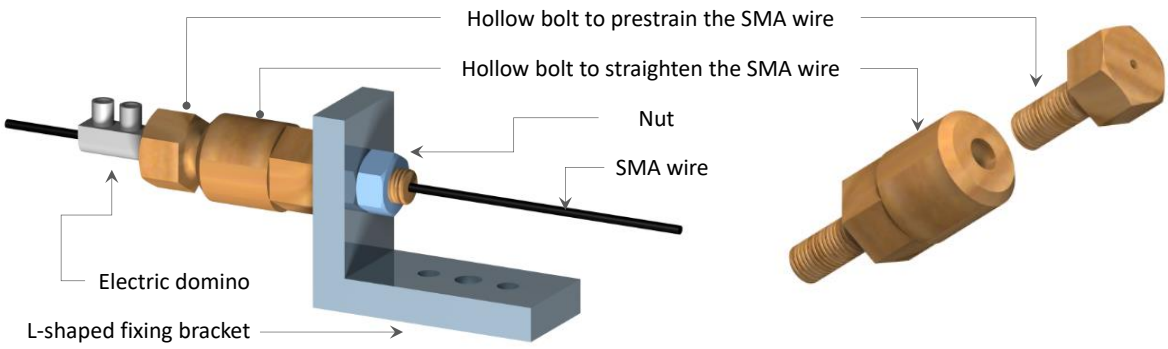

Figure 3.12. Components of the prestraining system.

Figure 3.12 pictures the chosen design assembled with the L-shaped fixing bracket, the SMA wire and the electric domino. The hollow bolts were machined using

Celeron material. Celeron is a composite plastic known namely for its "excellent" mechanical properties and low wear to friction. It is frequently used for electrical insulation parts. Thus, it is judicious to use this material to be in contact with the SMA wires.

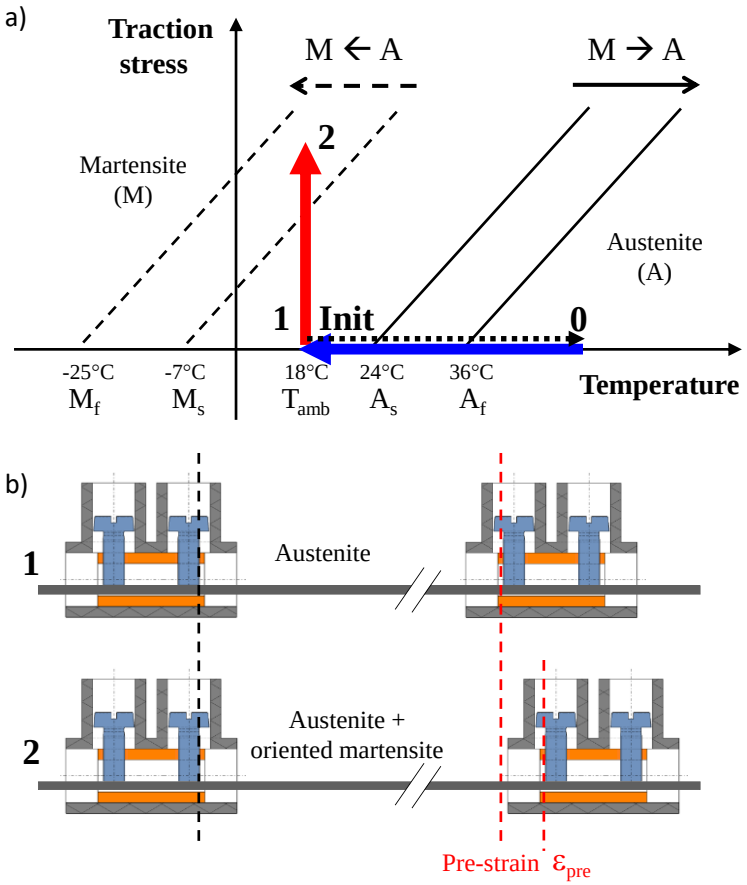

Figure 3.13. (a) Simplified state diagram of a SMA wire: b) with preliminary steps to pre-stretch the six SMA wires in the mechanism before starting a thermal activation sequence.

Figure 3.13 presents the steps of wire pre-stretching before starting a thermal activation sequence. The initial step (0) consists in "initializing" the SMA wire in the austenite state under zero stress. Let us recall that the tightening of the wires by the dominos at the two ends was previously carried out according to the procedure described above (see Fig. 3.11). Step (1) consists of cooling down under zero stress the SMA wire to ambient temperature. It shall be noted that the SMA wire keeps its austenitic state. Then, step (2) is to pre-stretch the wire transforming the austenite to mixture between austenite and oriented martensite.

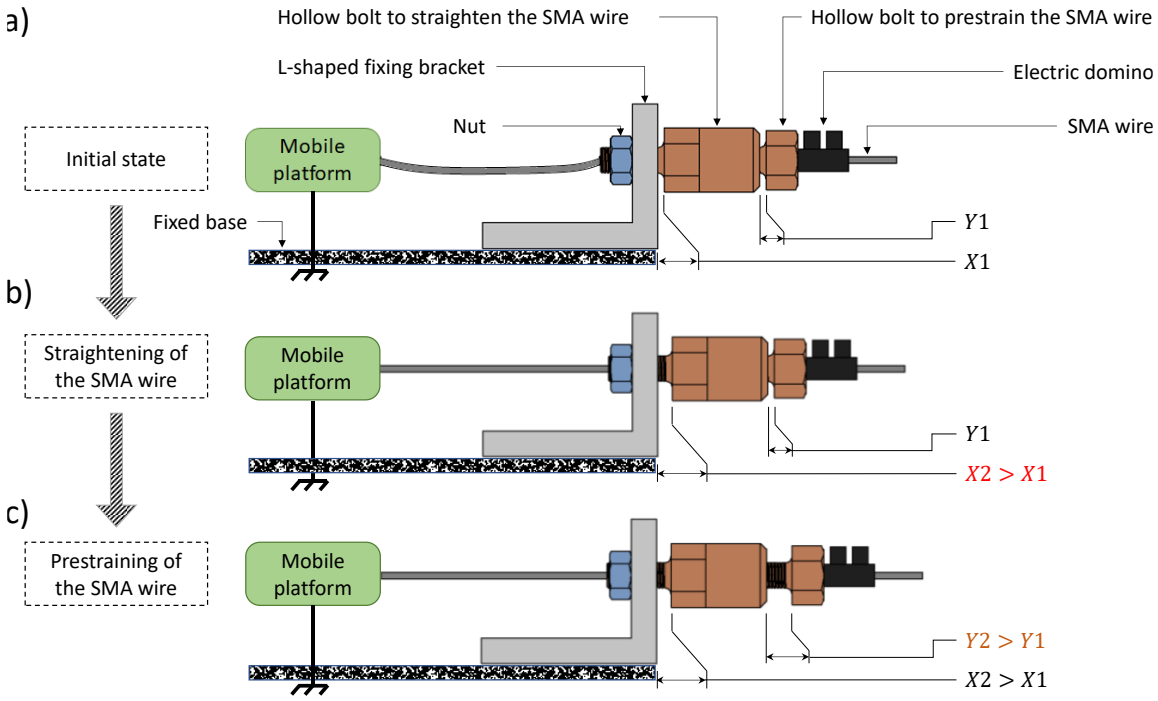

Figure 3.14. Principle of the prestraining system. (a) Initial state of SMA wire and hollow bolts. (b) Straightening the SMA wire by unscrewing the hollow bolt in contact with L-shape bracket. (c) Prestraining the SMA wire by unscrewing the hollow bolt in contact with the domino.

From a technological point of view, the prestraining process is illustrated in three steps in Figure 3.14. The following observations can be made about the initial step (a):

- the moving platform is temporary blocked by three rods that pass through it to the fixed base;
- the SMA wire is fixed from one side by an electric domino placed inside the moving platform and from the other side by another domino in direct contact with the head of the prestraining hollow bolt;
- the fillet between the bolt's head and its thread resulting from machining explains the small gaps between the L-shaped fixing bracket and the straightening hollow bolt and between the latter and the prestraining hollow bolt (respectively, X1 and Y1);
- the SMA wire is slightly bent due to gravity.

The objective of the second step (b) is to straighten the SMA wires without creating significant forces. Hence, after loosening the nuts, we start unscrewing the straightening hollow bolts until bending is nearly cancelled. It can be noted that this is a difficult point in the preparation of the mechanism.

The aim of the third step (c) is to prestrain the SMA wires. Firstly, the nuts must be fastened in order to block the movement of the straightening hollow bolt. Then, similarly to the previous step, we proceed unscrewing the prestraining hollow bolt until we reach the chosen prestrain value.

This section presented the design of the mechanism and its components as well as the prestraining system. The following section is dedicated to the preliminary preparation of the SMA wires before being installed in the mechanism.

3.5. Preliminary preparation of the SMA wires

Since the SMA wires are the actuators of the mechanism, they must be carefully handled. The objective of the present section is to present the mechanical characterization of the SMA wire using a uniaxial testing machine, and to present its mechanical "training". Such a preliminary training from a virgin SMA wire is important for the repeatability of the mechanism.

3.5.1. Mechanical characterization of the SMA wire

The previous chapters gave generic information about the mechanical behavior of the SMA wire used in this study. This section describes the result of a tensile test on a MTS uniaxial testing machine instrumented by a non-contact measurement technique. Digital image correlation (DIC) was used for the measurement of the wire strain. This type of measurement was done thanks to the help of Benoit Blaysat, Associate Professor in my laboratory.

Figure 3.15-a shows a picture of the experimental setup. A SMA wire, 80 mm in gauge length, was gripped in jaws of the testing machine: see Fig. 3.15-b. The ambient temperature was 25 °C. Note that the SMA wire was in the austenitic state at the beginning of the loading thanks to a preliminary heating (see Fig. 3.13-a). The loading was force controlled at a rate of 4 N/s until rupture of the SMA wire. For DIC measurement, black paint was first sprayed on the wire surface, on top of which white pant spots were added in order to enhance the image contrast. A Canon 5DSR camera equipped with a Tamron 90 mm SP macro lens was used. Macroscopic strain was calculated considering the displacements of two material points A and B, which are located near the top and bottom jaws of the testing machine respectively (see Fig. 3.15-b). Figure 3.15-c shows several stress-strain curves. True and engineering strains were calculated using both the displacement of the actuator and the displacement measured by DIC. True and engineering

stresses were defined from the force sensor measurement. Two main comments can be done from the graphs:

- Logically, the true and engineering curves are less and less similar as the deformation increases. A difference is also observed between the curves calculated with the actuator displacement and the displacement measured by DIC. This can be explained by the presence of slip at the clamping jaws.
- All the plots present an inflexion point for a stress of about 650 MPa, which can be attributed to the start of plastification. This value represents the plastic yield stress, which is used in this study as the maximum allowed stress in the SMA wires in the mechanism

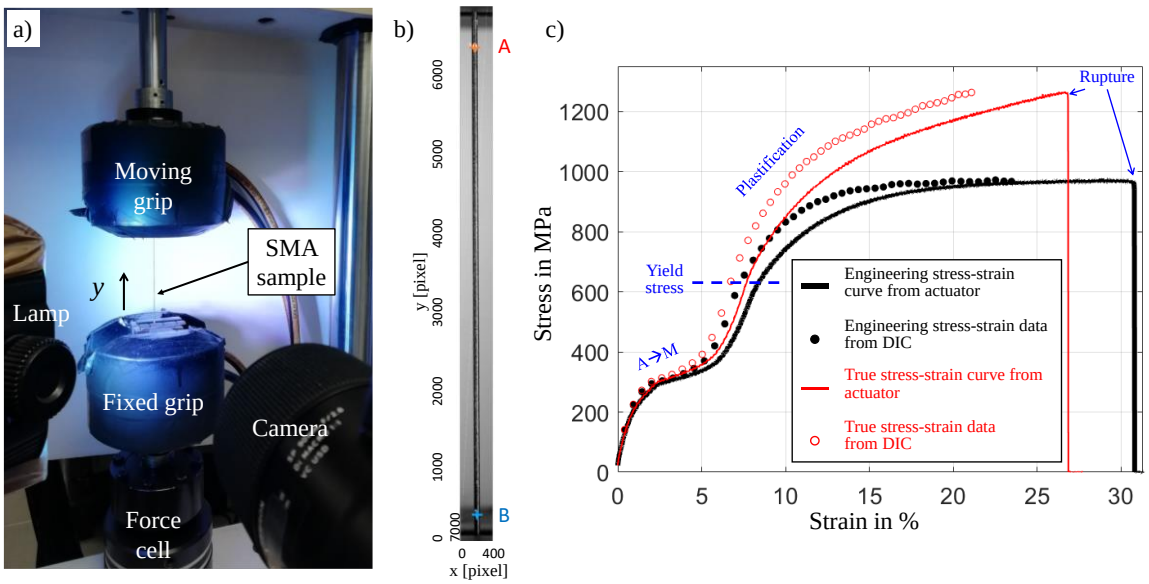

Figure 3.15. Mechanical characterization of the SMA wire: (a) experimental setup, (b) picture of the sample under test, 80 mm in gauge length, (c) stress-strain curves until rupture.

3.5.2. Preliminary mechanical training of the SMA wires

According to the specifications drawn in section 3.2, a good performing mechanism needs to be accurate, repeatable and with a good resolution. Therefore, each component matters as the mechanism functions as a one structure. Nevertheless, actuators are significantly the ones behind an efficient reliable mechanism or a poor performing mechanism. As for SMA wires, to function properly, they need to be preliminary "trained". More precisely, residual strains are observed along the first superelastic cycles. Mechanical training thus consists of applying several load-unload cycles until residual strain no longer evolves.

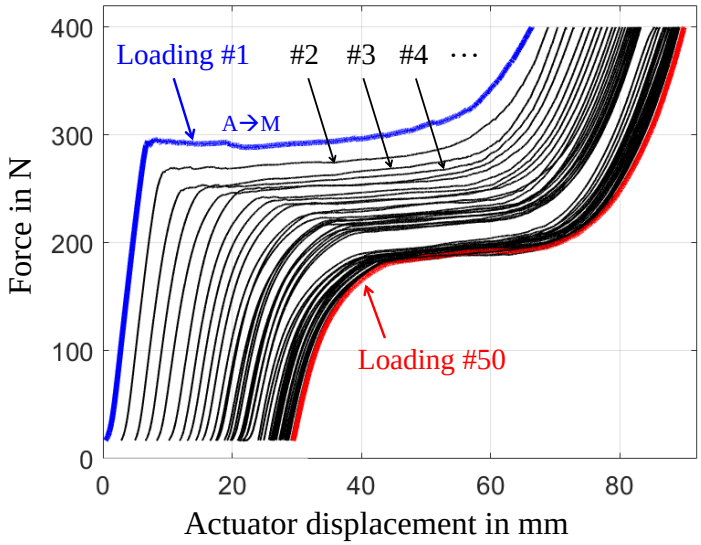

Figure 3.16. Mechanical training of the SMA wires before placement in the mechanism: displacement-controlled training of a long SMA wire (810 mm in useful length). Heating is performed after each load-unload cycle.

As training devices, a Zwick Roell tensile machine and a hot dryer were used. A long SMA wire (810 mm) was trained and was cut in several pieces afterwards. Figure 3.16 shows the force-displacement curve over 50 loadings (unloading phases are not displayed because the procedure simply consisted in loosening the bottom jaws). The displacement rate was set to 0.5 mm/s, until a maximum force of 400 N. The force plateaus correspond to the A→M transformation. It can be noted that the martensitic state is kept upon loading as the ambient temperature is higher than the M_s temperature. After each unloading, the SMA wire was heated in order to return to austenite state. Figure 3.16 shows that residual displacement is observed at each load-unload cycle. However, it can be seen that the behavior of the SMA wire is stabilized at the loading #50. Next, the long SMA wire was thus cut in several pieces to create the 6 SMA wires to be placed in the mechanism. It should be noted that the experiments to obtain such a stabilized SMA are long and difficult to carry out due to the numerous mechanical cycles and heating operations to apply.

Finally, Figure 3.17 shows a stress-controlled stabilized mechanical cycle after the training of a SMA piece (80 mm in useful length). The SMA wire transforms from austenite to martensite upon loading, then we have nearly elastic unloading and finally the reverse transformation (martensite to austenite) is induced by heating. Only when the SMA wire is stabilized, it can be used as an actuator.

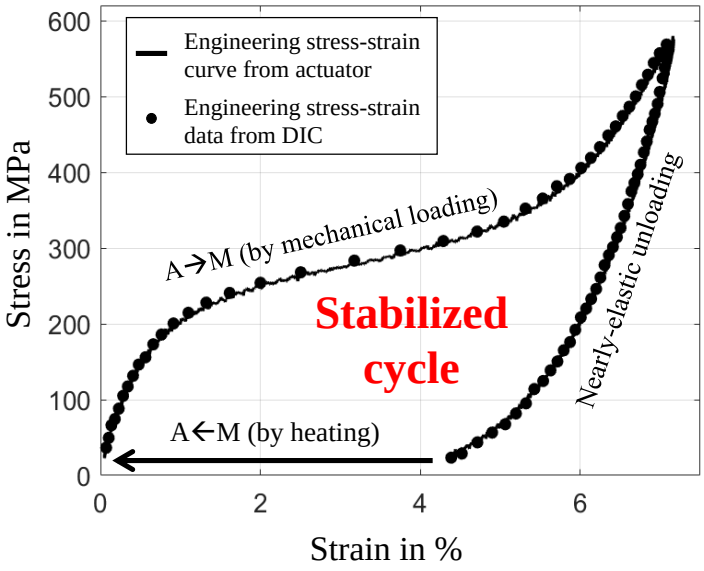

Figure 3.17. Stress-controlled stabilized mechanical cycle after training of a SMA wire (80 mm in useful length).

3.6. Conclusion

A functional design is a design where all its components work together to meet the specifications defined through a theoretical study. In this chapter, we tried to explain and justify the evolution of the design and each choice that led to a physical prototype. Both thermal and electrical insulations were thought in this mechanism. In brief, the mechanism is composed of a two-part ABS moving platform, an aluminum fixed base, a Celeron prestraining system, electric dominos and six trained SMA wires. Besides, the design allows different possible angles between the SMA wires. To ensure both accuracy and repeatability, the tightening procedure and the preliminary mechanical training process of the SMA wires were detailed. In particular, a specific procedure for the tightening of the SMA wires at their two ends by electric dominos was proposed based on the specific transformation temperatures with respect to the ambient temperature. Since all the components are ready, the next step is to put the theory into reality through experiments. Therefore, chapter 4 will be about the experimental results and numerical validation.

"With experimentation comes surprise and discovery."— Kim Lee Kho

Chapter 4: Experimentations and results

Contents

4.1. Introduction 79
4.2. Experimental setup and thermal analysis 80
4.2.1. Experimental setup 80
4.2.2. Preliminary thermal analysis 81
4.3. Experimental cases of cyclic rotation and translation 83
4.3.1. Cyclic rotation 84
4.3.2. Cyclic translation 86
4.4. Discrete workspace and attraction effect 87
4.4.1. Discrete workspace 87
4.4.2. Evidence of attraction effect 88
4.5. Example of a "complex" thermal sequence and stiffness variability 91
4.5.1. Example of a complex thermal sequence 91
4.5.2. Stiffness variability 92
4.6. Conclusion 94

4.1. Introduction

Earlier in this manuscript, we presented the numerical study of the considered prestressed mechanism (in Chapter 2), and then we presented its design as well as the preparation of the six SMA wires used in the mechanism (in Chapter 3). Hence, the established concepts need to be tested through several experimental cases of study. In the present chapter, the setup of the experiments and the results of the experimentations will be discussed as follows:

- Section 4.2 presents the experimental setup including the instrumentation devices, and a preliminary thermal analysis using an infrared camera.
- Section 4.3 considers two specific cases of thermal actuation: a cyclic pure rotation and a cyclic pure translation of the mobile platform.
- Section 4.4 discusses the evolution of the discrete workspace (as a consequence of the binary actuation of each of the SMA wires) and the "attraction" effect of any heating configuration to the following of the thermal activation sequence.
- Finally, additional experiments are presented in Section 4.5: an example of a "complex" thermal activation sequence (corresponding to the sequence tested in Section 2.5 in Chapter 2) and an experimental evidence of the stiffness variability (similarly to the case treated in Section 2.4.5 in Chapter 2).

Before starting this chapter, it is worth noting that the finalized procedure for the experiments required a lot of preliminary tests (not reported here). Besides, the preparation steps of the SMA wires are long and difficult: mechanical training requiring numerous thermo-mechanical cycles (see Section 3.5.2) and tightening with the specific thermomechanical procedure (see Section 3.4.3 and in particular Fig. 3.11). Also, the huge number of thermal activations (recall the 64 configurations in Fig. 2.6) with required waiting times to reach thermal equilibrium made the experiments very long. Some of the graphs in this chapter required several days of preparation, more than one week of measurement by camera, and still more time to extract the data before starting the analysis.

4.2. Experimental setup and thermal analysis

4.2.1. Experimental setup

The previous chapter provided details on the design of the mechanism and the preparation and placement of the SMA wires. The transition to a physical prototype of the mechanism is now illustrated in Fig. 4.1. Figure 4.1-a shows the assembly of the mechanism placed vertically to allow the positioning of cameras. The dominos are press-fitted into the mobile platform and they make the connection between the SMA wires and the electrical cables (blue in Fig. 4.1-b and red in Fig. 4.1-a and c). Two useful lengths of SMA wires were used in the test campaigns: 170 and 190 mm., which can be simply done by changing the length of the straightening Celeron bolt.

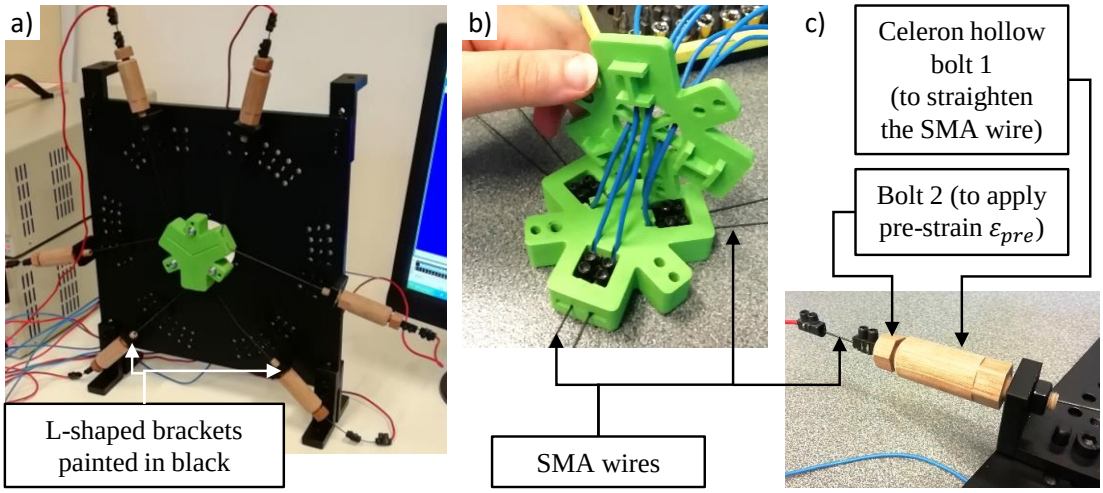

Figure 4.1. Manufactured prototype: a) assembly of the physical mechanism, b) details of the mobile platform, c) details of the prestraining system.

Figure 4.2 shows the tools and the instrumentations used in the experiments. To generate electric power, we use two triple-channel DC power supplies ref. 72-13330 from TENMATM. Each power supply allows a voltage range of 0-30V and a current range of 0-5A in two channels. As for the third channel of the electric power supply, three voltages are allowed 2.5V, 3.3V and 5V with a fixed amperage of 3A.

To ensure a better precision during the thermal analysis, the metallic parts of the mechanism were painted in black (limitation of the reflections in the infrared range of the metallic surfaces). Two infrared measurement systems were used: a Cedid Jade III research infrared camera and a Flir One Pro thermal camera for smartphone. The former camera was used for the preliminary thermal study (see

next section 4.2.2) whereas the latter was used for rapid thermal verification during the test campaign. Finally, a visible-range camera (D3 Nikon) was used to picture the movement of the mobile platform.

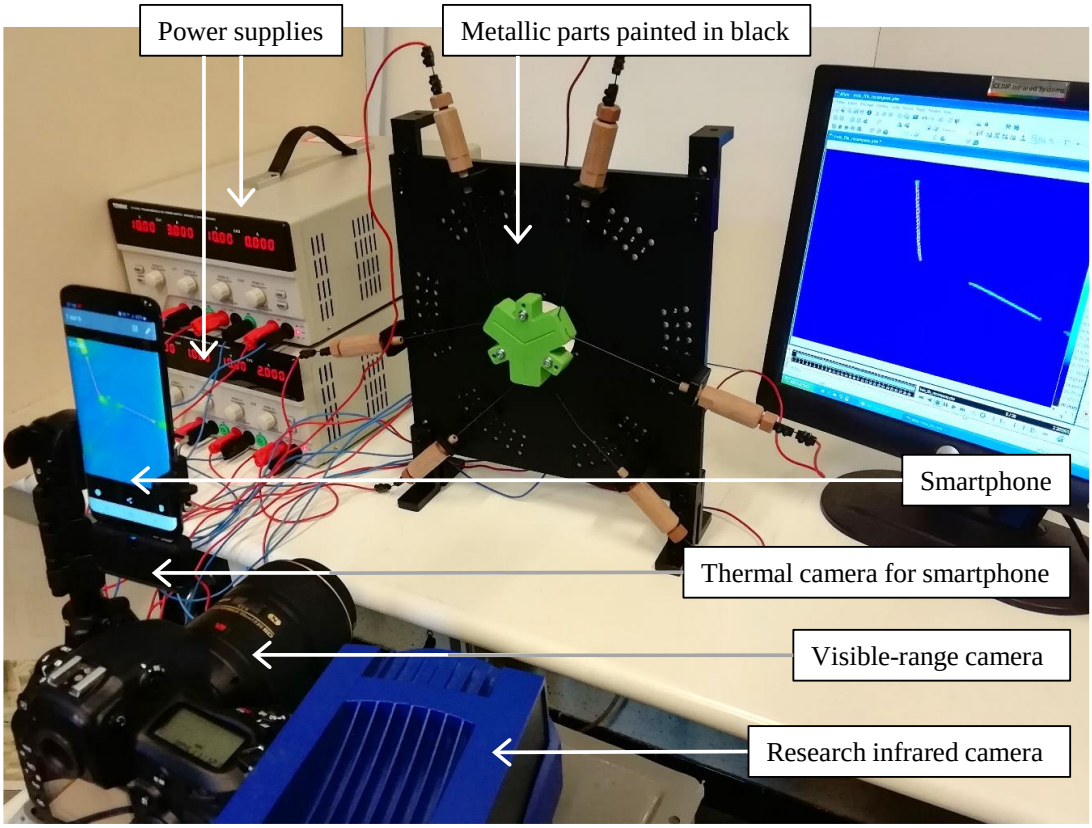

Figure 4.2. Experimental setup.

4.2.2. Preliminary thermal analysis

As SMA is a temperature-activated smart material, it is essential to start by a thermal study in order to define certain experimental parameters: electric power and duration of heating and cooling. Figure 4.3 shows two examples of steady temperature fields: in Fig. 4.3-a, an intensity of 3A was applied in SMA1, 3 and 5 (corresponding to Configuration #41 in Fig. 2.7, Chapter 2) and in Fig. 4.3-b different intensity values were applied in SMA1, 3 and 5 (respectively 1A, 2A and 3A). Both temperature maps are here displayed yielding the maximum value of the color scale to 50°C and 30°C, respectively, in order to better visualize the temperature of the environment of the wires. Indeed, it can be observed that the parts connected to the wires were also heated by conduction. This is clearly visible for the mobile platform: in Fig. 4.3-b, the sizes of the three "hot zones" in the mobile

platform are different as a consequence of the different current intensities in the three SMA wires.

It can be noted that the temperature in the SMA wires for an amperage of 3A is higher than 50 °C, which is therefore higher than the Austenite-finish temperature of the SMA (A_f = 36°C, see Section 2.3.2). On the contrary, an amperage of 1A leads to a temperature lower than A_f (see the 1A wire in Fig. 4.3-b), which is not enough to obtain a full return to austenite.

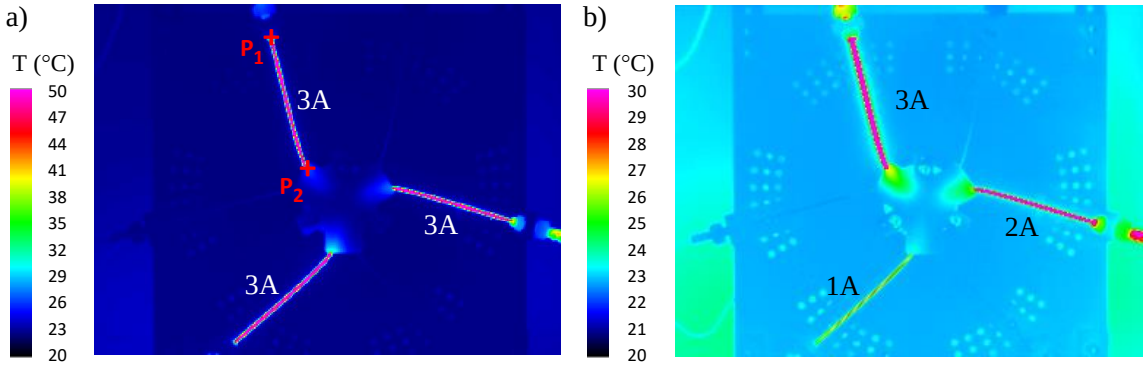

Figure 4.3. Thermal analysis: a) example of steady temperature field for an intensity of 3A in SMA1, 3 and 5; b) same for other intensity values. Note that temperature maps in a and b are yielded to 50°C and 30°C respectively.

To get further information, we followed the thermal response of SMA5 wire between its two attachment points P_1 et P_2 (see Fig. 4.3-a): see Figure 4.4. In Fig. 4.4-a, we were interested in the temperature distribution along the wire for four different amperage values: 1A, 2A, 3A and 4A. As expected, the temperature is maximum in the central part of the wire and lower at the edges due to heat conduction in the tightening systems at the two ends of the wire. It can be also noted that the temperature drops a little more towards point P_2 than towards point P_1. This can be explained by the material that surrounds the wire at point P_2, which is the copper of the domino (a good thermal conductor) compared to the Celeron at point P_1 (a thermal insulator). This non-homogeneity of temperature is important to consider in the thermal activation of a SMA wire to be completely transformed to austenite.

It is also important to define the time needed for a thermal actuation to reach a steady state (both for heating and return to ambient temperature). Fig. 4.4-b shows the time evolution of the maximum temperature measured along the SMA wire. It can be seen that after 3 minutes the temperature is stabilized during both heating and cooling. In the following experiments, the duration for heating and cooling stages was fixed to 3 minutes.

Finally, Fig.4.4-c shows the behaviour of the temperature in the SMA wire as a function of the applied electric intensity. The quadratic trend was expected from the Joule law. From this graph, we extract two “hot” temperature values for the test campaign: 88°C and 105°C, corresponding respectively to an intensity of 3A and 3.5A. These temperature values will be also used to run the numerical model (“hot” temperature referred to as T_1 in Chapter 2) for comparison purpose with the experiments.

Next, several experimental cases taking into consideration the conclusions of the preliminary thermal analysis are presented in the next section.

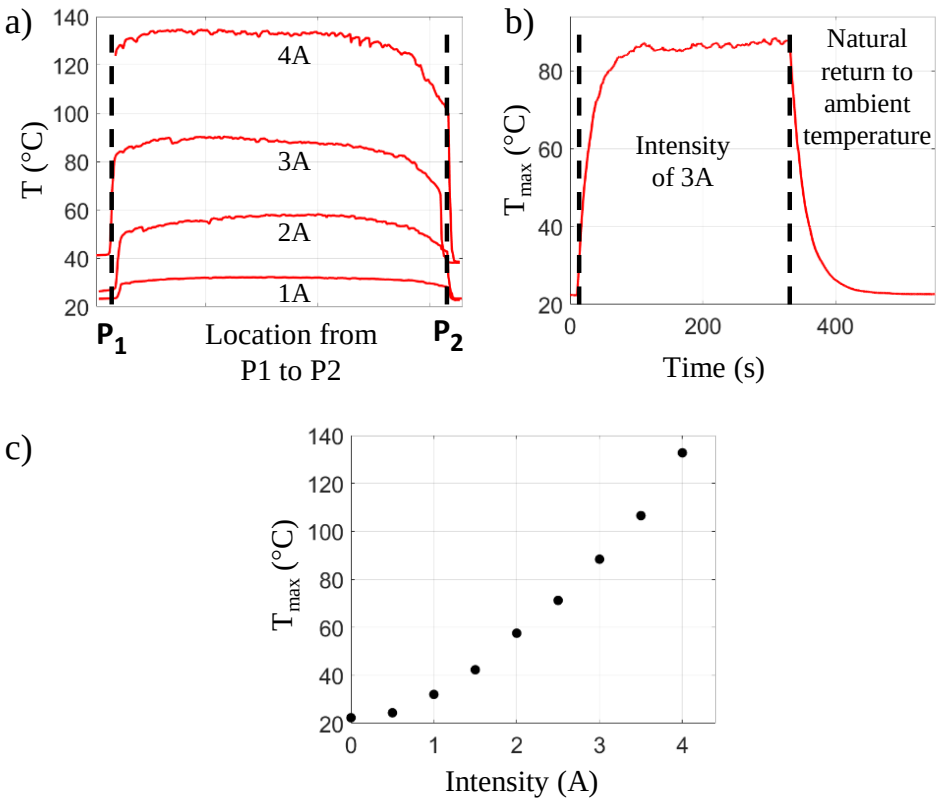

Figure 4.4. Thermal analysis: a) steady temperature profiles along the SMA5 wire, b) time evolution of the maximum temperature, c) maximum steady temperature vs. intensity.

4.3. Experimental cases of cyclic rotation and translation

Previously, Section 2.4.4 in Chapter 2 presented a numerical study about the creation of a cyclic movement of the mobile platform through the cases of "pure rotation” and “pure translation”. Thus, in this section, we will approach these two specific cases experimentally and discuss the obtained results.

4.3.1. Cyclic rotation

By alternating Configurations #41 (heating of SMA wires 1, 3 and 5 to generate a clockwise rotation) and #42 (heating of SMA wires 2, 4 and 6 to generate a counterclockwise rotation) with intermediate returns to ambient (Configuration #1), a cyclic pure rotation is a priori created. Figure 4.5-a illustrates the thermal activation sequence. After several preliminary tests (not reported here), a specific configuration was considered for the analysis. Figure 4.5-b shows the experimental variation in rotation angle θ_z with six cycles for $L = 190$ mm, $\alpha = 90°$ and $\varepsilon_{pre} = 1.6\%$. Angle values were extracted manually from the pictures taken in steady thermal state (i.e. after a waiting time of 3 min). It can be noted that from the fourth cycle onwards, the rotation values have stabilized reaching a maximum rotation amplitude of $(\Delta\theta_z)_{max} = 4.2°$. The rotation amplitude taking into account the intermediate returns to ambient temperature is equal to $(\Delta\theta_z)_{min} = 2.2°$. The movement of the moving platform for the sixth cycle (step 23-26) is illustrated in Figure 4.5-c. It can be noted that the angle evolution is in good qualitative agreement with the numerical results in Fig. 2.12-b. Quantitatively, two discrepancies can be noted:

- the rotation evolution is not "centered around zero" contrary to the simulation results: e.g. the absolute value of θ_z at step 23 is much lower than the value at step 25; same upon cooling at steps 24 and 26 (θ_z is at step 24 is even nearly equal to zero...). This "drift" is difficult to explain. General remarks about the difficulties in performing the experiments will be given in the conclusion section of this chapter.
- the $(\Delta\theta_z)_{max}/(\Delta\theta_z)_{min}$ ratio is higher in the simulation than in the experiment.

As the amplitude of movement depends on the initial prestrain ε_{pre} of the SMA wires, Figure 4.6 compares two angle evolutions as a function of time using two prestrain values: 1.6% and 3%. For the two experiments, we used the Configuration #41 (corresponding to step 3 in Fig. 4.5-b) with return to ambient temperature (corresponding to step 4 in Fig. 4.5-b), capturing images all along the time. The magnitude of the angle reached 3° and 4.8° upon heating and 2.2° and 3.7° upon cooling, for $\varepsilon_{pre} = 1.6\%$ and 3% respectively. As expected, the higher the prestrain value, the higher the steady rotation, both upon heating and upon cooling.

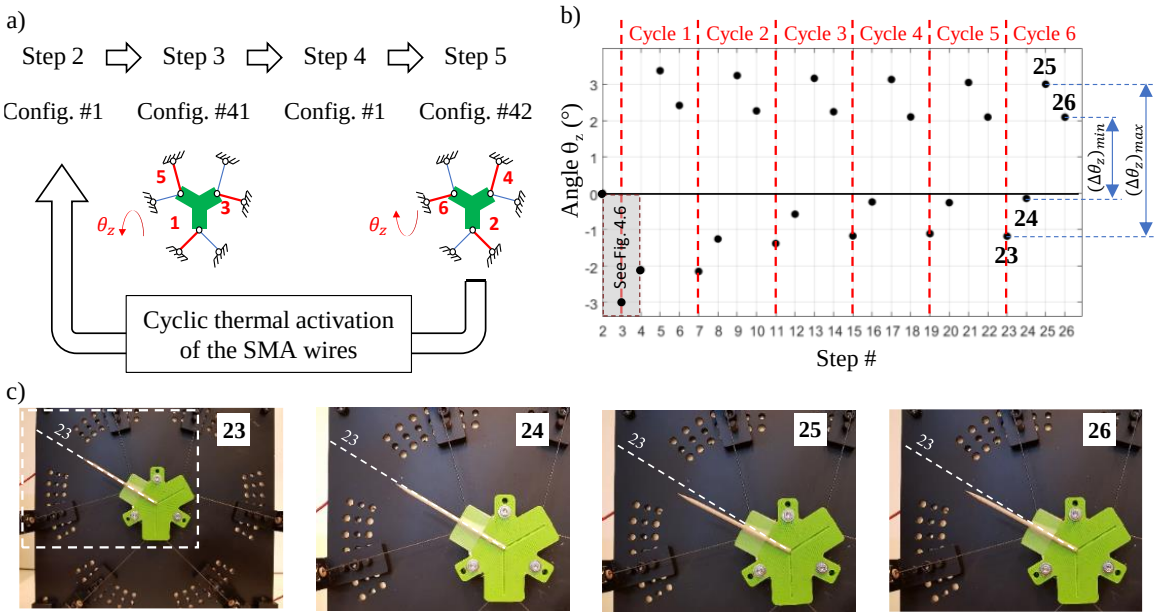

Figure 4.5. Creation of a cyclic rotation for $\alpha = 90°$, $L = 190$ mm and $\varepsilon_{pre} = 1.6\%$: a) thermal activation sequence considered, b) variation in rotation θ_z in each step, c) movement of the moving platform for the sixth cycle.

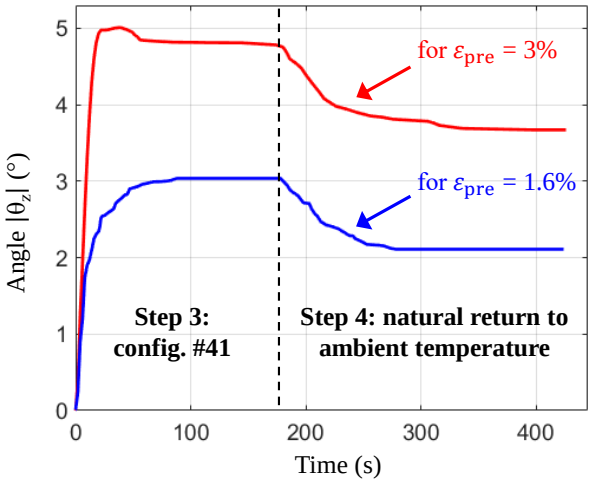

Figure 4.6. Comparison of two levels of SMA pre-strain ε_{pre} for $\alpha = 90°$ and $L = 190$ mm: time evolution of the absolute value of the rotation angle θ_z from Step 2 to Step 4.

The curve for ε_{pre}=1.6% is nicely monotonous upon heating and upon cooling. On the contrary the curve for ε_{pre}=3% presents a small "drop" upon heating before reaching a steady state. This could be related to non-linear structural deformations (well known elastic energy storage/release effect e.g. in concentric tubes). It may also be due to the clearance in the assembly which appears from certain configurations far from equilibrium. Using the same experimental parameters, the numerical simulations were resumed. Comparing with the

simulation results, it turns out that the experimental rotation magnitudes are close to the numerical values for 3% of prestrain: 4.8° and 3.7° at steps 3 and 4 respectively in the experiment, to be compared with 4.5° and 3.9° respectively in the simulation. For 1.6% of prestrain, the experimental rotation magnitudes are much higher than the numerical values: 3° and 2.1° at steps 3 and 4 respectively in the experiment, to be compared with 1.8° and 1.6° respectively in the simulations.

4.3.2. Cyclic translation

Unlike cyclic rotation, which can only be generated using two configurations #41 and #42, cyclic translation can be obtained using several configurations, for instance (#8; #43), (#9; #11), (#10; #12), etc.

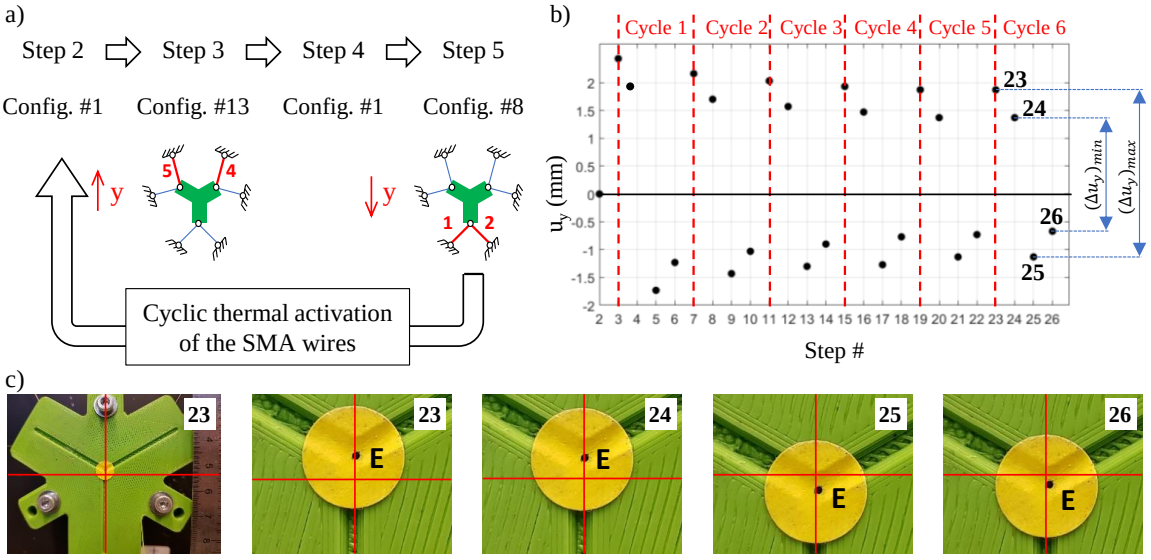

Figure 4.7. Creation of a cyclic translation for $\alpha = 60°$, $L = 190$ mm and $\varepsilon_{pre} = 1.6\%$: a) thermal activation sequence considered, b) variation in displacement u_y in each step, c) movement of the moving platform for the sixth cycle.

For the experimental case, we chose to alternate Configurations #8 and #13 with intermediate returns to ambient temperature in order to create a cyclic pure *vertical* translation. The thermal activation sequence followed in this experiment is illustrated in Fig. 4.7-a. Figure 4.7-b shows the variation in displacement amplitude u_y for six cycles for $L = 190$ mm, $\alpha = 60°$ and $\varepsilon_{pre} = 1.6\%$. Similar to the case of cyclic rotation, it can be noted that the behavior of SMA wires stabilizes from the fifth cycle onwards. The translation has stabilized reaching a maximum rotation amplitude of $(\Delta u_y)_{max} = 3$ mm. The translation amplitude when the SMA wires return to ambient temperature is equal to $(\Delta u_y)_{min} = 2$ mm. Figure 4.7-c illustrates the movement of the mobile platform for the sixth cycles (step 23-26). The same

comments as for the cyclic pure rotation can be drawn, except that the qualitative results are much better:

- the "drift" over the cycles is coherent, as a logical consequence of an "attraction" effect of the first activation (#13). See next section about his effect;
- the $(\Delta U_y)_{max}/(\Delta U_y)_{min}$ ratio is similar to that of the simulations (compare with Fig. 2.13-b).

4.4. Discrete workspace and attraction effect

Above, particular cases of thermal actuation were presented. The present section discusses case studies that are more general, involving the 64 possibilities of thermal activation. It must be noted that between the previous cases of studies (Sections 4.3.1 and 4.3.2) and the following ones, other experiments were performed. In Appendix B, one of those case studies was presented through a conference paper.

4.4.1. Discrete workspace

Resetting the mechanism to the reference position, i.e. to ($u_x = 0$, u_y =0, θ_z = 0), is quite delicate. It would require the resumption of the whole preparation steps (removing the SMA wires from the mechanism, heating to initialize to austenite, tightening the SMA wires in the dominos using the specific procedure in Fig. 3.11 in Chapter 3, placement in the mechanism and pre-stretching to a certain prestrain of ε_{pre}), which is a heavy and time-consuming task. That would be also not relevant from a practical point of view. Since the system control that would allow a quick reset procedure is not yet available at this stage of experimentations, we have chosen a simple initialization approach: we proceed by heating the six wires at the same time on the mechanism (corresponding to Configuration #64), assuming that no plasticity occurs when they all transform to austenite.

Figure 4.8-a illustrates the thermal actuation sequence used to generate the workspace of the 64 distinct configurations. The parameters used for this experiment are α = 60°, L = 170 mm and ε_{pre} =3.25%. Figure 4.8-b displays the different positions of the mobile platform, where each point in the graph is defined by the in-plane translation (u_x,u_y) of point E and the rotation θ_z of the mobile platform. Figure 4.8-c presents the projection of the points onto plane (u_x, u_y) and Figure 4.8-d gives the values for the rotation θ_z only. Numbers in Fig. 4.8-c and Fig. 4.8-d refer to the configuration numbers provided in Fig. 2.6 in Chapter 2. The first thing to notice is that the amplitudes of movement are small compared to

numerical results presented in Fig. 2.8. This may be explained by the fact that the returns to reference position between the tests are not perfect. Second, qualitative results are in fair agreement with the simulation results in Fig. 2.8 in Chapter 2. However, some configurations that theoretically have a pure translation (like Configurations #9 and #13) exhibit a non-null rotation. Also, Configuration #42 that theoretically has a pure rotation exhibits a non-null translation. Then, errors related to the assembly of the mechanism, to the extraction of the movement values and to the operator led to uncertainties. As indicated above, general remarks about the difficulties in performing the experiments will be given in the conclusion section of this chapter. Anyway, for better results the control is a needed step.

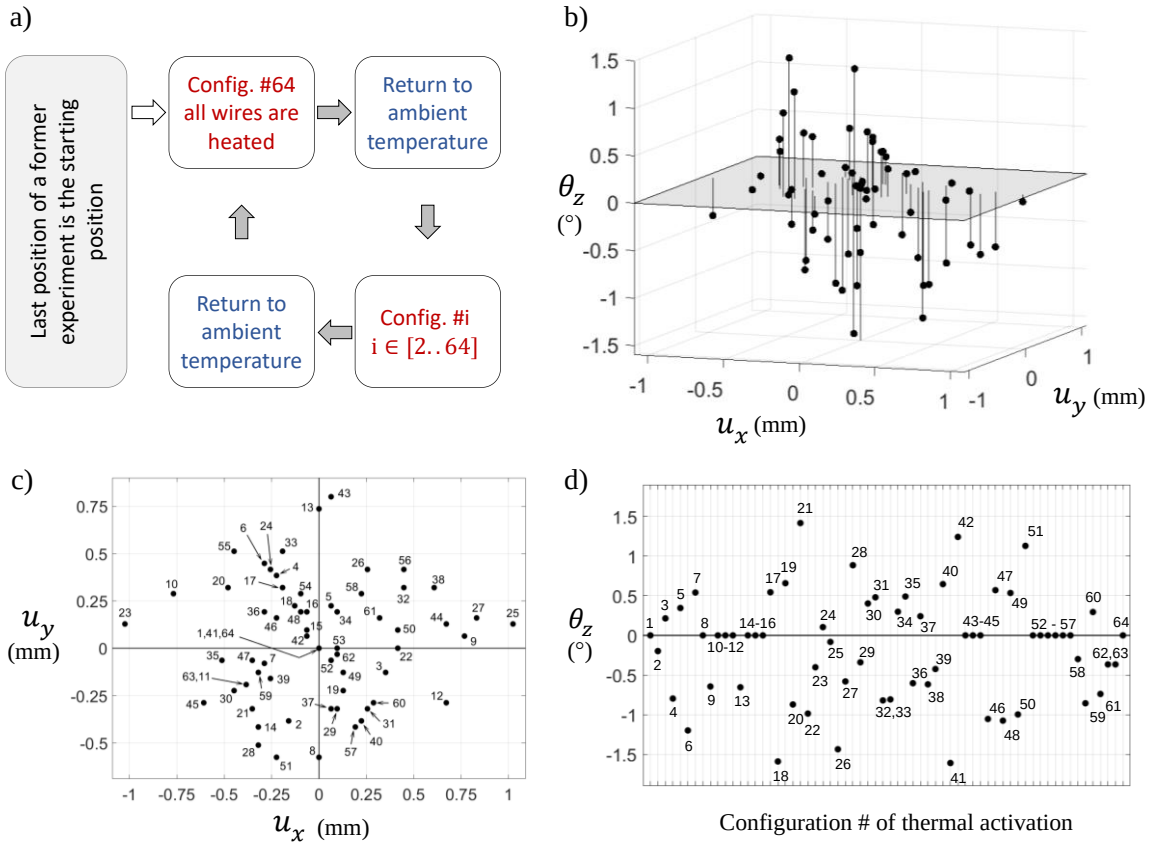

Figure 4.8. Workspace for $\alpha = 60°$, $L = 170$ mm and ε_{pre} =3.25%: a) thermal actuation sequence, b) movement of the mobile platform for different heating configurations, c) same in projection onto plane (u_x,u_y), d) rotation θ_z of the platform.

4.4.2. Evidence of attraction effect

In the previous section, it was noted that a non-perfect reset to the reference position (u_x=0, u_y=0, θ_z=0) may have led to differences between the experimental discrete workspace in Fig. 4.8 and its theoretical expectation such as in Fig. 2.8 in

Chapter 2. The inheritance of the previous thermal activation steps can be seen as an "attraction" effect, which was also evidenced from simulations in Section 2.4.5 in Chapter 2. The parameters of the proposed experiment are $\alpha = 60°$, $L = 190$ mm and $\varepsilon_{pre} = 1.6\%$.

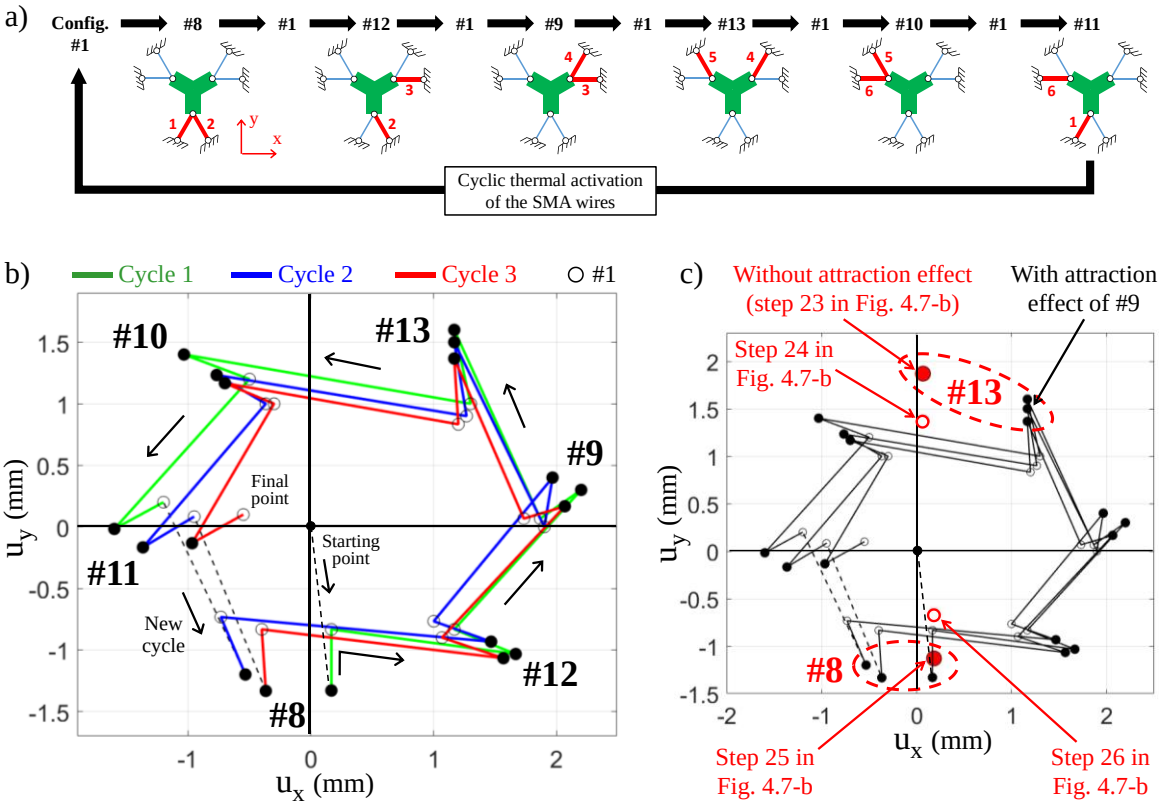

Figure 4.9. Evidence of the attraction effect (for $\alpha = 60°$, $L = 190$ mm and $\varepsilon_{pre} = 1.6\%$): a) thermal activation sequence considered, b) in-plane translation of point E of the mobile platform, c) comparison with the results in Fig. 4.7-b (steps 23 to 26).

Figure 4.9-a presents the thermal activation sequence considered for this case of study: the sequence involves 2 *adjacent* wires in each thermal activation, rotating (see red wires in Fig. 4.9-a). Note that each time two adjacent SMA wires are activated, they return to ambient temperature afterwards (Configuration #1). Three cycles were performed, starting from Configuration #8. Figure 4.9-b shows the in-plane translation of point E of the mobile platform corresponding to thermal activation sequence in Fig. 4.9-a. It can be recalled that Configurations #8 and #13 corresponded to pure *vertical* translations ($u_x \approx 0$) in Fig. 4.7-b in Section 4.3.2, due to the initialization of the system before applying these two thermal activations. Figure 4.9-c shows the comparison with these previous results at Steps 23 to 26 in Fig. 4.7-b (for which $u_x \approx 0$). For the present experiment, it can be seen that the three configurations #13 led to $u_x \neq 0$. This is a consequence of the

preceding thermal activations, namely Configurations #9, which themselves were attracted by preceding thermal activations #12, which themselves were attracted by preceding thermal activations #8, etc. The situation is the same for the configurations #8, except for the first one giving $u_x \approx 0$ because it was the first thermal activation of the sequence. It can be concluded that any previous configuration attracts to it the following configurations (in particular the next one).

Figure 4.10 presents the experimental results corresponding to the thermal activation sequence that was tested in Fig. 2.14 in Chapter 2, aiming at evidencing the attraction effect of Configuration #24 in Step 3 on subsequent steps. Figure 4.10-a recalls the sequence.

[*Results in Fig. 4.10-b and -c will be available in the oral defence of the thesis and added in the final version of the manuscript, due to practical constraints in the experimental facilities given the sanitary state*].

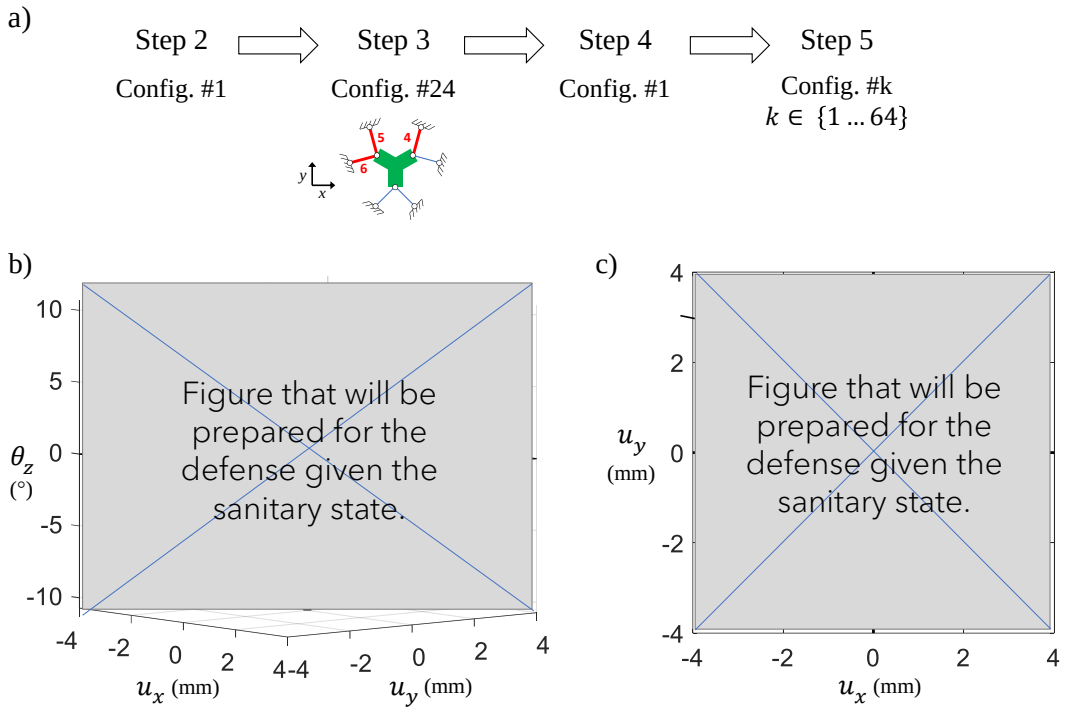

Figure 4.10. Evidence of an attraction effect: a) thermal activation sequences considered to observe the effect of Configuration #24 in Step 3 on subsequent steps, b) and c) same plot as Figures 4.8-a and -b.

4.5. Example of a “complex” thermal sequence and stiffness variability

4.5.1. Example of a complex thermal sequence

Earlier in this chapter, we considered several simple cases of thermal activation sequences. We dealt with cyclic pure rotation, cyclic pure translation and then the 64 configurations separately. The present section discusses a more complex thermal actuation sequence that contains different configurations. The sequence actually corresponds to that used in Section 2.5, Fig. 2.16 in Chapter 2, namely:

[#1→#24→#1→#16→#1→#6→#1→#10→#1].

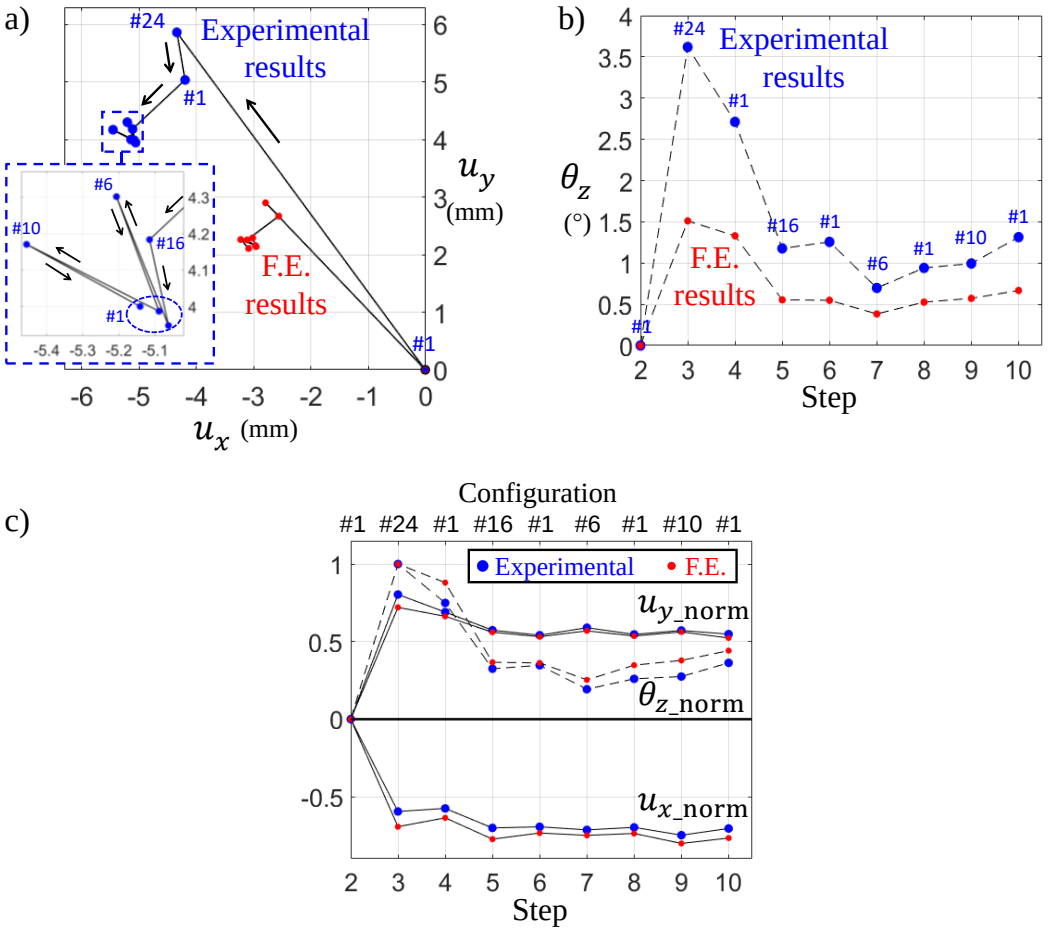

Figure 4.11. Example of a thermal activation sequence for $\alpha = 90°$ and $\varepsilon_{pre} = 3.5\%$: a) movement in the plane (u_x, u_y), b) variation in angle θ_z c) normalized experimental and F.E. results.

The parameters used in this experiment are $\alpha = 90°$, $L = 170$ mm, $\varepsilon_{pre} = 3.5\%$ and $T_1 = 105$ °C. Figure 4.11 displays the experimental and the F.E. results in terms of mobile platform movement.

Figures 4.11-a and -b compare the in-plane (u_x, u_y) translation and the angle θ_z respectively between the experiment and the simulation. Quantitative results appeared to be strongly different: the experimental values are much higher than the FE results in terms of magnitude. However, experimental and simulated results appear to feature the same behavior and the path shape along the thermal activation sequence. To have a clearer idea, we proceeded by normalizing the results. Figure 4.11-c displays the data *normalized* with respect to the maximum translation magnitude for u_x and u_y, and to the maximum rotation magnitude for θ_z, i.e. dividing by $\sqrt{{u_x}^2 + {u_y}^2}$ and θ_z respectively at step 24. It appeared than the experimental and simulated results are nearly similar once normalized. The difficulty in applying the prestrain to the SMA wires may explain the difference without normalization.

4.5.2. Stiffness variability

Section 2.4.5 in Chapter 2 presented a numerical evidence of the variable stiffness of the system as a function of the thermal sequence applied, even for close platform positions. The present section aims at evidencing experimentally this concept.

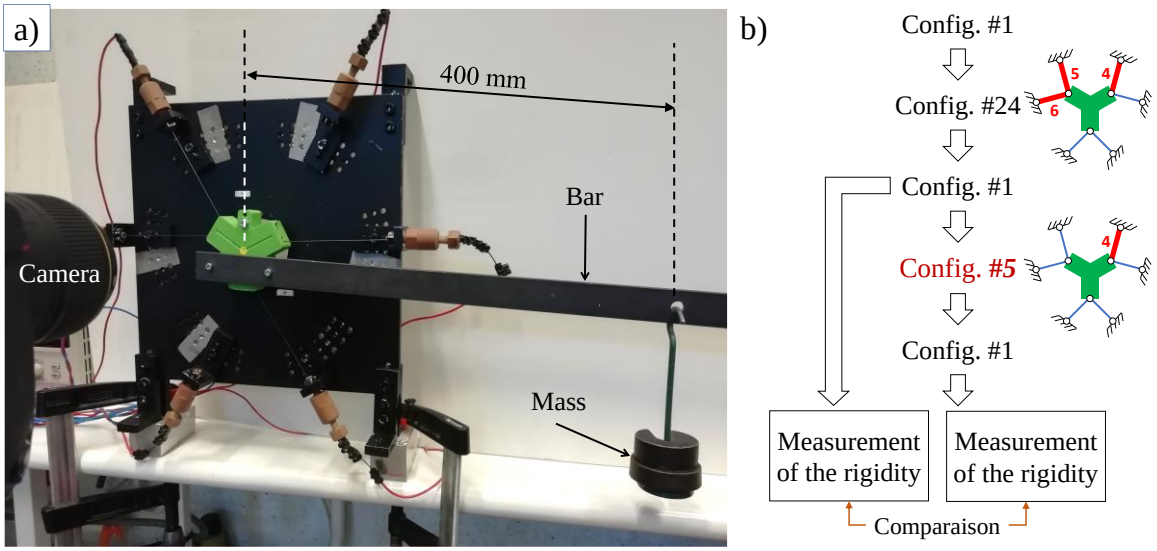

Figure 4.12. Stiffness variability trial: a) experimental setup, b) two thermal actuation sequences before measuring the stiffness.

Figure 4.12-a shows the experimental setup in which a steel bar that weighs 0.627 kg is fixed on the moving platform. Added masses can be then suspended at a distance of 400 mm from the center of the moving platform. Figure 4.12-b presents the two thermal activation sequences considered for this analysis. The aim is to compare the stiffness between two sequences leading to nearly the same position of the mobile platform:

- the first sequence is [#1→#24→#1]. It was named "Ref." in Table 2.7 in Chapter 2;
- the second is [#1→#24→#1→#5→#1].

Figure 4.13 shows the evolution of component $K_{\theta\theta}$ of the stiffness matrix by applying several masses for both thermal activation sequences. Table 4.1 gives the rotational stiffness values obtained numerically and experimentally through the application of a mass corresponding to 2 N (greater masses leads to too large platform translations to compare the stiffness measurements). Experimentally, the reference value (Configuration #24 only) is equal to 85 kN.mm.rad^{-1} whereas the sequence #24+#5 exhibits 143 kN.mm.rad^{-1}, thus highlighting a stiffness variability. As in simulation, the stiffness is higher after sequence #24+#5 (181 kN.mm.rad^{-1}) than after Configuration #24 only (109 kN.mm.rad^{-1}).

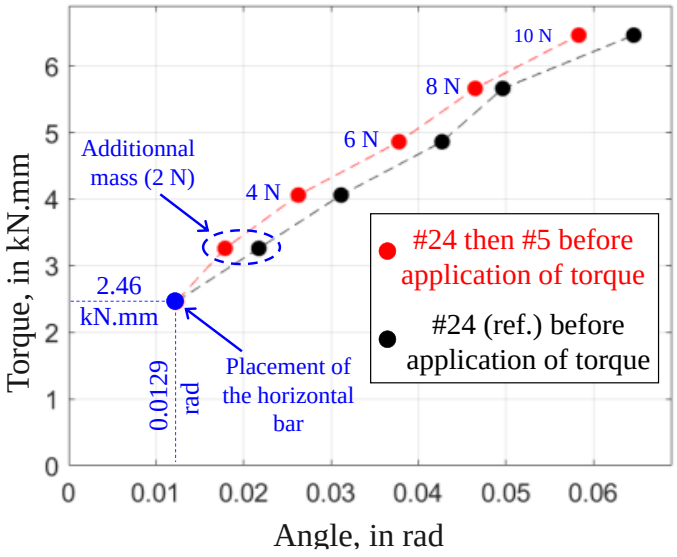

Figure 4.13. Measurement of stiffness for two heating actuations (for $\alpha = 60°$, $L = 170$ mm and $\varepsilon_{pre} = 3.25\%$), see Figure 4.12-b.

Heating sequence	$(K_{\theta\theta})_{num}$ [kN.mm.rad^{-1}]	$(K_{\theta\theta})_{exp}$ [kN.mm.rad^{-1}]
#1→#24→#1→#5→#1	181	143
#1→#24→#1 (Ref.)	109	85

Table 4.1. Evidence of stiffness variability through both simulation and experiments. $K_{\theta\theta}$ was obtained by applying a mass of 2 N on the bar in Fig. 4.12-a.

4.6. Conclusion

During this research work, we were interested in exploring a concept of *prestressed* mechanism driven by *multi-antagonistic* SMA wires. Since the best way to gain knowledge is to experiment, in this chapter we have tested several study cases that led to the identification of certain limitations and constraints using a physical demonstrator.

The experiments reported in this chapter are only a selection among several experiments carried out. The process was not easy. It must be recalled that the time needed to position the SMA wires in the mechanism and to prestrain them before thermal actuation is considerably long. Moreover, the huge number of heating configurations leads to long duration of experiments. Also, extracting the data from the images captured by a camera in steady thermal states and transforming it into graphs require a long time before analyzing the results. As a result, we chose to make do with experiments that address the "general" concepts identified in the numerical study in Chapter 2.

We studied several cases of activation: simple thermal actuation sequences leading to cyclic pure rotation and translation movements, thermal actuation using the 64 possible heating to build the discrete workspace, and a "complex" thermal sequence (that was tested in the Chapter 2). Also, we were able to experimentally evidence the attraction effect of a previous configuration on a current one. Moreover, we showed a stiffness variability of the mechanism depending on the thermal activation sequence.

Comparing the experimental results to the numerical results by F.E methods (see Chapter 2), we observed a fair qualitative agreement. But quantitatively the trends are sometimes different. Generally, we obtain a similar behavior and shape, but different magnitudes. As a general comment, applying a prestrain in SMA wires remains a delicate point in experiments, which may explain the discrepancy with the simulations. As discussed in the conclusion chapter, two points could help in

improving the concept of prestressed mechanism driven by multi-antagonistic SMA components:

- changing the SMA wires into SMA *springs* with much lower stiffness. Indeed, the strong stiffness of wires makes the prestrain difficult to apply. Considering the large displacement magnitude of SMA springs should help in applying correctly the prestrain;
- through the performed experiments, the need of a control of the mechanism was evidenced. Indeed, initialization the mobile platform to the reference configuration is delicate to perform without control. A preliminary work about the control of the studied mechanism is presented in Appendix B.

"There are two types of PhD thesis: perfect and submitted." — Unknown

Conclusions and perspectives

Conclusions

The primary focus of this doctoral thesis was to study and explore a pre-stressed mechanism actuated by *multi-antagonistic* SMA wires with several DOFs. Starting with the state of art, conducting a numerical study, designing a prototype, and then experimenting it led to several conclusions, which are recalled bellow

Before tackling the core of the thesis, chapter 1 highlighted the must-knows about SMAs from their thermomechanical behaviors to their possible applications in engineering. In this thesis, we were interested in SMA-based mechanisms and actuators using the shape-memory effect feature. Considering the provided motion, SMA actuators can be classified into three groups: linear, revolute and multi-DOF actuators. Moreover, the first chapter addressed various design architectures of the arrangement of the SMA components. It pointed out the lack of understanding in of *multi-antagonistic* response of multi-DOFs mechanisms driven by SMAs. Hence, in this thesis, we decided to study a parallel planar pre-stressed mechanism actuated by six SMA wires where each wire is allowed to be thermally activated individually. In order to better investigate the behavior of such mechanism, we conducted a finite element analysis (presented in chapter 2) using the Auricchio's thermo-mechanical model for the SMA behavior implemented in Ansys. In the numerical study, we set general concepts to prove through several cases of study that are given below. With six wires, we obtain 64 thermal activation configurations when considering a *binary* thermal actuation of each SMA wire (namely a fixed ambient temperature and a fixed higher temperature reachable experimentally by the Joule effect). By referring to these configurations, we were able to study various movements of the mobile platform, including cyclic pure rotation and cyclic pure translation. We quantified the dependency of the movement of the mechanism on the SMA pre-strain value and the angles between the SMA wires. The studied mechanism featured a small translation workspace but a quite better angular stroke. We demonstrated the possibility to reach a certain position and the stiffness variability of the mechanism. The important result in chapter 2 is the analysis

of an "attraction" effect of any heating configuration on its following one along a thermal activation sequence. This effect is complex as it results from the *multi-antagonistic* and *hysteretic* response of the actuation. It is the key point for the development of such type of mechanism involving several SMA components acting in interaction.

Since the only way to pass from numerical to practical is through a prototype, chapter 3 presented the process of the design and manufacturing of a physical demonstrator. Because thermal and electrical insulations are crucial to ensure a good performing mechanism, the choice of the materials was thoughtfully considered. The preliminary mechanical training process of the SMA wires, which ensure better accuracy and repeatability of the actuation, was highlighted. The important result in chapter 3 is the proposition of a procedure of tightening of SMA wires at their two ends. This procedure was made possible thanks to the specific transformation temperatures of the SMA wires with respect to the ambient temperature.

After building the prototype, we carried out several experiments. It must be recalled that the preparation steps of the SMA wires and the measurements are long: mechanical training requiring numerous thermo-mechanical cycles; tightening with the specific thermomechanical procedure; huge number of thermal activations (recall the 64 configurations) with required waiting times to reach thermal equilibrium. Certain results required several days of test preparation, weeks of measurement by camera, and time for data extraction before starting the analysis. We reproduced some heating sequences that were previously performed in the simulations. The important result in chapter 4 is the confirmation of the "attraction" effect, as well as the evidence of unavoidable discrepancies between experiments and simulations (see the perspectives). We proved the fact that unless we reset the system, a heating configuration is attracted by the former configuration. Results were qualitatively in fair agreement with the expectations, but some of them were quantitatively far from the simulated ones.

Finally, let us note that the studied mechanism could find potential applications as an end effector, manipulator, micro positioning or micro robotics for applications requiring long-term and stable positioning at ambient temperature. In the following section, some perspectives are presented that may improve the research work.

Perspectives

To improve the concept of prestressed mechanism driven by multi-antagonistic SMA components, two main changes can be proposed based on the problems identified in the experimental part of the work:

1) establishing the control of the mechanism — This will allow the reset of the system when needed and the possibility to perform a continuous motion. An automatic method of extracting the platform movement from the images should be also developed. For this purpose, an electronic board is needed to monitor and control the temperature evolution in real time and thus the deformation of the wires. This board will be connected to the power supplies. The software Labview can be used to control the current intensity, which allows a better precision of the activation,
2) replacing the SMA wires by SMA "springs", more precisely by SMA components with larger strokes and lower stiffness than wires — (Figure 5.1 illustrate the idea). This will reduce the uncertainty in the initial placement and the pre-straining of the SMA components. More generally, using SMA springs should solve many technical problems (tightening, initialization, manual manipulations by the operator...), However, by construction, the mechanism will be much less rigid and will be *a priori* dedicated to applications in soft robotics. In particular, a highly flexible mobile platform could be considered, using for instance rubber-like materials: see figure below. It must be noted that such a mechanism including hyper-elastic material could be "simply" implemented in the numerical model proposed in the present work. Indeed, using a commercial FE package (as done in the present work) opens the possibility of model complex materials and behavior.

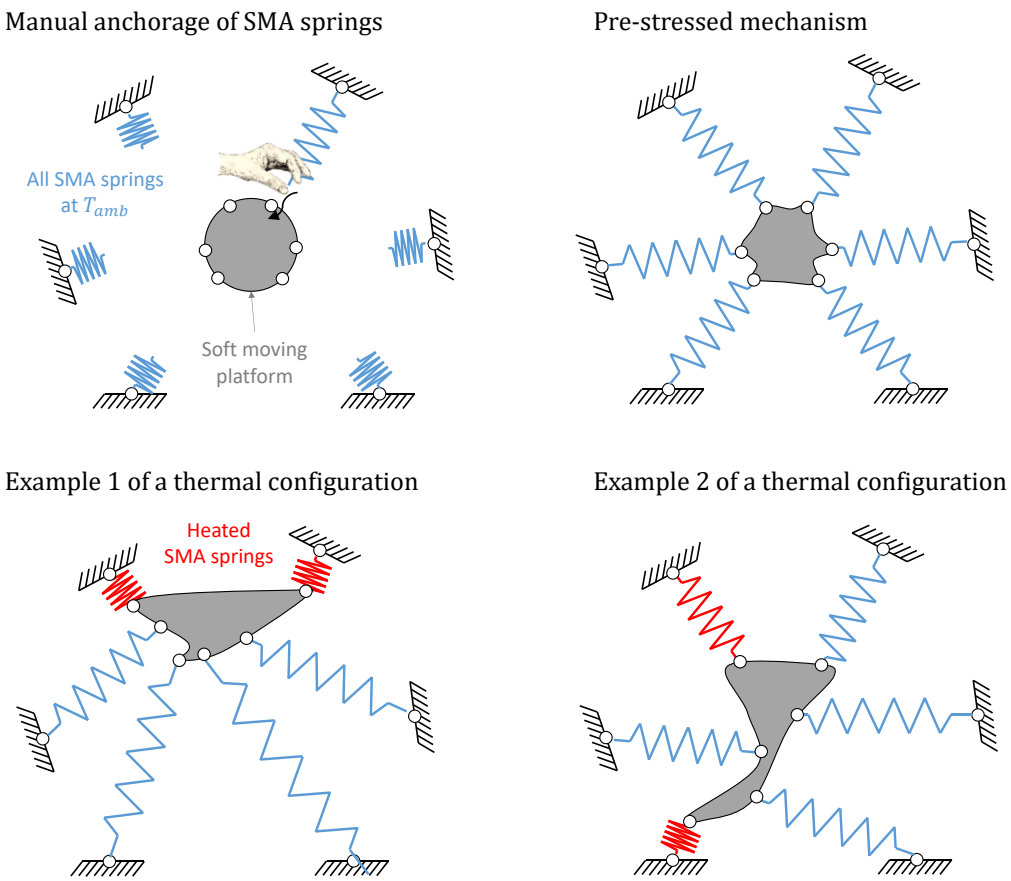

Figure 5.1. Proposed solutions for future work, using soft components.

"So many books, so little time." — Frank Zappa

Bibliography

[1] M. V. Gandhi et B. D. Thompson, *Smart Materials and Structures*. Springer Science & Business Media, 1992.

[2] Z. X. Khoo *et al.*, « 3D printing of smart materials: A review on recent progresses in 4D printing », *Virtual Phys. Prototyp.*, vol. 10, nº 3, p. 103-122, juill. 2015, doi: 10.1080/17452759.2015.1097054.

[3] M. M. Schwartz, Éd., *Encyclopedia of smart materials*. New York: J. Wiley, 2002.

[4] J. M. Jani, M. Leary, A. Subic, et M. A. Gibson, « A review of shape memory alloy research, applications and opportunities », *Mater. Des.*, vol. 56, p. 1078-1113, 2014.

[5] M. M. Kheirikhah, S. Rabiee, et M. E. Edalat, « A Review of Shape Memory Alloy Actuators in Robotics », in *RoboCup 2010: Robot Soccer World Cup XIV*, vol. 6556, J. Ruiz-del-Solar, E. Chown, et P. G. Plöger, Éd. Berlin, Heidelberg: Springer Berlin Heidelberg, 2011, p. 206-217.

[6] H. Tran, X. Balandraud, et J.-F. Destrebecq, « Curvature effect on the mechanical behaviour of a martensitic shape-memory-alloy wire for applications in civil engineering », *Smart Mater. Struct.*, vol. 24, nº 2, p. 025025, janv. 2015, doi: 10.1088/0964-1726/24/2/025025.

[7] A. Debska, X. Balandraud, J.-F. Destrebecq, P. Gwozdziewicz, et A. Seruga, « Influence of Thermal Boundary Effects on the Process of Creating Recovery Stresses in a SMA Wire Activated by Joule Heating », *J. Mater. Eng. Perform.*, vol. 26, nº 7, p. 3336-3346, juill. 2017, doi: 10.1007/s11665-017-2732-5.

[8] H.Tran, A. Debska, X. Balandraud, J. Destrebecq, « Use of shape memory alloys wires for the creation of prestress states in concrete beams », *Annales du Bâtiment et des Travaux Publics*, Edition Eska, vol. 1, pp. 41- 46, 2011.

[9] A. Waibaye, X. Balandraud, et J.-F. Destrebecq, « Création de structures à précontrainte adaptative à base d'alliages à mémoire de forme », Bayonne, France, mai 2015

[10] H. Yuan, X. Balandraud, J. C. Fauroux, et F. Chapelle, « Compliant Rotary Actuator Driven by Shape Memory Alloy », in *New Advances in Mechanisms, Mechanical Transmissions and Robotics*, Springer, Cham, 2017, p. 343-350.

[11] H. Yuan, F. Chapelle, J.-C. Fauroux, et X. Balandraud, « Concept for a 3D-printed soft rotary actuator driven by a shape-memory alloy », *Smart Mater. Struct.*, vol. 27, nº 5, p. 055005, mars 2018, doi: 10.1088/1361-665X/aab56f.

[12] A. Mekaouche, F. Chapelle, et X. Balandraud, « A compliant mechanism with variable stiffness achieved by rotary actuators and shape-memory alloy ». Meccanica 53, 2555–2571 (2018). doi:10.1007/s11012-018-0844-0

[13] J. Mohd Jani, M. Leary, et A. Subic, « Designing shape memory alloy linear actuators: A review », *J. Intell. Mater. Syst. Struct.*, p. 1045389X16679296, 2016.

[14] H. Yuan, J. Fauroux, F. Chapelle, et X. Balandraud, « A review of rotary actuators based on shape memory alloys », *J. Intell. Mater. Syst. Struct.*, vol. 28, n° 14, p. 1863-1885, août 2017, doi: 10.1177/1045389X16682848.

[15] M. Salerno, K. Zhang, A. Menciassi, et J. S. Dai, « A Novel 4-DOF Origami Grasper With an SMA-Actuation System for Minimally Invasive Surgery », *IEEE Trans. Robot.*, vol. 32, n° 3, p. 484-498, juin 2016, doi: 10.1109/TRO.2016.2539373.

[16] A. M. Bertetto et M. Ruggiu, « A Two Degree of Freedom Gripper Actuated by SMA with Flexure Hinges », *J. Robot. Syst.*, vol. 20, n° 11, p. 649-657, nov. 2003, doi: 10.1002/rob.10114.

[17] E. L. White, J. C. Case, et R. Kramer-Bottiglio, « A Soft Parallel Kinematic Mechanism », *Soft Robot.*, vol. 5, n° 1, p. 36-53, déc. 2017, doi: 10.1089/soro.2017.0033.

[18] Dimitris C. Lagoudas, *Shape memory alloys: Modeling and Engineering Applications*. New-York, USA: Springer Science & Business Media, 2010.

[19] G. B. KAUFFMAN et I. MAYO, « The Story of Nitinol: The Serendipitous Discovery of the Memory Metal and Its Applications », *Chem. Educ.*, vol. 2, n° 2, p. 1-21, juin 1997, doi: 10.1007/s00897970111a.

[20] W. J. Buehler, J. V. Gilfrich, et R. C. Wiley, « Effect of Low-Temperature Phase Changes on the Mechanical Properties of Alloys near Composition TiNi », *J. Appl. Phys.*, vol. 34, n° 5, p. 1475-1477, mai 1963, doi: 10.1063/1.1729603.

[21] T. W. Duerig et K. Bhattacharya, « The Influence of the R-Phase on the Superelastic Behavior of NiTi », *Shape Mem. Superelasticity*, vol. 1, n° 2, p. 153-161, juin 2015, doi: 10.1007/s40830-015-0013-4.

[22] S. S. M. Prabu *et al.*, « Thermo-mechanical behavior of shape memory alloy spring actuated using novel scanning technique powered by ytterbium doped continuous fiber laser », *Smart Mater. Struct.*, vol. 28, n° 4, p. 047001, mars 2019, doi: 10.1088/1361-665X/ab06d8.

[23] S. S. Cheng, Y. Kim, et J. P. Desai, « Modeling and characterization of shape memory alloy springs with water cooling strategy in a neurosurgical robot », *J. Intell. Mater. Syst. Struct.*, vol. 28, n° 16, p. 2167-2183, sept. 2017, doi: 10.1177/1045389X16685443.

[24] A. Doroudchi, M. R. Zakerzadeh, et M. Baghani, « Developing a fast response SMA-actuated rotary actuator: modeling and experimental validation », *Meccanica*, juill. 2017, doi: 10.1007/s11012-017-0726-x.

[25] D. J. Hartl et D. C. Lagoudas, « Aerospace applications of shape memory alloys », *Proc. Inst. Mech. Eng. Part G J. Aerosp. Eng.*, vol. 221, nº 4, p. 535-552, avr. 2007, doi: 10.1243/09544100JAERO211.

[26] K. Wada et Y. Liu, « On the mechanisms of two-way memory effect and stress-assisted two-way memory effect in NiTi shape memory alloy », *J. Alloys Compd.*, vol. 449, nº 1, p. 125-128, janv. 2008, doi: 10.1016/j.jallcom.2006.01.128.

[27] M. J. Bigeon et M. Morin, « Thermomechanical study of the stress assisted two way memory effect fatigue in TiNi and CuZnAl wires », *Scr. Mater.*, vol. 35, nº 12, déc. 1996, doi: 10.1016/S1359-6462(96)00228-X.

[28] L. P. Chen et N. C. Si, « Influence of thermomechanical training deformations on TWSME in TiNiCu alloy spring », *J. Alloys Compd.*, vol. 448, nº 1, p. 219-222, janv. 2008, doi: 10.1016/j.jallcom.2006.10.109.

[29] H. Scherngell et A. C. Kneissl, « Generation, development and degradation of the intrinsic two-way shape memory effect in different alloy systems », *Acta Mater.*, vol. 50, nº 2, p. 327-341, janv. 2002, doi: 10.1016/S1359-6454(01)00342-1.

[30] L. Sun *et al.*, « Stimulus-responsive shape memory materials: A review », *Mater. Des.*, vol. 33, p. 577-640, janv. 2012, doi: 10.1016/j.matdes.2011.04.065.

[31] S. Kustov et J. Van Humbeeck, « Damping Properties of SMA », *Mater. Sci. Forum*, vol. 583, p. 85-109, mai 2008, doi: 10.4028/www.scientific.net/MSF.583.85.

[32] Y. Chen, H. C. Jiang, S. W. Liu, L. J. Rong, et X. Q. Zhao, « Damping capacity of TiNi-based shape memory alloys », *J. Alloys Compd.*, p. 5, 2009.

[33] D. Hartl, B. Volk, D. C. Lagoudas, F. Calkins, et J. Mabe, « Thermomechanical Characterization and Modeling of Ni60Ti40 SMA for Actuated Chevrons », in *Aerospace*, Chicago, Illinois, USA, janv. 2006, p. 281-290, doi: 10.1115/IMECE2006-15029.

[34] J. N. Kudva, « Overview of the DARPA Smart Wing Project », *J. Intell. Mater. Syst. Struct.*, vol. 15, nº 4, p. 261-267, avr. 2004, doi: 10.1177/1045389X04042796.

[35] B. Huett et C. Willey, « Design and Development of Miniature Mechanisms for Small Spacecraft », p. 14.

[36] S. Barbarino, E. S. Flores, R. M. Ajaj, I. Dayyani, et M. I. Friswell, « A review on shape memory alloys with applications to morphing aircraft », *Smart Mater. Struct.*, vol. 23, nº 6, p. 063001, 2014.

[37] S. Barbarino, R. Pecora, L. Lecce, A. Concilio, S. Ameduri, et E. Calvi, « A Novel SMA-based Concept for Airfoil Structural Morphing », *J. Mater. Eng. Perform.*, vol. 18, nº 5-6, p. 696-705, août 2009, doi: 10.1007/s11665-009-9356-3.

[38] S. Barbarino, R. Pecora, L. Lecce, A. Concilio, S. Ameduri, et L. De Rosa, « Airfoil Structural Morphing Based on S.M.A. Actuator Series: Numerical and Experimental Studies », *J. Intell. Mater. Syst. Struct.*, vol. 22, nº 10, p. 987-1004, juill. 2011, doi: 10.1177/1045389X11416032.

[39] R. Pecora, S. Barbarino, A. Concilio, L. Lecce, et S. Russo, « Design and Functional Test of a Morphing High-Lift Device for a Regional Aircraft », *J. Intell. Mater. Syst. Struct.*, vol. 22, n° 10, p. 1005-1023, juill. 2011, doi: 10.1177/1045389X11414083.

[40] Y. T. B. Tekap *et al.*, « Design of a Large-Scale High-Lift Morphing A320 Wing Based on Electro-Mechanical Actuators and Shape Memory Alloys », in *AIAA Aviation 2019 Forum*, American Institute of Aeronautics and Astronautics.

[41] A. Y. N. Sofla, S. A. Meguid, et K. T. Tan, « Novel morphing wing design using antagonistic shape memory alloy actuation », *Proceedings of the ASME 2010 International Mechanical Engineering Congress and Exposition.* Volume 1: Advances in Aerospace Technology. Vancouver, British Columbia, Canada. November 12–18, 2010. pp. 33-36. ASME. doi: 10.1115/IMECE2010-38851

[42] C. Bil, K. Massey, et E. J. Abdullah, « Wing morphing control with shape memory alloy actuators », *J. Intell. Mater. Syst. Struct.*, vol. 24, n° 7, p. 879-898, 2013.

[43] H. Basaeri, A. Yousefi-Koma, M. R. Zakerzadeh, et S. S. Mohtasebi, « Experimental study of a bio-inspired robotic morphing wing mechanism actuated by shape memory alloy wires », *Mechatronics*, vol. 24, n° 8, p. 1231-1241, 2014.

[44] J. Szewczyk, E. Marchandise, P. Flaud, L. Royon, et R. Blanc, « Active catheters for neuroradiology », *J. Robot. Mechatron.*, vol. 23, n° 1, p. 105-115, 2011.

[45] A. T. Tung, B.-H. Park, D. H. Liang, et G. Niemeyer, « Laser-machined shape memory alloy sensors for position feedback in active catheters », *Sens. Actuators Phys.*, vol. 147, n° 1, p. 83-92, sept. 2008, doi: 10.1016/j.sna.2008.03.024.

[46] J. H. Wiest et G. D. Buckner, « Path optimization and control of a shape memory alloy actuated catheter for endocardial radiofrequency ablation », *Robot. Auton. Syst.*, vol. 65, p. 88-97, 2015.

[47] J. Abadie, N. Chaillet, et C. Lexcellent, « Modeling of a new SMA micro-actuator for active endoscopy applications », *Mechatronics*, vol. 19, n° 4, p. 437-442, 2009.

[48] V. De Sars, S. Haliyo, et J. Szewczyk, « A practical approach to the design and control of active endoscopes », *Mechatronics*, vol. 20, n° 2, p. 251-264, 2010.

[49] B. Kim, S. Lee, J. H. Park, et J.-O. Park, « Design and fabrication of a locomotive mechanism for capsule-type endoscopes using shape memory alloys (SMAs) », *Mechatron. IEEEASME Trans. On*, vol. 10, n° 1, p. 77-86, 2005.

[50] J. Szewczyk, V. De Sars, et P. Bidaud, « Design and control of a SMA based active endoscope », in *Actes de ISMCR'02: 12th International Symposium on Measurement and Control in Robotics*, 2002, p. 143-149,

[51] J. B. Gafford, R. J. Wood, et C. J. Walsh, « A high-force, high-stroke distal robotic add-on for endoscopy », in *Robotics and Automation (ICRA), 2017 IEEE International Conference on*, 2017, p. 1117-1124.

[52] N.-K. Persson, J. G. Martinez, Y. Zhong, A. Maziz, et E. W. H. Jager, « Actuating Textiles: Next Generation of Smart Textiles », *Adv. Mater. Technol.*, vol. 3, nº 10, p. 1700397, oct. 2018, doi: 10.1002/admt.201700397.

[53] K. Eschen et J. Abel, « Performance and prediction of large deformation contractile shape memory alloy knitted actuators », *Smart Mater. Struct.*, vol. 28, nº 2, p. 025014, févr. 2019, doi: 10.1088/1361-665X/aaf215.

[54] M. C. Yuen, R. A. Bilodeau, et R. K. Kramer, « Active Variable Stiffness Fibers for Multifunctional Robotic Fabrics », *IEEE Robot. Autom. Lett.*, vol. 1, nº 2, p. 708-715, 2016.

[55] H. Dong, X. Du, et Q. Han, « Seismic responses of steel frame structures with self-centering energy dissipation braced on shape memory alloy cables », *Adv. Struct. Eng.*, vol. 22, nº 9, p. 2136-2148, juill. 2019, doi: 10.1177/1369433219834752.

[56] L. Dieng, G. Helbert, S. A. Chirani, T. Lecompte, et P. Pilvin, « Use of shape memory alloys damper device to mitigate vibration amplitudes of bridge cables », *Eng. Struct.*, vol. 56, p. 1547-1556, 2013.

[57] F. A. dos Santos, A. Rodrigues, et A. Micheletti, « Design and experimental testing of an adaptive shape-morphing tensegrity structure, with frequency self-tuning capabilities, using shape-memory alloys », *Smart Mater. Struct.*, vol. 24, nº 10, p. 105008, oct. 2015, doi: 10.1088/0964-1726/24/10/105008.

[58] M. M. Kheirikhah, S. Rabiee, et M. E. Edalat, « A Review of Shape Memory Alloy Actuators in Robotics », in *RoboCup 2010: Robot Soccer World Cup XIV*, vol. 6556, J. Ruiz-del-Solar, E. Chown, et P. G. Plöger, Éd. Berlin, Heidelberg: Springer Berlin Heidelberg, 2011, p. 206-217.

[59] W. Coral Cuellar, C. Rossi, J. Colorado Montaño, et A. Barrientos Cruz, *SMA-based muscle-like actuation in biologically inspired robots: a state of the art review*. Intech, 2012.

[60] J. S. Koh et K. J. Cho, « Omega-shaped inchworm-inspired crawling robot with large-index-and-pitch (LIP) SMA spring actuators », *IEEE ASME Trans. Mechatron.*, vol. 18, nº 2, p. 419-429, avr. 2013.

[61] G. Balaji *et al.*, « An SMA-actuated, compliant mechanism-based pipe-crawler », 2008, Consulté le: mai 15, 2017. [En ligne]. Disponible sur: http://www.mecheng.iisc.ernet.in/~suresh/journal/CrawlerISSS2008.pdf.

[62] P. Singh et G. K. Ananthasuresh, « A Compact and Compliant External Pipe-Crawling Robot », *IEEE Trans. Robot.*, vol. 29, nº 1, p. 251-260, févr. 2013, doi: 10.1109/TRO.2012.2214560.

[63] J. Ko, M. B. Jun, G. Gilardi, E. Haslam, et E. J. Park, « Fuzzy PWM-PID control of cocontracting antagonistic shape memory alloy muscle pairs in an artificial finger », *Mechatronics*, vol. 21, nº 7, p. 1190-1202, 2011.

[64] T. Hino et T. Maeno, « Development of a miniature robot finger with a variable stiffness mechanism using shape memory alloy », in *International*

Symposium on Robotics and Automation, Querétaro, México, Aug, 2004, p. 25-27, Consulté le: juill. 02, 2015.

[65] S. Dilibal et E. D. Engeberg, « Finger-like manipulator driven by antagonistic nickel-titanium shape memory alloy actuators », in *Advanced Robotics (ICAR), 2015 International Conference on*, 2015, p. 152-157.

[66] J. Li, L. Zu, G. Zhong, M. He, H. Yin, et Y. Tan, « Stiffness characteristics of soft finger with embedded SMA fibers », *Compos. Struct.*, vol. 160, p. 758-764, 2017.

[67] E. D. Engeberg, S. Dilibal, M. Vatani, J.-W. Choi, et J. Lavery, « Anthropomorphic finger antagonistically actuated by SMA plates », *Bioinspir. Biomim.*, vol. 10, n° 5, p. 056002, 2015.

[68] C.-C. Lan, C.-M. Lin, et C.-H. Fan, « A Self-Sensing Microgripper Module With Wide Handling Ranges », *IEEEASME Trans. Mechatron.*, vol. 16, n° 1, p. 141-150, févr. 2011, doi: 10.1109/TMECH.2009.2037495.

[69] N. F. Rad, A. Yousefi-Koma, H. Rezaei, et M. A. Bazrafshani, « Design and fabrication of a gripper actuated by shape memory alloy spring », in *Robotics and Mechatronics (ICROM), 2016 4th International Conference on*, 2016, p. 455-458.

[70] W. Wang, H. Rodrigue, H.-I. Kim, M.-W. Han, et S.-H. Ahn, « Soft composite hinge actuator and application to compliant robotic gripper », *Compos. Part B Eng.*, vol. 98, p. 397-405, août 2016, doi: 10.1016/j.compositesb.2016.05.030.

[71] E. A. Peraza-Hernandez, D. J. Hartl, R. J. Malak Jr, et D. C. Lagoudas, « Origami-inspired active structures: a synthesis and review », *Smart Mater. Struct.*, vol. 23, n° 9, p. 094001, 2014.

[72] K. Zhang, C. Qiu, et J. S. Dai, « Helical kirigami-enabled centimeter-scale worm robot with shape-memory-alloy linear actuators », *J. Mech. Robot.*, vol. 7, n° 2, p. 021014, mai 2015.

[73] H. Fang, Y. Zhang, et K. W. Wang, « Origami-based earthworm-like locomotion robots », *Bioinspir. Biomim.*, vol. 12, n° 6, p. 065003, oct. 2017, doi: 10.1088/1748-3190/aa8448.

[74] M. Salerno, K. Zhang, A. Menciassi, et J. S. Dai, « A novel 4-DOF origami grasper with an SMA-actuation system for minimally invasive surgery », *IEEE Trans. Robot.*, vol. 32, n° 3, p. 484-498, juin 2016.

[75] A. Nespoli, S. Besseghini, S. Pittaccio, E. Villa, et S. Viscuso, « The high potential of shape memory alloys in developing miniature mechanical devices: A review on shape memory alloy mini-actuators », *Sens. Actuators Phys.*, vol. 158, n° 1, p. 149-160, 2010.

[76] G. Scirè Mammano et E. Dragoni, « Elastic compensation of linear shape memory alloy actuators using compliant mechanisms », *J. Intell. Mater. Syst. Struct.*, vol. 25, n° 9, p. 1124-1138, 2014.

[77] P. Motzki, R. Britz, et S. Seelecke, « Modular SMA-Based Bi-Directional Rotational Actuator », in *ASME 2016 Conference on Smart Materials, Adaptive Structures and Intelligent Systems*, 2016, p. V001T04A001-V001T04A001.

[78] D. Hwang et T. Higuchi, « A planar wobble motor with a XY compliant mechanism driven by shape memory alloy », *IEEEASME Trans. Mechatron.*, vol. 21, n° 1, p. 302-315, 2016.

[79] E. A. Peraza-Hernandez, D. J. Hartl, et R. J. Malak, « Design and numerical analysis of an SMA mesh-based self-folding sheet », *Smart Mater. Struct.*, vol. 22, n° 9, p. 094008, 2013.

[80] A. Mekaouche, F. Chapelle, et X. Balandraud, « Using shape memory alloys to obtain variable compliance maps of a flexible structure: concept and modeling », *AIMETA Mecc.*, vol. 51, n° 6, p. 1287-1299, 2016.

[81] O. Benafan et D. J. Gaydosh, « High temperature shape memory alloy Ni50.3Ti29.7Hf20 torque tube actuators », *Smart Mater. Struct.*, vol. 26, n° 9, p. 095002, 2017.

[82] A. Micheletti, F. A. dos Santos, et P. Sittner, « Superelastic tensegrities: matrix formulation and antagonistic actuation », *Smart Mater. Struct.*, vol. 27, n° 10, p. 105028, oct. 2018.

[83] P.-A. Gédouin, L. Pino, S. A. Chirani, S. Calloch, E. Delaleau, et J.-M. Bourgeot, « R-phase shape memory alloy helical spring based actuators: modeling and experiments », *Sens. Actuators Phys.*, vol. 289, p. 65-76, 2019.

[84] Z. Shi, H. Al Hajjar, C. Prelle, X. Liu, L. Ilou, et F. Lamarque, « Optimization of an optically controlled bistable micro-actuator », in *IEEE ASME International Conference on Advanced Intelligent Mechatronics (AIM)*, 2018, p. 1148-1153.

[85] H. Yuan, F. Chapelle, J.-C. Fauroux, et X. Balandraud, « Concept for a 3D-printed soft rotary actuator driven by a shape-memory alloy », *Smart Mater. Struct.*, vol. 27, n° 5, p. 055005, 2018.

[86] T. D. White et D. J. Hartl, « Exploration of static equilibrium in elastically biased shape memory alloy components », in *Behavior and Mechanics of Multifunctional Materials XIII*, 2019, vol. 10968, p. 109680B.

[87] M. Moallem et V. A. Tabrizi, « Tracking control of an antagonistic shape memory alloy actuator pair », *IEEE Trans. Control Syst. Technol.*, vol. 17, n° 1, p. 184-190, 2008.

[88] A. Y. N. Sofla, D. M. Elzey, et H. N. G. Wadley, « Two-way antagonistic shape actuation based on the one-way shape memory effect », *J. Intell. Mater. Syst. Struct.*, vol. 19, n° 9, p. 1017-1027, 2008.

[89] M. Kciuk, W. Kuchcik, Z. Pilch, et W. Klein, « A novel SMA drive based on the Graham Clock escapement and resistance feedback », *Sens. Actuators Phys.*, vol. 285, p. 406-413, 2019.

[90] M. H. Moghadam, M. R. Zakerzadeh, et M. Ayati, « Robust sliding mode position control of a fast response SMA-actuated rotary actuator using temperature and strain feedback », *Sens. Actuators Phys.*, vol. 292, p. 158-168, 2019.

[91] A. Hadi, A. Yousefi-Koma, M. M. Moghaddam, M. Elahinia, et A. Ghazavi, « Developing a novel SMA-actuated robotic module », *Sens. Actuators Phys.*, vol. 162, n° 1, p. 72-81, juill. 2010, doi: 10.1016/j.sna.2010.06.014.

[92] A. Rosl, V. Amirtham, T. Nagarajan, et F. Hashim, « SMA Actuator Technology Application in Stewart Platform Construction », *J. Appl. Sci.*, vol. 11, p. 3783-3790, déc. 2011, doi: 10.3923/jas.2011.3783.3790.

[93] R. Dunlop et A. C. Garcia, « A Nitinol Wire Actuated Stewart Platform », *In Australasian conference on robotics and automation* (pp. 27-29). (2002, November)

[94] M. Mollaei et S. Mascaro, « Optimal Control Algorithm for Multi-Input Binary-Segmented SMA Actuators Applied to a Multi-DOF Robot Manipulator », in *Dynamic Systems and Control Conference* (Vol. 56147, p. V003T38A006). American Society of Mechanical Engineers., California, USA, oct. 2013, p. V003T38A006, doi: 10.1115/DSCC2013-4094.

[95] F. Auricchio, « A robust integration-algorithm for a ®nite-strain shape-memory-alloy superelastic model », *Int. J. Plast.*, p. 20, 2001.

[96] A. Mekaouche, F. Chapelle, et X. Balandraud, « FEM-Based Generation of Stiffness Maps », *IEEE Trans. Robot.*, vol. 31, nº 1, p. 217-222, févr. 2015, doi: 10.1109/TRO.2015.2392351.

[97] A. Mekaouche, F. Chapelle, et X. Balandraud, « A compliant mechanism with variable stiffness achieved by rotary actuators and shape-memory alloy », 2018, *Meccanica*, 2018, vol. 53, no 10, p. 2555-2571.

[98] H. Yuan, F. Chapelle, J.-C. Fauroux, et X. Balandraud, « Concept for a 3D-printed soft rotary actuator driven by a shape-memory alloy », *Smart Mater. Struct.*, vol. 27, nº 5, p. 055005, mars 2018, doi: 10.1088/1361-665X/aab56f.

[99] H. Tran, X. Balandraud, et J. F. Destrebecq, « Improvement of the mechanical performances of concrete cylinders confined actively or passively by means of SMA wires », *Arch. Civ. Mech. Eng.*, vol. 15, nº 1, p. 292-299, janv. 2015, doi: 10.1016/j.acme.2014.04.009.

[100] L. Heller *et al.*, « Beyond the strain recoverability of martensitic transformation in NiTi », *Int. J. Plast.*, vol. 116, p. 232-264, mai 2019, doi: 10.1016/j.ijplas.2019.01.007.

[101] H. Yuan, J. Fauroux, F. Chapelle, et X. Balandraud, « A review of rotary actuators based on shape memory alloys », *J. Intell. Mater. Syst. Struct.*, vol. 28, nº 14, p. 1863-1885, août 2017, doi: 10.1177/1045389X16682848.

[102] J.-P. Merlet, « Wire-driven Parallel Robot: Open Issues », in *Romansy 19 – Robot Design, Dynamics and Control*, Vienna, 2013, p. 3-10, doi: 10.1007/978-3-7091-1379-0_1.

[103] M. Jin et X. Zhang, « A new topology optimization method for planar compliant parallel mechanisms », *Mech. Mach. Theory*, vol. 95, p. 42-58, 2016.

[104] A. Mekaouche, F. Chapelle, et X. Balandraud, « Using shape memory alloys to obtain variable compliance maps of a flexible structure: concept and modeling », *Meccanica*, vol. 51, nº 6, p. 1287-1299, juin 2016, doi: 10.1007/s11012-015-0301-2.

"If you have knowledge, let others light their candles in it." — Margaret Fuller

List of publications

Thesis related publications

International peer-reviewed journal

R. Boufayed, F. Chapelle, J. Destrebecq, Xavier Balandraud. *Finite element analysis of a prestressed mechanism with multi-antagonistic and hysteretic SMA actuation*. Meccanica, Springer Verlag, 2020, 55 (5), pp.1007-1024, doi: 10.1007/s11012-020-01155-9.

International peer-reviewed conference proceedings

R. Boufayed, F. Chapelle, J. -F. Destrebecq and X. Balandraud, "*Numerical and experimental analysis of the discrete workspace of a prestressed planar mechanism driven by six SMA wires*," ACTUATOR; International Conference and Exhibition on New Actuator Systems and Applications 2021, 2021, pp. 1-4.

National peer-reviewed conference proceedings

R. Boufayed, F. Chapelle, Xavier Balandraud, J. Destrebecq. *Mécanisme plan piloté par six fils en alliage à mémoire de forme : analyse numérique de l'actionnement hystérétique et multi-antagoniste*. Proc. of the 24th edition of Congrès Français de Mécanique (CFM), Brest, 2019. 3rd prize poster.

Communication

R. Boufayed, F. Chapelle, Xavier Balandraud, J. Destrebecq. *Planar parallel mechanism actuated by shape-memory alloy wires*. The French Robotics Workshop 2020 GT6, Innovative design and mechatronics, Virtual workshop, November, 2020.

International collaborations

T. Yachai, R. Boufayed, P. Jongchansitto, I. Preechawuttipong, X. Balandraud. *Calorific Analysis of a Granular System Made in Shape Memory Alloy.* (eds) Residual Stress, Thermomechanics & Infrared Imaging and Inverse Problems, 2020, Volume 6. Conference Proceedings of the Society for Experimental Mechanics Series. Springer, Cham.

P. Jongchansitto, T. Yachai, I. Preechawuttipong, R. Boufayed, X. Balandraud. *Concept of mechanocaloric granular material made from shape memory alloy.* Energy, Volume 219, 2021, 119656, ISSN 0360-5442.

"It's the little details that are vital. Little things make big things happen." — John Wooden

List of Appendices

Contents

Appendix A: Technical documentation of the CAD of the studied mechanism 111
Appendix B: Preliminary incremental model for the control of the mechanism 116
Input parameters for the model 116
General geometrical data 116
Geometrical data for the SMA wires: 116
Thermomechanical data for the SMA wires: 117
Wire operation mode at ambient temperature 117
Activation of a SMA wire (j) 120
Procedure 1 120
Procedure 2 121
Appendix C: Conference paper Actuator 21 122
Appendix D: Example of an Ansys APDL script used in the thesis 126

Appendix A: Technical documentation of the CAD of the studied mechanism

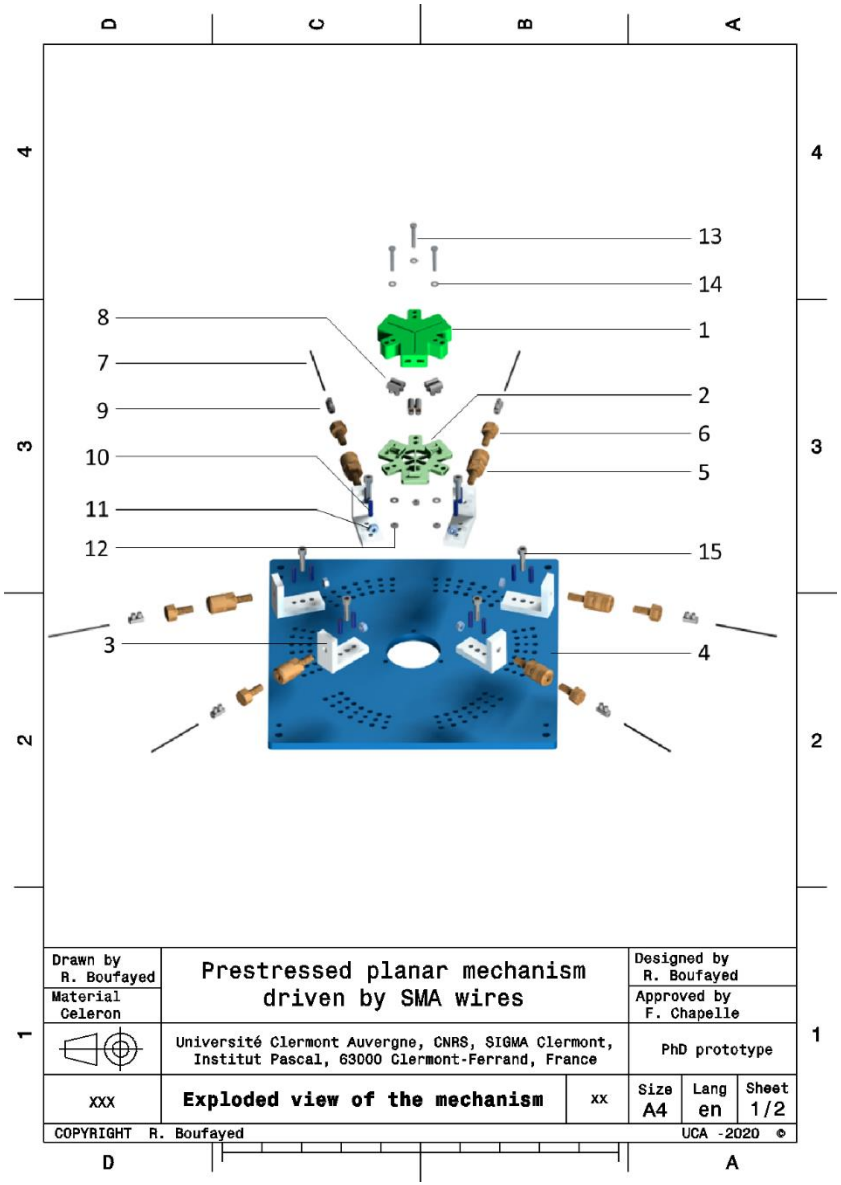

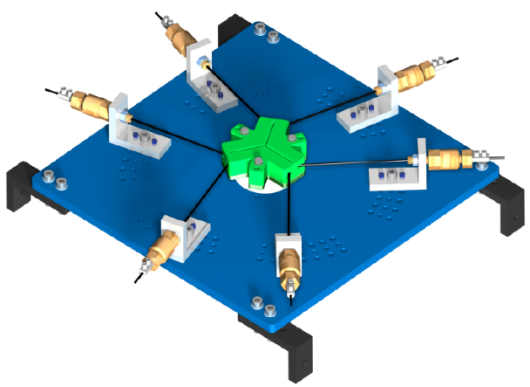

Ref.	NB	Description
15	6	M5x25 - Hexagon Socket Head Cap Screw
14	6	M4 - Washer
13	3	M4x35 - Hexagon Socket Head Cap Screw
12	3	M4 - Hegagon Nut
11	6	M8 - Hexagon Nut
10	12	Positioning pins
9	6	Single-block electric domino
8	3	Double-block electric domino
7	6	SMA wire
6	6	Prestraining hollow bolt for SMA wire
5	6	Straightening hollow bolt for SMA wire
4	1	Fixed base
3	6	L-shaped bracket for SMA wire
2	1	Lower part of the moving platform
1	1	Upper part of the moving platform

Drawn by R. Boufayed	Prestressed planar mechanism driven by SMA wires		Designed by R. Boufayed		
Material Celeron			Approved by F. Chapelle		
	Université Clermont Auvergne, CNRS, SIGMA Clermont, Institut Pascal, 63000 Clermont-Ferrand, France		PhD prototype		
XXX	**Exploded view of the mechanism**	XX	Size A4	Lang en	Sheet 2/2

COPYRIGHT R. Boufayed UCA -2020 ©

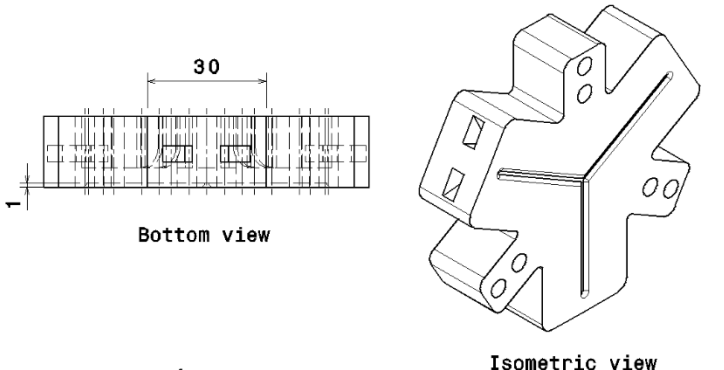

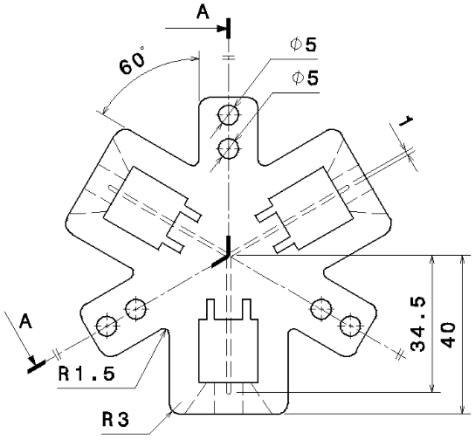

Front view

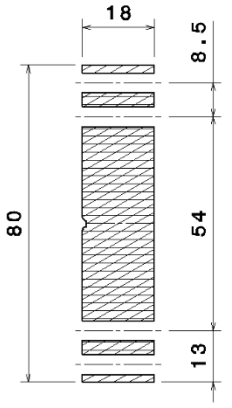

Section cut A-A

Drawn by R. Boufayed	Prestressed planar mechanism driven by SMA wires		Designed by R. Boufayed		
Material ABS polymer			Approved by F. Chapelle		
	Université Clermont Auvergne, CNRS, SIGMA Clermont, Institut Pascal, 63000 Clermont-Ferrand, France		PhD prototype		
Scale 1:1	**Upper part of the moving platform**	Ref. 1	Size A4	Lang. en	Sheet 1/2

COPYRIGHT R. Boufayed UCA -2020 ©

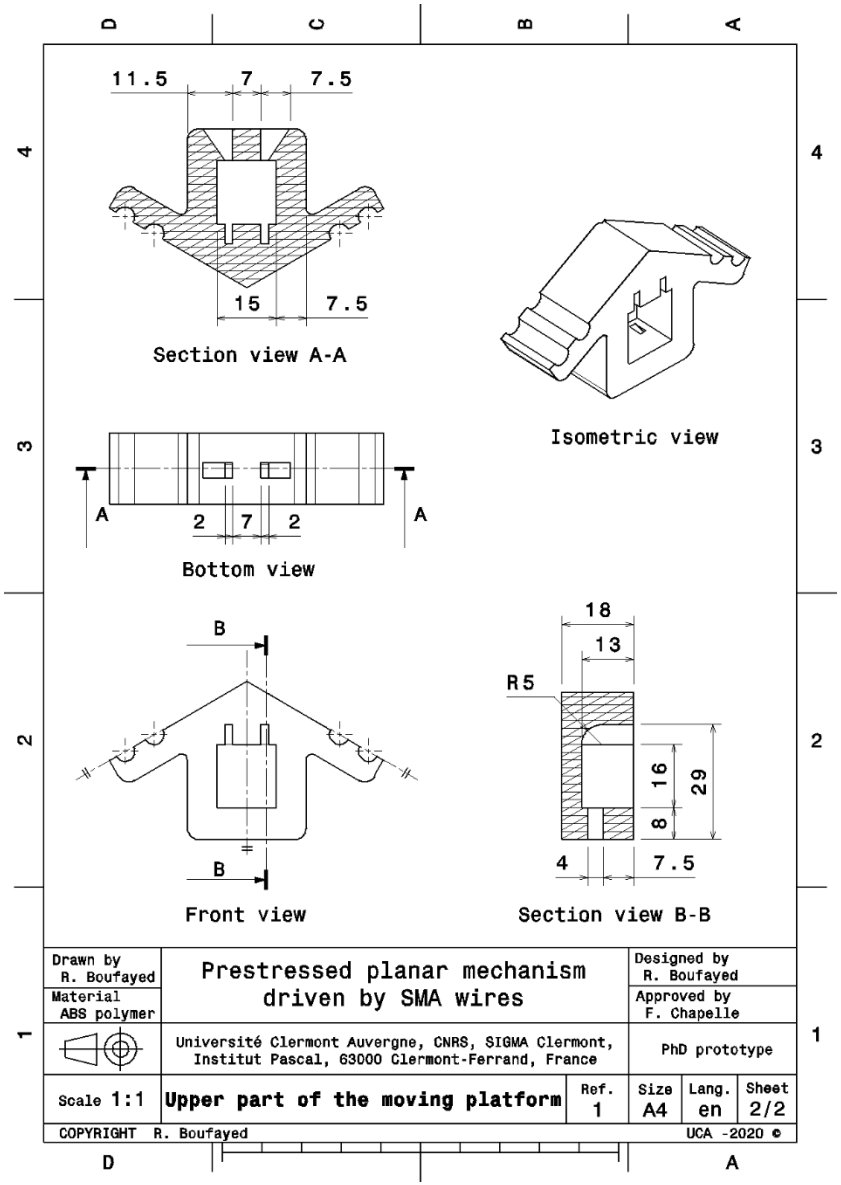
11.5
7
7.5
15
7.5
Section view A-A
Isometric view
A
2
7
2
A
Bottom view
B
B
Front view
18
13
R5
16
8
29
4
7.5
Section view B-B
Drawn by R. Boufayed
Material ABS polymer
Prestressed planar mechanism driven by SMA wires
Designed by R. Boufayed
Approved by F. Chapelle
Université Clermont Auvergne, CNRS, SIGMA Clermont, Institut Pascal, 63000 Clermont-Ferrand, France
PhD prototype
Scale 1:1
Upper part of the moving platform
Ref. 1
Size A4
Lang. en
Sheet 2/2
COPYRIGHT R. Boufayed
UCA -2020 ©

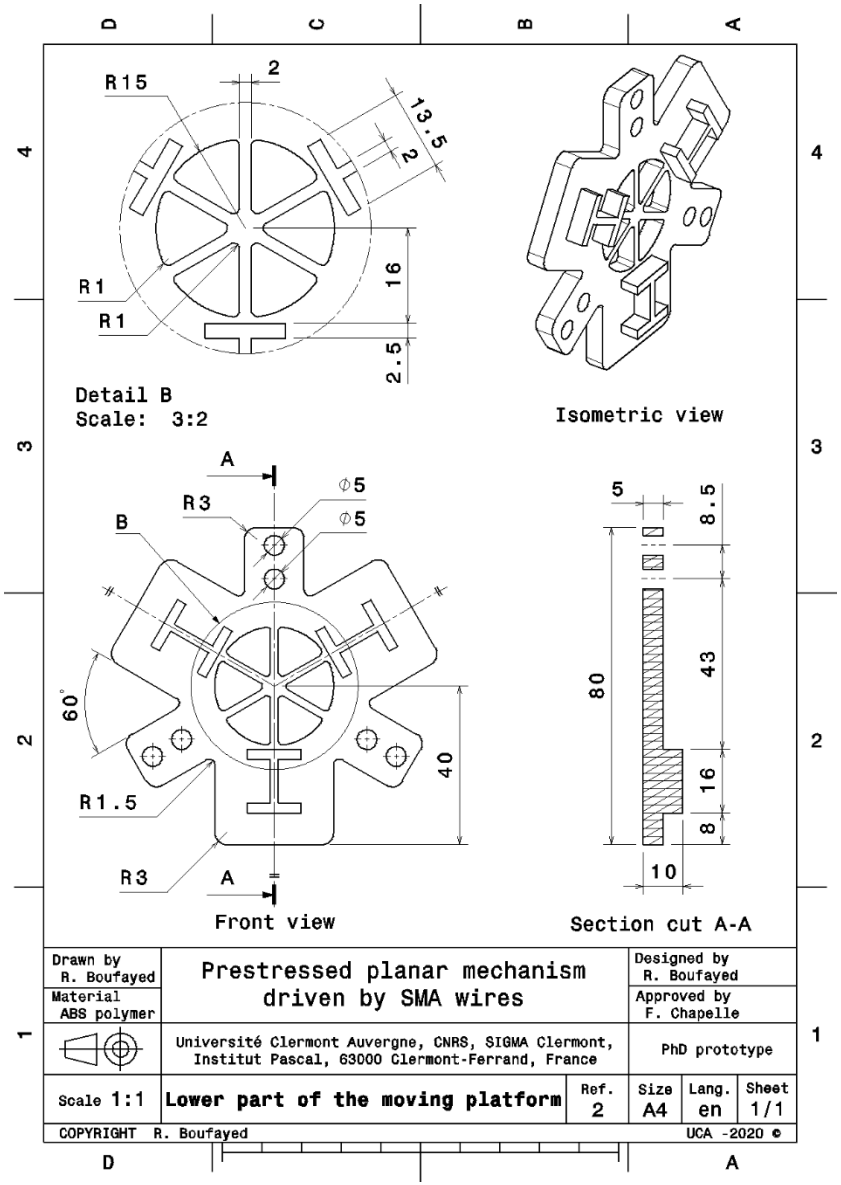
R15
2
13.5
2
16
R1
R1
2.5
Detail B
Scale: 3:2
Isometric view
A
R3
⌀5
⌀5
B
60°
40
R1.5
R3
A
Front view
5
8.5
43
80
16
8
10
Section cut A-A
Drawn by R. Boufayed
Material ABS polymer
Prestressed planar mechanism driven by SMA wires
Designed by R. Boufayed
Approved by F. Chapelle
Université Clermont Auvergne, CNRS, SIGMA Clermont, Institut Pascal, 63000 Clermont-Ferrand, France
PhD prototype
Scale 1:1
Lower part of the moving platform
Ref. 2
Size A4
Lang. en
Sheet 1/1
COPYRIGHT R. Boufayed
UCA -2020 ©

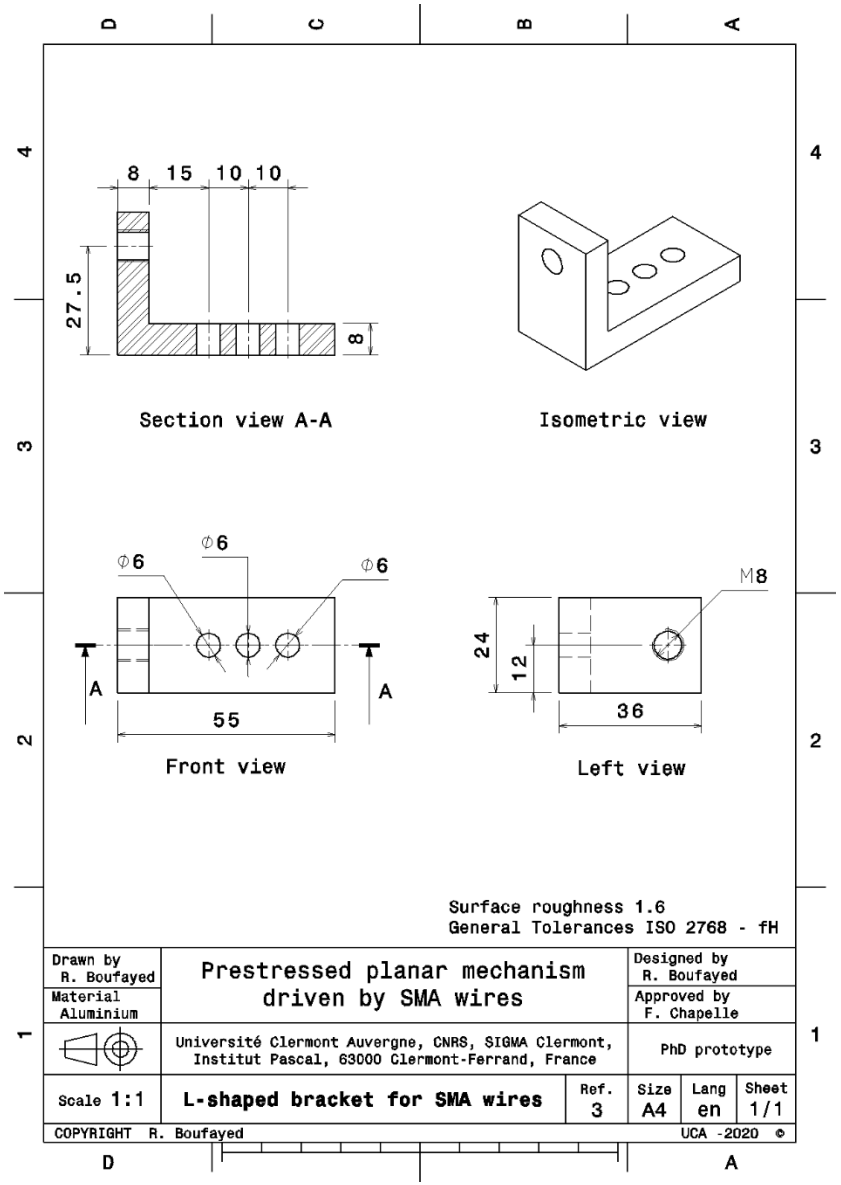
8 15 10 10
27.5
8
Section view A-A
Isometric view
ϕ6
ϕ6
ϕ6
A
A
55
Front view
M8
24
12
36
Left view
Surface roughness 1.6
General Tolerances ISO 2768 - fH
Drawn by R. Boufayed
Material Aluminium
Prestressed planar mechanism driven by SMA wires
Designed by R. Boufayed
Approved by F. Chapelle
Université Clermont Auvergne, CNRS, SIGMA Clermont, Institut Pascal, 63000 Clermont-Ferrand, France
PhD prototype
Scale 1:1
L-shaped bracket for SMA wires
Ref. 3
Size A4
Lang en
Sheet 1/1
COPYRIGHT R. Boufayed
UCA -2020 ©

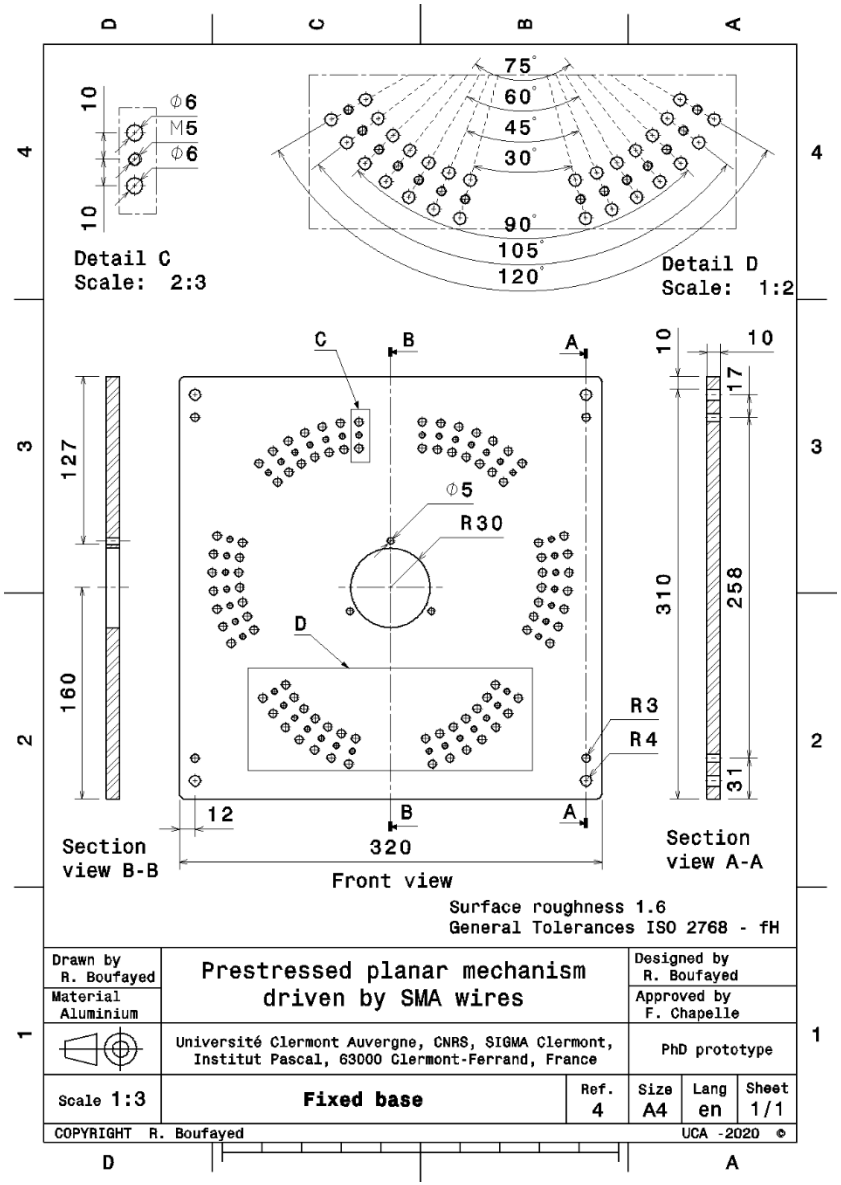
10
ϕ6
M5
ϕ6
10
Detail C
Scale: 2:3
75°
60°
45°
30°
90°
105°
120°
Detail D
Scale: 1:2
C
B
A
127
160
ϕ5
R30
D
R3
R4
12
B
A
320
Front view
Section view B-B
10
10
17
310
258
31
Section view A-A
Surface roughness 1.6
General Tolerances ISO 2768 - fH
Drawn by R. Boufayed
Material Aluminium
Prestressed planar mechanism driven by SMA wires
Designed by R. Boufayed
Approved by F. Chapelle
Université Clermont Auvergne, CNRS, SIGMA Clermont, Institut Pascal, 63000 Clermont-Ferrand, France
PhD prototype
Scale 1:3
Fixed base
Ref. 4
Size A4
Lang en
Sheet 1/1
COPYRIGHT R. Boufayed
UCA -2020 ©

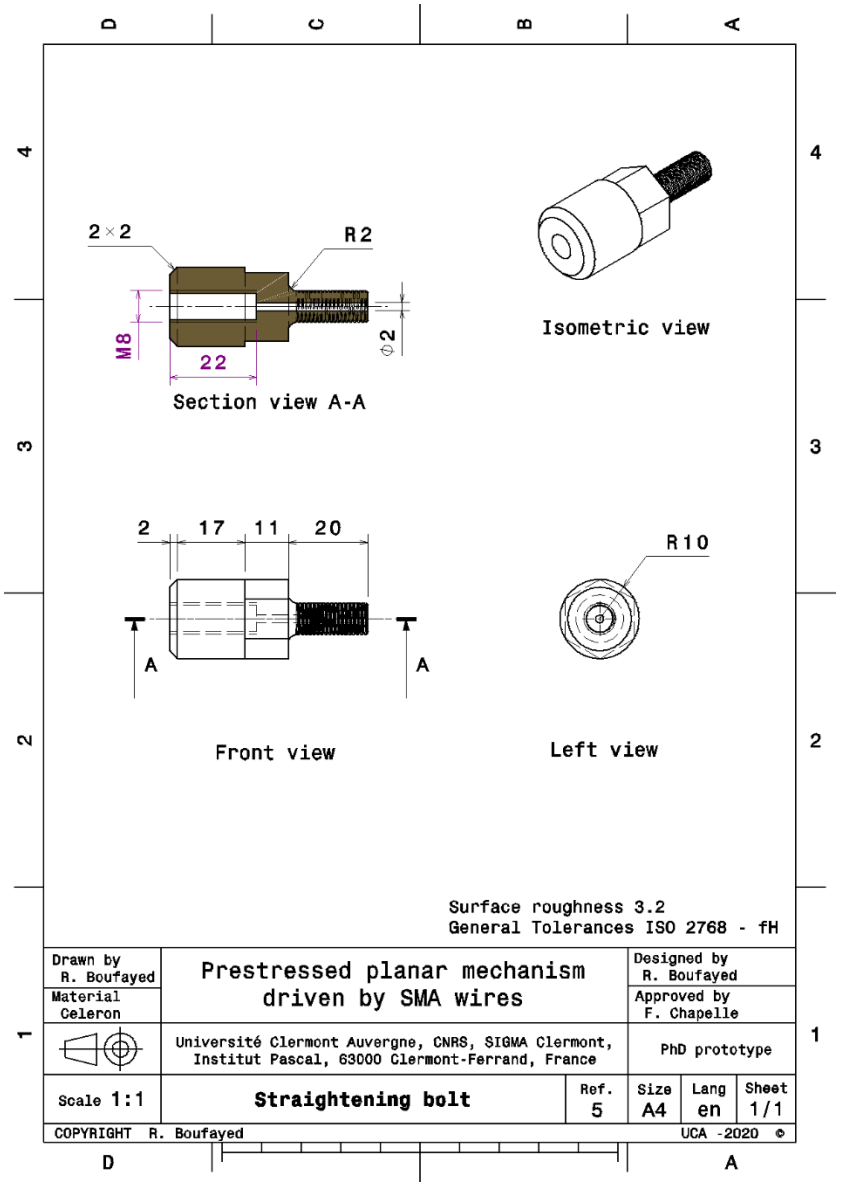
2×2
R2
M8
22
Ø2
Section view A-A
Isometric view
2
17
11
20
A
A
Front view
R10
Left view
Surface roughness 3.2
General Tolerances ISO 2768 - fH
Drawn by R. Boufayed
Material Celeron
Prestressed planar mechanism driven by SMA wires
Designed by R. Boufayed
Approved by F. Chapelle
Université Clermont Auvergne, CNRS, SIGMA Clermont, Institut Pascal, 63000 Clermont-Ferrand, France
PhD prototype
Scale 1:1
Straightening bolt
Ref. 5
Size A4
Lang en
Sheet 1/1
COPYRIGHT R. Boufayed
UCA -2020 ©

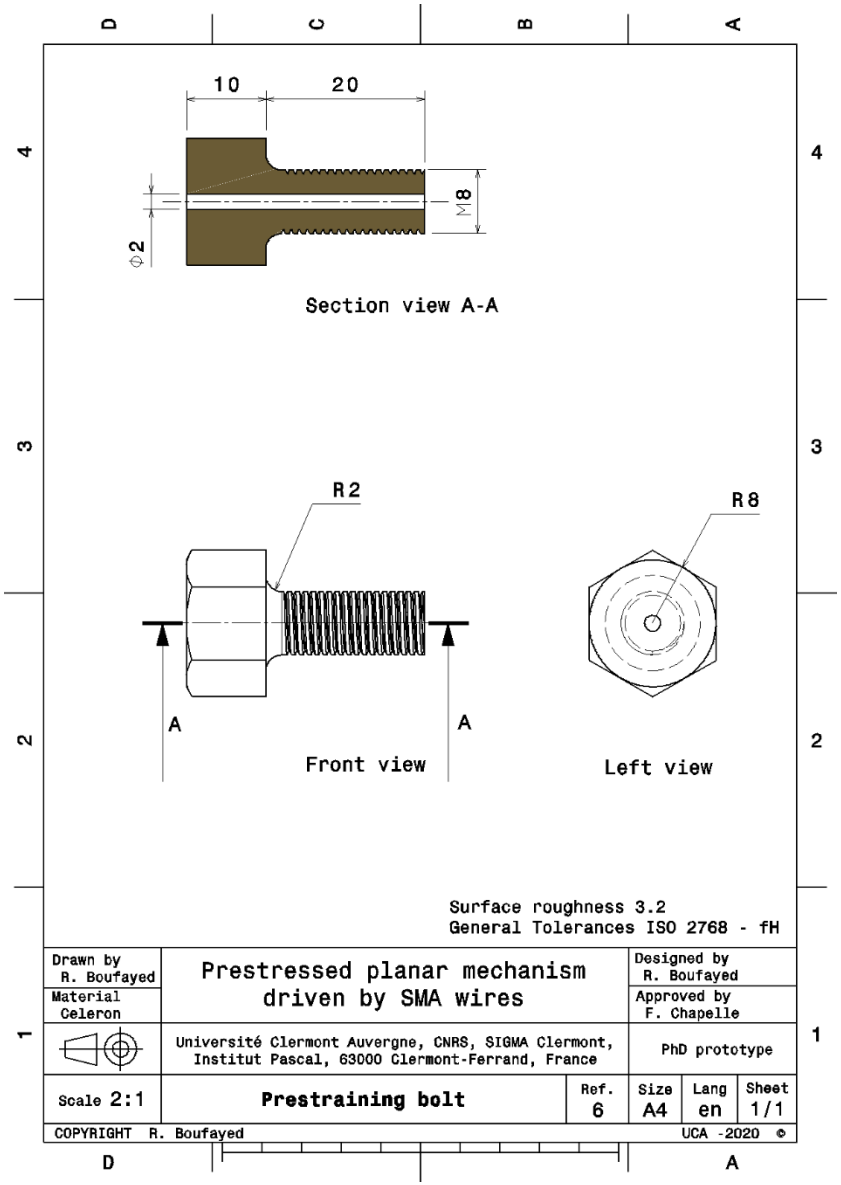
10
20
M8
Ø2
Section view A-A
R2
A
A
Front view
R8
Left view
Surface roughness 3.2
General Tolerances ISO 2768 - fH
Drawn by R. Boufayed
Material Celeron
Prestressed planar mechanism driven by SMA wires
Designed by R. Boufayed
Approved by F. Chapelle
Université Clermont Auvergne, CNRS, SIGMA Clermont, Institut Pascal, 63000 Clermont-Ferrand, France
PhD prototype
Scale 2:1
Prestraining bolt
Ref. 6
Size A4
Lang en
Sheet 1/1
COPYRIGHT R. Boufayed
UCA -2020 ©

Appendix B: Preliminary incremental model for the control of the mechanism

This appendix proposes a first incremental model for the control of the mechanism. Although it was not used in the present thesis, it corresponds to a first work that could be used in the future.

Input parameters for the model

General geometrical data

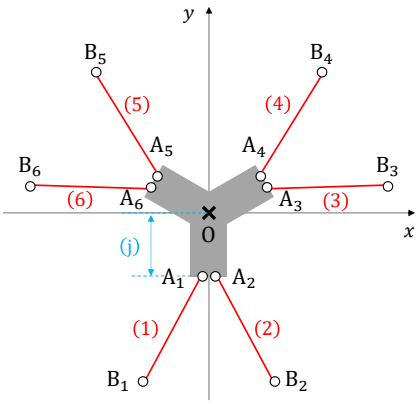

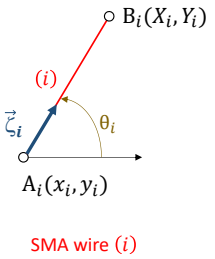

Geometry	Coordinates	Initial values
Point O	x_o, y_o	$x_o = y_o = 0$
Arm (j)	---	a (length) ; δ_j (angle/Ox)
Points A_i	x_i, y_i	$x_i = a\cos\delta_j$; $y_i = a\sin\delta_j$
Points B_i	X_i, Y_i (invariants)	$X_i = a\cos\delta_j + L_i\cos\theta_i$ $Y_i = a\sin\delta_j + L_i\sin\theta_i$

Geometrical data for the SMA wires:

SMA wire (i)	Notations	Initial values
Cross section:	Ω_i	Ω_i (invariant)
Martensite rate	$z \in [0,1]$	z_{ini}
Pre-strain	ϵ_{ini}	$[(1-\alpha/E_A)\sigma_{cr} + z_{ini}E_z\gamma]/(E_z-\alpha)$
Length before stretching	L_{oi}	$L_{oi} = L_{ini}/(1+\epsilon_{ini})$
Initial length	L_{ini}	$L_{ini} = \sqrt{[X_i - x_i]^2 + [Y_i - y_i]^2}$
Current length	L_i	L_{ini}
Orientation	$\vec{\theta}_i(0,0,\theta_i)$	$\theta_i = \tan^{-1}[(Y_i - y_i)/(X_i - x_i)]$
Unit vector	$\vec{\zeta}_i(\cos\theta_i, \sin\theta_i, 0)$	← idem with initial θ_i

Thermomechanical data for the SMA wires:

Definition	Notation	Unit
Transformation temperatures	$< M_s < T_A < A_s < A_f$	[°C]
Slope of the martensitic transformation	β	[MPa.K^{-1}]
Critical stress ($T = T_A$)	$\sigma_{cr} = \beta(T_A - M_s)$	[MPa]
End of transformation stage	$\sigma_{cr'} = \beta(T_A - M_f)$	[MPa]
Critical stress ($T > T_A$)	$\sigma_{cr,T} = \sigma_{cr} + \beta(T - T_A)$	[MPa]
Total transformation	γ	[-]
Austenite Young's modulus	E_A	[MPa]
Martensite Young's modulus	E_M	[MPa]
Straight transformation slope	α	[MPa]
Proportion of martensite	[Pure austenite] $0 \leq z \leq 1$ [pure martensite]	[-]

Expression of α: $\alpha = \frac{\sigma_{cr'} - \sigma_{cr}}{\epsilon_{cr'} - \epsilon_{cr}} = \frac{E_A E_M (M_s - M_f)}{(E_A - E_M)T_A + E_M M_s - E_A M_f + E_A E_M \gamma/\beta}$

Wire operation mode at ambient temperature

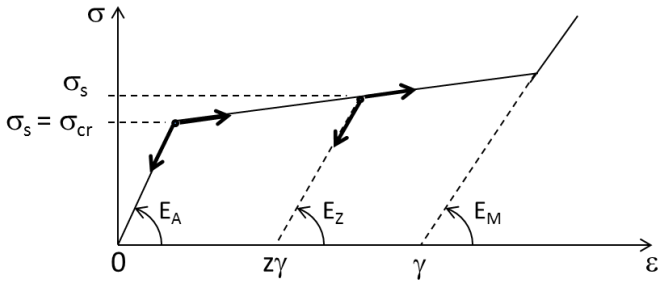

Tri-linear diagram: $\sigma = E_z(\epsilon - z \cdot \gamma)$ $\quad z \in [0,1]$ (proportion of martensite)
where: $E_z = (1-z)E_A + zE_M = E_A - z(E_A - E_M)$
Equation of the transformation line: $\sigma = \alpha\epsilon + (1 - \alpha/E_A)\sigma_{cr}$
Incremental relation: $d\sigma = k \cdot d\epsilon \quad \Leftrightarrow \quad dF = K \cdot dL$ with $K = k\Omega/L_o$

- Value of k:

$$\forall\, z \geq 0 \begin{cases} \sigma < \sigma_s & k = E_z \ (\forall \text{ sign of } d\sigma \text{ and } d\epsilon) \\ \sigma = \sigma_s & \begin{cases} \text{if } d\sigma \text{ or } d\epsilon < 0: & k = E_z \\ \text{if } d\sigma \text{ or } d\epsilon > 0: & k = \alpha \end{cases} \end{cases}$$

- Equations of σ_s and dz:

$$\forall\, z \geq 0 \begin{cases} \sigma < \sigma_s & d\sigma_s = 0 \text{ and } dz = 0 \ (\forall \text{ sign of } d\sigma \text{ and } d\epsilon) \\ \sigma = \sigma_s & \begin{cases} \text{if } d\sigma \text{ or } d\epsilon < 0: & d\sigma_s = 0 \text{ and } dz = 0 \\ \text{if } d\sigma \text{ or } d\epsilon > 0: & d\sigma_s = d\sigma \ ; \ dz > 0 \end{cases} \end{cases}$$

NB: the behaviour of each SMA wire is linear as long as the threshold value σ_s is not crossed.

Case of an imposed displacement at point O (SMA wires at ambient temperature)

We start from a supposedly known position of the centre O of the platform:

- Coordinates (x_o, y_o)
- Rotation θ_o
- Displacement increment imposed at point O:
- Translation increment: $\overrightarrow{dU} : (du, dv, 0)$
- Rotation increment: $\overrightarrow{d\theta} : (0, 0, d\theta)$

→ Induced translation increment at point A_i :

$$\overrightarrow{dU_i} = \overrightarrow{dU} + \overrightarrow{OA_i} \wedge \overrightarrow{d\theta} \quad \Longrightarrow \quad \begin{pmatrix} du_i \\ dv_i \\ 0 \end{pmatrix} = \begin{pmatrix} du \\ dv \\ 0 \end{pmatrix} + \begin{pmatrix} x_i - x_o \\ y_i - y_o \\ 0 \end{pmatrix} \wedge \begin{pmatrix} 0 \\ 0 \\ d\theta \end{pmatrix}$$

→ Evolution of the coordinates of point $A_i \rightarrow A_i'$:

$$\begin{pmatrix} x_i \\ y_i \\ 0 \end{pmatrix} \rightarrow \begin{pmatrix} x_i \\ y_i \\ 0 \end{pmatrix} + \begin{pmatrix} du_i \\ dv_i \\ 0 \end{pmatrix} \quad \text{where} \quad \begin{pmatrix} du_i \\ dv_i \\ 0 \end{pmatrix} = \begin{pmatrix} du + (y_i - y_o)d\theta \\ dv - (x_i - x_o)d\theta \\ 0 \end{pmatrix}$$

→ Wire length variation (i): $dL_i = \overline{A_i'B_i} - \overline{A_iB_i}$

$$\overline{A_iB_i} = \sqrt{[X_i - x_i]^2 + [Y_i - y_i]^2} \quad ; \quad \overline{A_i'B_i} = \sqrt{[X_i - (x_i + du_i)]^2 + [Y_i - (y_i + dv_i)]^2}$$

$$\Longrightarrow \quad dL_i = \sqrt{[X_i - (x_i + du_i)]^2 + [Y_i - (y_i + dv_i)]^2} - \sqrt{[X_i - x_i]^2 + [Y_i - y_i]^2}$$

→ Strain and stress increment in wire (i):

$$d\varepsilon_i = dL_i / L_{oi} \quad \rightarrow \quad d\sigma_i = k_i d\varepsilon_i$$

→ Force increments in wire (i):

$$d\vec{F}_i = \Omega_i d\sigma_i \vec{\zeta}_i = k_i \Omega_i d\varepsilon_i \vec{\zeta}_i \quad \Longrightarrow \quad d\vec{F}_i = K_i dL_i \vec{\zeta}_i \quad \text{with} \quad K_i = k_i \Omega_i / L_{oi}$$

where $\vec{\zeta}_i(\cos\theta_i, \sin\theta_i, 0)$ and $\theta_i = \tan^{-1}\left[[Y_i - (y_i + dv_i)]/[X_i - (x_i + du_i)]\right]$

→ Resultant at point O:

- Resulting force: $d\vec{F} = \sum_i d\vec{F}_i$

$$d\vec{F} = \sum_i k_i \Omega_i \frac{dL_i}{L_{oi}} \vec{\zeta}_i \quad \Longrightarrow \quad \begin{pmatrix} dF_x \\ dF_y \\ 0 \end{pmatrix} = \frac{\Omega}{L_o} \sum_i \begin{pmatrix} \cos\theta_i \\ \sin\theta_i \\ 0 \end{pmatrix} k_i dL_i$$

- Resulting torque: $d\vec{M} = \sum_i \overrightarrow{OA_i'} \wedge d\vec{F}_i$

$$\Longrightarrow \quad \begin{pmatrix} 0 \\ 0 \\ dM_z \end{pmatrix} = \frac{\Omega}{L_o} \sum_i \begin{pmatrix} x_i + du_i - x_o \\ y_i + dv_i - y_o \\ 0 \end{pmatrix} \wedge \begin{pmatrix} \cos\theta_i \\ \sin\theta_i \\ 0 \end{pmatrix} k_i dL_i$$

→ Vectorial writing:

- Displacement increment in O: $\overrightarrow{dU}(du, dv, 0)$; $\overrightarrow{d\theta}(0, 0, d\theta)$

→ Force and torque resulting in O: $\begin{cases} d\vec{F} = \sum_i d\vec{F}_i \\ d\vec{M} = \sum_i \overrightarrow{OA'_i} \Lambda d\vec{F}_i \end{cases}$

- SMA wire (i):

$$\overrightarrow{dU_i} = \overrightarrow{dU} + \overrightarrow{OA_i} \Lambda \overrightarrow{d\theta} \quad \Longrightarrow \quad \begin{pmatrix} du_i \\ dv_i \\ 0 \end{pmatrix} = \begin{pmatrix} du + (y_i - y_o)d\theta \\ dv - (x_i - x_o)d\theta \\ 0 \end{pmatrix}$$

$A_i(x_i\,, y_i) \quad \rightarrow \quad A'_i(x_i + du_i\,,\ y_i + dv_i)$

$d\vec{F}_i = \dfrac{\Omega}{L_o} k_i dL_i \vec{\zeta}_i$

where $\vec{\zeta}_i(\cos\theta_i\,, \sin\theta_i\,, 0)$ and $\theta_i = \tan^{-1}\left[[Y_i - (y_i + dv_i)]/[X_i - (x_i + du_i)]\right]$

$dL_i = L_i^+ - L_i \quad \begin{cases} L_i^+ = \sqrt{[X_i - (x_i + du_i)]^2 + [Y_i - (y_i + dv_i)]^2} \\ L_i = \sqrt{[X_i - x_i]^2 + [Y_i - y_i]^2} \end{cases}$

Matrix representation:

$$\text{Coupled} \begin{cases} (1): \quad \overrightarrow{dU} \quad \Longrightarrow \quad \text{fil(i)} \ \overrightarrow{dU_i^{(1)}} \quad \rightarrow \quad d\vec{F}^{(1)}, d\vec{M}^{(1)} \\ (2): \quad \overrightarrow{d\theta} \quad \Longrightarrow \quad \text{fil(i)} \ \overrightarrow{dU_i^{(2)}} \quad \rightarrow \quad d\vec{F}^{(2)}, d\vec{M}^{(2)} \end{cases}$$

$$(1): \quad \begin{pmatrix} dF_x^{(1)} \\ dF_y^{(1)} \\ dM_z^{(1)} \end{pmatrix} = \begin{bmatrix} K_{11}^{(1)} & K_{12}^{(1)} & 0 \\ K_{21}^{(1)} & K_{22}^{(1)} & 0 \\ K_{31}^{(1)} & K_{32}^{(1)} & 0 \end{bmatrix} \begin{pmatrix} du \\ dv \\ 0 \end{pmatrix}$$

$$(2): \quad \begin{pmatrix} dF_x^{(2)} \\ dF_y^{(2)} \\ dM_z^{(2)} \end{pmatrix} = \begin{bmatrix} 0 & 0 & K_{13}^{(2)} \\ 0 & 0 & K_{23}^{(2)} \\ 0 & 0 & K_{33}^{(2)} \end{bmatrix} \begin{pmatrix} 0 \\ 0 \\ d\theta \end{pmatrix}$$

$$\Longrightarrow \quad \begin{pmatrix} dF_x \\ dF_y \\ dM_z \end{pmatrix} = \begin{bmatrix} K_{11} & K_{12} & K_{13} \\ K_{21} & K_{22} & K_{23} \\ K_{31} & K_{32} & K_{33} \end{bmatrix} \begin{pmatrix} du \\ dv \\ d\theta \end{pmatrix} \quad \Leftrightarrow \quad \begin{pmatrix} d\vec{F} \\ d\vec{M} \end{pmatrix} = \left[K(\vec{U}, \vec{\theta})\right] \begin{pmatrix} \overrightarrow{dU} \\ \overrightarrow{d\theta} \end{pmatrix}$$

NB: The terms K_{ij} of the matrix $[K]$ depend on the three components (u, v, θ) of the displacement at the point O → geometrical non-linearity.
(Reminder: the wires behave linearly for each increment).

Activation of a SMA wire (j)

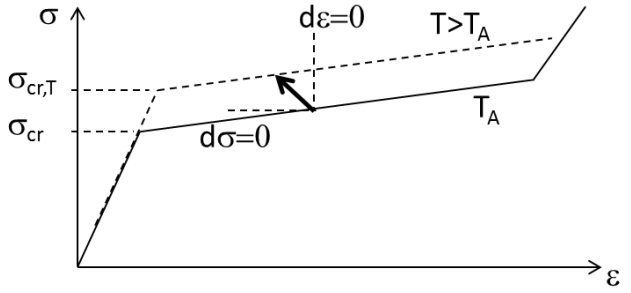

Behaviour of a heated SMA wire: $d\sigma = k_j \cdot d\epsilon \quad \Leftrightarrow \quad dF_j = k_j dL_j \Omega / L_o$

Signs: $d\sigma > 0$; $d\epsilon < 0 \quad \Leftrightarrow \quad dF_j > 0$; $dL_j < 0$

NB: The value of k_j results from the reaction of the rest of the system (where $-\infty < k_j < 0$)

Procedure 1

- Activation of the wire (j) causes shortening $dL_j \rightarrow dF_j$ (to be determined)
- This results in a displacement increment $(\overrightarrow{dU}, \overrightarrow{d\theta})$ at point O:
  (NB: $\overrightarrow{dU}$ and $\overrightarrow{d\theta}$ are the unknowns of the problem)
  → Displacement increments at points A_i : $\overrightarrow{dU_i} = \overrightarrow{dU} + \overrightarrow{OA_i} \wedge \overrightarrow{d\theta}$
  → Incremental relationship for unheated wires:

$$\sum_i \begin{pmatrix} d\vec{F}_i \\ d\vec{M}_i \end{pmatrix}_{\text{SMA wire at ambient temperature}} = \left[K(\vec{U}, \vec{\theta})\right] \begin{pmatrix} \overrightarrow{dU} \\ \overrightarrow{d\theta} \end{pmatrix}$$

- General equilibrium of the system (in the absence of an external force applied in O):

$$\Sigma_i \begin{pmatrix} d\vec{F}_i \\ d\vec{M}_i \end{pmatrix}_{\text{wires at ambient temperature}} + \begin{pmatrix} d\vec{F}_j \\ d\vec{M}_j \end{pmatrix} = \begin{pmatrix} \vec{0} \\ \vec{0} \end{pmatrix}$$

$$\Rightarrow \begin{pmatrix} d\vec{F}_j \\ d\vec{M}_j \end{pmatrix} = -\Sigma_i \begin{pmatrix} d\vec{F}_i \\ d\vec{M}_i \end{pmatrix}_{\text{SMA wire at ambient temperatures}}$$

$$\Rightarrow \begin{cases} d\vec{F}_j = -\Sigma_i \left(d\vec{F}_i\right)_{\text{SMA wire at ambient temperature}} \\ d\vec{M}_j = -\Sigma_i \left(d\vec{M}_i\right)_{\text{SMA wire at ambient temperature}} \end{cases}$$

- Finally, $\overrightarrow{dU}$ and $\overrightarrow{d\theta}$ must be such that $d\vec{F}_j$ satisfies the following 2 conditions (iterative procedure):
  (1) The orientation of $d\vec{F}_j$ must match that of the wire (j): $d\vec{F}_j \;//\; A'_j B_j$
  (2) $d\vec{M}_j = \overrightarrow{OA'_j} \wedge d\vec{F}_j = -\Sigma_i \left(d\vec{M}_i\right)_{\text{SMA wire at ambient temperature}}$

Note: non-explicit solution requiring the use of an iterative procedure - not very effective!

Procedure 2

- A displacement increment is imposed in O: $\overrightarrow{dU}(du, dv, 0)$; $\overrightarrow{d\theta}(0, 0, d\theta)$

  → This results in:

  - a displacement of each point $A_i(x_i, y_i)$ → $A_i'(x_i + du_i,\ y_i + dv_i)$
  - a variation in the length of each SMA wire: $dL_i = \overline{A_i'B_i} - \overline{A_iB_i}$
  - a variation in force of each SMA wire: $d\vec{F}_i = K_i dL_i \vec{\zeta}_i$

  → Force and torque resulting in O: $\begin{cases} d\vec{F} = \sum_i d\vec{F}_i \\ d\vec{M} = \sum_i \overrightarrow{OA_i'} \wedge d\vec{F}_i \end{cases}$

- We identify the 3 wires that have undergone the strongest shortening ($dL_j < 0$) and then we assume that the displacement increment of the point O results from the three dL_j caused by thermal activation:

  → shortening of the wire (j): $dL_j < 0$ (identical to the previous case "at ambient temperature")

  → force increment in the wire (j): $dF_j > 0$

  - The three dL_j are known (the result of the "ambient temperature" calculation), the three dF_j must be determined (unknowns of the problem); for this, it is written that the resultant of the forces is zero in:

$$\sum_i \begin{pmatrix} d\vec{F}_i \\ d\vec{M}_i \end{pmatrix}_{\text{Heated SMA wire}} + \sum_j \begin{pmatrix} d\vec{F}_j \\ d\vec{M}_j \end{pmatrix}_{\text{Heated SMA wire}} = \begin{pmatrix} \vec{0} \\ \vec{0} \end{pmatrix}$$

$$\Rightarrow \begin{cases} \sum_j \left(d\vec{F}_j\right)_{\text{Heated SMA wire}} = -\sum_i \left(d\vec{F}_i\right)_{\text{SMA wire at ambient temperature}} \\ \sum_j \left(d\vec{M}_j\right)_{\text{Heated SMA wire}} = -\sum_i \left(d\vec{M}_i\right)_{\text{SMA wire at ambient temperature}} \end{cases}$$

where: $\begin{cases} d\vec{F}_i \text{ and } d\vec{M}_i = \overrightarrow{OA_i'} \wedge d\vec{F}_i \text{ given by the ambient temperature calculation} \\ d\vec{F}_j = dF_j \vec{\zeta}_j \ ;\ d\vec{M}_j = \overrightarrow{OA_j'} \wedge d\vec{F}_j \ ) \end{cases}$

(dF_i to be determined ; A_j' and $\vec{\zeta}_j \leftarrow$ ambient temperature calculation

→ which corresponds (written in components) to a system of 3 linear equations (2 equations of force + 1 equation of moment) whose unknowns are the 3 forces dF_j to be determined (written in components).

Note: this time we get an explicit solution (no iteration) more efficient!

NB: It is possible to heat n>3 wires, which introduces n-3 overabundant unknowns, thus requiring the introduction of additional linking equations to manage the distribution of forces between the wires.

Appendix C: Conference paper Actuator 21

Numerical and experimental analysis of the discrete workspace of a prestressed planar mechanism driven by six SMA wires

Ph.D. Rym Boufayed[1*], Assoc. Prof. Frédéric Chapelle[1], Prof. Jean-François Destrebecq[1] and Prof. Xavier Balandraud[1]
[1] Université Clermont Auvergne, CNRS, SIGMA Clermont, Institut Pascal, 63000 Clermont-Ferrand, France
[*] Corresponding author. Miss Rym Boufayed. E-mail address: rym.boufayed@sigma-clermont.fr

Abstract

This paper deals with the workspace of a multi-antagonistic prestressed planar mechanism driven by six shape memory alloy (SMA) wires. The mechanism is organized in a ternary rotational symmetry enabling a same initial prestressed state in all the wires before applying a thermal activation sequence. The SMA wires can be activated individually, one or more at a time. The workspace is generated by their binary thermal actuation considering either the ambient temperature or a given higher temperature. The resulting discrete workspace that results from this binary activation is created from a finite element calculation software, namely Ansys Mechanical APDL. The objective of the model is to study the influence of the thermal actuation history on the discrete workspace. An experimental example is also presented.

Keywords

Shape memory alloy - Prestressed mechanism - Multi-antagonistic actuation - Finite element simulation – Discrete workspace - Experiment

1 Introduction

Innovative actuators are increasingly sought in order to create new technological opportunities for industrial applications and meet with the continuous development of science [1]. One way to achieve this aim is to integrate smart materials as components of the products, notably for instance shape memory alloy (SMA) actuators [2,3]. Despite the fact that SMAs have interesting qualities like their reduced cost, noiseless operation mode, capability to function under harsh constraints and reliability, they present two major constraints, which are the non-linear nature of their mechanical response and a wide thermal and mechanical hysteretic behaviour [4,5]. These constraints have a significant impact on the controllability of SMA actuators, which explains why they are often limited to linear and angular actuators offering one degree of freedom [6,7]. Hence, a further research is required to design new architectures with higher numbers of freedom and explore their workspace for the purpose of controllability.

In this aim, this paper deals with a planar prestressed mechanism actuated by six SMA wires offering three degrees of freedom. Thanks to their interesting mechanical properties and their simple Joule effect operation mode, SMA wires are used to move a rigid mobile platform to which they are connected. The one-way shape memory of each SMA wire is employed to create a two-way memory effect through the antagonistic effect of the other SMA wires. Geometrically, the mechanism is organized in a ternary rotational symmetry enabling a same initial prestressed state in all the wires before applying a thermal activation sequence. The wires can be activated individually one or several at a time. The workspace is generated by their binary thermal actuation considering either the ambient temperature or a given higher temperature, resulting in a discrete workspace. The authors presented in a previous paper a finite element (FE) analysis of the mechanism through different cases of study [8]. The FE model was developed with Ansys Mechanical APDL using Auricchio's model for the SMA behaviour. The objective of the present paper is to discuss the influence of the thermal actuation history on the discrete workspace. An experimental example is also presented.

2 Presentation of the case of study

The studied mechanism is composed of a mobile platform, a fixed base and six SMA wires placed in ternary symmetry by pair (see **Figure 1**). SMA wires can be considered in connection to the fixed base and mobile platform through revolute joints due to their low bending stiffness (small wire diameter). An angle of 60° is chosen between each pair of SMA wires. The useful length of the SMA wire is equal to 170 mm. Considering a nickel-titanium (Ni-Ti) SMA featuring typically 6% of recoverable strain (shape memory effect), it gives a potential change in length of about 10 mm. In practice, the SMA component which is considered in the study is a Ni50.8–Ti49.2 (at.%) SMA wire 1 mm in diameter, provided by Nimesis, Metz, France. Its phase transformation temperatures at zero stress are -25 °C, -7 °C, 24 °C and 36 °C (respectively martensite finish M_f, martensite start M_s, austenite start A_s and austenite finish A_f) [8]. It must be noted that this SMA allows an ambient temperature T_{amb} between A_s and M_s,

i.e. $M_s < T_{amb} < A_s$. This specificity enables various settings. In particular, the SMA can be either in austenite phase or martensite phase at ambient temperature depending whether it was previously heated above A_f or cooled below M_f respectively. In the present work, the SMA wires are placed in austenitic state in the mechanism before being partially transformed in martensite by mechanical loading (prestress). In practice, it means they were "initialized" in the austenitic state by heating above A_f before returning to ambient temperature.

Under zero stress, heating of a martensitic SMA wire above A_f would lead to a return to full austenitic state (accompanied with a return to the initial length). In the present prestressed mechanism with antagonistic wires, the situation is more complex as the transformation temperatures increase with the stress. Moreover, the shape memory effect of an activated SMA wire is hindered by other SMA wires. Consequently, in spite of the symmetry of the mechanism, a history effect is expected, causing the symmetry of the discrete workspace to be lost a priori.

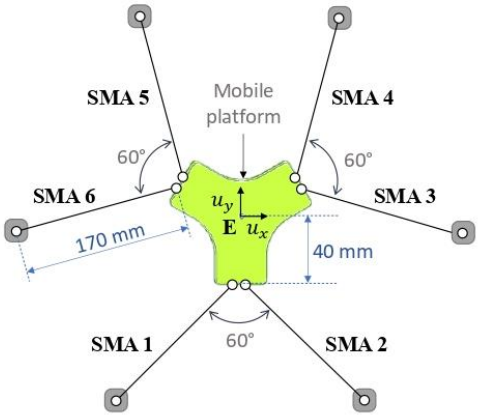

Figure 1 Architecture of the prestressed planar mechanism under study.

The workspace is generated by a binary thermal actuation of the SMA wires. Since six wires are employed here, we can distinguish 64 possible heating configurations, from no wire actuated (all at ambient temperature) to six wires actuated (all heated) as presented in **Figure 2a**. For this study, two operating temperatures are set: 18 °C (ambient temperature T_{amb} between A_s and M_s) and 110 °C (activation temperature, which is much higher than A_f). In **Figure 2a**, the red bold lines correspond to SMA wires at activation temperature while blue lines correspond to wires at ambient temperature. Each configuration is identified by a six-digit binary number corresponding to the thermal state of the wires, for which "0" and "1" correspond to the non-actuated state and actuated state respectively.

The present paper is focused on the in-plane translation (u_x, u_y) of the middle point E of the mobile platform following a certain sequence of thermal actuations (see **Figure 2b**). The preliminary step is to prestress the mechanism by applying a same prestrain to all the SMA wires simultaneously at ambient temperature (configuration #1), leading to no movement of the mobile platform. The heating activation sequence thus starts with no wire actuated (configuration #1); then one wire is actuated, then two, three, five, and finally all wires are actuated (configuration #64). Note that we proceed by alternating the actuated wires in a rotational way. Note also that after each heating configuration, a return to ambient temperature (configuration #1) is applied.

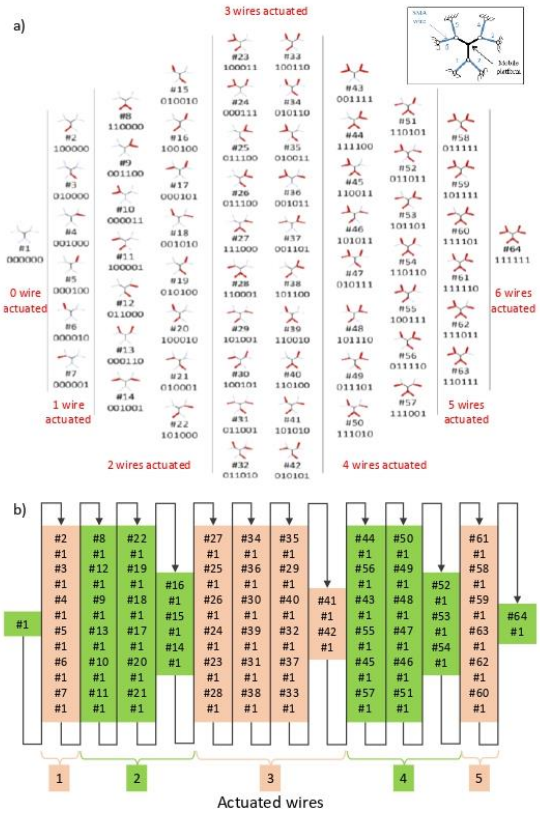

Figure 2 a) 64 possible heating configurations. **b)** Thermal activation sequence considered in the present case of study.

3 Finite element analysis of the discrete workspace

The movements of the mobile platform are calculated using the Ansys Mechanical APDL FE model with the Auricchio's model for the SMA behaviour [8]. Following the thermal actuation sequence presented in **Figure 2b**, we obtain the discrete workspace displayed in **Figure 3** in terms of 127 positions of the centre E of the mobile platform (63 actuated configurations and 64 ambient temperature state). It can be noted that the displacement amplitude along the x-axis and y-axis is about 7 mm and 6 mm respectively. The movement of the mobile platform

is significantly sensitive to the thermal sequence history. Indeed, it can be noted for instance that the final heating configuration (#64, all wires heated) does not lead to a return to the initial position ($u_x = 0$, $u_y = 0$) due to the previous steps. This can be explained by the fact that the heating of all SMA wires simultaneously did not lead to a return to full austenitic state of all. Differences in remaining martensite between the SMA wires (due to an history effect) led to a difference in their lengths although a same heating, and therefore to $u_x \neq 0$ and $u_y \neq 0$.

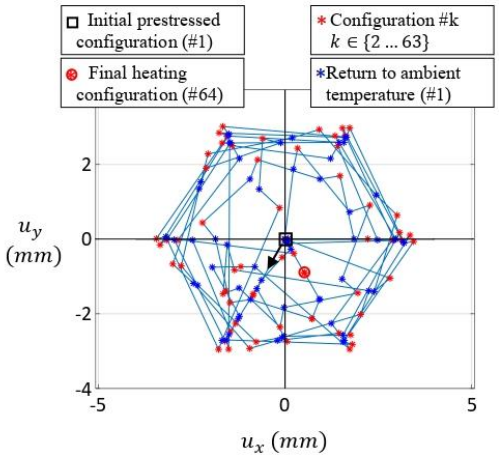

Figure 3 Discrete workspace following the thermal sequence in Fig. 2b: in-plane translation (u_x, u_y) of the mobile platform centre E.

4 First experimental test

Thanks to a physical prototype of the mechanism (see **Figure 4**), we were able to conduct a preliminary experimental test applying the thermal sequence from configuration #1 to configuration #21 in **Figure 2b**. Heating to 110 °C was performed using constant power by the Joule effect. Using an infrared camera, the duration to reach temperature stabilization in an actuated wire was estimated to about three minutes. To measure the displacements of the mobile platform, we used a D3 Nikon camera. Images were captured in the steady thermal state at each step of the thermal activation sequence.

Figure 5 shows the experimental results in terms of in-plane translation (u_x, u_y) of the mobile platform centre E. It can be noted that the envelop of the discrete workspace has a hexagonal shape with top and bottom sides that are horizontal, similarly to the numerical workspace in **Figure 3**. Moreover, the amplitude of translation is of more than 5 mm, which is similar to the order of magnitude of the numerical results. At each heating configuration, the impact of the previous steps can be evidenced by analysing the return to ambient temperature configuration (configurations #1): it can be seen that the corresponding points (back stars) in the graph are placed "in the direction" of the previous heating configuration.

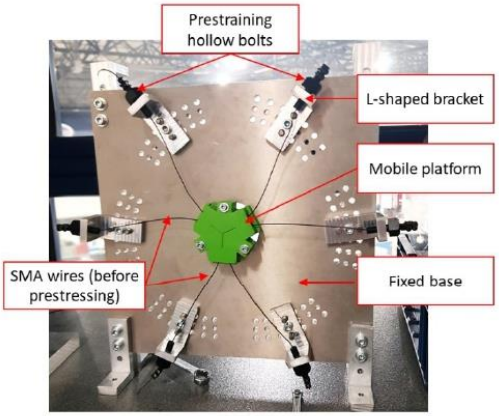

Figure 4 Physical prototype of the mechanism.

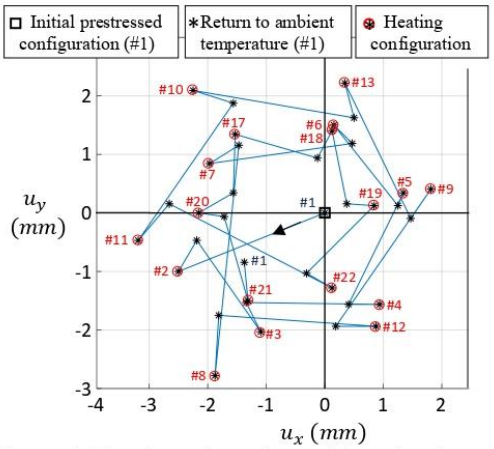

Figure 5 Experimental results applying the thermal sequence from configuration #1 to configuration #21 in Fig. 2b: in-plane translation (u_x, u_y) of the mobile platform centre E measured by camera.

5 Conclusion

This paper dealt with a case of study of the workspace of a SMA-driven mechanism. A discrete workspace was obtained due to the binary thermal actuation (either the ambient temperature or a given higher temperature) of the SMA wires. Both a numerical simulation and a preliminary experimental test evidenced the influence of the thermal actuation history on the workspace. Each heating configuration has an impact on the following heating steps. This is an important point to be considered in the future for the command of such type of mechanism. Although the studied mechanism featured a small translation workspace, it can easily accommodate size reduction. Further work is planned to improve the accuracy of the physical prototype in order to conduct more experiments.

6 References

[1] Higuchi T, Suzumori K, *Next-generation actuators leading breakthroughs*. Springer, London, UK, Japan, 2010

[2] Jani JM, Leary M, Subic A, Gibson MA, *A review of shape memory alloy research, applications and opportunities*. Materials and Design, 56:1078–1113, 2014

[3] Sofla AYN, Elzey DM, Wadley HNG, *Two-way antagonistic shape actuation based on the one-way shape memory effect*. Journal of Intelligent Material Systems and Structures, 19:1017–1027, 2008

[4] Mertmann M, Vergani G, *Design and application of shape memory actuators*. The European Physical Journal-Special Topics, 158:221–230, 2008

[5] Mekaouche A, Chapelle F, Balandraud X, *A compliant mechanism with variable stiffness achieved by rotary actuators and shape-memory alloy*. Meccanica, 53:2555–2571, 2018

[6] Mohd Jani J, Leary M, Subic A, *Designing shape memory alloy linear actuators: a review*. Journal of Intelligent Material Systems and Structures, 28:1699–1718, 2017

[7] Yuan H, Chapelle F, Fauroux JC, Balandraud X, *Concept for a 3D-printed soft rotary actuator driven by a shape-memory alloy: a review*. Smart Materials and Structures, 27:055005, 2018

[8] Boufayed R, Chapelle F, Destrebecq JF , Balandraud X, *Finite element analysis of a prestressed mechanism with multi-antagonistic and hysteretic SMA actuation*. Meccanica, 55:1007–1024, 2020

Appendix D: Example of an Ansys APDL script used in the thesis

This appendix proposes an example of an APDL script to model a cyclic rotation.

```
FINISH
/CLEAR
/FILNAME, Cyclic_rotation, 1
/TITLE, Cyclic_rotation


/COM,#=================================================================#
/COM,#-----------------------------------------------------------------#
/COM,#                          PREPROCESSOR                           #
/COM,#-----------------------------------------------------------------#
/COM,# ================================================================#

/PREP7
NLGEOM,ON      ! Large-deflection (large rotation/strain effects)

!*********************************************************************!
!                   DEFINITION OF SMA PARAMETERS
!*********************************************************************!

T_ambient_C=18       ! Ambient Temperature in[°C]
T_heating_C=88       ! Heating Temperature in[°C]

/COM,-----------------------------------------------------------------
/COM,              Physical parameters of SMA
/COM,-----------------------------------------------------------------

E_A=63000            ! Young Modulus Austenite [MPa]
E_M=35000            ! Young Modulus Martensite [MPa]
PR_SMA=0.33          ! Possion's ratio of SMA
A_s_C=24             ! Temperature of Austenite Start   in °C
A_f_C=36             ! Temperature of Austenite finish  in °C
M_s_C=-7             ! Temperature of Martensite start  in °C
M_f_C=-25            ! Temperature of Martensite finish in °C
Gamma=0.06           ! Max Transformation Strain 6%
Beta_1=8             ! Tilting of the transformation boundaries
                     ! in the phase diagram [MPa/K]

/COM,-----------------------------------------------------------------
/COM,                ANSYS parameters of SMA
/COM,-----------------------------------------------------------------

A_s=A_s_C+273.15     ! Temperature of Austenite Start   in [K]
A_f=A_f_C+273.15     ! Temperature of Austenite finish  in [K]
M_s=M_s_C+273.15     ! Temperature of Martensite start  in [K]
M_f=M_f_C+273.15     ! Temperature of Martensite finish in [K]
T_ambient=T_ambient_C+273.15      ! Ambient temperature in [K]
T_heating=T_heating_C+273.15      ! Heating temperature in [K]

h=(2* Beta_1*(M_s - M_f))/(3*Gamma) ! HARDENING PARAMETER   C1
T_0=M_s+((A_s - M_f)/2)             ! REF TEMP              C2
R_res_elas=(Beta_1*(A_s - M_f))/sqrt(6) ! ELASTIC LIMIT     C3
Beta=Beta_1*sqrt(2/3)  ! TEMPERATURE SCALING PARAMETER      C4
Deformee_max=Gamma*sqrt(3/2) ! MAX TRANSFORMATION STRAIN    C5


!*********************************************************************!
!                           BUILD GEOMETRY
!*********************************************************************!
/COM,-----------------------------------------------------------------
/COM,                        Parameterization
/COM,-----------------------------------------------------------------

Pt_ref_X=0               ! Reference point coordinate - X
Pt_ref_Y=0               ! Reference point coordinate - Y
Pt_ref_Z=0               ! Reference point coordinate - Z

Pi=acos(-1)              ! Value of Pi

Pre_strain=3.25          ! Pre-strain of the SMA wire
l_SMA=170                ! Length of the SMA wire
l_bar=40                 ! Length of one bar of the moving platform
ang_30=30*(Pi/180)       ! Angle 30°
ang_60=60*(Pi/180)       ! Angle 60°
ang_120=120*(Pi/180)     ! Angle 120°

theta=90*(Pi/180)        ! Angle between the first bar and the horizontal
ang_SMAs=60*(Pi/180)     ! Angle between two SMA wires
theta_SMA=Pi-(ang_SMAs/2) ! Angle between cross-bar and SMA wire

nbr_cycle=3


/COM,-----------------------------------------------------------------
/COM,             STRUCTURE OF THE CROSS-BARS
/COM,-----------------------------------------------------------------

! The first end of the cross-bars
```

```
Cr_1_X=Pt_ref_X
Cr_1_Y=Pt_ref_Y
Cr_1_Z=Pt_ref_Z

! The center of the cross-bars
Cr_0_X=l_bar*cos(theta)
Cr_0_Y=l_bar*sin(theta)
Cr_0_Z=0

! The second end of the cross-bars
Cr_2_X=Cr_0_X+l_bar*cos(ang_60-theta)
Cr_2_Y=Cr_0_Y-l_bar*sin(ang_60-theta)
Cr_2_Z=0

! The third end of the cross-bars
Cr_3_X=Cr_0_X-l_bar*cos(ang_120-theta)
Cr_3_Y=Cr_0_Y+l_bar*sin(ang_120-theta)
Cr_3_Z=0

/COM,---------------------------------------------------------------------
/COM,                    PLACEMENT OF SMA wires
/COM,---------------------------------------------------------------------

! First SMA wire SMA_1 and Second SMA wire SMA_2
SMA_1_X=Cr_1_X+l_SMA*cos(theta_SMA+theta)
!SMA_1_X=Cr_1_X-l_SMA*cos(theta_SMA+theta-Pi)
SMA_1_Y=Cr_1_Y+l_SMA*sin(theta_SMA+theta)
!SMA_1_Y=Cr_1_Y-l_SMA*sin(theta_SMA+theta-Pi)
SMA_1_Z=0

SMA_12_X=Pt_ref_X
SMA_12_Y=Pt_ref_Y
SMA_12_Z=Pt_ref_Z

SMA_2_X=Cr_1_X+l_SMA*cos(theta_SMA-theta)
!SMA_2_X=Cr_1_X-l_SMA*cos(Pi-theta_SMA+theta)
SMA_2_Y=Cr_1_Y-l_SMA*sin(theta_SMA-theta)
!SMA_2_Y=Cr_1_Y-l_SMA*sin(theta_SMA-theta)
SMA_2_Z=0

! Third SMA wire SMA_3 and Fourth SMA wire SMA_4
SMA_3_X=Cr_2_X+l_SMA*cos(ang_120+theta_SMA+theta)
!SMA_3_X=Cr_2_X+l_SMA*cos(-(ang_120+theta_SMA+theta))
SMA_3_Y=Cr_2_Y+l_SMA*sin(ang_120+theta_SMA+theta)
!SMA_3_Y=Cr_2_Y-l_SMA*sin(-(ang_120+theta_SMA+theta))
SMA_3_Z=0

SMA_34_X=Cr_2_X
SMA_34_Y=Cr_2_Y
SMA_34_Z=0

SMA_4_X=Cr_2_X+l_SMA*cos(ang_120-theta_SMA+theta)
SMA_4_Y=Cr_2_Y+l_SMA*sin(ang_120-theta_SMA+theta)
SMA_4_Z=0

! Fifth SMA wire SMA_5 and Sixth SMA wire SMA_6
SMA_5_X=Cr_3_X+l_SMA*cos(-ang_120+theta_SMA+theta)
SMA_5_Y=Cr_3_Y+l_SMA*sin(-ang_120+theta_SMA+theta)
SMA_5_Z=0

SMA_56_X=Cr_3_X
SMA_56_Y=Cr_3_Y
SMA_56_Z=0

SMA_6_X=Cr_3_X-l_SMA*cos(-ang_60-theta+theta_SMA)
SMA_6_Y=Cr_3_Y+l_SMA*sin(-ang_60-theta+theta_SMA)
SMA_6_Z=0

/COM,---------------------------------------------------------------------
/COM,            Creating Keypoints and Lines
/COM,---------------------------------------------------------------------
! Defining Keypoints
K,1,SMA_1_X ,SMA_1_Y ,SMA_1_Z      ! SMA_L_1
K,2,SMA_12_X,SMA_12_Y,SMA_12_Z     ! SMA_R_1
K,3,SMA_12_X,SMA_12_Y,SMA_12_Z     ! SMA_L_2
K,4,SMA_2_X ,SMA_2_Y ,SMA_2_Z      ! SMA_R_2

K,5,SMA_3_X ,SMA_3_Y ,SMA_3_Z      ! SMA_L_3
K,6,SMA_34_X,SMA_34_Y,SMA_34_Z     ! SMA_R_3
K,7,SMA_34_X,SMA_34_Y,SMA_34_Z     ! SMA_L_4
K,8,SMA_4_X ,SMA_4_Y ,SMA_4_Z      ! SMA_R_4

K,9,SMA_5_X ,SMA_5_Y ,SMA_5_Z      ! SMA_L_5
K,10,SMA_56_X,SMA_56_Y,SMA_56_Z    ! SMA_R_5
K,11,SMA_56_X,SMA_56_Y,SMA_56_Z      ! SMA_L_6
K,12,SMA_6_X ,SMA_6_Y ,SMA_6_Z       ! SMA_R_6

K,13, Cr_0_X, Cr_0_Y, Cr_0_Z         ! Center of the cross-bars
K,14, Cr_1_X, Cr_1_Y, Cr_1_Z         ! End_1 of the cross-bars
K,15, Cr_2_X, Cr_2_Y, Cr_2_Z         ! End_2 of the cross-bars
K,16, Cr_3_X, Cr_3_Y, Cr_3_Z         ! End_3 of the cross-bars

! Creating lines ( SMA wires )
l,1,2                                ! SMA_1
l,3,4                                ! SMA_2
l,5,6                                ! SMA_3
l,7,8                                ! SMA_4
l,9,10                               ! SMA_5
l,11,12                              ! SMA_6

! Creating lines ( Sturcture )
l,13,14                              ! Bar_1
l,13,15                              ! Bar_2
l,13,16                              ! Bar_3


!*********************************************************************!
!                           DEFINE MATERIALS !
!*********************************************************************!
/COM,---------------------------------------------------------------------
/COM,                     Define Element Types
/COM,---------------------------------------------------------------------

ET,1,BEAM188            ! Defining Element Type 1
```

```
SECTYPE,1,BEAM, CSOLID  ! Type of bars: Cylinder
SECDATA,.5

ET,2,BEAM188            ! Defining Element Type 2
SECTYPE,2,BEAM, RECT    ! Type of bars: Rectangular
SECDATA,26,20,2,2

ET,3,MPC184,6,,,1       ! Defining Element Type 3
SECTYPE,3,JOINT,REVO    ! REVOLUTE JOINT

/COM,---------------------------------------------------------------------
/COM,                    Define Material Properties
/COM,---------------------------------------------------------------------

! Defining Material Properties SMA
MP,EX,1,E_A
MP,PRXY,1,PR_SMA

! Defining MEFF parameters
C1=h                    ! [MPa]
C2=T_0                  ! [K]
C3=R_res_elas           ! [MPa]
C4=Beta                 ! [MPa/K]
C5=Deformee_max         ! %
C6=E_M                  ! [MPa]
C7=0                    ! M = 0, SYMMETRICAL BEHAVIOR
TB,SMA,1,,7,MEFF
TBDATA,1,C1, C2, C3, C4, C5, C6, C7

! Defining Material Properties: Steel
E_steel=200000
PR_steel=0.3

MP,EX,2,E_steel
MP,PRXY,2,PR_steel

!*********************************************************************!
!                          GENERATE MESH !
!*********************************************************************!

! Mesh generation
Type,1
Mat,1
SECNUM,1
LESIZE,1,,,10
LESIZE,2,,,10
LESIZE,3,,,10
LESIZE,4,,,10
LESIZE,5,,,10
LESIZE,6,,,10
LMESH,1,6,

! Mesh generation
Type,2
Mat,2
SECNUM,2
LESIZE,7,,,10
LESIZE,8,,,10
LESIZE,9,,,10
LMESH,7,9,

!*********************************************************************!
!                    CREATING REVOLUTE JOINTS !
!*********************************************************************!

TYPE,3
SECNUM,3

KSEL,S,KP,,2
NSLK,S
*GET,NODEKP2,NODE,0,NUM,MAX

KSEL,S,KP,,3
NSLK,S
*GET,NODEKP3,NODE,0,NUM,MAX

KSEL,S,KP,,6
NSLK,S
*GET,NODEKP6,NODE,0,NUM,MAX

KSEL,S,KP,,7
NSLK,S
*GET,NODEKP7,NODE,0,NUM,MAX

KSEL,S,KP,,10
NSLK,S
*GET,NODEKP10,NODE,0,NUM,MAX

KSEL,S,KP,,11
NSLK,S
*GET,NODEKP11,NODE,0,NUM,MAX

KSEL,S,KP,,14
NSLK,S
*GET,NODEKP14,NODE,0,NUM,MAX

KSEL,S,KP,,15
NSLK,S
*GET,NODEKP15,NODE,0,NUM,MAX

KSEL,S,KP,,16
NSLK,S
*GET,NODEKP16,NODE,0,NUM,MAX

ALLSEL

E,NODEKP2,NODEKP3
E,NODEKP2,NODEKP14
E,NODEKP6,NODEKP7
E,NODEKP6,NODEKP15
E,NODEKP10,NODEKP11
E,NODEKP10,NODEKP16

NSEL , ALL
```

```
316
317 SMA1_NODE_X=NINT((SMA_1_X+SMA_12_X)/2)
318 SMA1_NODE_Y=NINT((SMA_1_Y+SMA_12_Y)/2)
319 SMA1_NODE_Z=NINT((SMA_1_Z+SMA_12_Z)/2)
320
321 SMA2_NODE_X=NINT((SMA_2_X+SMA_12_X)/2)
322 SMA2_NODE_Y=NINT((SMA_2_Y+SMA_12_Y)/2)
323 SMA2_NODE_Z=NINT((SMA_2_Z+SMA_12_Z)/2)
324
325 SMA3_NODE_X=NINT((SMA_3_X+SMA_34_X)/2)
326 SMA3_NODE_Y=NINT((SMA_3_Y+SMA_34_Y)/2)
327 SMA3_NODE_Z=NINT((SMA_3_Z+SMA_34_Z)/2)
328
329 SMA4_NODE_X=NINT((SMA_4_X+SMA_34_X)/2)
330 SMA4_NODE_Y=NINT((SMA_4_Y+SMA_34_Y)/2)
331 SMA4_NODE_Z=NINT((SMA_4_Z+SMA_34_Z)/2)
332
333 SMA5_NODE_X=NINT((SMA_5_X+SMA_56_X)/2)
334 SMA5_NODE_Y=NINT((SMA_5_Y+SMA_56_Y)/2)
335 SMA5_NODE_Z=NINT((SMA_5_Z+SMA_56_Z)/2)
336
337 SMA6_NODE_X=NINT((SMA_6_X+SMA_56_X)/2)
338 SMA6_NODE_Y=NINT((SMA_6_Y+SMA_56_Y)/2)
339 SMA6_NODE_Z=NINT((SMA_6_Z+SMA_56_Z)/2)
340
341 SMA1_NODE = NODE (SMA1_NODE_X,SMA1_NODE_Y,SMA1_NODE_z )
342 SMA2_NODE = NODE (SMA2_NODE_X,SMA2_NODE_Y,SMA2_NODE_z )
343 SMA3_NODE = NODE (SMA3_NODE_X,SMA3_NODE_Y,SMA3_NODE_z )
344 SMA4_NODE = NODE (SMA4_NODE_X,SMA4_NODE_Y,SMA4_NODE_z )
345 SMA5_NODE = NODE (SMA5_NODE_X,SMA5_NODE_Y,SMA5_NODE_z )
346 SMA6_NODE = NODE (SMA6_NODE_X,SMA6_NODE_Y,SMA6_NODE_z )
347
348 SMA1_ELM = ENEARN (SMA1_NODE)
349 SMA2_ELM = ENEARN (SMA2_NODE)
350 SMA3_ELM = ENEARN (SMA3_NODE)
351 SMA4_ELM = ENEARN (SMA4_NODE)
352 SMA5_ELM = ENEARN (SMA5_NODE)
353 SMA6_ELM = ENEARN (SMA6_NODE)
354
355 size_array = 4*(nbr_cycle)+2
356 jmax=size_array+2
357 i=1
358
359 ! Creating Stresses Arrays for the 6 wires
360 *DIM, S_SMA1, array, size_array
361 *DIM, S_SMA2, array, size_array
362 *DIM, S_SMA3, array, size_array
363 *DIM, S_SMA4, array, size_array
364 *DIM, S_SMA5, array, size_array
365 *DIM, S_SMA6, array, size_array
366
367 ! Creating Stresses Arrays for the 6 wires
368 *DIM, ep_SMA1, array, size_array
369 *DIM, ep_SMA2, array, size_array
370 *DIM, ep_SMA3, array, size_array
371 *DIM, ep_SMA4, array, size_array
372 *DIM, ep_SMA5, array, size_array
373 *DIM, ep_SMA6, array, size_array
374
375 ! Creating DOFs Arrays for the center
376 *DIM, DepCentreX, array, size_array
377 *DIM, DepCentreY, array, size_array
378 *DIM, RotCentreZ, array, size_array
379
380
381
382 /COM,#=============================================================================#
383 /COM,#-----------------------------------------------------------------------------#
384 /COM,#                      PROCESSOR : SOLUTION                                   #
385 /COM,#-----------------------------------------------------------------------------#
386 /COM,#=============================================================================#
387
388 !*****************************************************************************!
389 ! APPLY LOADS - CONSTRAINTS
390 !*****************************************************************************!
391
392 /SOLU
393 NROPT,UNSYM              ! Use full Newton-Raphson with unsymmetric
394                          ! matrices of elements where the unsymmetric
395                          ! option exists
396 NSUBST,10,5000,1         ! Specifies the nbr of substeps to be taken
397                          ! this load step
398 OUTRES,ALL,ALL           ! Writes the solution of the specified
399                          ! solution results item for every substep
400
401 !*****************************************************************************!
402 !                           LOADS STEPS
403 !*****************************************************************************!
404
405 /COM,-----------------------------------------------------------------
406 /COM,                 TIME1 : Initial conditions
407 /COM,-----------------------------------------------------------------
408
409 TIME,1
410 BFUNIF,TEMP,A_f+100  ! Temperature to be sure that we have austenite
411 DK,1,UX,0            ! UX(SMA_L_1)=0
412 DK,1,UY,0            ! UY(SMA_L_1)=0
413 DK,4,UX,0            ! UX(SMA_R_2)=0
414 DK,4,UY,0            ! UY(SMA_R_2)=0
415
416 DK,5,UX,0            ! UX(SMA_L_3)=0
417 DK,5,UY,0            ! UY(SMA_L_3)=0
418 DK,8,UX,0            ! UX(SMA_R_4)=0
419 DK,8,UY,0            ! UY(SMA_R_4)=0
420
421 DK,9,UX,0            ! UX(SMA_L_5)=0
422 DK,9,UY,0            ! UY(SMA_L_5)=0
423 DK,12,UX,0           ! UX(SMA_R_6)=0
424 DK,12,UY,0           ! UY(SMA_R_6)=0
425 solve
426
427 /COM,-----------------------------------------------------------------
428 /COM,               TIME2 : Ambient temperature
429 /COM,-----------------------------------------------------------------
```

```
430
431 TIME,2
432 BFUNIF,TEMP,T_ambient ! Apply ambient temperature
433 solve
434
435 /COM,---------------------------------------------------------------------
436 /COM,                       TIME3 : Prestrain
437 /COM,---------------------------------------------------------------------
438 TIME,3
439 DK,13,All
440 DK,1,UX,Pre_strain*cos(theta_SMA+theta)
441 !DK,1,UX,-Pre_strain*cos(theta_SMA+theta-Pi)
442 DK,1,UY,Pre_strain*sin(theta_SMA+theta)
443 !DK,1,UY,-Pre_strain*cos(theta_SMA+theta-Pi)
444
445 DK,4,UX,Pre_strain*cos(theta_SMA-theta)
446 !DK,4,UX,-Pre_strain*cos(Pi-theta_SMA+theta)
447 DK,4,UY,-Pre_strain*sin(theta_SMA-theta)
448
449
450 DK,5,UX,Pre_strain*cos(ang_120+theta_SMA+theta)
451 DK,5,UY,Pre_strain*sin(ang_120+theta_SMA+theta)
452
453 DK,8,UX,Pre_strain*cos(ang_120-theta_SMA+theta)
454 DK,8,UY,Pre_strain*sin(ang_120-theta_SMA+theta)
455
456 DK,9,UX,Pre_strain*cos(-ang_120+theta_SMA+theta)
457 DK,9,UY,Pre_strain*sin(-ang_120+theta_SMA+theta)
458
459 DK,12,UX,-Pre_strain*cos(-ang_60-theta+theta_SMA)
460 DK,12,UY,Pre_strain*sin(-ang_60-theta+theta_SMA)
461 SOLVE
462
463
464 *DO, i, 1, nbr_cycle, 1
465
466 /COM,---------------------------------------------------------------------
467 /COM,                     Configuratio #41
468 /COM,---------------------------------------------------------------------
469 TIME,3+4*(i-1)+1
470 DKDELE, 13, ALL
471 BFL, 1, Temp, T_heating
472 BFL, 3, Temp, T_heating
473 BFL, 5, Temp, T_heating
474 BFL, 2, Temp, T_ambient
475 BFL, 4, Temp, T_ambient
476 BFL, 6, Temp, T_ambient
477 !CNVTOL,U, ,0.001,2, ,
478 SOLVE
479
480 /COM,---------------------------------------------------------------------
481 /COM,                      Configuratio #1
482 /COM,---------------------------------------------------------------------
483 TIME,3+4*(i-1)+2
484 BFL, 1, Temp, T_ambient
485 BFL, 3, Temp, T_ambient
486 BFL, 5, Temp, T_ambient
487 BFL, 2, Temp, T_ambient
488 BFL, 4, Temp, T_ambient
489 BFL, 6, Temp, T_ambient
490 !CNVTOL,U, ,0.001,2, ,
491 SOLVE
492
493 /COM,---------------------------------------------------------------------
494 /COM,                      Configuratio #42
495 /COM,---------------------------------------------------------------------
496 TIME,3+4*(i-1)+3
497 BFL, 2, Temp, T_heating
498 BFL, 4, Temp, T_heating
499 BFL, 6, Temp, T_heating
500 BFL, 1, Temp, T_ambient
501 BFL, 3, Temp, T_ambient
502 BFL, 5, Temp, T_ambient
503 !CNVTOL,U, ,0.001,2, ,
504 SOLVE
505
506 /COM,---------------------------------------------------------------------
507 /COM,                      Configuratio #1
508 /COM,---------------------------------------------------------------------
509 TIME,3+4*(i-1)+4
510 BFL, 2, Temp, T_ambient
511 BFL, 4, Temp, T_ambient
512 BFL, 6, Temp, T_ambient
513 BFL, 1, Temp, T_ambient
514 BFL, 3, Temp, T_ambient
515 BFL, 5, Temp, T_ambient
516 !CNVTOL,U, ,0.001,2, ,
517 SOLVE
518
519 *ENDDO
520
521 /COM,#======================================================================#
522 /COM,#----------------------------------------------------------------------#
523 /COM,#                          POSTPROCESSOR                               #
524 /COM,#----------------------------------------------------------------------#
525 /COM,#======================================================================#
526
527 /POST1
528 /ESHAPE,1 ,1
529 /DSCALE,,1
530
531 !*********************************************************************!
532 !                        STRESSES IN THE 6 SMA WIRES
533 !*********************************************************************!
534
535 /COM,---------------------------------------------------------------------
536 /COM, STRESS in the first SMA wire (S_SMA_1)
537 /COM,---------------------------------------------------------------------
538
539 S1_inc=1
540 *DO, j, 3, jmax, 1
541 SET,,,,,j
542 ETABLE, SSMA1, LS,1
543 *VGET, S_SMA1(S1_inc),ELEM,SMA1_ELM,ETAB,SSMA1
```

```
S1_inc=S1_inc+1
*ENDDO

/COM,---------------------------------------------------------------
/COM,            STRESS in the second SMA wire (S_SMA_2)
/COM,---------------------------------------------------------------

S2_inc=1
*DO, j, 3, jmax, 1
SET,,,,,j
ETABLE, SSMA2, LS,1
*VGET, S_SMA2(S2_inc),ELEM,SMA2_ELM,ETAB,SSMA2
S2_inc=S2_inc+1
*ENDDO

/COM,---------------------------------------------------------------
/COM,             STRESS in the third SMA wire (S_SMA_3)
/COM,---------------------------------------------------------------

S3_inc=1
*DO, j, 3, jmax, 1
SET,,,,,j
ETABLE, SSMA3, LS,1
*VGET, S_SMA3(S3_inc),ELEM,SMA3_ELM,ETAB,SSMA3
S3_inc=S3_inc+1
*ENDDO

/COM,---------------------------------------------------------------
/COM,           STRESS in the fourth SMA wire (S_SMA_4)
/COM,---------------------------------------------------------------

S4_inc=1
*DO, j, 3, jmax, 1
SET,,,,,j
ETABLE, SSMA4, LS,1
*VGET, S_SMA4(S4_inc),ELEM,SMA4_ELM,ETAB,SSMA4
S4_inc=S4_inc+1
*ENDDO

/COM,---------------------------------------------------------------
/COM,            STRESS in the fifth SMA wire (S_SMA_5)
/COM,---------------------------------------------------------------

S5_inc=1
*DO, j, 3, jmax, 1
SET,,,,,j
ETABLE, SSMA5, LS,1
*VGET, S_SMA5(S5_inc),ELEM,SMA5_ELM,ETAB,SSMA5
S5_inc=S5_inc+1
*ENDDO

/COM,---------------------------------------------------------------
/COM,           STRESS in the sixth SMA wire (S_SMA_6)
/COM,---------------------------------------------------------------

S6_inc=1
*DO, j, 3, jmax, 1
SET,,,,,j
ETABLE, SSMA6, LS,1
*VGET, S_SMA6(S6_inc),ELEM,SMA6_ELM,ETAB,SSMA6
S6_inc=S6_inc+1
*ENDDO

/COM,---------------------------------------------------------------
/COM,          STRAIN in the first SMA wire (ep_SMA_1)
/COM,---------------------------------------------------------------

ep1_inc=1
*DO, j, 3, jmax, 1
SET,,,,,j
ETABLE, epSMA1, LEPTO,1
*VGET, ep_SMA1(ep1_inc),ELEM,SMA1_ELM,ETAB,epSMA1
*VOPER, ep_SMA1(ep1_inc),ep_SMA1(ep1_inc),MULT,100,,
ep1_inc=ep1_inc+1
*ENDDO

ep2_inc=1
*DO, j, 3, jmax, 1
SET,,,,,j
ETABLE, epSMA2, LEPTO,1
*VGET, ep_SMA2(ep2_inc),ELEM,SMA2_ELM,ETAB,epSMA2
*VOPER, ep_SMA2(ep2_inc),ep_SMA2(ep2_inc),MULT,100,,
ep2_inc=ep2_inc+1
*ENDDO

ep3_inc=1
*DO, j, 3, jmax, 1
SET,,,,,j
ETABLE, epSMA3, LEPTO,1
*VGET, ep_SMA3(ep3_inc),ELEM,SMA3_ELM,ETAB,epSMA3
*VOPER, ep_SMA3(ep3_inc),ep_SMA3(ep3_inc),MULT,100,,
ep3_inc=ep3_inc+1
*ENDDO

ep4_inc=1
*DO, j, 3, jmax, 1
SET,,,,,j
ETABLE, epSMA4, LEPTO,1
*VGET, ep_SMA4(ep4_inc),ELEM,SMA4_ELM,ETAB,epSMA4
*VOPER, ep_SMA4(ep4_inc),ep_SMA4(ep4_inc),MULT,100,,
ep4_inc=ep4_inc+1
*ENDDO

ep5_inc=1
*DO, j, 3, jmax, 1
SET,,,,,j
ETABLE, epSMA5, LEPTO,1
*VGET, ep_SMA5(ep5_inc),ELEM,SMA5_ELM,ETAB,epSMA5
*VOPER, ep_SMA5(ep5_inc),ep_SMA5(ep5_inc),MULT,100,,
ep5_inc=ep5_inc+1
*ENDDO

ep6_inc=1
*DO, j, 3, jmax, 1
```

```
SET,,,,j
ETABLE, epSMA6, LEPTO,1
*VGET, ep_SMA6(ep6_inc),ELEM,SMA6_ELM,ETAB,epSMA6
*VOPER, ep_SMA6(ep6_inc),ep_SMA6(ep6_inc),MULT,100,,
ep6_inc=ep6_inc+1
*ENDDO

!*********************************************************************!
!            DEGREES OF FREEDOM OF THE MOVING PLATFORM CENTER
!*********************************************************************!
/COM,-----------------------------------------------------------------
/COM,               Displacement of the center UX
/COM,-----------------------------------------------------------------

UX_inc=1
*DO, j, 3, jmax, 1
SET,,,,j
*VGET, DepCentreX(UX_inc),NODE,NODE(Cr_0_X, Cr_0_Y, Cr_0_Z),U,X
UX_inc=UX_inc+1
*ENDDO

/COM,-----------------------------------------------------------------
/COM,               Displacement of the center UY
/COM,-----------------------------------------------------------------

UY_inc=1
*DO, j, 3, jmax, 1
SET,,,,j
*VGET, DepCentreY(UY_inc),NODE,NODE(Cr_0_X, Cr_0_Y, Cr_0_Z),U,Y
UY_inc=UY_inc+1
*ENDDO


/COM,-----------------------------------------------------------------
/COM,                 Rotation of the center ROTZ
/COM,-----------------------------------------------------------------

RZ_inc=1
*DO, j, 3, jmax, 1
SET,,,,j
*VGET, RotCentreZ(RZ_inc),NODE,NODE(Cr_0_X, Cr_0_Y, Cr_0_Z),ROT,Z
*VOPER, RotCentreZ(RZ_inc),RotCentreZ(RZ_inc),MULT,(180/Pi),,
RZ_inc=RZ_inc+1
*ENDDO


/COM,-----------------------------------------------------------------
/COM,                         Outputs File
/COM,-----------------------------------------------------------------

/out,Stress_Cyclic_rotation,txt
*vwrite,S_SMA1(1),S_SMA2(1),S_SMA3(1),S_SMA4(1),S_SMA5(1),S_SMA6(1)
(F12.6,' ',F12.6,' ',F12.6,' ',F12.6,' ',F12.6,' ',F12.6,' ')%/
/out
*cfclos
!--------------------------------------------------------------------
/out,Strain_Cyclic_rotation,txt
*vwrite,ep_SMA1(1),ep_SMA2(1),ep_SMA3(1),ep_SMA4(1),ep_SMA5(1),ep_SMA6(1)
(F12.6,' ',F12.6,' ',F12.6,' ',F12.6,' ',F12.6,' ',F12.6,' ')%/
/out
*cfclos
!--------------------------------------------------------------------
/out,UX_UY_RotZ_ROTZ_Cyclic_rotation,txt
*vwrite,DepCentreX(1),DepCentreY(1),RotCentreZ(1)
(F12.6,' ',F12.6,' ',F12.6,' ')%/
/out
*cfclos


```

Modelling, design and testing of a multi-antagonistic and hysteretic mechanism driven by shape memory alloy wires

Abstract

This thesis manuscript describes the modeling, design and experimentation of a plane-parallel prestressed mechanism whose actuators are shape memory alloy (SMA) components working in an antagonistic way. The integration of this type of active materials in robotic systems is becoming more and more important due to their remarkable properties for metals: superelasticity, high damping capacities, as well as different shape memory effects depending on the applied thermomechanical conditions. The so-called "one-way" shape memory effect is particularly interesting from an application point of view for the creation of new generation actuators. Linear and rotary SMA-based actuators are widely developed in the literature. However, several obstacles hinder the development of such systems: difficulty in coupling thermal/electrical insulation and mechanical fixity; complexity in modeling the behavior due to a nonlinear and hysteretic response; strong thermomechanical couplings; need for restoring forces to create a two-way actuation. This last point is even more complex to manage in the presence of several SMA components working in parallel in a mechanism: the multi-antagonistic character of the actuation, coupled with a non-linear hysteretic response of each SMA, is the main focus of this scientific research. In practice, a finite element model of a plane parallel prestressed mechanism with three degrees of freedom and driven by six SMA wires has been developed. These wires are binary actuated independently in the first approach, but they all interact together, making the prediction of the actuation complex. Different cases of study have been treated: discrete workspace, configurations to be avoided, variable stiffness, attraction and hysteresis effects acting on the workspace. A physical demonstrator was also designed and tested. A key point was the thermomechanical "preparation" of the SMA wires before their use, as well as the implementation of a specific procedure for anchoring the wires in the mechanism thanks to a judicious choice of the phase transformation temperatures of the selected nickel-titanium alloy. The experimental results showed the efficiency of the system implementation, and the good qualitative agreement of the measurements with the simulations makes it possible to control the system. The study brings elements of understanding of the complex phenomena involved, which allows to consider the design of innovative actuators with new architectures of arrangement of the SMA components.

Keywords: shape memory alloys; prestressed parallel mechanism; actuation; multi-antagonism; finite element modeling; demonstrator

Modélisation, conception et expérimentations d'un mécanisme multi-antagoniste et hystérétique actionné par des fils en alliage à mémoire de forme

Résumé

Ce manuscrit de thèse décrit la modélisation, conception et expérimentation d'un mécanisme précontraint parallèle plan dont les actionneurs sont des composants en alliage à mémoire de forme (AMF) travaillant de manière antagoniste. L'intégration de ce type de matériaux actifs dans des systèmes robotiques prend de plus en plus d'ampleur du fait de leurs propriétés remarquables pour des métaux : superélasticité, grandes capacités d'amortissement, ainsi que différents effets de mémoire de forme dépendant des conditions thermomécaniques appliquées. L'effet mémoire de forme dit « simple-sens » est particulièrement intéressant d'un point de vue applicatif pour la création d'actionneurs de nouvelle génération. Les actionneurs linéaires et rotatifs à base d'AMF sont largement développés dans la littérature. Plusieurs verrous freinent toutefois le développement de tels systèmes : difficulté à coupler isolation thermique/électrique et fixité mécanique ; complexité à modéliser le comportement du fait d'une réponse non-linéaire et hystérétique ; couplages thermomécaniques forts ; nécessité de forces de rappel pour créer un actionnement à double-sens. Ce dernier point est d'autant plus complexe à gérer en présence de nombreux composants AMF travaillant en parallèle dans un mécanisme : le caractère multi-antagoniste de l'actionnement, couplé à une réponse non-linéaire hystérétique de chaque AMF, est le verrou scientifique sur lequel ce travail de recherche s'est focalisé. En pratique, un modèle par éléments finis a été développé sur un mécanisme précontraint parallèle plan à trois degrés de liberté et piloté par six fils AMF. Ceux-ci sont actionnés indépendamment de manière binaire en première approche, mais interagissent tous ensemble, rendant complexe la prédiction de l'actionnement. Différents cas d'étude ont été traités : espace de travail discret, configurations à éviter, rigidité variable, effet d'attraction et d'hystérésis agissant sur l'espace de travail. Un démonstrateur physique a également été conçu et testé. Un point clé a été la « préparation » thermomécanique des fils AMF avant leur utilisation, ainsi que la mise en place d'une procédure spécifique d'ancrage des fils dans le mécanisme grâce à un choix judicieux des températures de transformation de phase de l'alliage nickel-titane sélectionné. Les résultats expérimentaux ont montré l'efficacité de mise en œuvre du système, et le bon accord qualitatif des mesures par rapport aux simulations rend envisageable une commande du système. L'étude apporte des éléments de compréhension des phénomènes complexes impliqués, ce qui permet d'envisager la conception d'actionneurs innovants avec de nouvelles architectures d'arrangement des composants AMF.

Mots clés : alliages à mémoire de forme ; mécanisme parallèle précontraint ; actionnement ; multi-antagonisme ; modélisation par éléments finis ; démonstrateur